



UNIVERSITEIT VAN PRETORIA  
UNIVERSITY OF PRETORIA  
YUNIBESITHI YA PRETORIA

**Study of the wear and rolling contact fatigue of class B wheel against the  
R350HT and R260 rail steels using the twin-disc wear simulator**

Candidate: **Tshenolo Phinah Leso**

Supervisors: Prof Charles Witness Siyasiya and Prof Roelf Johannes Mostert

A dissertation submitted in partial fulfilment of the requirements for the degree of

**PhD (Metallurgical Engineering)**

Department of Materials Science and Metallurgical Engineering


Faculty of Engineering, Built Environment and Information Technology

University of Pretoria, South Africa

September 2023

## Declaration by author

I Tshenolo Phinah Leso declare that this thesis, submitted in fulfilment of the requirements for the degree Doctor of Philosophy (Metallurgical Engineering) from the University of Pretoria, is entirely my own work unless otherwise referenced or acknowledged. This document has not been submitted to any other academic institution for qualification.

Signature: 

Date: 25 September 2023

## Acknowledgements

First and foremost, I would like to thank God for giving me this opportunity to study and for his continued love by making it possible for me to complete my studies. To the following people and institutions, I am grateful for your support towards my studies:

- My supervisors Prof Charles Siyasiya and Prof Roelf Mostert for their supervision, support, and guidance for the entire duration of my PhD studies.
- Lepalakata Mahlatse Mongalo and Edwin Mohale from the Department of Mechanical and Aeronautical Engineering for assisting during manufacturing of the test rig and allowing the use of their facilities. Mr Kau Winston Mohlamonyane from the department Electrical, Electronic and Computer Engineering who helped with some electrical and electronics work.
- Industrial Minerals and Metals Research Institute (IMMRI) staff, Rorisang Maubane, Ruzanne Prins and Carel Coetzee for their assistance with materials characterisation.
- Gabi Ngema, Sibusiso Mahlalela and Kabelo Matea from the Department of Materials Science & Metallurgical Engineering at UP for their support.
- Department of Science and Innovation (DSI) through the Ferrous Materials Development Network (FMDN) and Mintek for the technical and financial support. A special thanks to Joseph Moema and Absalom Mabeba for their assistance towards my work.
- To my parents Maphakela and Manani, my siblings Mmusi and Botshelo, and my fiancée Mpho, I thank you for your love and support.
- Lastly, to my friends and colleagues: Thabang Mokoba, Bokamoso Phuthego, Dr Pearl Moruti, Boikaego Marumo, Tshepho Gaogane, Bonani Sekonopo, Mpho Mahlobogoane, Muhammed Salojee and Dr Tulani Mukarati thank you for your support and words of encouragement.

## Table of contents

Declaration by author.....	i
Acknowledgements.....	ii
Table of contents.....	iii
List of peer-reviewed publications.....	viii
Abstract.....	ix
List of figures.....	xi
List of tables.....	xxiii
List of symbols and abbreviations .....	xxiv
Chapter 1: Introduction.....	1
1.1 Background .....	1
1.2 Problem statement.....	5
1.3 Objectives.....	6
Chapter 2: Wheel and rail contact.....	7
2.1 Introduction .....	7
2.2 The sticking/slipping behaviour at the wheel-rail contact patch.....	9
2.3 Contact theories.....	10
2.3.1 The Hertz's theory .....	11
2.3.2 Carter's theory .....	16
2.3.3 Johnson and Vermeulen's theory .....	16
2.3.4 Kalker's theory .....	17
2.3.5 Polach's method .....	17
2.3.6 Recent finite element modelling approaches.....	18
2.4 Friction .....	20
Chapter 3: Wheel and rail materials.....	24
3.1 Introduction .....	24



3.2 Pearlitic steels.....	28
3.3 Bainitic steels .....	33
Chapter 4: Wear and rolling contact fatigue .....	35
4.1 Introduction .....	35
4.2 Wear mechanisms .....	38
4.2.1 Abrasive wear .....	38
4.2.2 Delamination wear.....	39
4.2.3 Corrosive wear.....	40
4.2.4 Fatigue wear .....	40
4.2.5 Fretting wear.....	41
4.3 Rolling contact fatigue .....	42
4.4 Material response to cyclic loading and shakedown maps .....	45
4.5 Wheel polygonal wear.....	47
4.6 Effects of non-metallic Inclusions on wear and RCF .....	49
4.7 Effects of wheel/rail contact temperature on wear and RCF .....	52
4.7.1 Wheel-rail contact patch flash temperature .....	54
4.8 Effects of wheel/rail hardness on wear and RCF .....	55
4.8.1 Plastic deformation of wheel and rail steels .....	57
4.9 Effect of slip ratio on wear and RCF.....	59
4.10 Effect of third body materials on wear and RCF .....	62
4.10.1 Liquid lubricants.....	63
4.10.2 Solid lubricants .....	65
4.10.3 Leaves .....	65
4.11 Measures to mitigate wear and RCF .....	66
4.11.1 Development of new materials .....	66
4.11.2 Friction modifiers .....	67

4.12 Wear prediction models .....	68
4.12.1 Archard wear model .....	69
4.12.2 The energy dissipation model.....	69
4.12.3 Sliding distance consideration in the wear model .....	71
4.13 Wear test rigs for railway applications.....	73
4.13.1 Pin-on-disc.....	74
4.13.2 Block-on- ring.....	74
4.13.3 Pin-on-reciprocating plate .....	75
4.13.4 Twin-disc .....	76
4.13.5 Requirements for downscaling twin-disc testing.....	77
Chapter 5: Test rig design and development.....	80
5.1 Introduction .....	80
5.2 Motors and variable speed drives.....	82
5.3 Load measurement .....	83
5.4 Torque and friction measurement .....	83
5.5 Wheel disc temperature measurement.....	84
5.6 Application of third body materials .....	85
Chapter 6: Experimental methods.....	86
6.1 Test materials .....	86
6.1.1 Wheel steel .....	89
6.1.2 Rail steels.....	90
6.2 Sectioning.....	91
6.3 Testing procedure.....	92
6.4 Validation of the test rig and results .....	95
6.4.1 Repeatability and reproducibility of the results.....	95
6.4.2 Load stability during testing .....	96

Chapter 7: Results and analysis .....	98
7.1 Dry contact .....	98
7.1.1 Coefficient of friction .....	98
7.1.2 Mass loss, wear rate and wear index .....	100
7.1.3 Surface morphology, roughness and topography .....	102
7.1.4 Plastic deformation and sub-surface damage .....	105
7.1.5 Wheel disc temperature .....	113
7.2 Lubricated contact (oil and water) .....	114
7.2.1 Effects of lubrication on coefficient of friction and wear rate .....	114
7.2.2 Effects of lubrication on surface morphologies and roughness.....	116
7.2.3 Effects of lubrication on plastic deformation .....	119
7.2.4 Effects of lubrication on rolling contact fatigue and sub-surface damage .....	121
7.2.5 Effects of lubrication on wheel disc temperature .....	124
Chapter 8: Discussion .....	126
8.1 Wear regimes and mechanisms .....	126
8.2 Wear prediction model for the wheel .....	126
8.2.1 Wheel wear rate and reduction in diameter .....	127
8.2.2 The wheel reprofiling model .....	133
8.2.3 Problems with the proposed wheel wear prediction model.....	136
8.3 Limitations of the test rig .....	137
8.3.1 The Hertzian downscaling rule.....	137
8.3.2 Maximum contact load .....	138
8.3.3 The negative slope effect.....	139
Chapter 9:.....	141
9.1 Conclusions .....	141
9.2 Recommendations for future work.....	142

9.3 References .....	143
9.4 Appendices .....	177
9.4.1 Appendix B: Test rig drawings.....	177
9.4.2 Appendix C: Pictures during development of the test rig .....	180
9.4.3 Appendix A: Wheel model drawings .....	181

## List of peer-reviewed publications

1. **T. P. Leso**, C. W. Siyasiya, R. J. Mostert & J. Moema, (2023). " Effects of lubrication on wear and rolling contact fatigue behaviour of class B wheel steels against R350HT rail steels using a twin disc wear simulator," Tribology Transactions, <https://doi.org/10.1080/10402004.2023.2217440>
2. **T. P. Leso**, C. W. Siyasiya, R. J. Mostert & J. Moema, (2022). "Effects of slip ratio on wear performance of class B wheel steels against softer R260 rail steels using the twin disc setup," South African Journal of Industrial Engineering, vol. 33, no. 3, pp. 290-298, <http://dx.doi.org//10.7166/33-3-2805>
3. **T. P. Leso**, C. W. Siyasiya, R. J. Mostert & J. Moema, (2022). Study of rolling contact fatigue, rolling and sliding wear of class B wheel steels against R350HT and R260 rail steels under dry contact conditions using the twin disc setup, Tribology International, Volume 174, <https://doi.org/10.1016/j.triboint.2022.107711>
4. **T. P. Leso**, C. W. Siyasiya, R. J. Mostert, & J. Moema, (2021). Study of wear performance of wheel and rail steels under dry sliding conditions. Suid-Afrikaans Tydskrif vir Natuurwetenskap en Tegnologie/South African Journal of Science and Technology, 40(1), 44-50. <https://doi.org/10.36303/SATNT.2021cosaami.09>

## Abstract

Maintenance due to the replacement of damaged wheels and rails as a result of wear and rolling contact fatigue (RCF) has been found to be the major problem to rail operating companies. This problem tends to lead to poor availability of railway networks. In order to solve this problem, cost effective wear simulators are developed to predict the wear behaviour of the rails and wheels in order to improve the preventive maintenance in pursuit of operational efficiency. Therefore, more studies that simulate a combination of rolling and sliding wear, together with RCF, are required, specifically for the Southern African region, where good rail wear simulators are not readily available. The problem with wear and RCF simulators is high production costs and, therefore, part of this work was to solve this problem by developing a cost-effective wear test rig that would be able to simulate RCF, sliding and rolling wear as experienced by the wheel and rail during movement of train on rail tracks. For this work, it was decided that twin-disc concept would be used, since literature clearly demonstrated that the method was successful in simulating the three damage mechanisms mentioned. The developed twin-disc wear test rig was successful in simulating both rolling and sliding wear and parameters such as applied load and speed (slip) were easily varied so to simulate the actual contact conditions between the wheel and rail. Outputs such as coefficient of friction and wheel disc temperature were obtained. The results obtained from the developed test rig agreed with literature as they are repeatable and comparable.

To validate the performance and accuracy of the rig, typical South African wheel and rail materials were used. The wear and RCF performance of AAR class B wheels against BS EN 13674 R350HT and R260 rail steels under different slip ratios and applied loads were investigated. The results showed that the severity of wear is heavily dependent on slip ratio i.e., increased with slip ratio. Severe plastic deformation was also observed at high values of slip ratio. The AAR class B wheels performed better against the softer R260 rail as compared to the harder R350HT rail. As expected, the R350HT performed better than the R260 due to it having higher hardness values and finer interlamellar spacing. Three wear regimes were identified from the plots of wear rate versus wear index ( $T\gamma/A$ ) namely; mild wear, severe wear and catastrophic wear. The effects of introducing water and oil on the contact surface were investigated. It was found that wear was much lower when water or oil was introduced at the wheel-rail interface compared to dry conditions, for all slip ratios. When water was used, the main cause of RCF was found to be fluid crack pressurisation. The RCF cracks were also

observed under dry contact. Therefore, the rig was successful in simulating wear and RCF at the wheel/rail contact under different contact conditions as experienced by the wheel and rail during movement of train on rail tracks. For the wear rates model, a data correlation coefficient to link twin disc and field wear rates was determined and used to predict the reprofiling times of wheels for two different distances of 100 000 and 200 000 km. Therefore, the purpose of this study was achieved in providing a tool for the predictive maintenance for the local rail industry that uses AAR class B wheels against R350HT or R260 rail combinations.

## List of figures

Figure 1.1: Transnet’s revenue contribution by division in (a) 2021 [9] and (b) 2022 [10] with the freight rail division being the major contributor. ....	2
Figure 1.2: South Africa’s rail status quo: SA freight rail network and rail infrastructure assets [11]. ....	3
Figure 2.1: Issues related to the wheel/rail contact [31]. ....	7
Figure 2.2: The wheel/rail contact; (a) front and (b) side views [32]. ....	8
Figure 2.3: (a) Schematic diagram showing different contact zones of the wheel/rail contact, adapted by Lewis and Olofsson [33] from Tournay [34]; (b) Schematic diagram illustrating two contact types at the wheel/rail contact being between the wheel tread and rail head (rolling/sliding contact) and between the wheel flange and the rail gauge (pure sliding) [35].	9
Figure 2.4: Schematic representation of typical (a) wheel and (b) rail profiles. ....	9
Figure 2.5: Relationship between traction and creep at the wheel-rail interface [28]. ....	10
Figure 2.6: Contact theories and their interrelations, adapted from [39]. ....	11
Figure 2.7: Hertzian contact: (a) general case, (b) the railway case [41]. ....	12
Figure 2.8: (a) A schematic illustration showing a contact between cylinders under a contact load, $F$ , along the contact length $l$ and (b) an illustration showing an elliptical contact between the contacting cylinders with a contact width of $2b$ [44]. ....	14
Figure 2.9: (a) Rolling of a sphere on a plane as per Johnson’s theory (where $U$ is the plane’s linear velocity, $\Omega$ is the sphere’s angular velocity relative to the plane about the normal axis $O_z$ and $\omega$ is the sphere’s angular velocity about a diametral axis parallel to $O_y$ ) [55]; (b) areas of slip and adhesion according to Vermeulen and Johnson, adapted from [56]. ....	17
Figure 2.10: Distribution of normal and tangential stresses in the wheel-rail contact area, Polach [61]. ....	18
Figure 2.11: Comparison of the maximum contact pressure with respect to the contact area; (a) FE ANSYS code by Telliskivi and Olofsson, (b) CONTACT code by Kalker and (c) Hertz method [63]. ....	19
Figure 2.12: Zhao and Li’s 3D transient FE model solutions [60], validated against Hertz theory and Kalker’s CONTACT code: (a) the surface shear stress distribution (absolute values) along	



the longitudinal axis when coefficient of friction=0.3; (b) distribution of micro-slip (absolute values) along the longitudinal axis when coefficient of friction=0.3 [60].....20

Figure 2.13: A schematic illustration showing two objects under (a) rolling and (b) sliding motions [68].....21

Figure 2.14: Example of wheel/rail damage in low adhesion conditions: (a) skidding marks on the rail surface and (b) wheel scratch on the tread [76].....23

Figure 2.15: Optimal wheel/rail contact friction coefficients [70]. .....23

Figure 3.1: (a) Isothermal transformation diagram for a eutectoid iron–carbon alloy, with superimposed isothermal heat treatment curve (ABCD), showing the microstructures before, during, and after the austenite-to-pearlite transformation (Adapted by [93] from [96]); (b) Schematic representation of the formation of pearlite from austenite; direction of carbon diffusion indicated by arrows [93].....29

Figure 3.2: (a) SEM micrograph of a fully pearlitic steel showing random orientation of ferrite and cementite alternating lamellae colonies [97]; (b) TEM micrograph of pearlite in rail steel showing high magnification of lamella structure consisting of alternating layers of ferrite and cementite [92]. .....29

Figure 3.3: Micrographs of (a) coarse pearlite and (b) fine pearlite, 3000X [98]. .....30

Figure 3.4: (a) Hardness and yield strength in fully pearlitic microstructures as a function of pearlite interlamellar spacing [99]; (b) The relationship between hardness and pearlite interlamellar spacing for different rail steels [102].....31

Figure 3.5: Wear rate against pearlite interlamellar spacing for several rail steel chemistries and heat treatments at 1220 and 900 N mm<sup>-2</sup> contact pressures [102]. .....32

Figure 3.6: Influences of (a) pearlite interlamellar spacing (b) pearlite colony size and (c) austenite grain size on the thickness of plastic deformation [79].....32

Figure 3.7: (a) Lower bainite obtained by isothermal transformation for 30 minutes at 453 °C causing the precipitation of carbides between the ferrite platelets; (b) distribution of cementite particles between ferrite platelets in upper bainite (AISI 4340 steel) [105].....33

Figure 3.8: (a) A schematic illustration showing the stages in the development of a bainitic microstructure [106], (b) Charpy curve of lower and upper bainite [105]. .....34

Figure 3.9: Wear rate for pearlitic and bainitic steels as a function of normal load [110]. .....34

Figure 4.1: Schematic diagram of (a) rail peeling (b) rail spalling and (c) wheel cracks [118].  
.....35

Figure 4.2: Different types of wheel wear; (a) Flange wear (b) flanking wear (c) Hollow wear  
(d) Dual-hollow wear and (e) Polygonal wear [119]. .....36

Figure 4.3: Typical rail damages on a heavy-haul railway curved rail: (a) Side wear; (b) surface  
crack; (c) spalling [120]. .....36

Figure 4.4: Examples of shelling from gauge corner collapse on rail steels [121]. .....37

Figure 4.5: (a) R8T wheel wear rates (against 900A rail) on twin-disc testing and (b) schematic  
diagram of wear features and regimes [20]. .....38

Figure 4.6: Two-body and three-body abrasive wear mechanisms [33]. .....39

Figure 4.7: Micrograph showing delamination wear under sliding wear testing [129]. .....39

Figure 4.8: Schematic illustration of the process of surface crack initiation and propagation  
during fatigue wear [133]. .....40

Figure 4.9: Schematic diagram showing different stages occurring during fretting wear; (a)  
cylinder fretting on a flat, (b) debris particles removed from the cylinder and flat, (c) Debris  
forming a compact layer, (d) the compacted debris layer becomes part of the cylinder changing  
its shape [135]. .....41

Figure 4.10: Surface fatigue cracks on the railway, (a) wheel tread; (b) rail head [150]. .....43

Figure 4.11: Typical rail RCF cracks: (a) head checks on the surface of a rail [151], and (b)  
typical squat defect (single squat) [152]. .....43

Figure 4.12: (a) The crash site at Hatfield (UK), showing disintegrated rail [154], (b)  
fragmented rail due to fractures from multiple rolling contact fatigue cracks [25]. .....44

Figure 4.13: Qualitative graph of damaged depth  $D_z$  vs. Number of cycles (N): (a) in condition  
of prevalent wear; (b) in condition of prevalent RCF [159]. .....45

Figure 4.14: Material response to cyclic loading: (a) purely elastic deformations, (b) elastic  
shakedown, (c) plastic shakedown and (d) ratchetting (adapted by [161] from [160]). Where  
 $\sigma_{FL}$  is the fatigue limit,  $\sigma_Y$  is the elastic yield limit,  $\sigma_{el}$  is the elastic shakedown limit and  $\sigma_{pl}$  is  
the plastic shakedown limit [164]. .....46

Figure 4.15: Shakedown map for a perfectly plastic and a kinematically hardening material, where  $P_0$  is the maximum Hertzian pressure,  $N$  normal load,  $a$  and  $b$  are semi axes of the wheel-rail contact patch and  $k_e$  is the shear yield limit, (Adapted from [160])......47

Figure 4.16: Wheel roughness and polygonal order before and after re-profiling: (a) wheel roughness; (b) polygon order [168]. .....48

Figure 4.17: Wheel profiles and wear within a reprofiling cycle [169].....48

Figure 4.18: (a) Model for rolling noise generation and (b) A schematic diagram showing the mechanism of generation of rolling noise [172]. .....49

Figure 4.19: a) SEM micrograph of a wheel rim sample showing the pearlite structure and an inclusion [178]; b) Manganese sulphide inclusions in a bainitic microstructure [176]. .....50

Figure 4.20: (a) The effect of number of inclusions on the fatigue life of ball bearings by oxide inclusions larger than  $30\ \mu\text{m}$  [181]. (b) Relationship between average inclusion diameter and fatigue strength reduction factor [179]. .....51

Figure 4.21: a) Dry wear rate vs. MnS length/unit area of field and MnS plus oxide length/unit area of field of C-Mn steels (as rolled-22 HRC, pearlitic-38 HRC and bainitic-42 HRC) and, b) dry wear rate vs. sulphide volume fraction percentage of all vacuum melted Cr-Mo steels [180]......51

Figure 4.22: (a) Appearance of brittle martensite (‘white layer’) and (b) spalling due to thermal cracking [115]. .....52

Figure 4.23: Periodic heating and cooling of the tread of a block-braked wheel [186]. .....53

Figure 4.24: Contact temperatures and wear coefficients of R8T wheel steel against UIC60 900A rail material on twin disc setup [190]......54

Figure 4.25: Thermal cracks created on the wheel tread [196]......55

Figure 4.26: Effect of hardness of metals on relative wear resistance in two body abrasion: (a) pure metals; and (b) steels with varying compositions and heat treatments [66]. .....56

Figure 4.27: Wear rate against hardness (BHN) at different contact pressures [102]. .....57

Figure 4.28: Micro hardness profiles for carbide-free bainitic steel after rolling and sliding wear testing at different rolling cycles [209]. .....58

Figure 4.29: Deformation depth of rail specimens under different contact loads [16]. .....58

Figure 4.30: Plastic deformation of rail and wheel specimens under different creepages (slip ratio) [22]. .....59

Figure 4.31: (a) Coefficient of friction against number of rolling cycles at different slip ratios, (b) average coefficient of frictions versus slip ratio for wheel and rail discs on twin disc setup [212]. .....60

Figure 4.32: (a) RCF life of rail discs vs. slip ratio and (b) Wear rate of rail discs vs. slip ratio [23]. .....61

Figure 4.33: Wheel specimen surfaces after wear testing at different slip ratios on a twin disc testing machine [213]. .....61

Figure 4.34: Classification of various wheel/rail contact contaminants [31]. .....62

Figure 4.35: Coefficient of traction (friction) against slip ratio at different contact conditions (third body materials) when R8T wheel was run against 900A rail under 1500 MPa contact pressure [214]. .....63

Figure 4.36: Fluid assisted mechanisms of crack growth: (a) shear mode crack growth, (b) hydraulic transmission of contact pressure, (c) entrapment and pressurisation of fluid inside the crack and (d) squeeze film pressure generation [216, 217]. .....64

Figure 4.37: Coefficient of friction versus number of rolling cycles at the wheel/rail under dry and after water was added [76]. .....64

Figure 4.38: A plot showing the relationship between the rotational number and the traction coefficient of wheel materials at different conditions of leaves on a twin disc setup [223]. ...65

Figure 4.39: (a) TEM micrograph of a carbide free bainitic steel with evidence of no inter-lath carbide precipitation [108], (b) TEM micrograph showing bainitic ferrite plates separated by films of stable austenite and (c) OM micrograph showing the large blocks of austenite left untransformed [105]. .....66

Figure 4.40: (a) Wear rates of new carbide free bainitic steels compared to conventional rail steels, (b) charpy impact toughness of new carbide free bainitic steels compared to old conventional rail steels [232]. .....67

Figure 4.41: (a) Typical coefficient of friction ranges for dry rail, friction modifiers, and lubricants [235]; (b) wear rates vs  $T\gamma/A$  for R8T wheel against R260 rail for run dry, water and grease (1500MPa, varying slip, 400rpm) [21]. .....68

Figure 4.42: Methodology of wheel wear prediction [240]..... 69

Figure 4.43: Wear rate as a function of wear index,  $T\gamma/A$  showing different regimes [243].. 70

Figure 4.44: Wear regimes identified during twin disc testing of BS11 rail material vs. Class D wheels, adapted by Lewis and Olofsson [37] from Bolton and Clayton [244]..... 71

Figure 4.45: Wear rate as a function of  $T\gamma/A$  [114]..... 71

Figure 4.46: Schematic illustration of the different possible wear test rig configurations for studying the wheel-rail interface [253]. ..... 73

Figure 4.47: A schematic diagram showing pin-on-disc wear test rig design [252]. ..... 74

Figure 4.48: A schematic diagram showing block-on-ring wear test rig design [252]..... 75

Figure 4.49: Block scar volume based on the width of the scar [256]..... 75

Figure 4.50: A schematic diagram showing pin-on-reciprocating plate wear test rig design [252]..... 76

Figure 4.51: Schematic diagram showing a twin-disc test rig design [260]..... 77

Figure 5.1: A schematic diagram of the twin disc test rig design showing its components. ... 81

Figure 5.2: A schematic diagram of the twin disc test rig showing; (a) full 3D and (b) isometric drawings..... 81

Figure 5.3: (a) Wear test rig configuration, (b) dimensions of the wheel and rail disc specimen. .... 82

Figure 5.4: (a) A drawing of the variable speed drives (VSD) showing their dimensions and (b) a photograph of one of the variable speed drives used to make the rig. .... 82

Figure 5.5: (a) Photograph of tachometer and (b) wiring diagram, (c) photograph of the LED speed digital display mounted on the rig. .... 83

Figure 5.6: (a) A photograph of the 10 kN C9C Force Transducer, (b) a photograph of the force transducer mounted into a holder..... 83

Figure 5.7: (a) Shaft mounted with strain gauges, transmitter, and power supply (battery); (b) receiver and antenna which are part of the TorqueTrak 10K-LP Torque Telemetry system. .84

Figure 5.8: (a) PyroMiniUSB Infrared temperature sensor and (b) CalexConfig data acquisition software display. .... 85

Figure 5.9: RS PRO diaphragm electric operated positive displacement pump.....85

Figure 6.1: Schematic diagram showing dimensions (mm) of the rail profiles, (a) 60E1/UIC60 and (b) 54E1/UIC54 rail profiles [91]. .....86

Figure 6.2: As-received hardness profiles of wheel and rail specimen, obtained at the rim and centre line of the rail head respectively. ....88

Figure 6.3: OM micrographs of the as-received (a) Class B wheel specimen obtained at the rim, (b) R350HT rail specimen and (c) R260 rail specimen showing pearlitic microstructures obtained at the rail head. ....89

Figure 6.4: SEM micrographs of the as-received (a) Class B wheel specimen obtained at the rim, (b) R350HT rail specimen and (c) R260 rail specimen showing different colonies of pearlite consisting of alternating layers of ferrite and cementite. ....89

Figure 6.5: OM micrographs of the as-received wheel specimen obtained at the rim, tread and flange showing a pearlitic microstructure.....90

Figure 6.6: SEM micrographs of the as-received (a) R350HT (b) R260 rail steels showing different interlamellar spacing and pearlite colonies.....90

Figure 6.7: A schematic illustration showing specimen sampling from: (a) the wheel and (b) the rail. ....91

Figure 6.8: A schematic diagram showing dimensions of wheel/rail disc shaped specimens.92

Figure 6.9: Photograph of the wheel and rail discs after machining showing the keyway.....92

Figure 6.10: (a) Coefficient of friction as a function of the number of rolling cycles, (b) average coefficient of friction for three tests under same test conditions (1.8 kN, dry contact, 62 000 rolling cycles and 10% slip ratio). ....95

Figure 6.11: (a) Mass loss of the wheel and R350HT rail after three tests under same test conditions as in Figure 6.10 and (b) cumulative mass loss (wheel + rail) after three tests under same test conditions. ....96

Figure 6.12: The contact surfaces of (a) the R350HT rail and (b) the wheel under the same test conditions as in Figure 6.10. ....96

Figure 6.13: Contact load variation about nominal values of 1, 1.4 and 1.8 kN during testing for 62000 rolling cycles under dry contact, at slip ratios of (a) 2% and (b) 10% when the wheel was run against R350HT rail under dry contact conditions.....97

Figure 6.14: Contact load variation about nominal value of 1.8 kN during testing for 62000 rolling cycles at 10% slip ratio under (a) water and (b) oil contacts when the wheel was run against R350HT rail.....97

Figure 7.1: Coefficient of friction as a function of the number of rolling cycles at different slip ratios; the wheel rolling and sliding against R260 rail under an applied load of (a) 1 kN and (b) 1.8 kN.....99

Figure 7.2: Coefficient of friction as a function of the number of rolling cycles at different slip ratios; the wheel rolling and sliding against R350HT rail under an applied load of (a) 1 kN and (b) 1.8 kN.....99

Figure 7.3: Average coefficient of friction as a function of slip ratio of the wheel when run against (a) R350HT and (b) R260 rails under applied loads of 1 kN and 1.8 kN for 62 000 rolling cycles..... 100

Figure 7.4: Mass loss of the wheel when run against (a) R350HT rail discs and (b) R260 rail as a function of slip ratio under different contact loads of 1 kN and 1.8 kN for 62 000 rolling cycles..... 101

Figure 7.5: Plots of wear rates (for wheel and rail discs) as a function of wear indexes ( $T\gamma/A$ ); AAR Class B wheel versus (a) R350HT rail and (b) R260 rail at applied loads of 1 kN and 1.8 kN and 62 000 rolling cycles. .... 102

Figure 7.6: SEM micrographs of AAR class B wheel surfaces (a) 2%, (b) 10% and (c) 27% slip ratios; R350HT rail surfaces (d) at 2%, (e) 10% and (f) 27% slip ratios under an applied load of **1.8 kN** and 62 000 rolling cycles..... 103

Figure 7.7: SEM micrographs of AAR class B wheel surfaces (a) 2%, (b) 10% and (c) 27% slip ratios; R350HT rail surfaces (d) at 2%, (e) 10% and (f) 27% slip ratios under an applied load of **1 kN** and 62 000 rolling cycles..... 103

Figure 7.8: The arithmetic mean of roughness value ( $R_a$ ) of wheel and R260 rail at applied loads of (a) 1 kN and (b) 1.8 kN and 62 000 rolling cycles..... 104

Figure 7.9: The arithmetic mean of roughness value ( $R_a$ ) of wheel and R350HT rail at applied loads of (a) 1 kN and (b) 1.8 kN and 62 000 rolling cycles..... 105

Figure 7.10: Depth of deformation as a function of slip ratio at applied loads of 1 kN and 1.8 kN when the wheel was run against (a) R350HT rail and (b) R260 rail under dry conditions for 62 000 rolling cycles. .... 106

Figure 7.11: OM micrographs of sub-surface layer (a) R350HT rail and (b) wheel showing the plastically deformed region at 5, 10 and 20% slip ratios, 1 kN load and 62 000 rolling cycles. .... 106

Figure 7.12: OM micrographs of sub-surface layer (a) R350HT rail and (b) wheel showing the plastically deformed region at 5, 10 and 20% slip ratios, 1.8 kN load and 62 000 rolling cycles. .... 107

Figure 7.13: OM micrographs of sub-surface layer (a) R260 rail and (b) wheel showing the plastically deformed region at 5, 10 and 20% slip ratios, 1 kN load and 62 000 rolling cycles. .... 107

Figure 7.14: OM micrographs of sub-surface layer (a) R260 rail and (b) wheel showing the plastically deformed region at 5, 10 and 20% slip ratios, 1.8 kN load and 62 000 rolling cycles. .... 108

Figure 7.15: Micro hardness (HV0.2) variation with depth at different slip ratios; (a) wheel and (b) R350HT at 1 kN and 62 000 rolling cycles confirming that work hardening occurred at the contact surface and sub-surface. .... 108

Figure 7.16: Micro hardness (HV0.2) variation with depth at different slip ratios; (a) wheel and (b) R350HT at 1.8 kN and 62 000 rolling cycles confirming that work hardening occurred at the contact surface and sub-surface. .... 109

Figure 7.17: Micro hardness (HV0.2) variation with depth at different slip ratios; (a) wheel and (b) R260 at 1 kN and 62 000 rolling cycles confirming that work hardening occurred at the contact surface and sub-surface. .... 109

Figure 7.18: Micro hardness (HV0.2) variation with depth at different slip ratios; (a) wheel and (b) R260 at 1.8 kN and 62 000 rolling cycles confirming that work hardening occurred at the contact surface and sub-surface. .... 110

Figure 7.19: SEM micrographs of (a) the wheel specimen and (b) R350HT rail showing sub-surface crack and crack branching at 27% slip ratio, 1.8 kN and 62 000 rolling cycles. .... 111

Figure 7.20: SEM micrographs of (a) the wheel and (b) R260 rail showing sub-surface cracks and crack branching at 27% slip ratio, 1.8 kN and 62 000 rolling cycles. .... 111

Figure 7.21: R350HT rail after testing at 1 kN (a) 2%, (b) 5% (c) 10% and (d) 20% slip ratios showing sub-surface damage and cracking..... 112



Figure 7.22: The wheel after testing at 1 kN against R260 rail (a) 5%, (b) 10%, (c) 20% and (d) 27% slip ratio showing sub-surface damage and cracking. .... 113

Figure 7.23: Maximum wheel disc temperature as a function of slip ratio at 1 and 1.8 kN for 62000 rolling cycles under dry conditions for the wheel versus (a) R350HT and (b) R260 rail. .... 114

Figure 7.24: (a) Coefficient of friction versus number of rolling cycles at (a) 10% and (b) 20% slip ratios under dry, water and oil contact conditions. .... 115

Figure 7.25: (a) Average coefficient of friction versus slip ratio; (b) Cumulative mass loss (wheel + rail) versus slip ratio under dry, water and oil contact conditions..... 115

Figure 7.26: SEM micrographs of the wheel showing worn surface morphologies; (a) dry contact at 2% and (b) dry at 20% slip ratios; (c) water at 2% and (d) water at 20% slip ratios; (e) oil at 2% and (f) oil at 20% slip ratios..... 117

Figure 7.27: SEM micrographs of the R350HT rail showing worn surface morphologies; (a) dry contact at 2% and (b) dry at 20% slip ratios; (c) water at 2% and (d) water at 20% slip ratios; (e) oil at 2% and (f) oil at 20% slip ratios..... 118

Figure 7.28: Surface roughness value as a function of slip ratio of (a) wheel and (b) rail under dry, water and oil conditions..... 119

Figure 7.29: Depth of deformation versus slip ratio of (a) the wheel and (b) R350HT rail under dry, water and oil conditions..... 120

Figure 7.30: OM micrographs of R350HT rail (a,b and c) and wheel (d, e and f) showing the depth of plastic deformation after testing at 20% slip ratio under different contact conditions (dry, water and oil)..... 120

Figure 7.31: Micro hardness (HV0.2) variation with depth under dry, water and oil conditions for the wheel at (a) 2% and (b) 20% slip ratios. .... 121

Figure 7.32: Micro hardness (HV0.2) variation with depth under dry, water and oil conditions for R350HT rail steel at (a) 2% and (b) 20% slip ratios. .... 121

Figure 7.33: SEM micrographs of the wheel showing sub-surface damage and RCF cracks, (a) dry at 2% and (b) dry at 20% slip ratios; (c) water at 2% and (d) water at 20% slip ratios; (e) oil at 2% and (f) oil at 20% slip ratios. .... 123

Figure 7.34: R350HT rail (a) RCF cracks that might have propagated by fluid crack pressurisation at 20% slip ratio under water, and (b) sub-surface multi layered RCF cracks with branching under dry contact..... 124

Figure 7.35: Wheel disc temperature as a function of the number of rolling cycles under different contact conditions (dry, water and oil) at (a) 2% and (b) 20% slip ratios..... 125

Figure 7.36: Maximum wheel disc temperature as a function of slip ratio at different contact conditions (dry, water and oil). ..... 125

Figure 8.1: Detailed drawing of the AAR class B wheel obtained using Fusion 360 computer-aided design software..... 127

Figure 8.2: Contour plot of twin discs wear rates of AAR class B wheel against R350HT rail at different slip ratios and contact pressures under dry contact and after 62 000 rolling cycles or 9.74 km of linear distance..... 128

Figure 8.3: A schematic diagram showing the wheel before (1) and after wear (2) with their respective masses and diameters obtained using Fusion 360 computer-aided design software. .... 130

Figure 8.4: Contour plots of the predicted reduction in wheel diameter ( $\Delta d$ ) as a function of the slip ratio and pressure after (a) 100 000 and (b) 200 000 km of travel distances under dry contact conditions. .... 133

Figure 8.5: A schematic diagram showing the removal of material by wear (red) and reprofiling (green) to restore the new profile. .... 134

Figure 8.6: Predicted reduction in diameter of the 915 mm wheel after reprofiling every (a) 100 000 km and (b) 200 000 km estimated from the twin disc wear rates at 740 MPa and 2% slip ratio. .... 134

Figure 8.7: (a) The predicted development of the surface crack length ( $\Delta L$ ) on a wheel of the Stockholm commuter train [164] (b) Measured length of the surface crack versus running distance for wheels [299]. .... 135

Figure 8.8: Slip as a function of friction showing the negative slope effect, adapted from [28]. .... 140

Figure 9.1: A schematic diagram showing the rig in 3D. .... 177

Figure 9.2: Main assembly of the rig showing different components (parts). .... 177

Figure 9.3: An orthographic diagram of the test rig. .... 178

Figure 9.4: A schematic diagram of the main frame of the test rig. .... 179

Figure 9.5: A schematic diagram of the base beam. .... 179

Figure 9.6: A schematic diagram of a 10 kN C9C compressive force transducer (load cell).  
..... 180

Figure 9.7: Pictures showing the test rig during different stages of manufacturing and  
assembling different components. .... 180

Figure 9.8: (a) A CAD drawing of the motors showing their dimensions (mm) and (b) a  
photograph of one of the motors used to make the rig. .... 181

Figure 9.9: Material properties used in Fusion 360 computer-aided design software. .... 181

Figure 9.10: Properties of the AAR class B wheel as per the Fusion 360 computer-aided design  
software. .... 182

## List of tables

Table 2.1: Hertzian contact calculations for parallel and crossed cylindrical contacts (adapted from [42]).	13
Table 2.2: Advantages and disadvantages of friction levels to train operation [78].	23
Table 3.1: Specifications for rim hardness for several classes of AAR wheel steels and their uses [90].	25
Table 3.2: Chemical composition of different grades of BS EN 13674-1:2011 standard rail steels (mass%) [91].	26
Table 3.3: Maximum residual elements of different grades of BS EN 13674-1:2011 standard rail steels (mass%) [91].	27
Table 4.1: Wear regimes and their corresponding $T\gamma/A$ and wear rate coefficients for R8T wheel and UIC60 900A rail steels [243].	70
Table 4.2: Available test rig to study the wheel-rail contact, adapted from [253].	79
Table 6.1: Chemical composition of the as-received wheel and rail steels.	87
Table 6.2: Mechanical properties and interlamellar spacing of the as-received wheel and rail steels.	88
Table 6.3: Vickers hardness values of the wheel steel at the rim, flange and tread respectively.	90
Table 6.4: Test matrix, note that the number of cycles and rail disc speed were kept at 62000 and 340 rpm respectively.	94
Table 8.1: Tread and flange wear rates for different wheel profiles from a study by Muhamedsalih et al. [293].	129
Table 8.2: Wear rates of ARR class B wheel at different slip ratios and maximum contact pressures from twin disc simulation with their estimated field wear rates obtained using a correlation coefficient of 0.0535.	132
Table 8.3: Actual wheel-rail contact patch sizes by different approaches at different maximum pressures.	138
Table 9.1: Parts list	177

## List of symbols and abbreviations

RCF	Rolling Contact Fatigue
$\mu$	Coefficient of Friction
$\gamma$	Slip ratio
T	Tractive force
A	Wheel/Rail contact area
$T\gamma/A$	Wear index
K	Wear coefficient
$R_w$	Wheel disc radius
$R_r$	Rail disc radius
$V_w$	Wheel disc rotational speed (angular velocity in rpm)
$V_r$	Rail disc rotational speed (angular velocity in rpm)
$E_w$	Elastic modulus of wheel disc material
$E_r$	Elastic modulus of rail disc material
$H_R$	Rail hardness
$H_w$	Wheel hardness
$H_R/H_w$	Hardness ratio
OM	Optical microscopy
SEM	Scanning electron microscopy

# Chapter 1: Introduction

## 1.1 Background

In recent years, there has been an increased demand for railway services resulting in an increase in speeds and axle loads to meet the demand. The demand for railway transportation is also due to climate change due to global warming hence a need to reduce carbon dioxide emissions as railway is energy efficient as it uses less energy per passenger/km [1]. In some areas, the rail industry is also used to transport people around places which reduces road traffic especially in big cities where traffic congestion is a problem. In South Africa, there are two main subsectors contributing to its rail industry being the passenger services (PRASA) and freight services (Transnet). Transnet has a rail network of approximately 31 000 track kilometres (20 900 route kilometres) [2] whereas PRASA owns 2 280 km of South Africa's rail network and also uses 22 000 km of rail track owned by of Transnet [3]. The mixed traffic between PRASA commuter trains, and Transnet freight services causes a lot of constrains on the route such as the one between Durban and Cato Ridge [4]. Mixed traffic between passenger and freight also causes problems of wheel and rail profile design as well as the operation and maintenance of the railway system [5, 6]. The other contributor is the passenger train known as 'Gautrain' which is a high-speed commuter rail system in Gauteng province. It has an 80 km rail line connecting Johannesburg, Pretoria, Ekurhuleni, and OR Tambo International Airport with speeds of 160 km/h [7] and was Africa's first highspeed rail project [8].

The rail industry contributes significantly to South Africa's economy by creating employment and generating income, with Transnet's freight rail sector being its largest division. In the year ending 31 March 2021 Transnet's freight rail sector contributed 51% (R34.3 billion) to its revenue [9] and 47% (R32.2 billion) in the year ending 31 March 2022 [10] as seen in Figure 1.1. Transnet's freight rail division is responsible for transporting a wide range of commodities such as from mining (coal, iron ore, manganese), agricultural, manufactured goods, bulk liquids, containerised freight and automotive [11]. South Africa has the 14<sup>th</sup> longest railway track in the world and largest in Africa with a rail track of  $\pm$  31 000 km [11] and its rail status quo is shown in Figure 1.2. The rail network in South Africa is regarded as one of the largest and most advanced rail networks on the African continent [12]. However, in contrast to the rest of the globe, South Africa's rail network is typically regarded as being outdated and in need of major investment and upgrading. A major issue for South Africa's rail system is a lack of funding for new construction, technology, and equipment. As a result, the rail system is

outdated and unreliable, making it difficult to meet the demands of both business and passengers. In an effort to boost performance and competitiveness, the South African government has recently announced intentions to invest extensively in the nation's rail system, with plans to spend R900 billion by 2027 on transportation infrastructure. [12, 13]. As part of these plans, current infrastructure will be improved, new rolling stock and technology will be purchased, and the rail network will be extended to new regions in order to accommodate the rising demand for rail services, higher loads, and faster speeds [12]. Currently, South Africa has a problem of load capacity and speed limits (maximum speed of 80 km/h) due to its national rail network having a narrow Cape gauge [14, 15]. To be able to carry loads at higher speeds (in excess of 250 km/h), a wider standard gauge line will have to be used [14, 15].

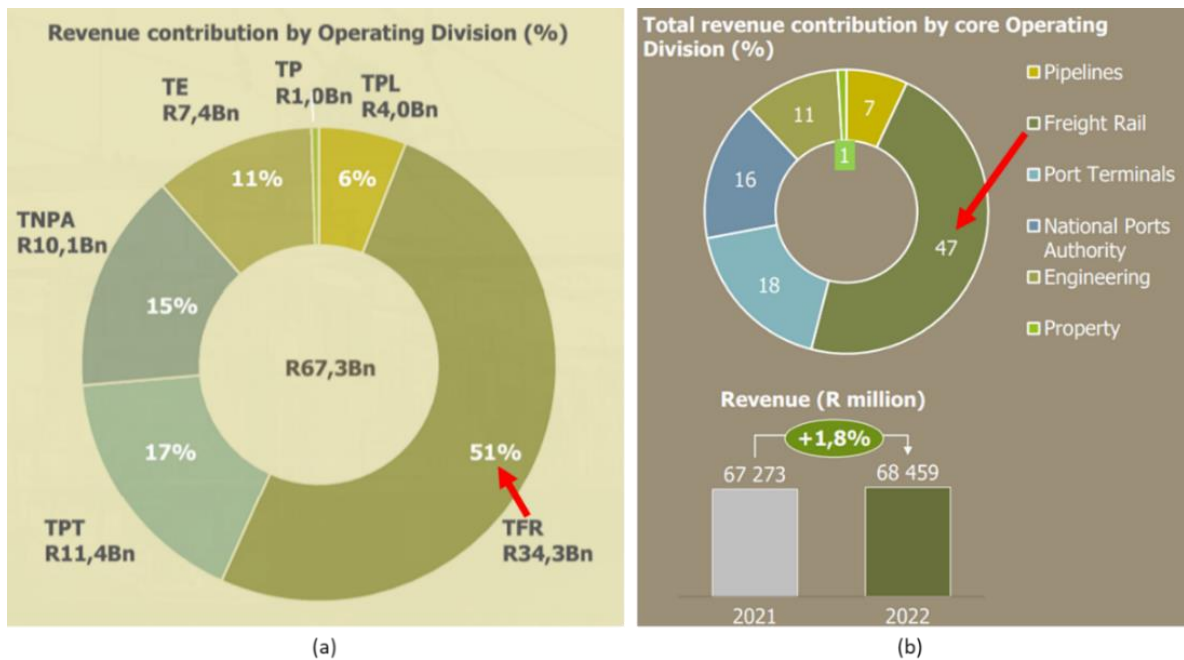


Figure 1.1: Transnet's revenue contribution by division in (a) 2021 [9] and (b) 2022 [10] with the freight rail division being the major contributor.

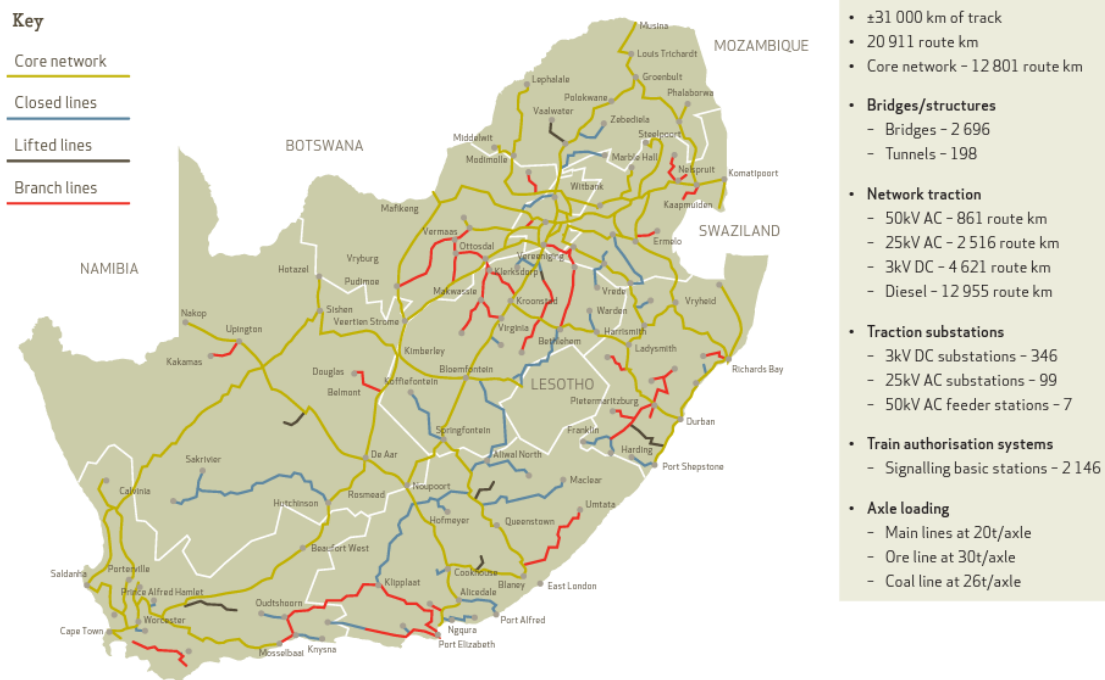


Figure 1.2: South Africa’s rail status quo: SA freight rail network and rail infrastructure assets [11].

The increase in loads and velocities has resulted in increased problems associated with wear and rolling contact fatigue (RCF) on the wheel and rail materials causing a significant reduction of their service life. Wear in wheel and rail systems is mostly visible and easy to control whereas RCF is difficult to detect and may be dangerous if not detected early [16]. Rail operating companies spend significant funds in maintenance and replacing damaged rails and wheels caused by wear and RCF. In addition, unscheduled maintenance due to wear and RCF often lead to poor availability of railway networks leading to delays and loss of income. To solve the problems caused by wear and RCF, more research needs to be done to understand the wear mechanics of wheel and rail materials by develop models or systems that can be used for prediction of preventive maintenance. Preventive maintenance prevents the system from failure unlike corrective maintenance which is done after failure and cost more. Therefore, in order to carry out preventive maintenance, more accurate models or systems should be developed to simulate a combination of rolling and sliding wear, together with RCF, specifically in the southern African context, where good rail wear simulators are not available. In this regard, literature review was performed which demonstrated that the most common wear test configurations (models) are: (a) pin-on-disc; (b) block-on- ring; (c) pin-on-reciprocating plate; (d) twin disc; (e) ring-on-ring. For the requirements of this study, it was decided that the twin-



disc concept should be used, since the literature clearly demonstrated that the method was successful in simulating the three damage mechanisms being sliding wear, rolling wear and RCF. The twin-disc concept consists of two rotating discs (cylinders) made of wheel and rail steel specimens to simulate the wheel/rail contact. This concept is easier to control and incorporate comprehensive data collection capabilities [17].

The twin disc concept has already been used to develop other wear test rigs such as the Leicester University Rolling-Sliding wear testing machine (LEROS) [18] which was later redeveloped and renamed Sheffield University Rolling Sliding (SUROS) roller rig [17]. The twin-disc concept can simulate rolling and sliding at the same time due to the ability to move the discs at different speeds which creates slip. Also, the ability to precisely control the discs dimensions (diameter and length) offers the opportunity to calculate Hertzian contact pressures which are useful for developing wear models (wear maps) for predicting the service life of the contacting materials. The twin disc approach provides the ability to control the slip ratio between the contacting discs by rotating them at different speeds [19]. For this study a positive slip ratio was used, instead of a negative one. A positive slip ratio is whereby the wheel disc is the driving disc moving faster than the rail disc (braking disc) which simulates acceleration conditions when a train is moving in rail tracks [19]. For a negative slip ratio, the rail disc moves faster than the wheel disc simulating braking conditions [19].

For this work, the wear and RCF performance of AAR class B wheel steels against both softer BS EN 13674 R260 rail and harder R350HT rail steels was studied which are some of the current materials used in local rail industry. Currently, literature is lacking in such combination of materials on a twin-disc simulation as most of the published work studied different combinations such as R8T wheel against 900A rail [20, 21], R7 wheel against R260 rail [22], R8 wheel against R260 rail [23]. Hence, this study was intended to help rail industries using such combinations to understand their wear and RCF performance at different contact conditions for the predictive maintenance. Effect of lubrication at the wheel/rail contact was also investigated. Knowledge regarding the combination of the two materials in the presence of fluids using a twin-disc simulator was not available at the time, hence this study now offers valuable information on their wear performance and behaviour under different contact conditions. On one hand, lubrication has been found to promote propagation and growth of RCF cracks. RCF defects include head cracks, spalling and shelling. It has been discovered that head cracks contribute to train noise and may also result into rail breakage causing accidents [24, 25]. On the other hand, measures taken to improve adhesion at the wheel and

rail contact such as application of sand can have negative effects on wear, hence the need to optimise the balance between wear and RCF. In other words, the wheel and rail interface management approach systems should be able to take into consideration all factors as they influence each other's performance. The knowledge that has been developed in this work is now available to the local rail sector for the optimisation of their predictive maintenance processes as well as for the better understanding of the wear behaviour of these wheel and rail combinations.

## **1.2 Problem statement**

Local rail operating companies are spending much money maintaining and replacing damaged rails and wheels due to problems caused by rolling contact fatigue and wear. Damage caused by RCF and wear can lead to poor availability of railway networks, causing delays in movement of goods and passengers. RCF and wear have also been found to cause rail accidents. Currently, there are no twin-disc simulators in South Africa that can be used by the local rail industry to predict wear and RCF and are also expensive to acquire as there is a limited number of them around the world which can simulate RCF, sliding and rolling wear at the same time. The local simulators currently available in the local industry can only simulate sliding wear (pin on disc or pin-on-reciprocating plate rigs) but as a train wheel moves on a rail it experiences a combination of RCF, rolling and sliding wear. To solve this problem, a cost-effective instrumented twin-disc test rig that can simulate a combination of RCF, sliding and rolling wear had to be developed using the twin-disc approach. The test rig had to be designed and manufactured at the University of Pretoria labs using locally machined components such as shafts and beams. Components such as motors, load cell, tachometers, torque measurements and data acquisition systems had to be procured from local suppliers. The total costs associated with design and manufacturing of the rig was to be in the order of 14 000 USD in order to be to be cost effective compared to other methods. This wear test rig had to be easy to control and should offer good instrumentation with accurate data acquisition capabilities. Information obtained from the test rig should be sufficient to predict wear behaviour maps simulating the actual rail and wheel experience in service, a critical tool for predictive maintenance.

### 1.3 Objectives

The objectives of the project were:

- To develop a cost-effective twin-disc wear test rig that can be used by the local rail industry to study the wear and RCF behaviour of wheel and rail steels under RCF, rolling and sliding conditions.
- To determine the wear and RCF performance of the AAR class B wheel steel against the harder R350HT rail and softer R260 rail steels by measuring wear rates, coefficient of friction, depth of deformation, wheel disc temperature and sub-surface damage under dry contact conditions.
- To investigate how introducing lubrication (oil and water) at the wheel/rail contact affects the wear and RCF performance AAR class B wheel steels against harder R350HT rail and softer R260 rail in comparison with the dry condition.
- To develop wear maps from the plots of wear index ( $T\gamma/A$ ) against wear rate to be used to identify the wear regimes identified as mild, severe and catastrophic wear.
- To find a data correlation coefficient to link twin disc and field wear rates to be used for predictive maintenance.

## Chapter 2: Wheel and rail contact

### 2.1 Introduction

The wheel-rail contact interface is a very complex system as it involves numerous factors such as wheel-rail geometry, lubrication such as humidity and precipitation and a variety of loading conditions which influences wheel/rail wear [26]. Some of the lubricants affect the coefficient of friction at the contact therefore causing braking problems by increasing the braking distance [27]. The wheel/rail contact is a crucial aspect of railway engineering because it affects the performance, stability, and safety of the train. The demand for high axle loads and high speeds trains has added problems to the complexity at the wheel-rail contact conditions making it difficult to study the interface. The wheel/rail contact area is small and usually around  $1 \text{ cm}^2$  and varies as the train moves along the track due to different rail-wheel profiles and the degree of curvature of the rail track [28]. Both sliding and rolling occur within the wheel/rail contact [29, 30]. A typical wheel-rail contact is shown in Figure 2.1 and Figure 2.2.

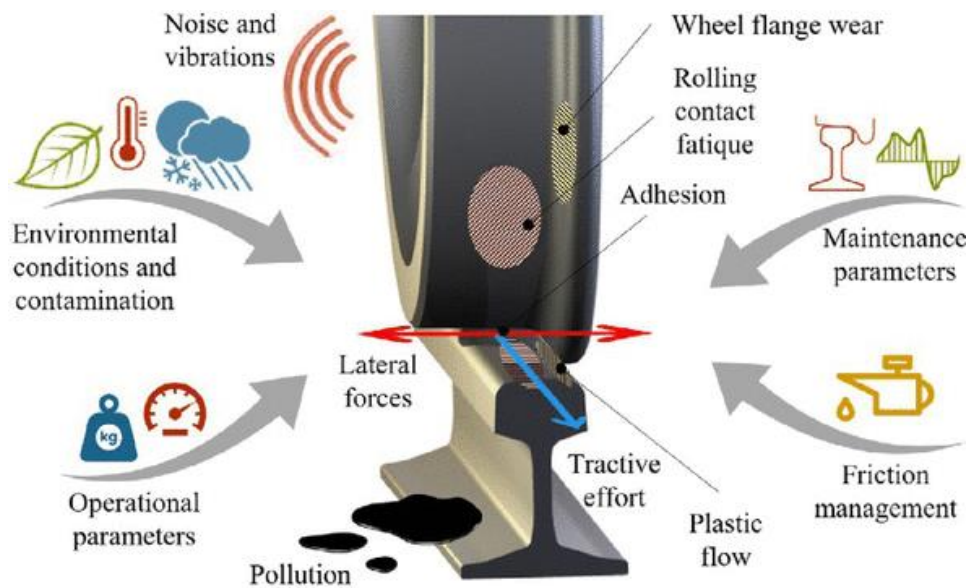


Figure 2.1: Issues related to the wheel/rail contact [31].

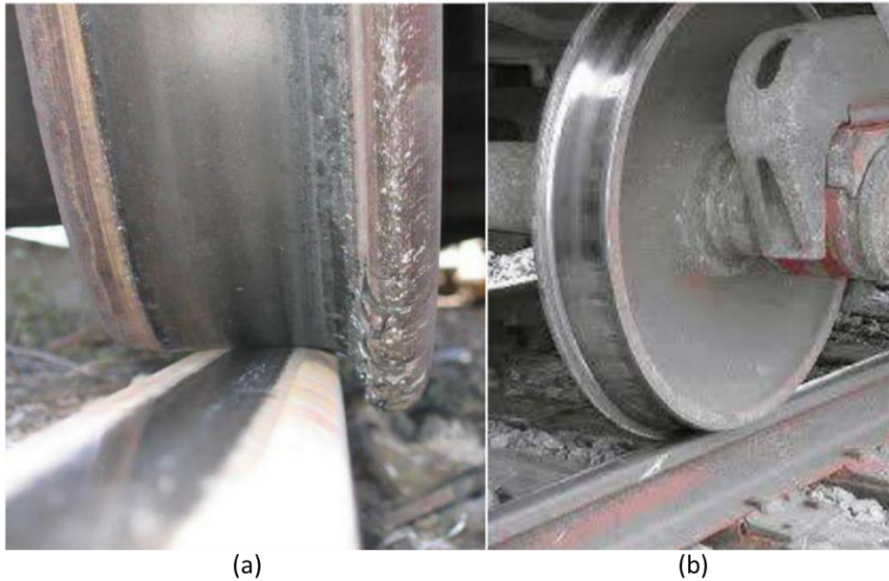


Figure 2.2: The wheel/rail contact; (a) front and (b) side views [32].

The wheel and rail have different profiles as shown in Figure 2.4 and only a few parts are in contact during sliding and rolling. There are three contact regions between the rail and wheel as shown on Figure 2.3 being; region A - Wheel tread/rail head, region B - Wheel flange/rail gauge face and region C - Field side. Each contact region experiences different contact conditions resulting in different wear rates.

- **Region A (Wheel tread/rail head):** This region experiences lower contact stresses and lateral forces as compared to the other regions. The wheel/rail contact is made mostly of this region and occurs as the railway vehicle moves on a straight track or very high radius curves [33]. In this region, the contact is under rolling and sliding and experiences mild to severe wear as seen in Figure 2.3.
- **Region B (Wheel flange/rail gauge face):** The contact region in this area is much smaller than in A and experiences much higher contact stresses and wear rates [33]. Pure sliding wear is being experienced in this region between the wheel flange and the rail gauge face causing severe to catastrophic wear.
- **Region C (Contact between field sides of wheel and rail):** In this region, contact is least likely to occur and when it does it induces high contact stresses causing undesirable wear features resulting in incorrect steering of the wheelset [33].

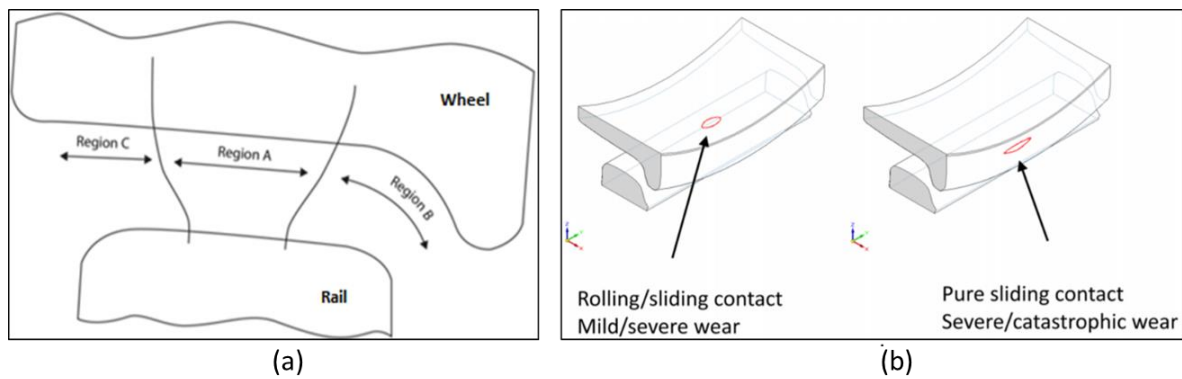


Figure 2.3: (a) Schematic diagram showing different contact zones of the wheel/rail contact, adapted by Lewis and Olofsson [33] from Tournay [34]; (b) Schematic diagram illustrating two contact types at the wheel/rail contact being between the wheel tread and rail head (rolling/sliding contact) and between the wheel flange and the rail gauge (pure sliding) [35].

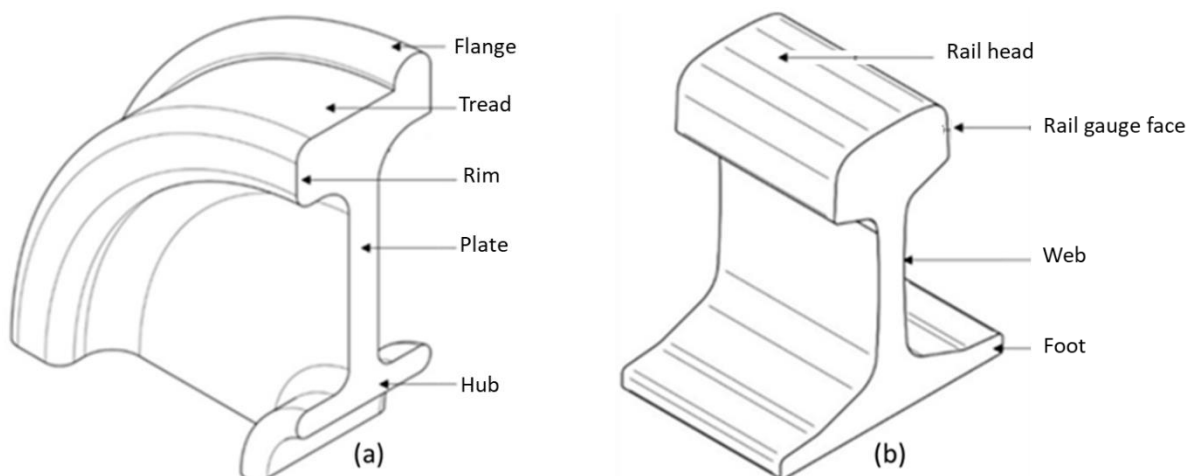


Figure 2.4: Schematic representation of typical (a) wheel and (b) rail profiles.

## 2.2 The sticking/slipping behaviour at the wheel-rail contact patch

The wheel-rail contact encounters both rolling and sliding as the train travels along the rail tracks experiencing different contact conditions. When the train is moving in a straight line, the rail head is found to be in contact with the wheel tread but when moving in curves the contact changes to wheel flange/rail gauge face contact. This causes a significant increase in severity of wear [36]. The wheel tread/rail head contact experience mild to severe wear whereas the wheel flange/rail gauge experience catastrophic wear [37] with rail gauge experiencing more wear than the rail head up to ten times more in magnitude [36]. The wheel-rail contact patch is divided into two zones: the stick zone (no slippage) and the slip zone [37]. As the tangential load increases, the slip zone grows and the stick zone contracts, resulting in rolling and sliding contact [37]. When the tangential load reaches its maximum, the stick zone

disappears completely, leaving the entire contact surface exposed to pure sliding, Figure 2.5. At pure sliding, the adhesion equals the frictional force between two contacting bodies [38]. The sticking-slipping behaviour at the wheel-rail contact has been studied by different contact theories which are discussed further in section 2.3.

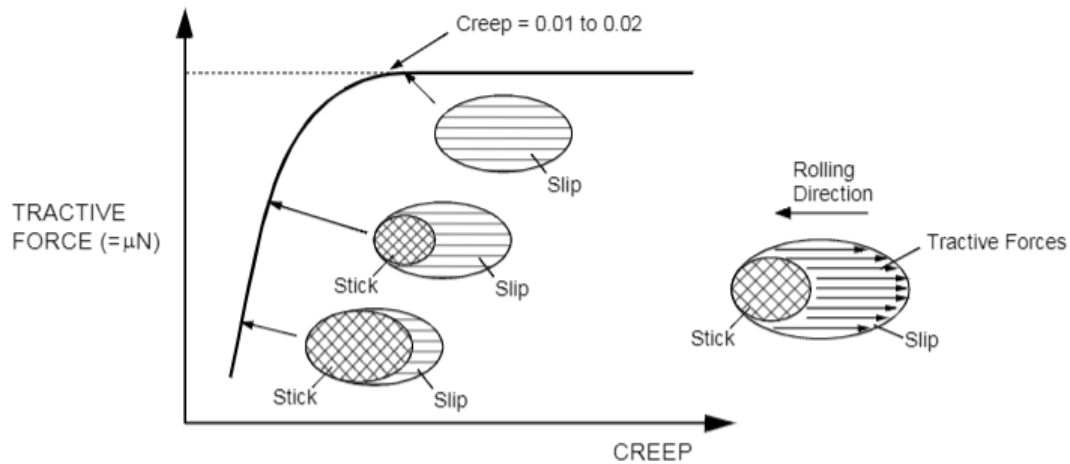


Figure 2.5: Relationship between traction and creep at the wheel-rail interface [28].

### 2.3 Contact theories

To understand the damage mechanisms on wheel and rail materials, a small contact area where the wheel is in contact with the rail needs to be studied. Traditionally, the Hertz theory has been used to study the wheel-rail contact area, and it is still being used to date by engineers to study different contacts. For wheel and rail contact, other contact theories have been developed, some derived from the Hertz's theory. Some include the Carter's theory, Johnson's theory, Johnson and Vermeulen, Kalker's (linear and simplified theories), Polach's method and others. Some have a point or linear contact whereas others have an elliptical contact. The timeline for different rolling contact theories and how their interrelations and period when they were developed are summarised in Figure 2.6. Some of the contact theories are discussed further in the subsequent sections.



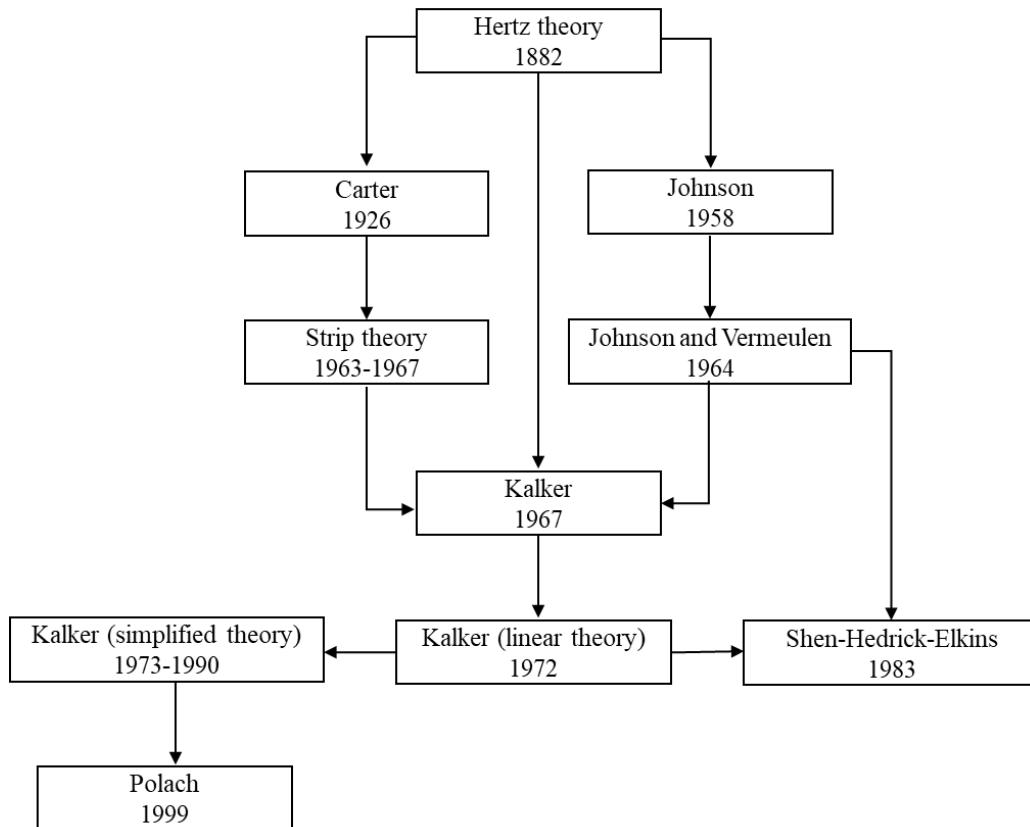


Figure 2.6: Contact theories and their interrelations, adapted from [39].

### 2.3.1 The Hertz's theory

The most common theory used to analyse contact stresses between two contacting elastic solids such as the wheel and rail is the Hertzian contact theory [40]. The Hertz's theory was developed by a German physicist Heinrich Hertz in 1882 based on the theory of elasticity. The theory can be used to calculate contact stresses in different contact applications such as sphere on sphere, sphere on flat plate, cylinder on cylinder, cylinder on flat plate etc. Knowing the contact stresses between contacting surfaces is useful as it helps in predicting the life of contacts such as in bearings, gear and worm drives and cylindrical rollers. The general and railway cases of Hertzian contacts are shown in Figure 2.7. The Hertz theory makes the following assumptions [40]:

- The surfaces are frictionless;
- The surfaces are continuous and non-conforming;
- The contact area is small compared to the bulk volume of the two contacting bodies;
- The contact stresses are large compared to the other stresses in the two bodies;
- Subsequent strains are small;



- Each body can be regarded as an elastic half-space bounded by the plane  $z=0$ .

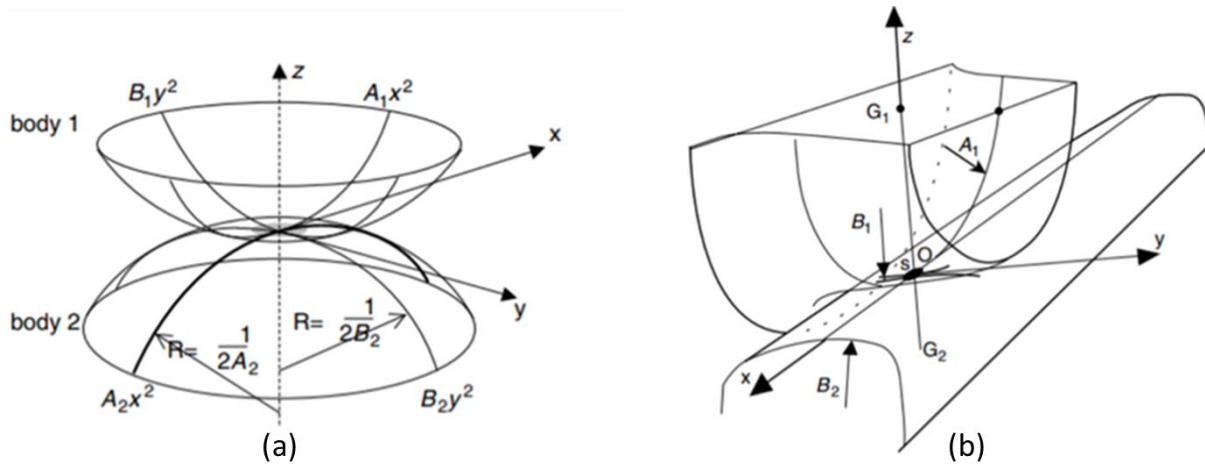
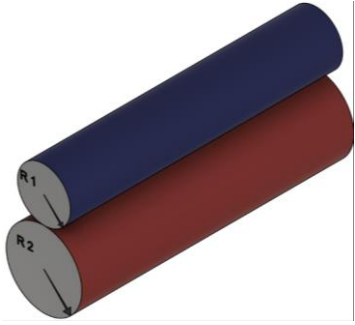
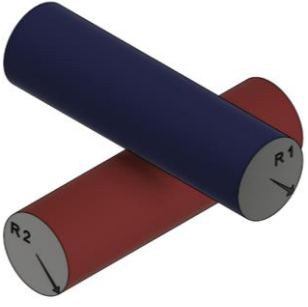
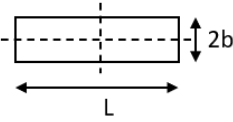
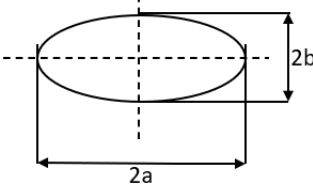


Figure 2.7: Hertzian contact: (a) general case, (b) the railway case [41].

The Hertz theory can be applied to both parallel and crossed cylindrical contacts. In reality the wheel and rail contact can be simplified as a crossed cylindrical contact, where the wheel is perpendicular to the rail surface (wheel cylinder in the longitudinal direction and rail head curved cylinder in the transverse direction). For twin disc simulation, a parallel cylindrical contact is used where the two contacting discs are parallel to each other. The main difference between the two and their Hertzian theory calculations are summarised in Table 2.1 respectively. The parallel cylindrical contact is discussed further in section 2.3.1.1 as it has been adopted for the twin-disc calculations for this study.

Table 2.1: Hertzian contact calculations for parallel and crossed cylindrical contacts (adapted from [42]).

	Parallel cylindrical contact	Crossed cylindrical contact
Axes of cylinders	Parallel	Intersect at an angle
Schematic		
Contact shape	Line (rectangular) 	Elliptical 
Reduced radius	$R = \left( \frac{1}{R_1} + \frac{1}{R_2} \right)^{-1}$	$R = \left( \frac{1}{R_1} + \frac{1}{R_2} \right)^{-1}$
Contact half width	$b = \left( \frac{4WR}{E^* \pi L} \right)^{0.5}$	$a = \left( \frac{3k^2 EWR}{\pi E^*} \right)^{\frac{1}{3}}$
Maximum contact pressure	$P_{max} = \frac{2W}{\pi b l}$	$P_{max} = \frac{3W}{2\pi a b}$
Contact pressure distribution	$P_{(x)} = P_{max} \left( 1 - \frac{x^2}{b^2} \right)^{0.5}$	$P_{(x)} = P_{max} \left( 1 - \frac{x^2}{a^2} - \frac{y^2}{b^2} \right)^{0.5}$
Other contact parameters	L=length of the contacting cylinders	$b = \left( \frac{3EWR}{\pi k E^*} \right)^{\frac{1}{3}}$

For both the line and elliptical contacts the following nomenclature are the same:  $E^*$  the reduced modulus of elasticity given by equation 2.4,  $R$  is the reduced radius given by equation 2.3,  $P_{\max}$  is the maximum contact pressure,  $P_{(x)}$  is the contact pressure distribution and  $W$  is the contact load. For an elliptical contact,  $x$  and  $y$  are the effective radii in the two contact bodies in perpendicular planes,  $k$  is the ellipticity parameter, and  $E$  an elliptical integral both found in tables or from approximate solutions,  $a$  and  $b$  are the respective major and minor semi-axes of the contact ellipse. For a line contact,  $b$  is the half-width and  $L$  is the transverse contact width.

### 2.3.1.1 Parallel cylindrical contact

Parallel cylindrical contact elements are used in many engineering applications such as in spur and helical gear teeth, and roller bearing components [43]. In railway applications, it is used in wear and RCF simulation at the wheel/rail contact in the twin-disc test rig setup. The parallel cylindrical contact is made up of two contacting cylinders of length  $L$  and diameters  $d_1$  and  $d_2$  with an area of contact being a narrow rectangle of width  $2b$  and length  $L$  as shown in Figure 2.8 with an elliptical pressure distribution [44].

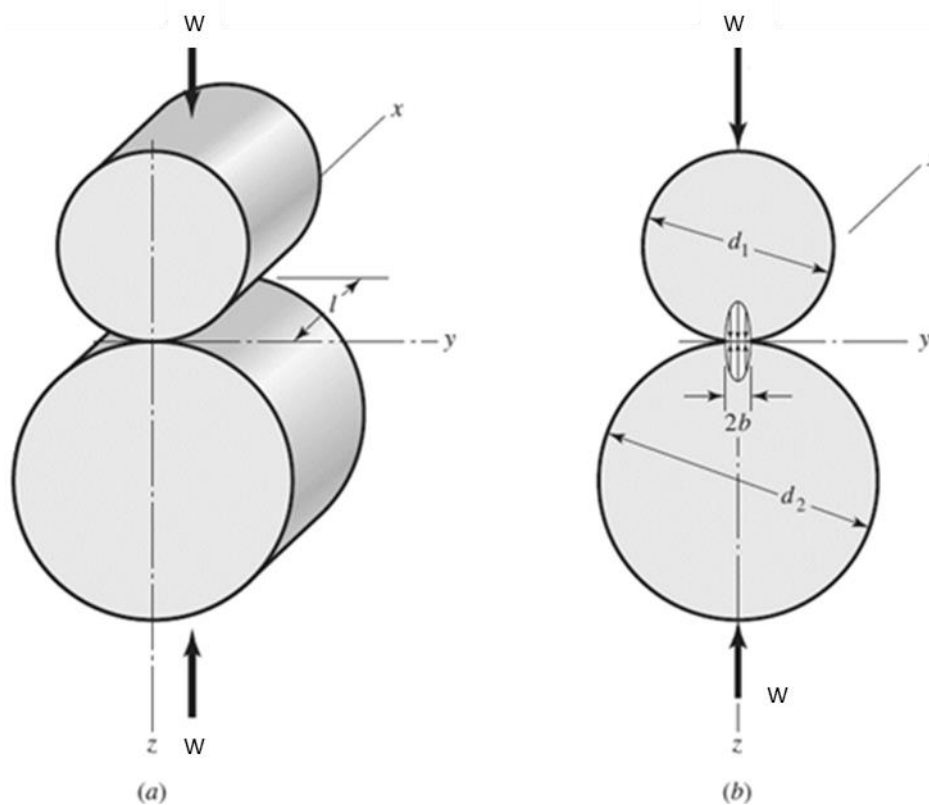


Figure 2.8: (a) A schematic illustration showing a contact between cylinders under a contact load,  $F$ , along the contact length  $l$  and (b) an illustration showing an elliptical contact between the contacting cylinders with a contact width of  $2b$  [44].

The half-width  $b$  is given by the equation 2.2.

$$b = \sqrt{\frac{2W \frac{1 - \nu_1^2}{E_1} + \frac{1 - \nu_2^2}{E_2}}{\pi L \left( \frac{1}{d_1} + \frac{1}{d_2} \right)}} \quad 2.1$$

Simplifying equation 2.1, the half-width  $b$  becomes equation 2.2:

$$b = \left( \frac{4WR}{E^* \pi L} \right)^{0.5} \quad 2.2$$

Where  $W$  is the contact load (N),  $L$  is the transverse contact width (mm) or cylindrical length,  $E^*$  is the reduced modulus of elasticity of steel (MPa) given by equation 2.4 and  $R$  is the reduced radius (mm) and is given by equation 2.3.

$$\frac{1}{R} = \frac{1}{R_1} + \frac{1}{R_2} \quad 2.3$$

where  $R_1$  and  $R_2$  are the radii of the two contacting cylinders respectively. The reduced modulus of elastic  $E^*$  is given by equation 2.4:

$$\frac{1}{E^*} = \frac{1 - (\nu_1)^2}{E_r} + \frac{1 - (\nu_2)^2}{E_w} \quad 2.4$$

Where  $\nu_1$  and  $\nu_2$  are Poisson's ratios of two contacting cylinders.  $E_1$  and  $E_2$  are the elastic moduli of two contacting cylinders.

The maximum contact pressure ( $P_{max}$ ) is given by:  $P_{max} = \frac{2W}{\pi bl}$  2.5

Substituting the half-width,  $b$  (equation 2.2) into 2.5, the maximum contact pressure now becomes equation 2.6 as suggested by Timoshanko and Gondier [45];

$$P_{max} = \frac{2W}{\pi bl} = \left( \frac{WE^*}{\pi LR} \right)^{0.5} \quad 2.6$$

The contact area ( $A$ ) is given by equation 2.7:

$$A = 2bL \quad 2.7$$

### *2.3.1.2 Limitations of the Hertz's theory*

Even though the Hertz contact theory is efficient and easy to use in many engineering applications, it has some limitations especially when applied to studying the wheel-rail contact mechanics [46]. The Hertz contact theory is only valid for normal aspects of the contact and does not reveal the tangential aspects of the wheel rail contact. It is only valid for elliptical contacts and cannot be used for non-Hertzian wheel-rail contact [47]. Literature [48, 49] has shown that the wheel-rail contact is not elliptical even at the wheel tread/rail head contact. The contact at the rail gauge corner as a result of the transverse movement of the wheel axle violates the Hertz contact theory. It does not obey the assumption of having the dimensions of the contact area being smaller than the dimensions and the radii of curvature of the bodies in contact [46, 50]. In this scenario the contact zone may spread into regions of different surface curvature, causing plastic deformation to occur on both wheels and rails especially at high axle loads [46].

### *2.3.2 Carter's theory*

Carter's theory was postulated in a publication entitled "On the action of a locomotive driving wheel" published in 1926 [51]. The theory is restricted to a line contact, as 2-dimensional approach with a cylinder used to represent the wheel, while an infinite half-space was used to represent the rail. It was the first theory of rolling contact with friction [52]. It does not take lateral slip, or spin into account and assumes that the cylinder is steadily rolling on a flat surface without any pure spin [53].

### *2.3.3 Johnson and Vermeulen's theory*

The Johnson-Vermeulen's theory (1964) [54] was generalised from the Johnson's (1958) [55] where, quasi-identical bodies are considered for steady-state rolling; spin is assumed to be absent, and the contact area is circular in form [39]. Johnson's theory examined an elastic rolling sphere on an elastic plane without sliding but taking into account the deformations of their contacting surfaces due to the exerted forces on them, Figure 2.9a [55] which is not the case in the railway application at the wheel-rail contact patch. This led to the development of the Johnson-Vermeulen's theory. The Johnson-Vermeulen theory used the same approach as in the Johnson's but using an elliptical contact area without spin and found that the contact area was divided into two regions: the area of adhesion where the slip vanishes, and the area of slip where it does not [39]. They assumed that the stick region was also enclosed by an ellipse, with

the same axial ratio and orientation as the contact ellipse, but touching the contact ellipse at its foremost point, Figure 2.9b [56].

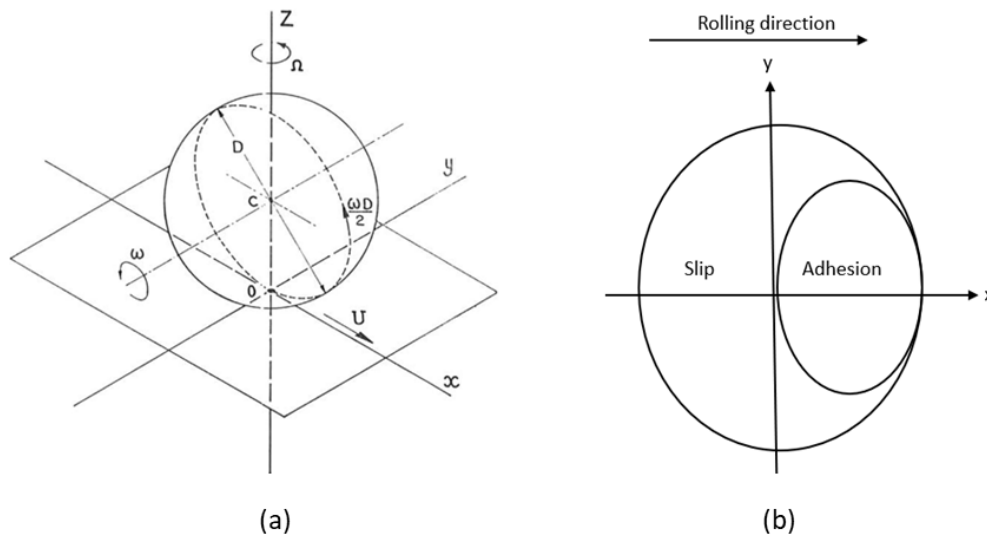


Figure 2.9: (a) Rolling of a sphere on a plane as per Johnson's theory (where  $U$  is the plane's linear velocity,  $\Omega$  is the sphere's angular velocity relative to the plane about the normal axis  $O_z$  and  $\omega$  is the sphere's angular velocity about a diametral axis parallel to  $Oy$ ) [55]; (b) areas of slip and adhesion according to Vermeulen and Johnson, adapted from [56].

### 2.3.4 Kalker's theory

Kalker's theory can be split into two: the linear theory (1967) where creep force is linearly proportional to creepage and the simplified theory (1973-1990) [57] where tangential displacement difference is proportional to the tangential traction [58]. The Kalker's simplified model is based on the Winkler's approximation (1867) for the elastic relationship between deformations and stresses [53] and uses the computer programme called CONTACT [59]. It has proven to be highly effective, exhibiting an error rate of no more than 15%, particularly in cases where the contact area is elliptic. CONTACT computer programme is still being used today for validation of new simplified theories. The Kalker's theory solved issues that were encountered by the Johnson-Vermeulen's theory such as the arbitrary longitudinal and lateral creepages and spin [60]. However, when dealing with non-elliptic contact areas, it does not appear to be useful [39].

### 2.3.5 Polach's method

Polach's method [61, 62] assumes ellipsoidal contact with semiaxis  $a$ ,  $b$  and normal distribution same as the Hertz's theory. The method assumes that there is a linear growth between the

contacting bodies from the leading point (A) to the trailing point (C) on the edge of the contact patch, Figure 2.10 [61]. Initially, the contacting surfaces stick firmly resulting in displacement on the bodies due to material creepage (area of adhesion) [61]. Tangential stress acts against the creep with its value growing linearly with the distance from the leading edge (same as Kalker's simplified theory) [61]. When the tangential stress reaches its maximum value at the adhesion area a relative motion of the contact surfaces appears, known as the slip area. Compared to Kalker's simplified theory, Polach's method is a much quicker computation method of wheel-rail contact and, therefore, can be used to improve or replace the Kalker's simplified theory.

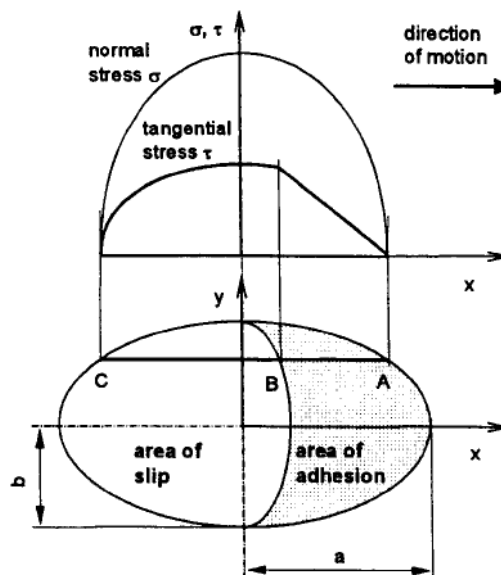


Figure 2.10: Distribution of normal and tangential stresses in the wheel-rail contact area, Polach [61].

### 2.3.6 Recent finite element modelling approaches

Several studies have been conducted by using finite element modelling (FEM) approaches to study the contact mechanics at the wheel-rail contact using different computer programmes. Telliskivi and Olofsson [63] have used a finite element code in ANSYS to model the contact mechanics at the wheel-rail contact. Unlike the traditional CONTACT code by Kalker [57] and Hertz's method where the linear elastic material model and the half-space assumptions were made, Telliskivi and Olofsson's model [63] is not limited by those two assumptions as the measurements from the wheel and rail profiles are used as inputs. The half-space assumptions put a geometrical limitation on the contact especially at the rail's gauge corner contact. In case

1, the wheel was in contact with the rail gauge face whereas in the second case the wheel was in contact with the rail head. The maximum contact pressure results from Hertz and CONTACT were found to be similar but the Telliskivi and Olofsson approach, Figure 2.11. In the first contact case, there was a significant difference between the maximum contact pressure by the model by Telliskivi and Olofsson [63], compared to both CONTACT and Hertz methods, Figure 2.11. In case 2, the maximum contact pressures of the 3 contact methods had no significant difference, Figure 2.11. The same observation was made by Sichan [47] when comparing the contact pressure distribution obtained by Damme [48] using FEM to ones obtained by CONTACT code. The maximum contact stresses were found to be lower in FEM at the contact area than in CONTACT code [47].

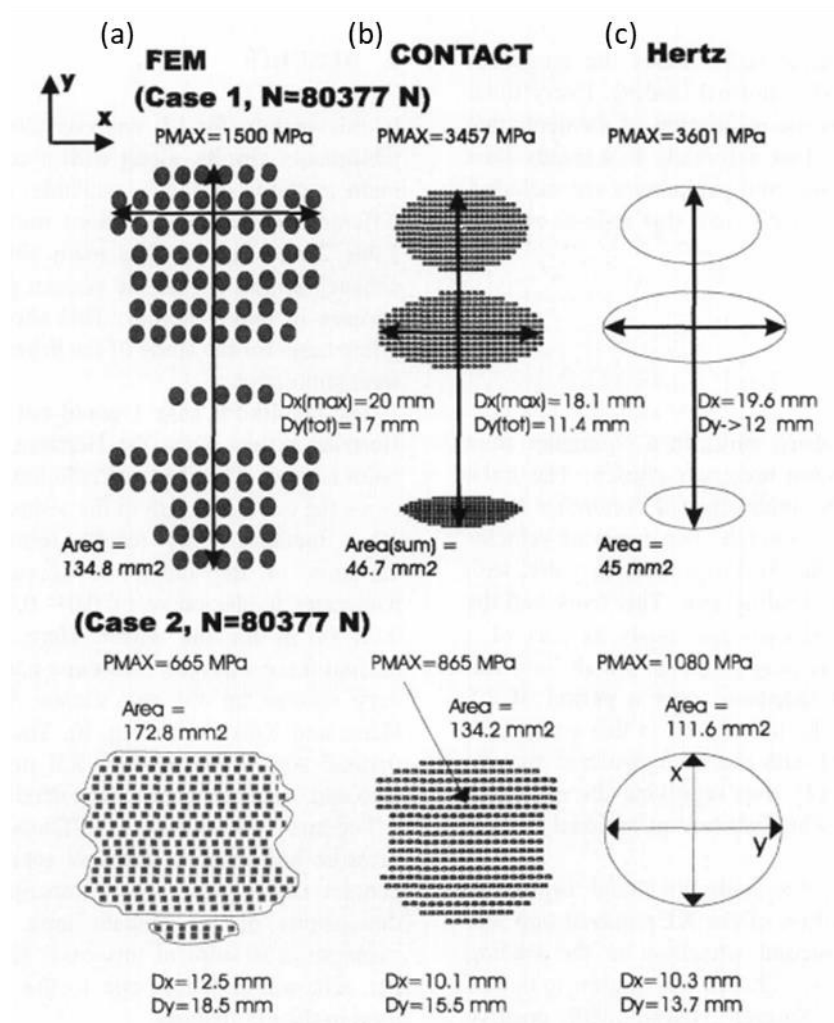


Figure 2.11: Comparison of the maximum contact pressure with respect to the contact area; (a) FE ANSYS code by Telliskivi and Olofsson, (b) CONTACT code by Kalker and (c) Hertz method [63].



A study by Zhao and Li (2011) [60] improved the 3D transient FE model developed by [64, 65]. Their solutions were validated against the Hertz theory and Kalker's CONTACT code [57] using the wheel tread-rail head contact in the normal and tangential solutions [60]. From their FE model, the surface shear stress distribution agreed with Kalker's CONTACT solutions at the slip area with up to 20% difference at the adhesion area. For the distributions of the micro slip along the longitudinal axis, their model agreed with CONTACT method by Kalker as seen in Figure 2.12b.

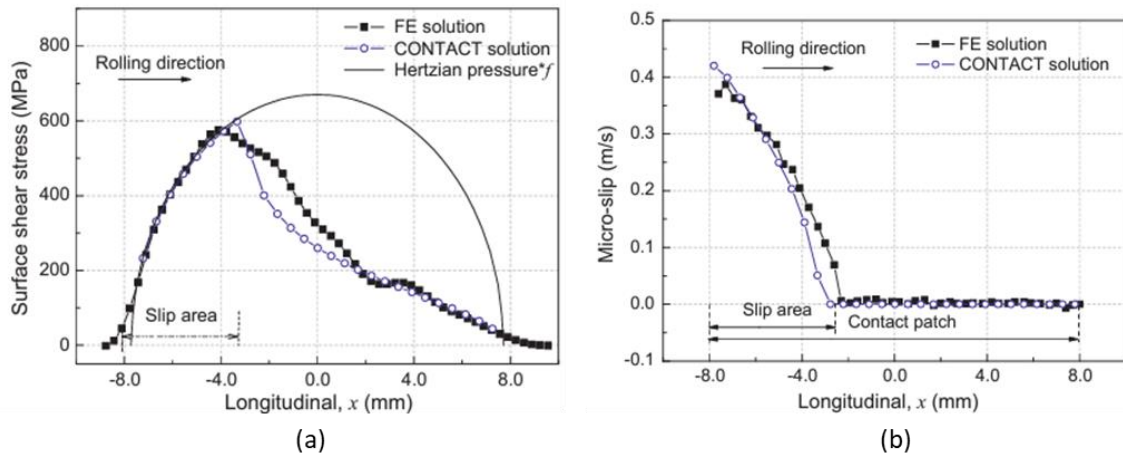


Figure 2.12: Zhao and Li's 3D transient FE model solutions [60], validated against Hertz theory and Kalker's CONTACT code: (a) the surface shear stress distribution (absolute values) along the longitudinal axis when coefficient of friction=0.3; (b) distribution of micro-slip (absolute values) along the longitudinal axis when coefficient of friction=0.3 [60].

## 2.4 Friction

Friction plays a crucial role at the wheel/rail contact. It is defined by [66, 67] as the resistance experienced when a body tangentially slides across another that it is in contact with. The friction coefficient ( $\mu$ ), which is the ratio of the frictional force ( $F$ ) to the normal load ( $W$ ), is used to define friction [68] equation 2.8 according to the theory of friction as stated by the Coulomb's law. The frictional force is defined as the resistive tangential force which acts in a direction opposite to the direction of motion [69]. Friction is a system-responsive and is not a property of a material; it is dependent on a number of variables, including lubrication and contact conditions [69]. For the same contacting surfaces and circumstances, friction caused by rolling has been found to be less than that caused by sliding [70].

$$F = \mu W \quad 2.8$$

As the wheel moves along the rail, it experiences both sliding and rolling friction. Sliding friction occurs when surfaces are rubbing against each other due to interlocking between microscopic surface of the contacting bodies. Rolling friction is as a result of rolling of an object over another due to surface deformation of the contacting bodies at the contact patch and it dependent on the diameter of the rolling body (wheel). Figure 2.13 shows a schematic illustration showing two objects under rolling and sliding friction. Under the micro-slipping region of the contact patch (during sliding) the Coulomb's friction model (equation 2.8) is applicable but not applicable for macro rolling. Micro-slip is defined by [71] as 'small relative tangential displacement in a contacting area at an interface, when the remainder of the interface in the contacting area is not relatively displaced tangentially'. Under rolling friction, the macro friction model for rolling (equation 2.9, where  $F$  is the rolling friction force,  $W$  is the normal load acting on the wheel,  $R$  is the radius of the wheel and  $\mu$  is the coefficient of rolling friction) now become applicable. In general, the coefficient of rolling friction is lower than the coefficient of sliding friction under the same conditions.

Friction is dependent on the texture (roughness or smoothness) of the surfaces that are in contact as well as the force that is pushing them together. Friction was used during the civilization of ancient North Africa by the ancient Egyptians during the construction of the pyramids to move heavy components. They utilised the use of third body materials to make movement of heavy materials much easier by lowering coefficient of friction [72]. Even today the same technique of using third body materials to lower the coefficient of friction is still used in different applications. The application of friction is also present in human bodies, for example at the joints (knee joint) where a joint is covered with cartilage to provide a smooth glassy surface and synovial fluid which reduces friction and wear. The other application of friction is in the mouth where the saliva and mucus (in the oesophagus) act as third body materials to provide lubrication aiding in swallowing and digestion of food.

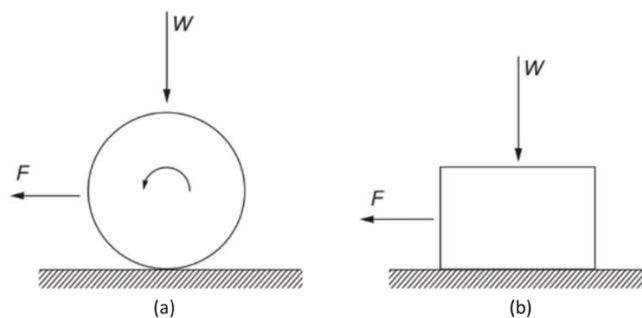


Figure 2.13: A schematic illustration showing two objects under (a) rolling and (b) sliding motions [68].

$$F = \mu \frac{W}{R} \quad 2.9$$

Friction is essential in rail applications because it influences the adhesion of the wheel to the rail, which impacts the train's acceleration and braking on the railway tracks, affecting wear and RCF [73, 74]. Friction also contributes significantly to noise generation in passenger trains affecting passengers' comfort. Studies have shown that a low coefficient of friction results in low adhesion, but a high coefficient of friction may cause accelerated wear, hence it is very important to control friction at the wheel/rail contact by having a balance between wear and adhesion [21, 28, 75]. Different pollutants, such as water, leaves, grease, and oil from train systems, cause low coefficient of friction. [76]. The surface of the wheel and rail may be damaged by low coefficient of friction, which can lead to skidding as shown in Figure 2.14 [77]. For wheel/rail friction management, the proposed ideal friction coefficients for high and low rails as shown in Figure 2.15 [70]. These friction coefficients are specified for each contact region and are important because values that are okay for one region may be detrimental to another. At the wheel flange/rail gauge contact low friction is required to reduce wear but at the wheel tread/rail head contact with moderate friction is required to attain braking and traction [42].

Table 2.2: Advantages and disadvantages of friction levels to train operation [78].

Friction Level	Advantages	Disadvantages
High	<ul style="list-style-type: none"> <li>• Good tractive capability</li> <li>• Good braking</li> </ul>	<ul style="list-style-type: none"> <li>• High wheel/rail wear rates</li> <li>• Increased wheel/rail rolling contact fatigue (RCF)</li> <li>• High ratio of lateral to vertical force (L/V)</li> <li>• High rail rollover forces</li> <li>• Increased hunting</li> </ul>
Low	<ul style="list-style-type: none"> <li>• Increase wheel-climb threshold</li> <li>• Reduced wear rates</li> <li>• Reduced RCF</li> <li>• Reduced hunting</li> </ul>	<ul style="list-style-type: none"> <li>• Rail burns/Engine burns</li> <li>• Wheel flats</li> <li>• Stalled trains</li> </ul>



Figure 2.14: Example of wheel/rail damage in low adhesion conditions: (a) skidding marks on the rail surface and (b) wheel scratch on the tread [76].

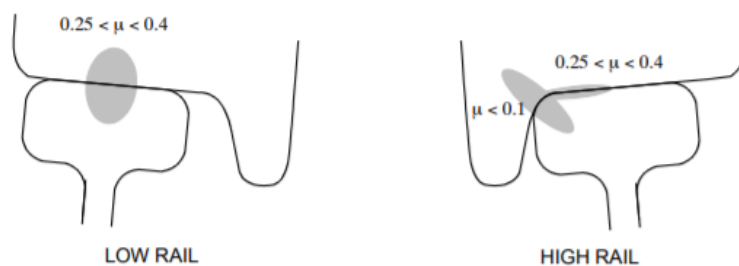


Figure 2.15: Optimal wheel/rail contact friction coefficients [70].

## Chapter 3: Wheel and rail materials

### 3.1 Introduction

The most popular materials for wheels and rail applications are pearlitic and bainitic steels because of their good combination of microstructure, properties and low manufacturing costs. Pearlitic steels are the dominant material across the world for wheels and rails whereas bainitic steels are being studied and developed as an alternative for rail and wheel materials [79, 80]. The need to develop alternative materials for wheel and rail steels is due to the limit on hardness that can be achieved on conventional pearlitic steels [81]. The wear and RCF characteristics of wheel and rail materials are heavily influenced by the microstructure [82, 83]. To determine the impact microstructure has on wear and RCF characteristics of wheel and rail steels, several studies have been carried out. Generally, most standards provide steel with hardness values between 250 and 300 HB for usage in wheel applications and between 300 and 400 HB for rail applications since hardness values above those ranges result in higher operational and production costs [84, 85]. Numerous research have been done to determine how hardness affects wear and RCF performance of rail and wheel steels. According to research by Stock and Pippin [86] on pearlitic steel grades tested on a voestalpine Schienen GmbH test rig, there is a correlation between hardness and wear resistance. From their research, the fatigue life of rail steels was improved by increasing the hardness since it increased both RCF life and wear resistance [86]. Work done by Aglan et al. [87] has shown that bainitic steels have ultimate strength, yield strength and strain to failure higher than those of pearlitic steels. However, newer research has demonstrated that pearlitic steels have exceptional wear resistance because of their distinct microstructure, consisting of interlamellar spacing comprised of alternating layers of cementite and ferrite [88, 89]. The lamellae spacing of pearlitic steels affects their hardness, with harder materials having finer lamellae [88].

In South Africa and the surrounding Sub-Saharan region, the railway industry uses the BS EN 13674 R260 and R350HT pearlitic rails for rail application. The R260 are used for general freight whereas the R350HT are used for heavy haul. For wheel application, AAR class B wheels are used for general freight whereas the class C are used for heavy haul with different classes AAR wheel steels and their applications shown in Table 3.1. For local rail industry, the loads experienced for heavy haul are 26 ton/axle for coal transportation and 30 ton/axle for iron ore transportation. Typical chemical compositions of different rail steels are shown in and Table 3.2 and Table 3.3.

Table 3.1: Specifications for rim hardness for several classes of AAR wheel steels and their uses [90].

Class	Brinell Hardness (Rim)	Type of Application
L	197–277	High-speed service with more severe braking conditions than other classes and light wheel loads.
A	255–321	High-speed service with severe braking conditions, but with moderate wheel loads
B	302–341	High-speed service with severe braking conditions and heavier wheel loads
C	321–363	Service with light braking conditions and heavy wheel loads and service with heavier braking conditions where off-tread brakes are employed



Table 3.2: Chemical composition of different grades of BS EN 13674-1:2011 standard rail steels (mass%) [91].

Steel grade		% by mass										10 <sup>-4</sup> % (ppm) by mass max.		Tensile strength <i>R<sub>m</sub></i> min. MPa	Elongation <i>A</i> min. %	Hardness of the rail running surface, centre line HBW
Steel name	Sample	C	Si	Mn	P max.	S max.	Cr	Al max	V max	N max	O'	H				
R200	Liquid	0,40 to 0,60	0,15 to 0,58	0,70 to 1,20	0,035	0,035	≤ 0,15	0,004	0,030	0,009	20	3,0				
	Solid	0,38 to 0,62	0,13 to 0,60	0,65 to 1,25	0,040	0,040	≤ 0,15	0,004	0,030	0,010	20	3,0	680	14	200 to 240	
R220	Liquid	0,50 to 0,60	0,20 to 0,60	1,00 to 1,25	0,025	0,025	≤ 0,15	0,004	0,030	0,009	20	3,0				
	Solid	0,48 to 0,62	0,18 to 0,62	0,95 to 1,30	0,030	0,030	≤ 0,15	0,004	0,030	0,010	20	3,0	770	12	220 to 260	
R260	Liquid	0,62 to 0,80	0,15 to 0,58	0,70 to 1,20	0,025	0,025	≤ 0,15	0,004	0,030	0,009	20	2,5				
	Solid	0,60 to 0,82	0,13 to 0,60	0,65 to 1,25	0,030	0,030	≤ 0,15	0,004	0,030	0,010	20	2,5	880	10	260 to 300	
R260Mn	Liquid	0,55 to 0,75	0,15 to 0,60	1,30 to 1,70	0,025	0,025	≤ 0,15	0,004	0,030	0,009	20	2,5				
	Solid	0,53 to 0,77	0,13 to 0,62	1,25 to 1,75	0,030	0,030	≤ 0,15	0,004	0,030	0,010	20	2,5	880	10	260 to 300	
R320Cr	Liquid	0,60 to 0,80	0,50 to 1,10	0,80 to 1,20	0,020	0,025	0,80 to 1,20	0,004	0,18	0,009	20	2,5				
	Solid	0,58 to 0,82	0,48 to 1,12	0,75 to 1,25	0,025	0,030	0,75 to 1,25	0,004	0,20	0,010	20	2,5	1 080	9	320 to 360	
R350HT	Liquid	0,72 to 0,80	0,15 to 0,58	0,70 to 1,20	0,020	0,025	≤ 0,15	0,004	0,030	0,009	20	2,5				
	Solid	0,70 to 0,82	0,13 to 0,60	0,65 to 1,25	0,025	0,030	≤ 0,15	0,004	0,030	0,010	20	2,5	1 175	9	350 to 390	
R350LHT	Liquid	0,72 to 0,80	0,15 to 0,58	0,70 to 1,20	0,020	0,025	≤ 0,30	0,004	0,030	0,009	20	2,5				
	Solid	0,70 to 0,82	0,13 to 0,60	0,65 to 1,25	0,025	0,030	≤ 0,30	0,004	0,030	0,010	20	2,5	1 175	9	350 to 390	
R370CrHT	Liquid	0,70 to 0,82	0,40 to 1,00	0,70 to 1,10	0,020	0,020	0,40 to 0,60	0,004	0,030	0,009	20	1,5				
	Solid	0,68 to 0,84	0,38 to 1,02	0,65 to 1,15	0,025	0,025	0,35 to 0,65	0,004	0,030	0,010	20	1,5	1.280	9	370 to 410	
R400HT	Liquid	0,90 to 1,05	0,20 to 0,60	1,00 to 1,30	0,020	0,020	≤ 0,30	0,004	0,030	0,009	20	1,5				
	Solid	0,88 to 1,07	0,18 to 0,62	0,95 to 1,35	0,025	0,025	≤ 0,30	0,004	0,030	0,010	20	1,5	1.280	9	400 to 440	

Table 3.3: Maximum residual elements of different grades of BS EN 13674-1:2011 standard rail steels (mass%) [91].

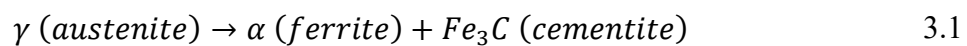
	Mo	Ni	Cu	Sn	Sb	Ti	Nb	Cu + 10 Sn	Others
R200, R220, R260, R260Mn	0,02	0,10	0,15	0,030	0,020	0,025	0,01	0,35	0,35 (Cr + Mo + Ni + Cu + V)
R320Cr	0,02	0,10	0,15	0,030	0,020	0,025	0,01	0,35	0,16 (Ni + Cu)
R350HT	0,02	0,10	0,15	0,030	0,020	0,025	0,04	0,35	0,25 (Cr + Mo + Ni + Cu + V)
R350LHT, R370CrHT, R400HT	0,02	0,10	0,15	0,030	0,020	0,025	0,04	0,35	0,20 (Mo + Ni + Cu + V)



### 3.2 Pearlitic steels

Pearlite is a microstructure produced by the eutectoid transformation in steels (equation 3.1 showing pearlite formation reaction) and it is made of a lamella structure consisting of alternating layers of ferrite ( $\alpha$ ) and cementite ( $Fe_3C$ ) [92]. Figure 3.1a shows a typical time-temperature-transformation (TTT) diagram for transformation of austenite to pearlite shown by a superimposed isothermal heat treatment curve (ABCD) and a schematic representation of the formation of pearlite in Figure 3.1b [93]. For a eutectoid steel (0.76 wt% C), the steel is heated to point A (above the eutectoid temperature,  $727^\circ C$ ) and held for some time for austenite formation, and slowly cooled to point B (below the eutectoid temperature) where it is held for some time to allow formation of 100% pearlite at point D, then slowly cooled to room temperature [93]. A typical micrograph of a fully pearlitic steel is shown in Figure 3.2.

Features such as pearlite interlamellar spacing, pearlite colony size and prior austenite grain size influences wear and other properties of pearlitic steels [79]. The prior austenite grain size influences the transformation reaction to pearlite, decreasing the grain size results in a faster reaction [94]. The interlamellar spacing is influenced by the cooling rate i.e., the faster the cooling rate, the finer interlamellar spacing while a slower cooling rate produces coarse interlamellar spacing [95]. Work by Sahay et al. [95] found that by increasing the cooling rate, the pearlite interlamellar spacing reduced from 200-400 nm to less than 100 nm. Micrographs of fine and coarse pearlite for eutectoid composition are shown in Figure 3.3.



*Pearlite*

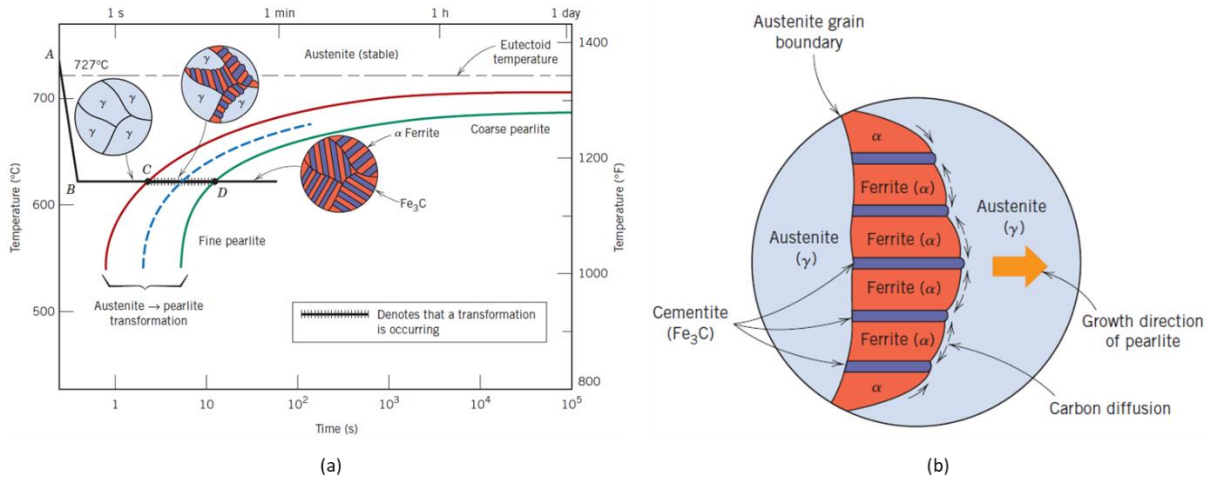


Figure 3.1: (a) Isothermal transformation diagram for a eutectoid iron–carbon alloy, with superimposed isothermal heat treatment curve (ABCD), showing the microstructures before, during, and after the austenite-to-pearlite transformation (Adapted by [93] from [96]); (b) Schematic representation of the formation of pearlite from austenite; direction of carbon diffusion indicated by arrows [93].

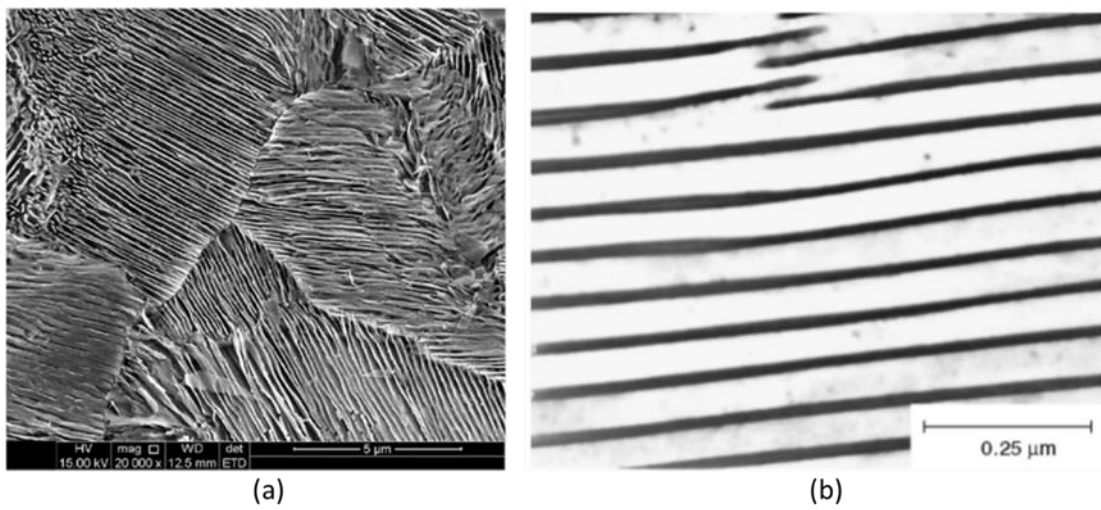


Figure 3.2: (a) SEM micrograph of a fully pearlitic steel showing random orientation of ferrite and cementite alternating lamellae colonies [97]; (b) TEM micrograph of pearlite in rail steel showing high magnification of lamella structure consisting of alternating layers of ferrite and cementite [92].

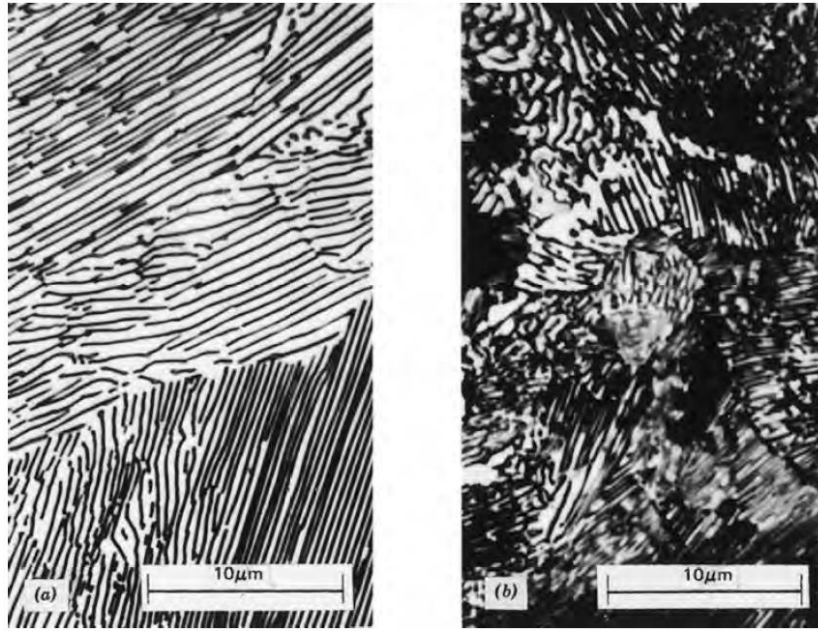


Figure 3.3: Micrographs of (a) coarse pearlite and (b) fine pearlite, 3000X [98].

The pearlite interlamellar spacing is a function of the transformation temperature, decreasing transformation temperature refines the pearlitic spacing [99]. The minimum pearlite spacing ( $d_{min}$ ) is obtained using equation 3.2 and it decreases with an increase in undercooling ( $\Delta T$ ).

$$d_{min} = \frac{2\gamma_{SF}}{\Delta H_v} \times \frac{1}{\Delta T} \quad 3.2$$

Where  $\gamma_{SF}$  is the surface energy of the  $\alpha/Fe_3C$  interface,  $\Delta H_v$  is the change in enthalpy between the parent and product phases and  $\Delta T$  undercooling ( $\Delta T = T - T_e$  where  $T$  is the transformation temperature and  $T_e$  is the eutectoid temperature) [100]. Several studies have shown that the strength of pearlitic steels have a Hall-Patch relationship (equation 3.3) with pearlite interlamellar spacing [101]. The Hall-Patch equation relates strength to grain size.

$$\sigma_y = \sigma_o + \frac{k_y}{\sqrt{d}} \quad 3.3$$

Where  $\sigma_y$  is the yield stress,  $\sigma_o$  material constant related to the resistance of lattice to dislocation motion,  $k_y$  is the strengthening coefficient (specific to each material), and  $d$  is the average grain size. Hyzak and Bernstein [99] have shown that interlamellar spacing ( $S$ ) is a major microstructural parameter that controls strength in pearlitic microstructures of steel containing 0.81% C and is related to yield strength using the regression equation 3.4 which incorporates other parameters such the austenite grain size ( $d$ ) and the pearlite colony size ( $P$ ) [92, 99].

$$\text{Yield Strength (MPa)} = 2.18(S^{-0.5}) - 0.40(P^{-0.5}) - 2.88(d^{-0.5}) + 52.30 \quad 3.4$$

Pearlitic steels have good wear resistance than most of the wheel/rail steels due to the lamella structure in pearlite microstructure. They also have high work hardening ability than most wheel/rail steels under rolling and sliding conditions which makes them have higher increase in surface hardness and strength during plastic deformation [101]. The pearlite interlamellar spacing also influences mechanical properties such as strength and hardness as shown in Figure 3.4 [101]. As may be seen in Figure 3.4a, decreasing the pearlite interlamellar spacing result in an increase in both strength and hardness of fully pearlitic steels [99]. This was also confirmed by a study by Clayton and Danks [102] who showed that decreasing the pearlite interlamellar spacing for various rail steels resulted in an increase in hardness, Figure 3.4b. Pearlitic steels are also used in heavy haul railway systems due to their stability, weldability, low production, and maintenance costs [103].

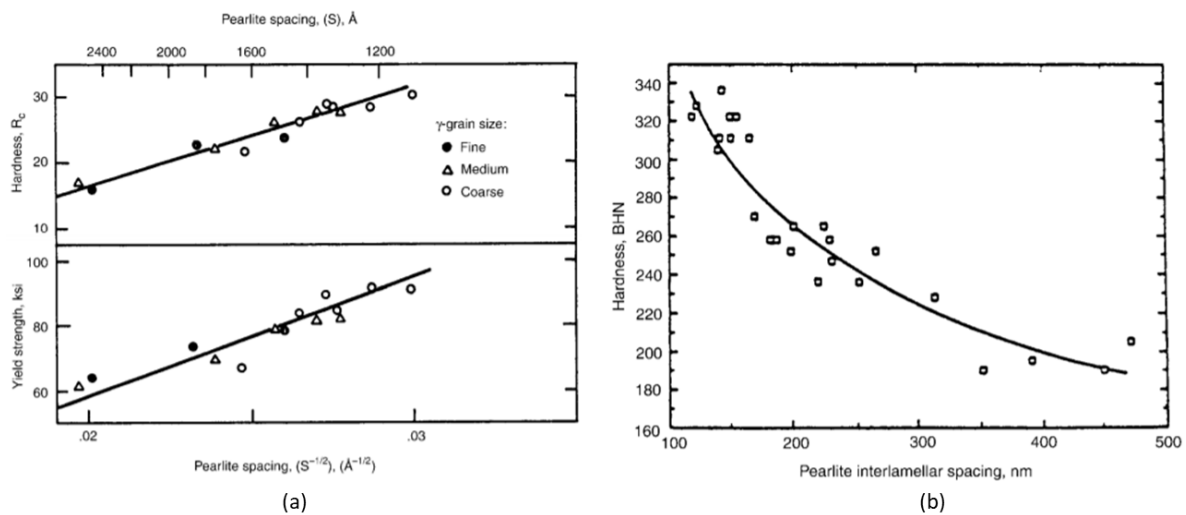


Figure 3.4: (a) Hardness and yield strength in fully pearlitic microstructures as a function of pearlite interlamellar spacing [99]; (b) The relationship between hardness and pearlite interlamellar spacing for different rail steels [102].

The pearlite interlamellar spacing has also been found to influence the wear resistance of pearlitic steels. Study by Perez-Unzueta and Beynon [89] on microstructure and wear resistance of pearlitic rail steels discovered that pearlitic rail steels with finer interlamellar spacing and thinner cementite lamellae are able to withstand high plastic deformation rates before they can fail, as compared to those with larger interlamellar spacing and thicker cementite lamellae [89]. Therefore, pearlitic rail steels with finer interlamellar spacing are more resistant to wear than those having larger interlamellar spacing [89]. This was also confirmed by Clayton and

Danks's research [102] who showed that pearlitic steels with smaller interlamellar spacing experience less wear than those with larger spacing as seen in Figure 3.5 [102]. Another study by Li et al. [79] studied the effects interlamellar spacing, pearlite colony size and austenite grain size have on wear and RCF by measuring the thickness of plastic deformation. As it may be seen in Figure 3.6, the thickness of the plastic deformation increased with increasing interlamellar spacing, pearlite colony size and austenite grain size [79]. Pearlitic microstructure can align parallel to the wear surface, generating a mosaic of cementite flakes, which contributes to the outstanding wear resistance of pearlitic rail steels [89]. The ability to form a mosaic of cementite by pearlitic steels makes them to be more superior than bainitic microstructures with regards to wear resistance [89].

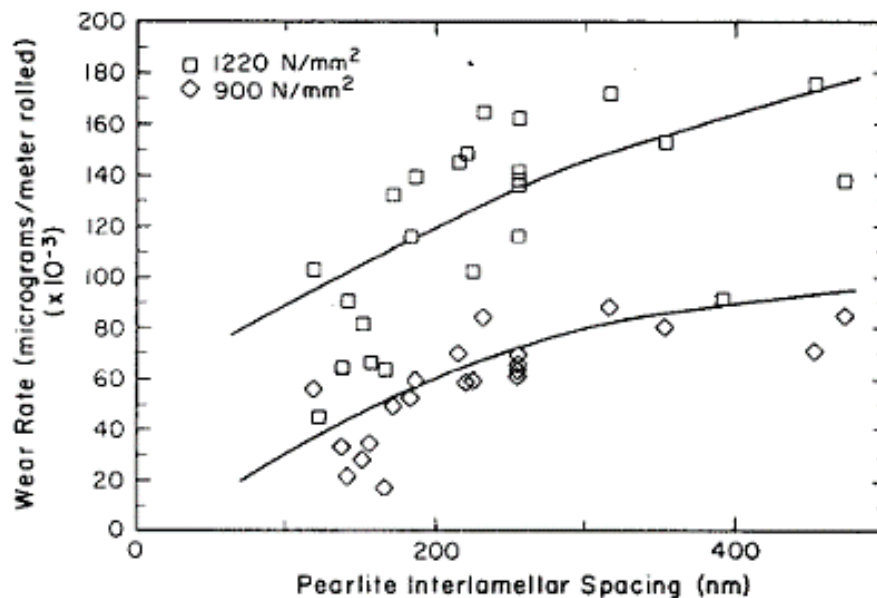


Figure 3.5: Wear rate against pearlite interlamellar spacing for several rail steel chemistries and heat treatments at 1220 and 900 N mm<sup>-2</sup> contact pressures [102].

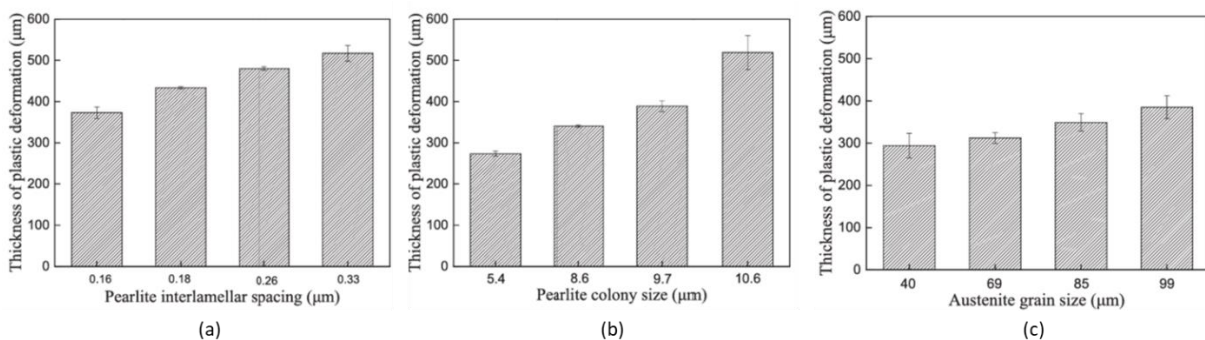


Figure 3.6: Influences of (a) pearlite interlamellar spacing (b) pearlite colony size and (c) austenite grain size on the thickness of plastic deformation [79].



### 3.3 Bainitic steels

Bainite is defined as a product of decomposition of austenite in steels at temperatures above martensitic transformation and below pearlite reaction temperatures [18, 104]. Bainitic microstructure is a mixture of ferrite and cementite same as pearlite, but unlike pearlite in bainitic microstructures ferrite and cementite do not show lamella structure and only exist as acicular crystals (needle-like crystals) [92, 104]. According Bhadeshia [105], bainite is mainly classified into two morphologies being upper bainite and lower bainite, Figure 3.7, the stages of development of the microstructures are shown in Figure 3.8a. Unlike lower bainite, upper bainite is free from precipitates as shown on Figure 3.7b [105]. Lower bainite is made up of sheaves with plate-like ferrite while upper bainite is made up of sheaves with lath-like ferrite [104]. The difference in their microstructures results in different properties such as hardness, wear and impact properties. For example, lower bainite has better impact properties and lower ductile to brittle transition temperature (DBTT) as compared to upper bainite, Figure 3.8b. The structure of bainite depends on the amount of carbon and other alloying elements as well as the specifics on how the constituent phases nucleate and grow [104].

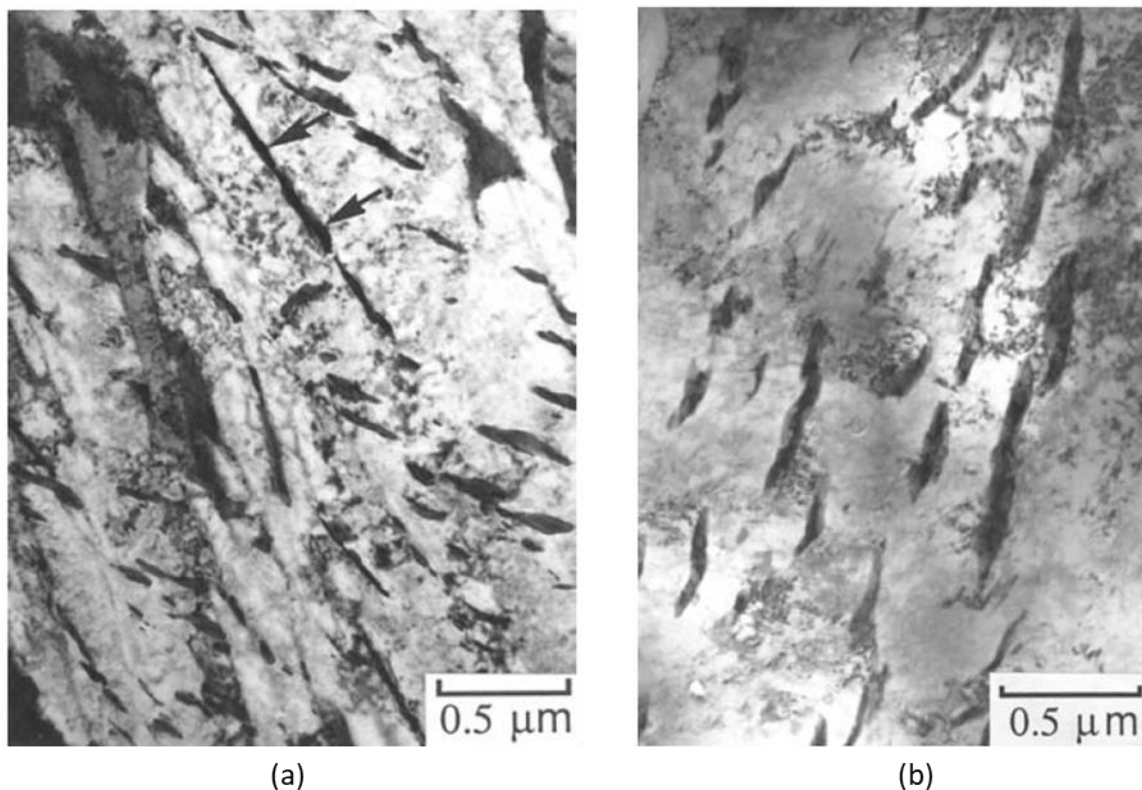


Figure 3.7: (a) Lower bainite obtained by isothermal transformation for 30 minutes at 453 °C causing the precipitation of carbides between the ferrite platelets; (b) distribution of cementite particles between ferrite platelets in upper bainite (AISI 4340 steel) [105].

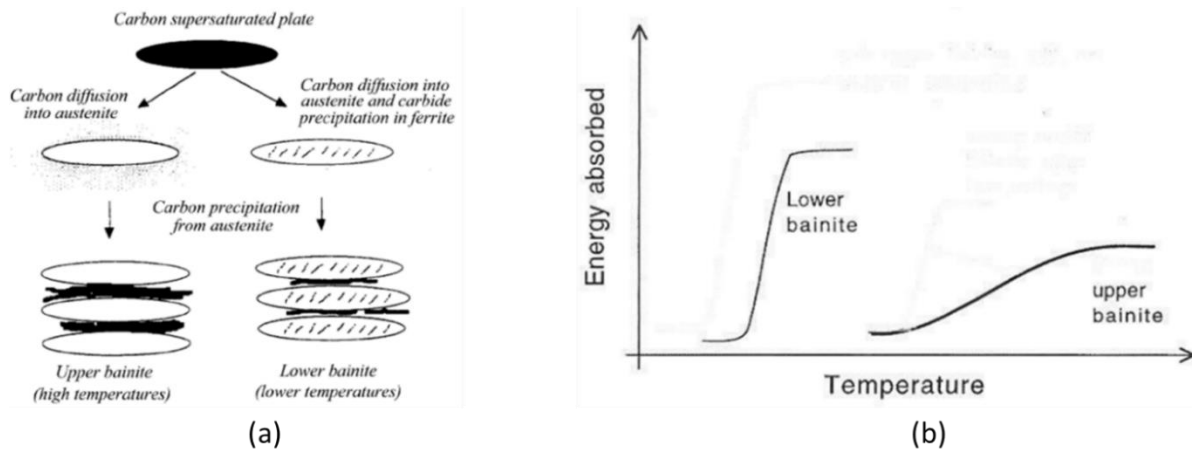


Figure 3.8: (a) A schematic illustration showing the stages in the development of a bainitic microstructure [106], (b) Charpy curve of lower and upper bainite [105].

Bainitic steels have better ductility, toughness and rolling contact fatigue resistance with lower wear resistance when compared to conventional pearlitic steels of the same hardness [107]. Studies have shown that the reason for this poor wear resistance under sliding and rolling wear by bainitic steels is attributed to the presence of carbides and poor work hardening ability [108, 109]. Study by Viafara et al. [110] has also confirmed that pearlitic steels have far much better wear resistance than bainitic steels on their work on unlubricated sliding wear of pearlitic and bainitic steels as shown in Figure 3.9 [110]. From their mass loss results, bainitic steel showed higher mass losses of three or more orders in magnitude as compared to pearlitic steels [110]. Poor wear performance of bainitic steels has led to development and study of carbide-free bainitic steels with better sliding/rolling wear resistance and rolling contact fatigue resistance than conventional pearlitic steels for railway applications which are discussed in section 4.11.1.

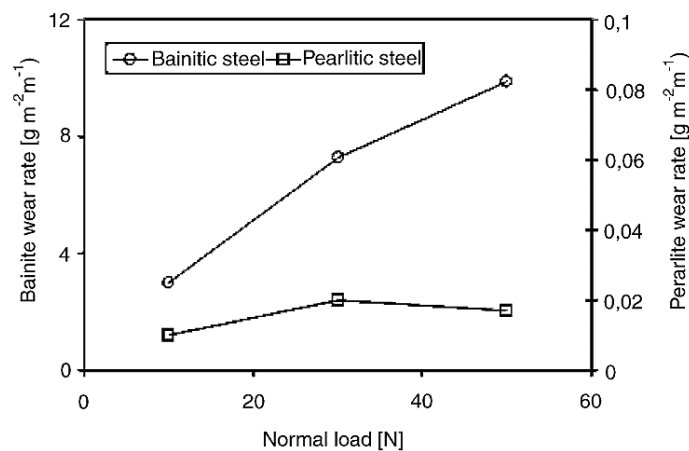


Figure 3.9: Wear rate for pearlitic and bainitic steels as a function of normal load [110].

## Chapter 4: Wear and rolling contact fatigue

### 4.1 Introduction

Wear is a process in which material is gradually removed from surfaces that are in contact due to mechanical, chemical, or physical factors [33, 111]. Many things, such as sliding, rolling, impact, corrosion, erosion, or cavitation, can cause it. Wear can cause a metal's mechanical qualities to degrade, shorten its lifespan, and ultimately cause the component or system it is employed in to fail. During sliding and rolling of a wheel on rail tracks, the wheel/rail contact experiences different types of wear such as mechanical wear, chemical wear, thermal wear or a combination of any of these depending on the working environment [112]. Rolling contact fatigue (RCF) is a phenomenon where pressure and creep forces are applied repeatedly in the rail/wheel contact area, reducing the durability of the contacting surfaces [112, 113]. There is a competitive relationship between wear and RCF on at the wheel/rail interface. When the wear rate exceeds RCF crack growth rate, the RCF crack will be worn away [114]. However, if the wear rate is lower than the crack growth rate, the crack will continue to grow until failure occurs [74]. The main defects that contribute significantly to cost associated to damage of the wheels and rails are shelling and spalling [115]. Shelling and spalling have been found to be the major causes of wheel tread damage resulting in wheel replacement costing up to 50% of freight car maintenance costs in North America railroad operations [116]. In the USA alone, repairing and replacing damaged wheels and rails due to wear and RCF cost approximately \$2.5 billion a year [117]. Figure 4.1 shows the different mechanisms of rail peeling, spalling and wheel cracks with typical wheel and rail wear from actual wheel and rail materials shown in Figure 4.2, Figure 4.3 and Figure 4.4.

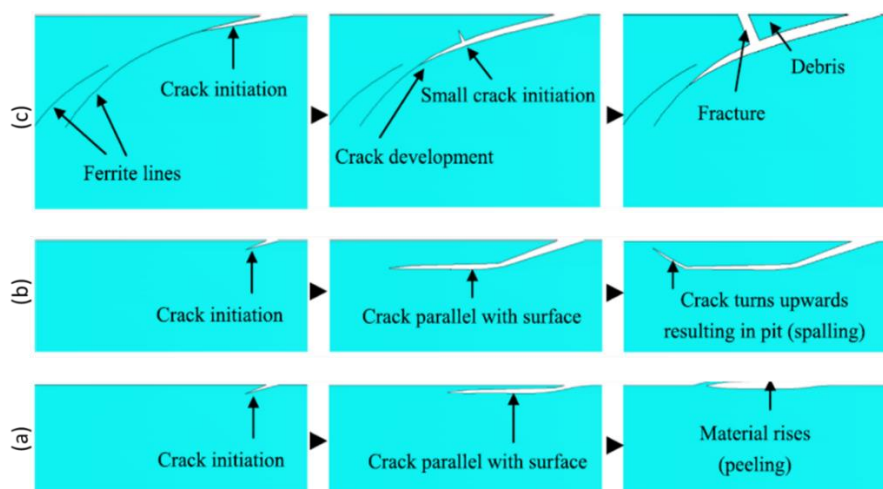


Figure 4.1: Schematic diagram of (a) rail peeling (b) rail spalling and (c) wheel cracks [118].



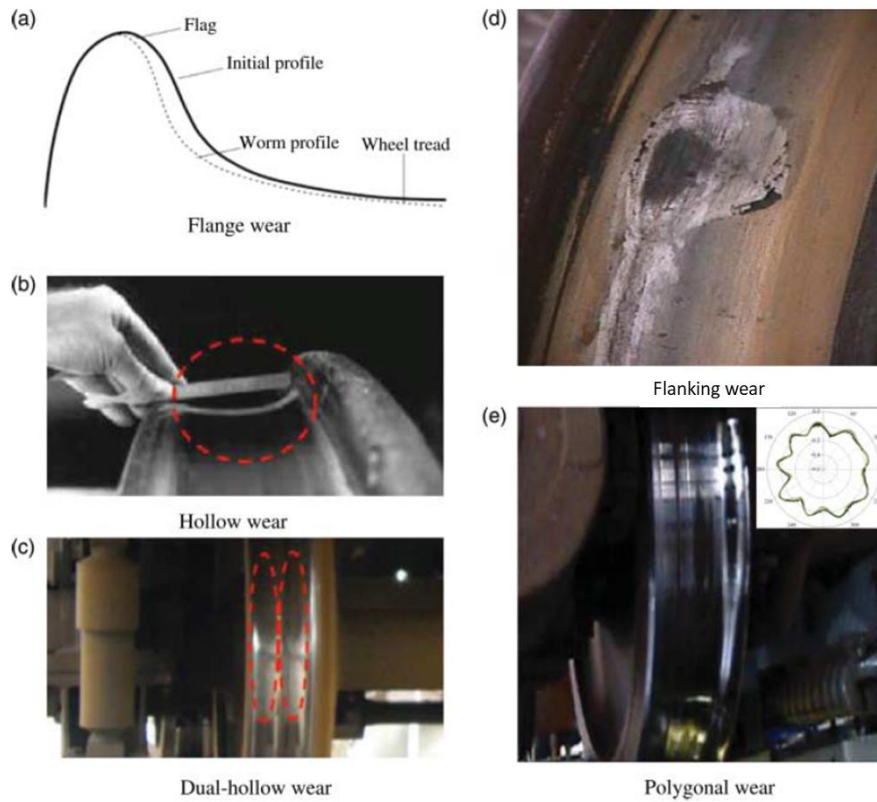


Figure 4.2: Different types of wheel wear; (a) Flange wear (b) flanking wear (c) Hollow wear (d) Dual-hollow wear and (e) Polygonal wear [119].

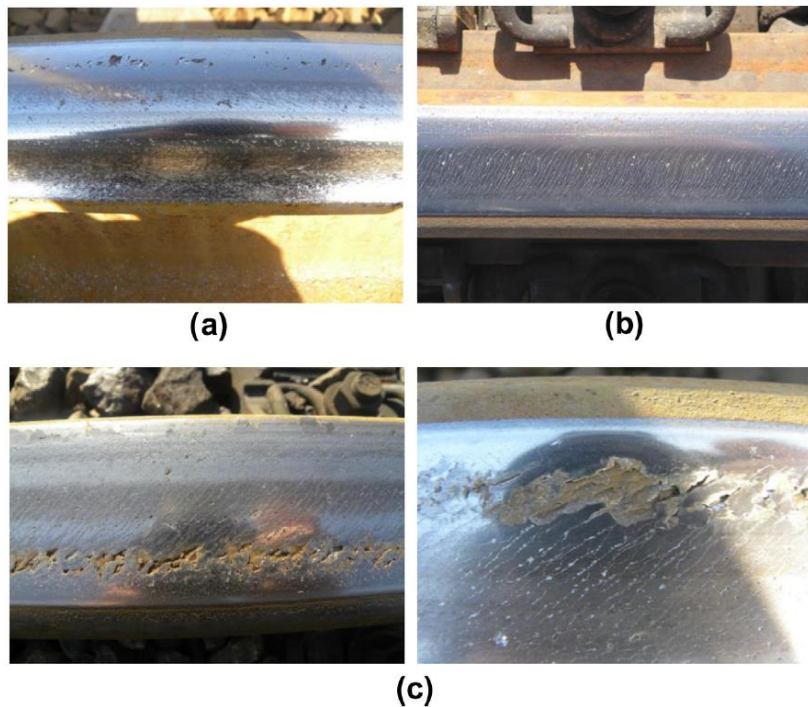


Figure 4.3: Typical rail damages on a heavy-haul railway curved rail: (a) Side wear; (b) surface crack; (c) spalling [120].

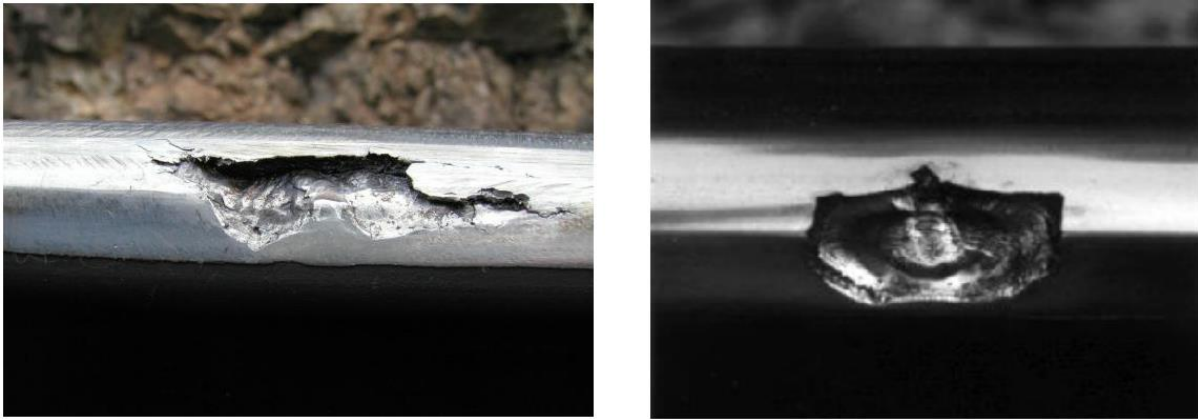


Figure 4.4: Examples of shelling from gauge corner collapse on rail steels [121].

Work done by Lewis and Dwyer-Joyce has shown that there are three wear regimes on wheel steels being mild, severe and catastrophic as shown on Figure 4.5 [20]. R8T wheels steels and UIC60 900A rail steels were used in their work on a twin-disc setup [9]. The three wear regimes identified were characterised in terms of their features, wear rates and morphology of their debris [9, 82]. Surface oxidation was the primary cause of wear at low slip, whereas surface cracking and mass loss by spalling were the primary causes of severe wear at high slip [20]. The catastrophic regime is primarily seen at high wear rates, where significant delamination occurs because of a rise in the severity of the contact conditions, which results in material loss by the ratcheting process [122, 123]. Ratcheting is a process that causes material deformation, which leads to the emergence of cracks and the subsequent removal of material [123]. Early research had limited information on the analysis of wear processes occurring at the regimes and had even less knowledge regarding the reasons for certain wear regimes and the existence of those wear regimes [122]. A deeper knowledge of those wear mechanisms at each wear regime and their existence has been achieved recently thanks to research like the one by Lewis and Dwyer-Joyce [20] and others [20, 122].

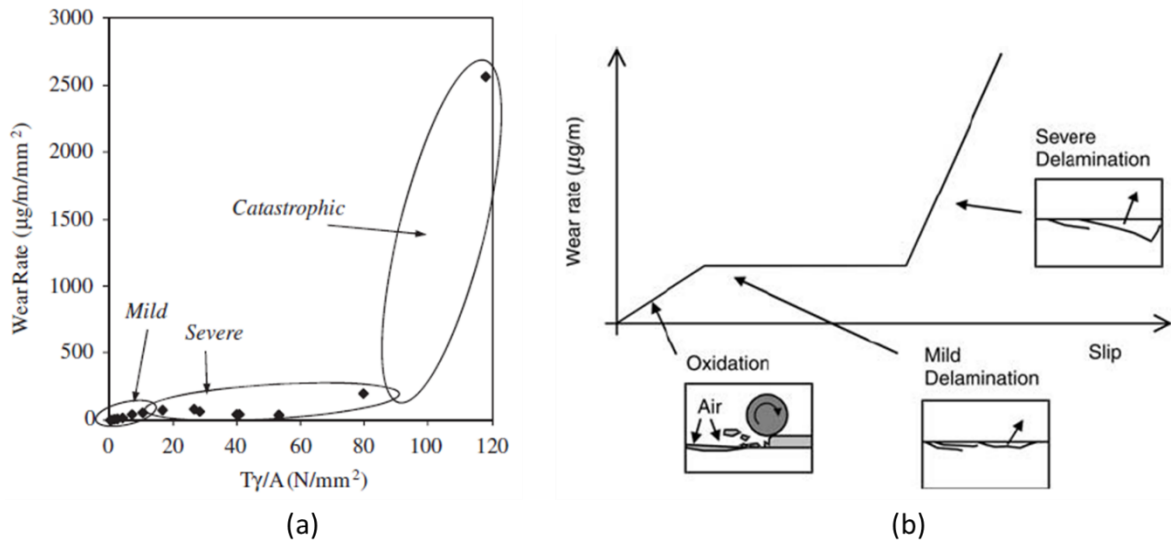


Figure 4.5: (a) R8T wheel wear rates (against 900A rail) on twin-disc testing and (b) schematic diagram of wear features and regimes [20].

Plots of wear rate ( $\mu\text{g}/\text{m}/\text{mm}^2$ , which is the weight of lost material ( $\mu\text{g}$ ), per distance travelled (m), per contact area ( $\text{mm}^2$ )) as a function of the wear index ( $T\gamma/A$ ,  $\text{N}/\text{mm}^2$  where  $T$  is the tractive force,  $\gamma$  the slip and  $A$  the contact area) are used to define wear regimes. The  $T\gamma/A$  values for a typical wheel/rail contact are usually between 0 and 10  $\text{N}/\text{mm}^2$  at the tread whereas they are larger than 20  $\text{N}/\text{mm}^2$  at the flange contact [124]. Equation 4.1 relates the wear rate to the work performed at the wheel/rail contact, where  $K$  is the wear coefficient.

$$\text{Wear rate} = K \frac{T\gamma}{A} \quad 4.1$$

## 4.2 Wear mechanisms

Wear occurs by several mechanisms some of which include adhesive, abrasive, delamination, corrosive, fatigue, and fretting wear [125]. Wear occurs by either one or a combination of those mechanism at the wheel/rail contact depending on contact conditions.

### 4.2.1 Abrasive wear

Abrasive wear is a material removal or displacement process on a surface by hard particles on surfaces that are under loading due to the relative motion to those contacting surfaces [126]. Abrasive wear occurs in two mechanisms being two-body and three-body as shown in Figure 4.6 [127]. In two body abrasive wear, material removal takes place due to rubbing of a softer surface by a hard and rough surface whereas in three body abrasive wear material removal takes place due to hard particles being entrapped between two sliding surfaces [127]. Abrasive

wear has been found to be the source of up to 50% of the wear problems [33]. In railway industry presence of third body materials such as sand, soil dust, concrete accelerates abrasive wear as they are harder than wheel and rail materials. For example, sand is constituted mainly of quartz which is harder than steel and is very abrasive so during sanding when there is loss of traction sand increases the wear rate at the wheel/rail.

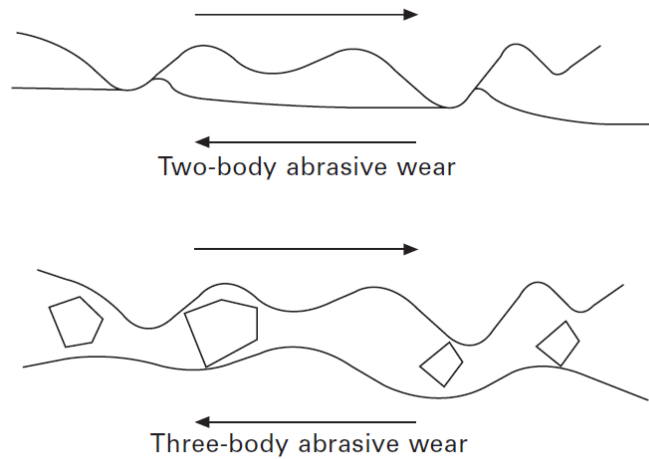


Figure 4.6: Two-body and three-body abrasive wear mechanisms [33].

#### 4.2.2 Delamination wear

Delamination wear is more severe as compared to abrasive wear [88]. Its wear debris are metallic, and it starts by crack initiation on the surface which later propagates under the surface until breaks out to producing a flake material which detaches from the wheel/rail surface producing a rougher surface as compared to adhesive wear [88]. The debris of delamination wear are larger in size as compared to abrasive and adhesive wear [128].

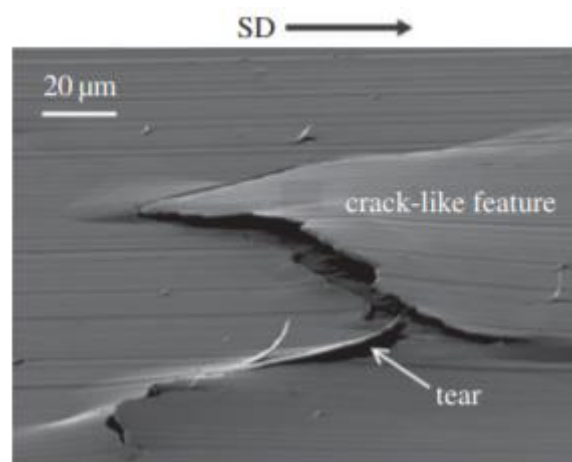


Figure 4.7: Micrograph showing delamination wear under sliding wear testing [129].

### 4.2.3 Corrosive wear

Corrosive wear is the removal of material where both wear and corrosion mechanisms occur in a corrosive environment [130]. The process begins by chemical attack on the surface by corrosive agents resulting in formation of corrosion products which are subsequently removed by wear mechanisms such as abrasion, fretting or adhesive. This is a continuous process unless stopped and causes material loss and surface degradation. Corrosive wear is serious problem in industries such as oil and gas, agriculture, food processing and in implanted medical devices such as artificial joints [130]. In railway industry, corrosion is also a problem and is mainly due to the presence of lubricants such as water. Corrosion is responsible for the formation of pits on the surface of rails which may cause crack initiation and propagation due to localised stress concentration.

### 4.2.4 Fatigue wear

Fatigue wear is a material removal or surface damage process that occurs due to repeated cyclic loading between two contacting surfaces when the load being applied is higher than the fatigue strength of the material [131]. It is a severe damage process consisting of crack propagation and failure because of repeated loading [132]. The process of crack initiation and propagation during fatigue wear is shown in Figure 4.8.

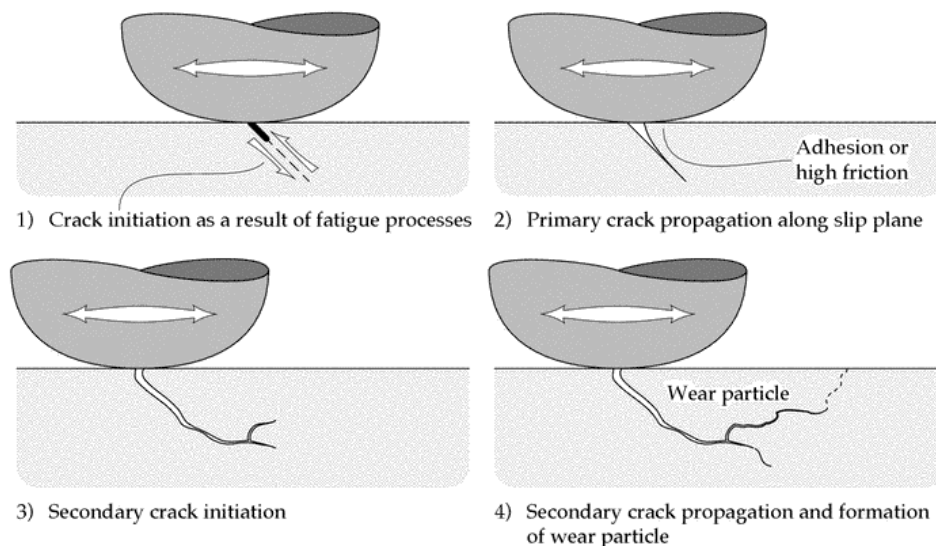


Figure 4.8: Schematic illustration of the process of surface crack initiation and propagation during fatigue wear [133].

#### 4.2.5 Fretting wear

Fretting wear is the removal of materials from surfaces of two contacting bodies that are in micro-level relative motion or small amplitude lateral displacements under contact loading [134, 135]. Fretting wear is affected by several factors such as relative humidity, temperature, material, number of cycles, amplitude and contact load [136]. This type of wear is mainly experienced in mechanical assemblies such as in bearings, shafts, turbine blade roots, biomedical applications and some electrical contacts [134]. In railway industry fretting wear is mainly experienced at the wheel/axle joint and some at the wheel/rail contact due to repeated loading which may cause failure by RCF due to rapid crack formation and surface degradation [137]. Mechanisms occurring during fretting wear are due to a combination of other types of wear such as adhesive wear, abrasive wear and corrosive wear occurring at different stages as shown in Figure 4.9. Sometimes fretting wear causes jamming in systems due to debris being held in at the contact area [138]. There are a number of preventative measures that have been done in different applications to stop or reduce occurrence of fretting wear. These preventative measures include the use of vibration absorbers, using materials that are resistant to fretting corrosion, shot peening in metals, keeping the amplitude below the level at which fretting occurs, etc [136].

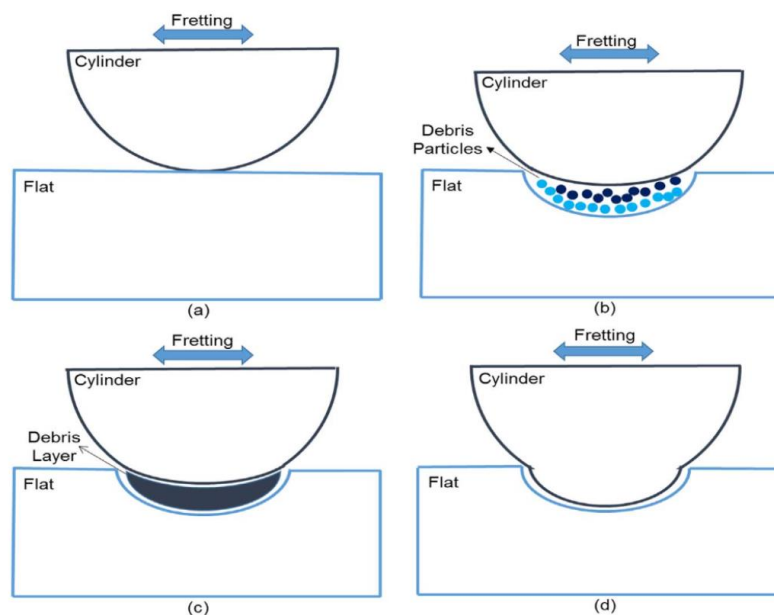


Figure 4.9: Schematic diagram showing different stages occurring during fretting wear; (a) cylinder fretting on a flat, (b) debris particles removed from the cylinder and flat, (c) Debris forming a compact layer, (d) the compacted debris layer becomes part of the cylinder changing its shape [135].



### 4.3 Rolling contact fatigue

Both the wheel and the rail track experience rolling contact fatigue (RCF) when the wheel travels down the rail track. RCF is a form of surface damage that can happen to materials when they are repeatedly subjected to rolling or sliding contact. Components like bearings, gears, and rails that experience cyclic loading and unloading under high contact pressures are susceptible to this type of damage. RCF is a type of material fatigue that can cause component failure by way of surface fractures, pitting, spalling, and other types of damage [139]. A mixture of mechanical and material factors can be attributed to the RCF mechanism. When a material is repeatedly subjected to contact loading, the stresses at its surface are greater than its fatigue limit, which causes microcracks to develop [140]. These microcracks can propagate and combine, leading to the formation of larger cracks and spalling [139]. There are various factors that can influence the occurrence of RCF, including the material properties, contact stress, lubrication, the geometry of the wheel/rail contact, inclusions and surface finish [141]. Entrapped hydrogen and other inclusions, such as the hard and soft inclusions in steel, are responsible for crack initiation and propagation which are key factors influencing RCF. For instance, under cyclic loading, soft manganese sulphide inclusions act as crack initiators (stress raisers), reducing the fatigue resistance of rail and wheel materials and potentially leading to fatigue failure [121, 142].

RCF defects include spalling, shelling, head cracks, squats, some are shown in Figure 4.10 and Figure 4.11. RCF cracks formation mechanisms have been previously described by a study by Makino et al. [143]. Their study also found out that as the slip ratio increased, so did the traction coefficient, while the fatigue strength decreased [143]. The decrease in fatigue strength was due to more formation of branching fatigue cracks with an increase in slip ratio causing shelling and spalling to occur leading to catastrophic wear. Previous works [144, 145] have shown that at high slips and contact pressures micro cracks initiate. With the presence of water at the contact, the initiated cracks propagate forming crack branching which may cause severe damage such as shelling compared to dry contact. As wear has a competitive relationship with RCF [145, 146], its presence at the wheel/rail contact is crucial. Higher wear rate can continuously help to remove any layers where cracks may have developed, lowering the possibility of serious damage [146]. Squats rail defects have been defined by Muhamedsalih et al. [147], as “a widening and a localised depression of the wheel-rail contact band, accompanied by a dark spot containing cracks with a circular arc or V shape” [147], as seen in Figure 4.11b. They can be caused by a number of factors which include plastic deformation,

rail surface irregularities (such as welds, wheel burns), high axle load and high train speeds. The main danger of squat defects is that the accompanying cracks will grow into the parent rail at a transverse plane, potentially resulting in a catastrophic full rail failure if the squats are not treated [148].

It has been observed that head cracks lead to rail breakage which may possibly result in accidents occurring [24, 25]. In Europe, it has been found that maintenance associated with damage caused by RCF is costing railway operating companies an estimated hundreds of million Euros annually [149]. To prevent RCF, various methods can be employed, such as improving the material properties, reducing the contact stress, and improving the surface finish. Additionally, routine maintenance and inspection can help to detect and mitigate RCF before it leads to component failure. RCF is a significant concern in many industries where rolling or sliding contact is common, such as the automotive, aerospace, and railway industries. By understanding the mechanisms of RCF and employing appropriate prevention methods, the risk of component failure can be reduced, leading to increased safety, efficiency, and cost savings.

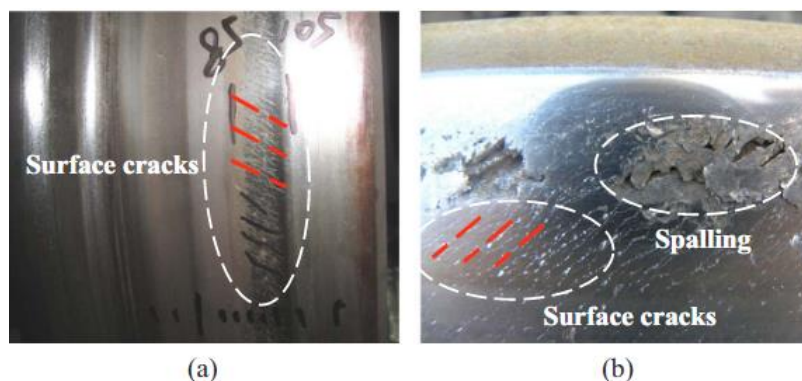


Figure 4.10: Surface fatigue cracks on the railway, (a) wheel tread; (b) rail head [150].

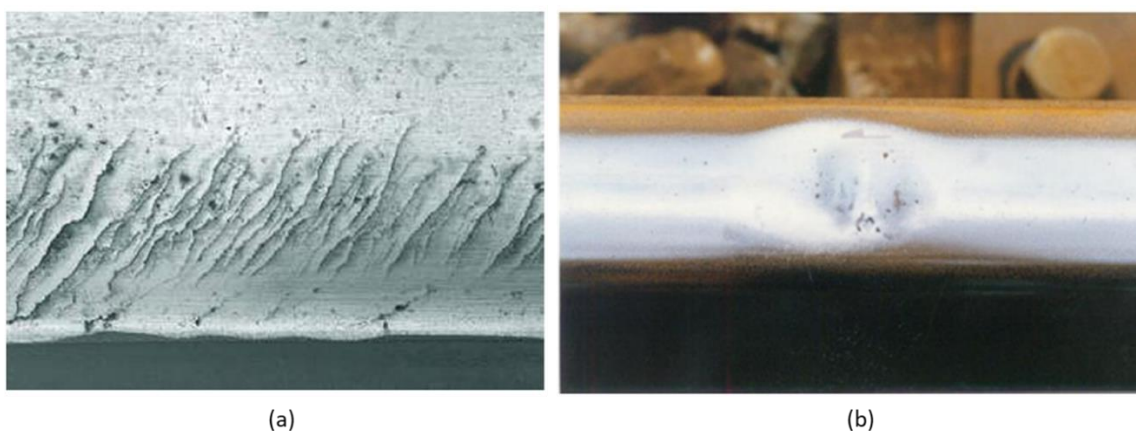


Figure 4.11: Typical rail RCF cracks: (a) head checks on the surface of a rail [151], and (b) typical squat defect (single squat) [152].



RCF has contributed to numerous railroad accidents worldwide, including the "Hatfield rail crash". On the 17<sup>th</sup> of October 2000 in Hatfield, Hertfordshire, UK there was a train accident known as "Hatfield rail crash" which a train derailed from the rail tracks travelling at about 185 km/h due to failure caused by RCF (Figure 4.12) [121, 153]. The train accident killed four people and injured more than 70 with costs exceeding one billion British Pounds [121, 153]. The RCF that caused the Hatfield rail crash was due to the presence of numerous and pre-existing fatigue cracks in the rail surface which resulted in fatigue failure due to repeated loading [153]. The investigation team found that the lack of proper maintenance practices resulted in the accident. The Hatfield rail crash led to acceleration and development of better preventative maintenance procedures to try to prevent similar accidents from occurring [154].



Figure 4.12: (a) The crash site at Hatfield (UK), showing disintegrated rail [154], (b) fragmented rail due to fractures from multiple rolling contact fatigue cracks [25].

As mentioned earlier, rolling contact fatigue has competitive relationship with wear as the latter reduces RCF by wearing away cracks and defects caused by RCF improving the rail fatigue life. In other words, reducing wear on wheel/rail contact may indirectly lead to an increase in RCF [155, 156]. The sliding and rolling wear removes partially or completely fatigue cracks and in the process prevent further growth of cracks by the RCF [157]. This competitive relationship between RCF and wear has been found to be more visible in dry rolling–sliding conditions than in wet conditions [145]. In dry conditions, there are high creep forces due to high coefficient of friction resulting in high removal rate of cracks by wear [158]. Whereas in wet conditions, the coefficient of friction is low and, therefore, RCF is more dominant resulting in crack growth and propagation as there is less wear to remove the cracks [158]. The liquid

lubricant at the wheel/rail contact plays a role in crack propagation by a process known as ‘fluid crack pressurisation’ [158] which is discussed further in section 4.10.1. Several studies have shown that increasing the rail head cross section and rail steel strength reduces wear problems. However, this tends to cause RCF problems resulting in propagation of surface cracks [159]. On the work done by Donzella et al. [159] on the comparison between wear and RCF, Figure 4.13, when the wear curve is above the RCF curve wear takes place preventing failure by RCF [159]. But when RCF curve is above the wear curve the opposite occurs, RCF becomes predominant resulting in surface cracking and fatigue failure with the actual crack depth being the difference between the two curves [159].

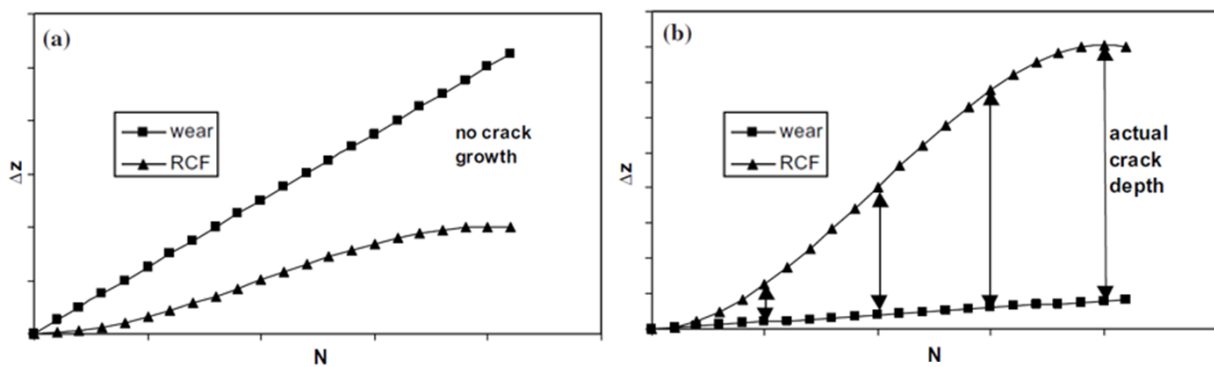


Figure 4.13: Qualitative graph of damaged depth  $\Delta z$  vs. Number of cycles ( $N$ ): (a) in condition of prevalent wear; (b) in condition of prevalent RCF [159].

#### 4.4 Material response to cyclic loading and shakedown maps

When a material is subjected to cyclic loading, under rolling contact fatigue it can respond in four ways being purely elastic, elastic shakedown, plastic shakedown and ratchetting depending on the contact conditions [160], Figure 4.14. For purely elastic response (response a), it occurs when the maximum stress does not exceed the yield stress of the softer material and the response is reversible throughout [160]. When the first yield limit is exceeded due to repeated loading, as a result of strain hardening the response become elastic shakedown (response b). The plastic shakedown (response c) occurs beyond the yield strength without any accumulation of plastic deformation and the loading cycle remains within the closed plastic stress-strain loop [161, 162]. Lastly, the ratchetting response (response d) occurs when the deformation exceeds the ductility of the material, and the material fails or breaks. It is where there is accumulation of plastic strain, and the plastic stress-strain is an open loop [161, 162]. Ratchetting corresponds to initiation of RCF cracks such as head cracks in rails and plays a key role in RCF failure in rails [163].

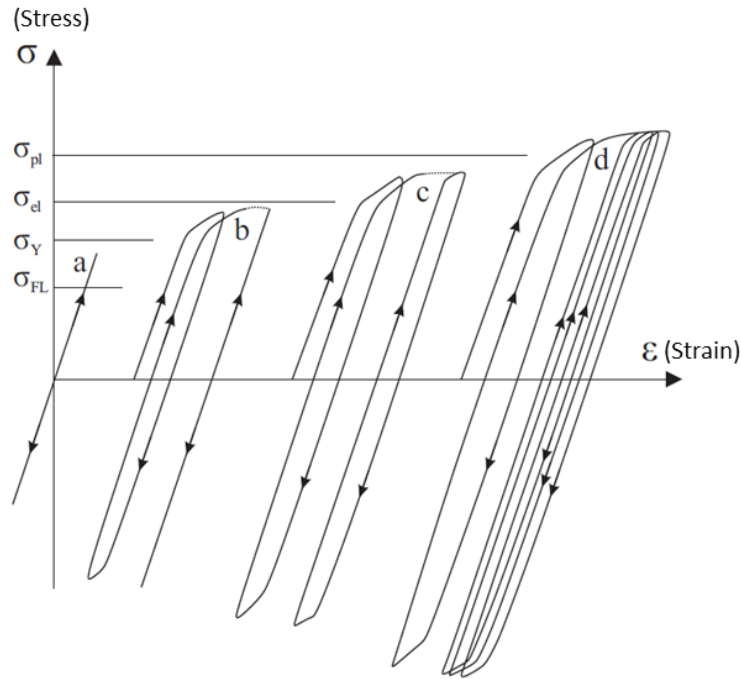


Figure 4.14: Material response to cyclic loading: (a) purely elastic deformations, (b) elastic shakedown, (c) plastic shakedown and (d) ratchetting (adapted by [161] from [160]). Where  $\sigma_{FL}$  is the fatigue limit,  $\sigma_Y$  is the elastic yield limit,  $\sigma_{el}$  is the elastic shakedown limit and  $\sigma_{pl}$  is the plastic shakedown limit [164].

To characterise the four materials responses to cyclic loading, shakedown maps are used, first proposed by Johnson [160]. The shakedown maps are based on the shakedown theorem, stating that if a material is exposed to cyclic loading that does not exceed its shakedown limit, plastic deformation will not occur. The shakedown limit is defined by the shear yield strength ( $k_c$ ), contact pressure ( $P_o$ ), and friction coefficient ( $\mu$ ) of the contacting materials (Figure 4.15) and can be used to study and predict the RCF damages mechanisms of wheel and rail materials [165]. Shakedown maps are an extremely useful tool for developing wheel and rail components. They can also be used to ensure that the wheel and rail components are free of plastic deformation and lies within the elastic limit hence a longer service life.

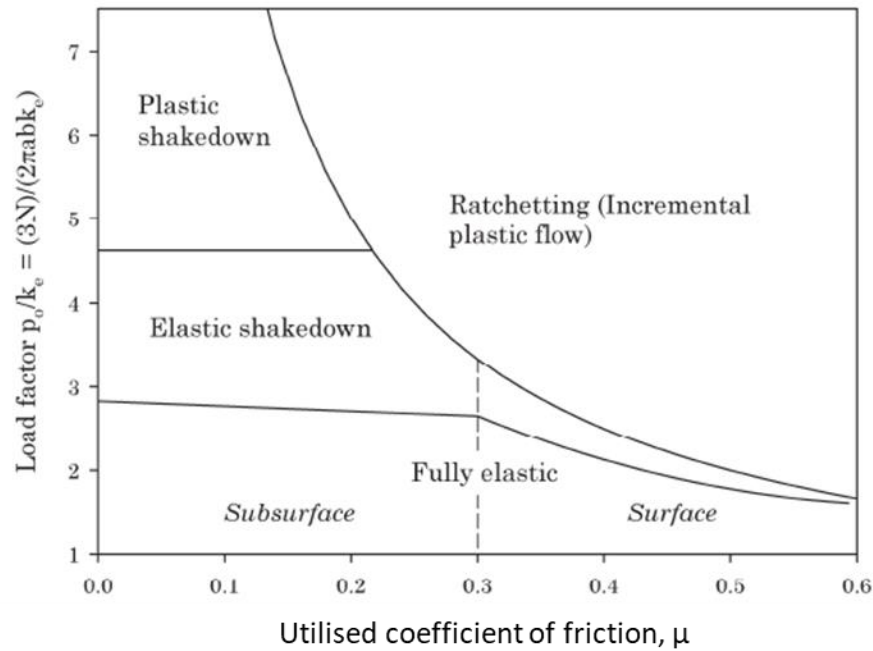


Figure 4.15: Shakedown map for a perfectly plastic and a kinematically hardening material, where  $P_0$  is the maximum Hertzian pressure,  $N$  normal load,  $a$  and  $b$  are semi axes of the wheel-rail contact patch and  $k_e$  is the shear yield limit, (Adapted from [160]).

#### 4.5 Wheel polygonal wear

Wheel polygonal wear is a periodic wear type of the wheel tread along its circumference also known as wheel harmonic wear causing the wheel to be out-of-round resulting in different surface profiles on the wheel [119, 166]. Studies have shown that an accumulation of plastic deformation on the wheel materials contributes significantly to wheel polygonal wear [119]. Out-of-round wheels caused by polygonal wear generate impact forces at the wheel/rail contact, which are transferred to the train and its component such as wheels, axles, rails, rail joints, bearings and concrete sleepers [167]. This causes vibrations between the wheel and rail resulting in damage to those train components [119]. These vibrations also cause some form of discomfort and high levels of noise to passengers in trains [119]. Figure 4.18 shows a model of noise generation at the wheel/rail contact as the wheel moves along the rail. There are several conditions that contribute towards noise generation. A study by Zhang et al. on the influence of wheel polygonal wear on interior noise of high-speed trains has found that there is relationship between wheel roughness and interior noise [168]. They found that higher wheel roughness causes high levels of interior noise [168]. When the wheels were re-profiled by machining the interior levels of noise decreased significantly as shown in Figure 4.16b. Figure 4.16b shows that at  $240^\circ$  before re-profiling, the wheel roughness was approximately 0.573

mm and after re-profiling it was approximately 0.001 mm. Similarly, before re-profiling, the diameter difference was approximately 0.795 mm and after re-profiling it was less than 0.1 mm [168]. The diameter difference ( $D$ ) is the difference between maximum and minimum wheel roughness numerical values given by equation 4.2:

$$D = R_{max} - R_{min} \quad 4.2$$

Where  $R_{max}$  and  $R_{min}$  are the maximum and minimum wheel roughness in numerical value, respectively [168]. A field study by Shi et al. [169] on evolution of wear on high-speed trains has found that the increasing operating distance (sliding distance) accelerates wear on both tread and flange parts of the wheel by increasing the wear depth, Figure 4.17.

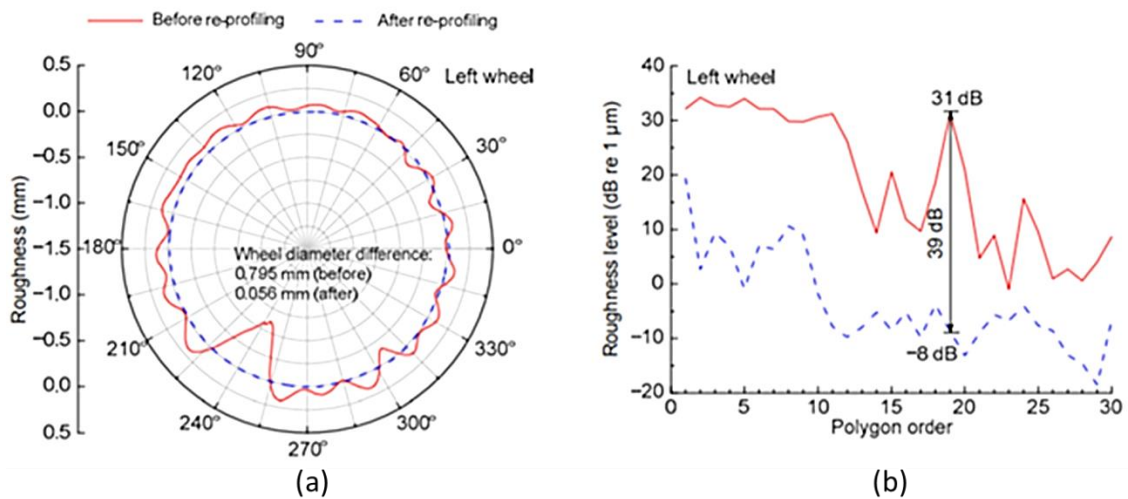


Figure 4.16: Wheel roughness and polygonal order before and after re-profiling: (a) wheel roughness; (b) polygon order [168].

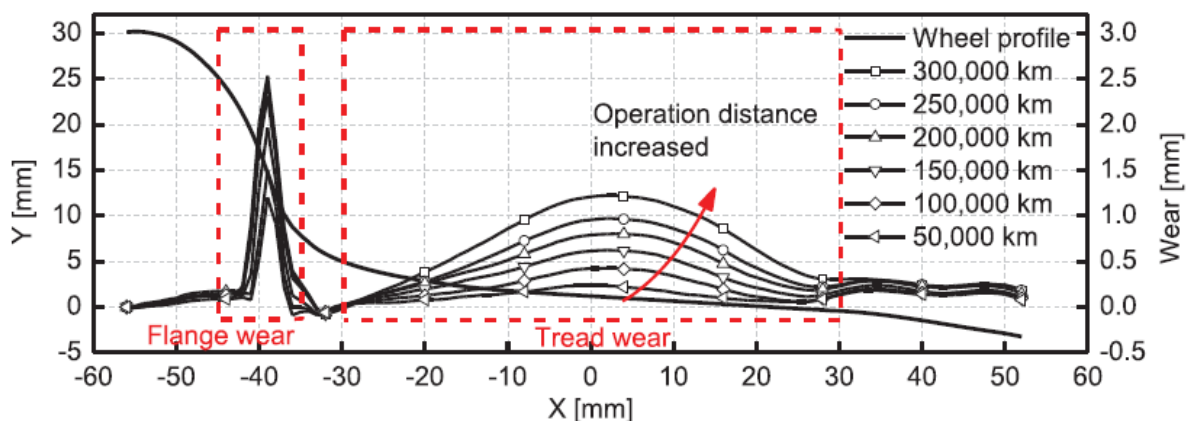


Figure 4.17: Wheel profiles and wear within a reprofiling cycle [169].



To reduce the noise caused by polygonal wheel wear on high-speed trains in Germany, a decision was made in 1991 by railroad authorities to replace all wheels with rubber-sprung wheels (elastic wheels) which reduced the noise significantly. The elastic wheels were using rubber blocks for connecting the rim and web resulting in vibration damping and reduced noise [170]. That introduction of elastic wheels in the structure was found to reduce fatigue strength of the wheels [170]. In 1998 a severe railroad accident happened near the village of Eschede in Germany killing 101 and injuring more than 100 passengers [171]. The cause of the accident was found to be a broken tire of a rubber-sprung wheel which got stuck under the carriage floor causing derailment and collision of the train [171]. After the accident all carriages with rubber-sprung wheels were removed from service to prevent further similar accidents from occurring [171].

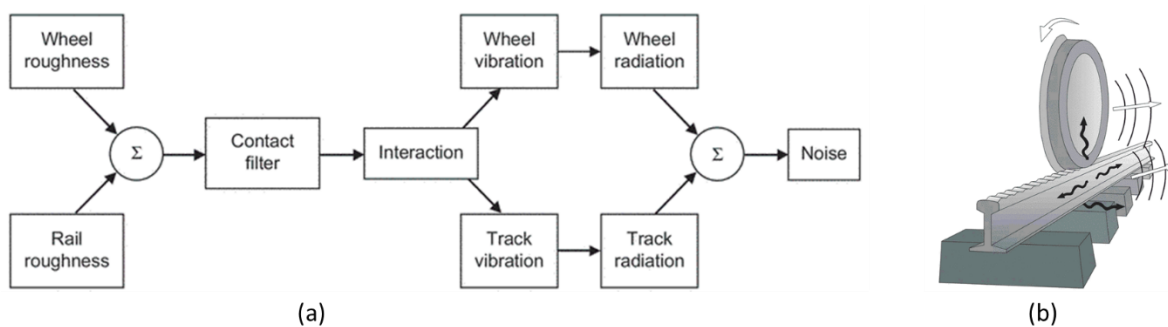


Figure 4.18: (a) Model for rolling noise generation and (b) A schematic diagram showing the mechanism of generation of rolling noise [172].

#### 4.6 Effects of non-metallic Inclusions on wear and RCF

Non-metallic inclusions have been found to affect both wear and RCF properties of wheel and rail steels. Therefore, it is important to control their distribution, morphology, composition, and size. Rail failures due to fatigue cracks initiated at inclusions sites has been observed in the railway industry [173]. Inclusions exist in different forms; some are harder than the steel matrix while others are softer [174]. Softer and ductile inclusions include manganese sulphides (MnS) which acts as stress raisers affect fatigue performance of steels as they aide in initiation of fatigue cracks [174]. MnS inclusions exist in different morphologies such as spherical, spindle-shaped and thread-shaped. Some examples of those morphologies of MnS inclusions are shown in Figure 4.19. During hot working processes, MnS inclusions have been found to easily elongate due to their high plasticity at those temperatures causing a reduction in transverse toughness and stress corrosion cracking of steels [175, 176]. MnS inclusions are not affected by heat treatment hence their ability to exist in any microstructure whether bainitic, pearlitic or

martensitic [176]. Large, hard and brittle inclusions mainly include oxides such as alumina ( $\text{Al}_2\text{O}_3$ ) and silica ( $\text{SiO}_2$ ). These inclusions are harder than the steel matrix and may cause development of micro-cracks under loading as they do not deform in line with the surrounding matrix resulting in fatigue cracking affecting performance of wheel and rail steels [177]. The effects on fatigue performance by hard and soft inclusions has been confirmed by a study by Liu et al. [173] on fully pearlitic rail steels who showed that brittle inclusions are more harmful to fatigue properties than those that can plastically deform.

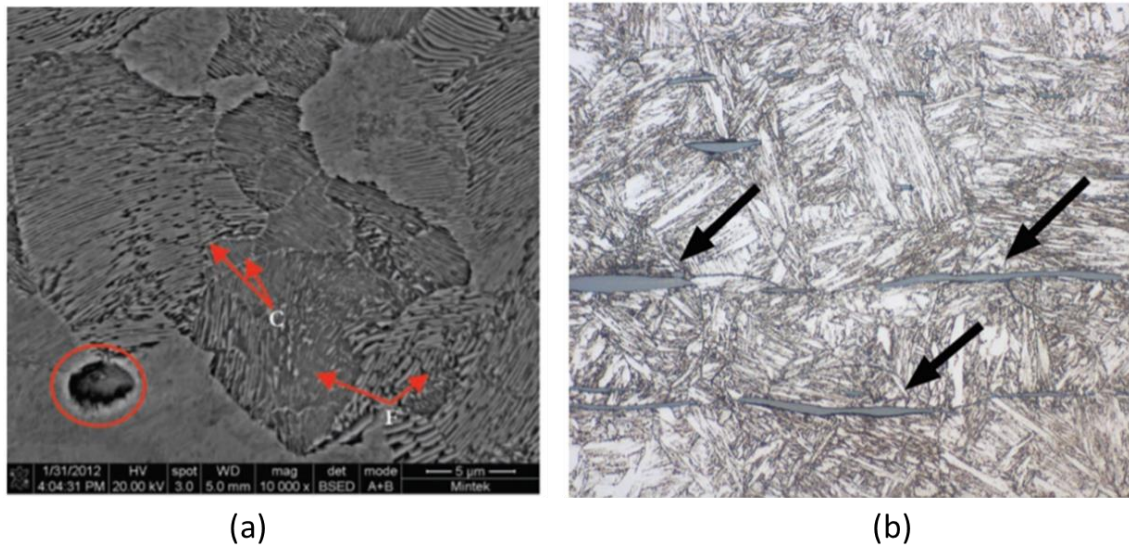


Figure 4.19: a) SEM micrograph of a wheel rim sample showing the pearlite structure and an inclusion [178]; b) Manganese sulphide inclusions in a bainitic microstructure [176].

Various research has been carried out to determine the impact different inclusions have on steel properties. On the study of the effects of oxide inclusions larger than  $30\mu\text{m}$  on fatigue life of ball bearings it has been found that inclusions negatively impacted the fatigue life, Figure 4.20a. As may be seen, increasing the number of inclusions resulted in a significant drop in fatigue life of ball bearings. For example, when the number of inclusions increased from 75 to 150  $\mu\text{m}$ , the fatigue life decreased by approx. 80%. This is also supported by the work by Duckworth and Ineson [179] who showed that larger inclusions increase the fatigue strength reduction factor of EN24 steel, Figure 4.20b. On another study by Fegredo et al. [180] on the effect of sulphide and oxide inclusions on wear rates of a standard C-Mn and a Cr-Mo alloy rail steels, it was found out that size (length) and volume fraction of inclusions had an influence on the wear performance of rail steel, Figure 4.21. When the length of inclusions increased (both sulphides and oxides), the wear rate increased significantly on both bainitic and pearlitic rail steels. This clearly shows that large inclusions are bad for wear resistance for both rail steels.

Hence, it is important to control their size to improve the wear performance of wheel and rail steels.

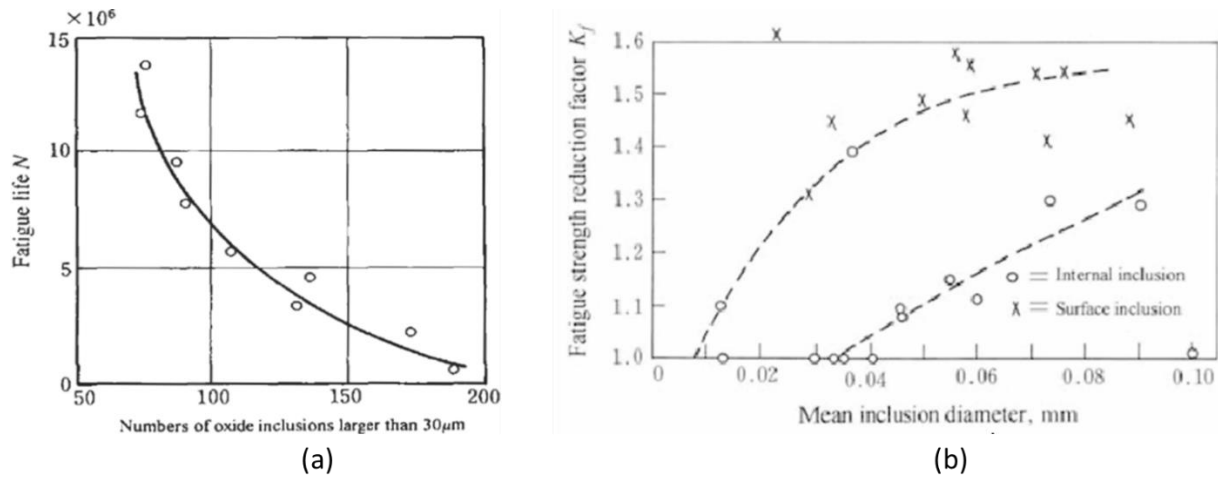


Figure 4.20: (a) The effect of number of inclusions on the fatigue life of ball bearings by oxide inclusions larger than  $30\mu\text{m}$  [181]. (b) Relationship between average inclusion diameter and fatigue strength reduction factor [179].

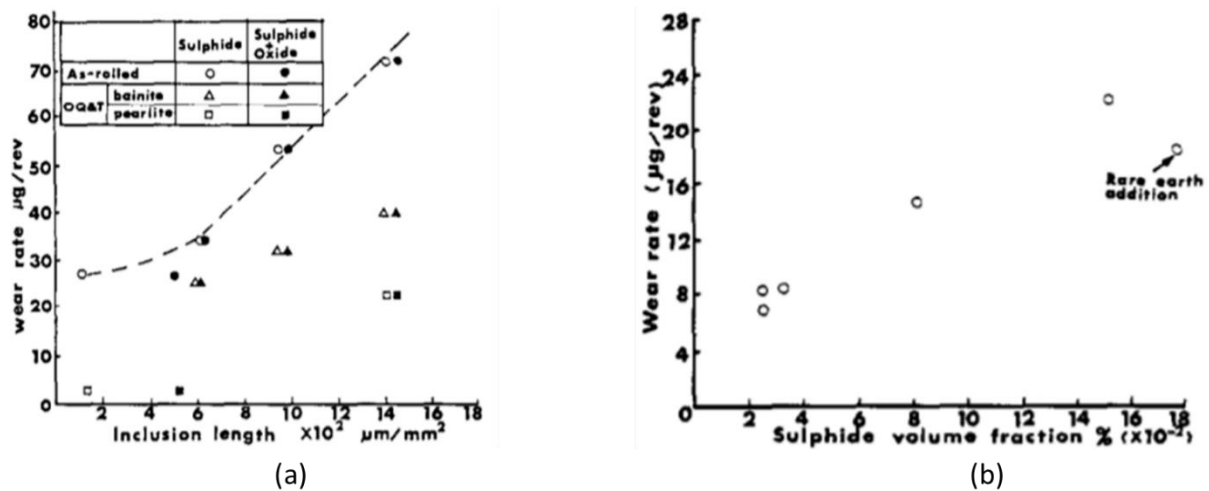


Figure 4.21: a) Dry wear rate vs. MnS length/unit area of field and MnS plus oxide length/unit area of field of C-Mn steels (as rolled-22 HRC, pearlitic-38 HRC and bainitic-42 HRC) and, b) dry wear rate vs. sulphide volume fraction percentage of all vacuum melted Cr-Mo steels [180].

In recent years steel cleanliness has significantly improved due to development of technologies aimed at controlling size, morphology, distribution and composition of inclusions. Inclusion control is achieved by producing clean steels with lower sulphur, phosphorus, hydrogen, nitrogen, and trace elements content using technologies such as Vacuum Arc Remelting (VAR) and Electro Slag Remelting (ESR). Wheel and rail steels now have low levels of sulphur



(0.05max), phosphorus (0.05max) and hydrogen which has significantly improved their fatigue performance.

#### 4.7 Effects of wheel/rail contact temperature on wear and RCF

During sliding and rolling of the wheel on the rail, frictional heat is generated, and it increases the temperature at the wheel/rail contact area [182, 183]. This change in temperature has been found to cause some phase transformations such as austenitise-martensite transformation [184, 185]. The phase transformation causes change in mechanical properties such as hardness and strength affecting wear and RCF properties [184]. The martensite layer has been found to be hard and brittle, and susceptible to cracking during service causing wear by spalling [185]. The formation of martensite layer and spalling due to rapid heating and cooling is shown in in Figure 4.22.

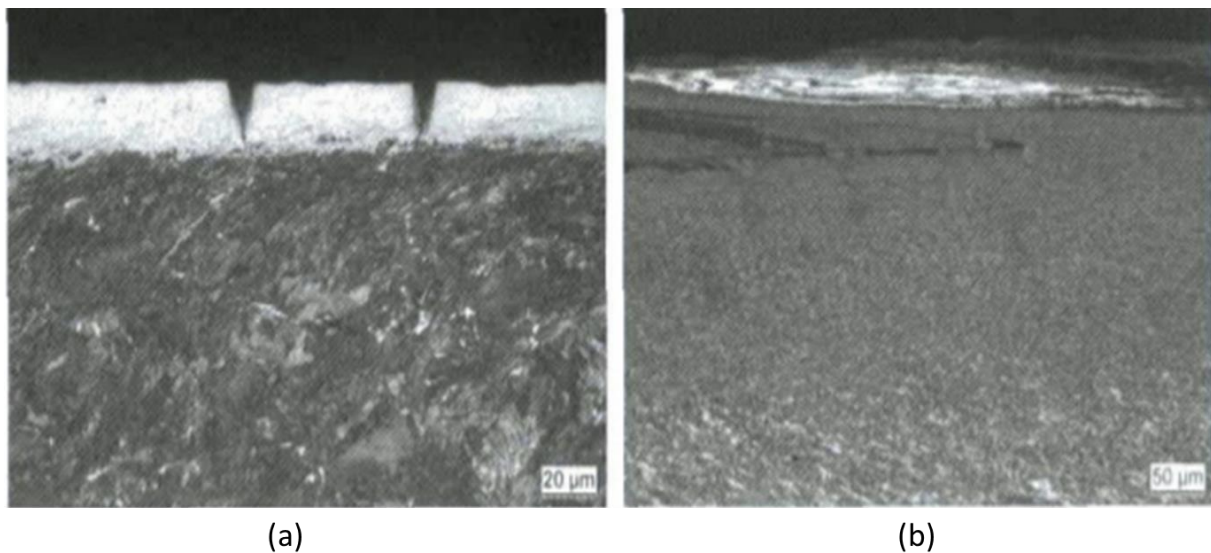


Figure 4.22: (a) Appearance of brittle martensite ('white layer') and (b) spalling due to thermal cracking [115].

When the train brakes, the wheel is subjected to thermal stresses due to friction which may result in formation of thermal surface cracks. The highly stressed areas are sources of crack initiation due to formation of austenite which is then rapidly cooled to brittle martensite after breaking because of an increase in temperature above the ferrite-austenite transformation temperature during braking [186, 187]. The periodic heating and cooling of the tread of a block-braked wheel is shown in Figure 4.23. A study by Lewis and Olofsson has also shown that an increase in temperature reduces yield strength of material hence increasing the wear rate of the wheel/rail material [37]. The subsequent cooling at the contact area after an increase in temperature may produce some induced tensile residual stresses due to restrained expansion

and contraction which may encourage crack propagation resulting in reduction in RFC life [188].

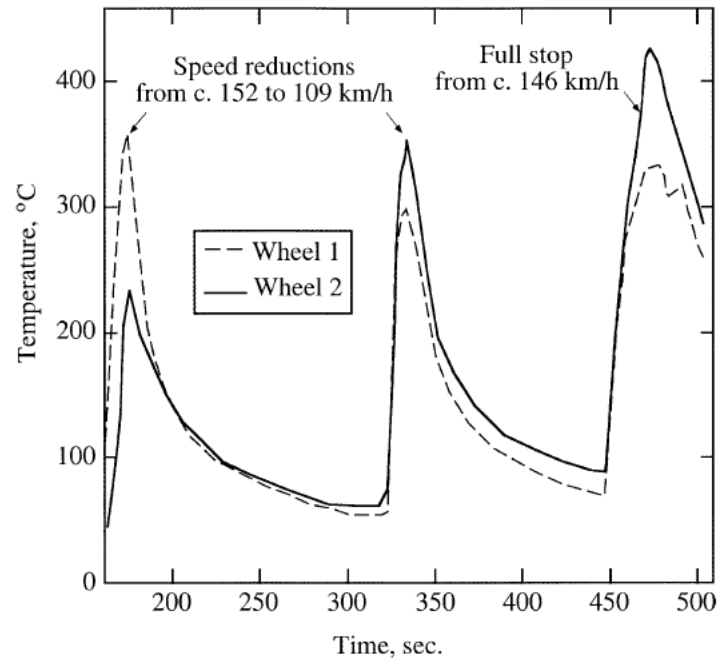


Figure 4.23: Periodic heating and cooling of the tread of a block-braked wheel [186].

In a study by Wei et al. [189], it was found that increasing the creep ratio resulted in an increase in the contact surface temperature at the wheel/rail contact using a thermo-mechanical coupling model of a 3-D wheel/rail contact system. When the creep ratio was increased to 1, the contact temperature increased to a maximum of 626°C [189]. This significant increase in temperature as previously discussed by Magel [121], may result in thermal softening occurring at those temperatures causing a reduction in material strength reducing wear resistance [121]. Other studies have also shown that an increase in temperature at the wheel/rail contact under severe contact conditions may result in transition from severe wear to catastrophic wear [190]. The wear transition from severe to catastrophic wear is shown in Figure 4.24 [190]. As can be seen, the transition from severe to catastrophic wear occurs at disc temperatures of 200 to 250 °C and this corresponds to the data from the study of similar steels where a drop in the yield strength is observed at 200 to 300 °C [191].

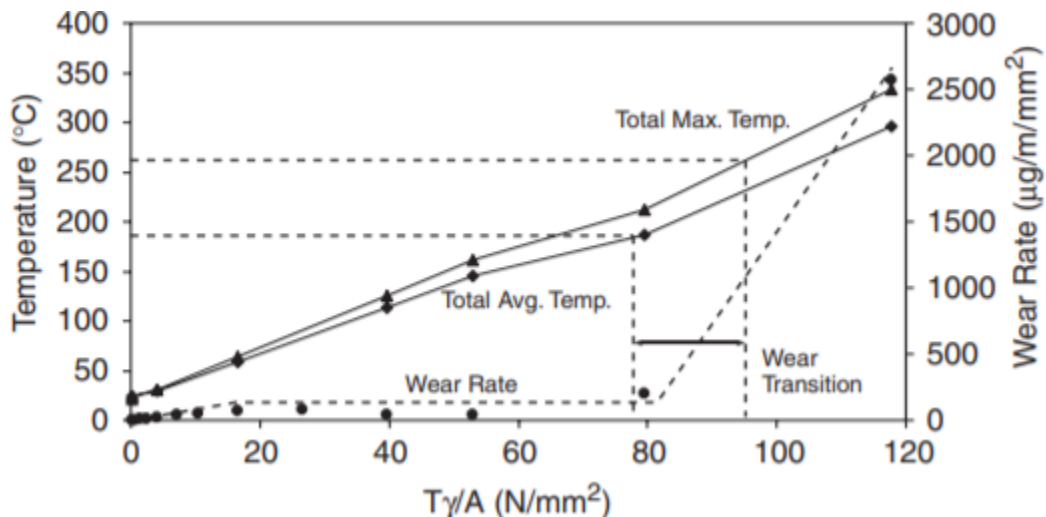


Figure 4.24: Contact temperatures and wear coefficients of R8T wheel steel against UIC60 900A rail material on twin disc setup [190].

#### 4.7.1 Wheel-rail contact patch flash temperature

The flash temperature is the maximum temperature at the wheel-rail contact patch [192], and it affects RCF and wear performance of wheel and rail steels as previously discussed in section 4.7. It is affected by number of factors including load, speed, friction, and thermal properties of the wheel and rail materials. The true flash temperature is a transient occurrence, which means it only lasts a short time with each wheel/rail passing. Even though contact temperature plays a significant role in wear and RCF performance of wheel and rail steels, it is not easy to measure due to heat loss by conduction (from the contact patch to the rail), convection (from the wheel to the ambient air) and radiation [193]. Also, the direct observation of the wheel-rail contact patch is not easy if not impossible as previously stated in literature [194]. The change in temperature may cause phase transformation and formation of the so-called white etching layer (WEL) which is hard and brittle affecting wear and RCF properties of the contacting bodies. Literature [195, 196] has stated that thermal loads are responsible for initiation and propagation of surface cracks in wheels, which are an indication of RCF, Figure 4.25. Wheels have also been found to fail by spalling (loss of material) due to the presence of RCF cracks caused by frictional heat generated at the wheel-rail contact patch [197]. Spalls as they cause loss of material of the wheel tread, causing wheel polygonal wear producing high dynamic forces. The thermal effects at the wheel-rail patch have been found to affect the shakedown elastic limits of wheel and rail materials by lowering the elastic limit [198, 199]. This causes the materials to yield at lower loads causing plastic deformation [198, 199].

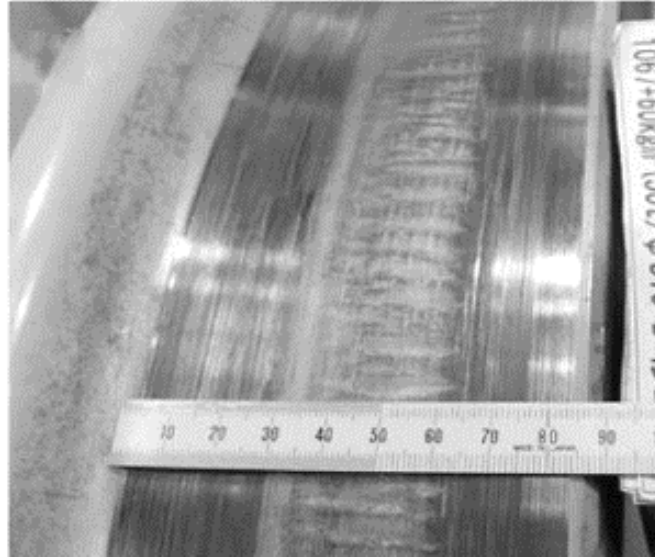


Figure 4.25: Thermal cracks created on the wheel tread [196].

Thermal cameras, infrared temperature sensor, thermocouples can be used to measure the flash temperature but do not give a true indication of the exact temperature. Other methods such as finite element method (FEM) and theoretical calculation (analytical methods) are better suited for prediction of the contact temperature. The information obtained from those methods can be used for better understanding and developing wheels and rail materials that can withstand frictional heat and limit effects of the flash temperature has on wear and RCF. Literature [200, 201] have used numerical analysis and FEM to study the flash temperature by developing models that are able to simulate and calculate the flash temperature as well as the strain stress responses at the wheel-rail patch under different contact conditions. Knothe and Liebelt [202] used the Laplace transform method to simulate the flash temperature of wheel-rail contact patch under sliding conditions and their results agreed with previous works. For the twin disc setup, the flash temperature is not easy to measure as well, hence the wheel disc temperature is measured which was the case for this study where an infrared sensor was used to measure the wheel disc temperature.

#### **4.8 Effects of wheel/rail hardness on wear and RCF**

Hardness has been found to influence the RCF and wear properties of wheel and rail steels. Recent studies have shown that there is a relationship between wear resistance and hardness for most wheel/rail steels with wear resistance increasing with an increase in hardness [97] [203, 204]. The relative wear resistance of most pure metals has been found to be directly proportional to hardness as shown in Figure 4.26a [66]. The relative wear resistance is defined as the wear volume of the material divided by that of some standard material tested under the

same experimental conditions [66]. This relationship become more complex for alloys for example in heat treated steels which give a wide range of hardness values with linear plot, but different slopes as compared to pure single-phase metals [66]. The effect of alloying elements such as carbon has been found to influence wear performance of steels as the wear resistance increases with increase in the carbon content as shown in Figure 4.26b.

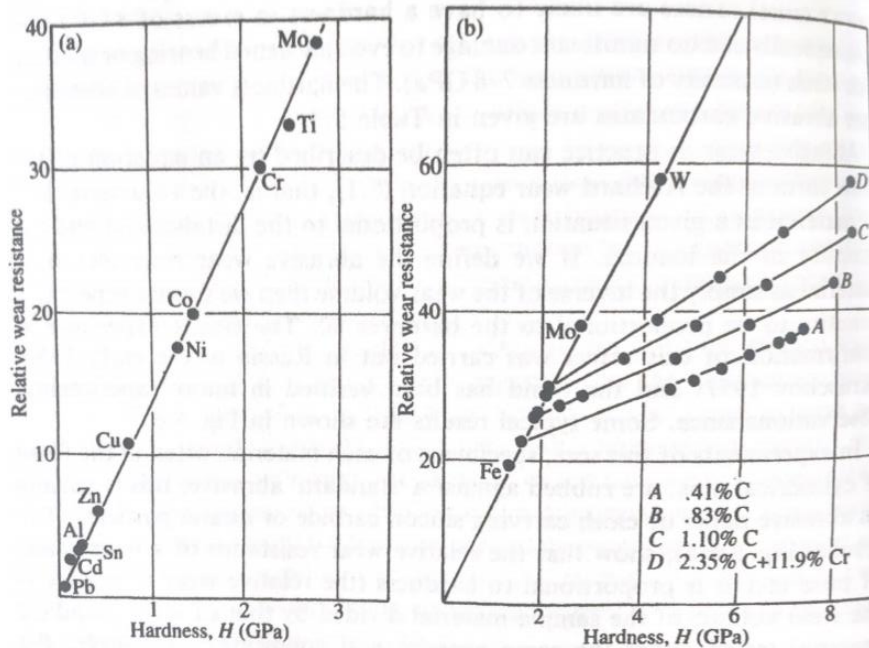


Figure 4.26: Effect of hardness of metals on relative wear resistance in two body abrasion: (a) pure metals; and (b) steels with varying compositions and heat treatments [66].

Work done by Clayton and Danks [102] demonstrates that at various contact pressures, rail materials with high hardness have lower wear rates compared to those with lower hardness as seen in Figure 4.27. In pearlitic steels, it has been found that increasing the hardness of pearlite and tempered martensite of rail specimens increases their wear resistance on a twin-disc wear test rig set up by Sato et al. [204] hence improving their wear performance. A study by Santa et al. [205] has shown that using a softer wheel and a harder rail material (R400HT-E8 pair) resulted in a higher wear rate on the wheel material as compared to that of rail sample at different slip ratios. This agrees with the work done by Lewis et al. [206] who proved that there is a relationship between hardness and wear of both rail and wheel materials as wheel wear resistance increased with an increase in rail hardness. On another study by Zhong et al. [207], it was found that steels with higher hardness values had lower wear rates as compared to those with lower hardness values. On the same study, it was noted that the amount of carbon in steel

also influences wear rate as the steel with higher carbon content had higher hardness values hence lower wear rates [207].

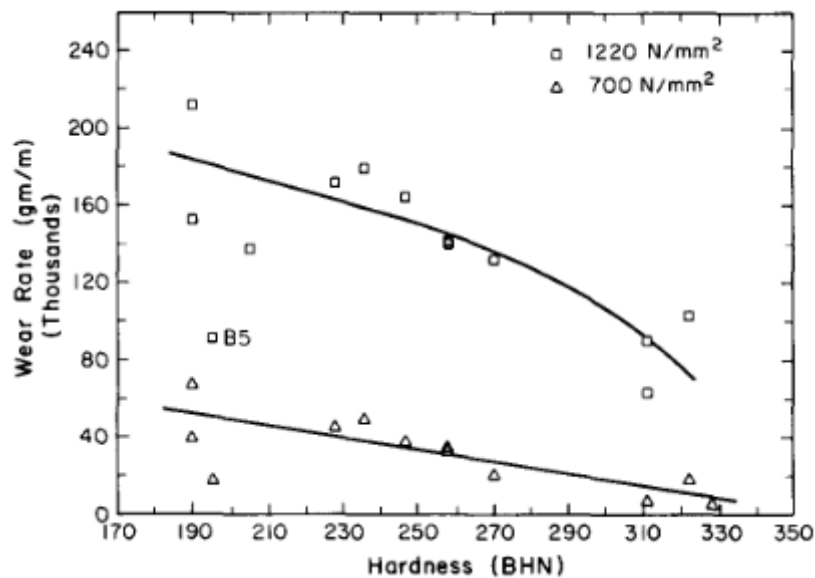


Figure 4.27: Wear rate against hardness (BHN) at different contact pressures [102].

#### 4.8.1 Plastic deformation of wheel and rail steels

During rolling and sliding of a wheel on rail, there is repeated loading at the contact surface of the two which may result in plastic deformation. Repeated loading causes the material to flow plastically when the load applied is greater than the elastic limit due to contact stresses exceeding the yield stresses of the contacting materials [70]. In heavy haul railway lines severe plastic deformation is mostly observed where extreme wheel loads are experienced causing incremental plastic flow known as “ratchetting” due to repeated loading [208]. Ratchetting has been found to cause nucleation of voids and microcracks below the wheel/rail contact surface [208]. The microcracks/voids grow as repeated loading is applied resulting in initiation of fatigue cracks [208]. During plastic deformation, work hardening occurs which is a cause for an increase in material surface hardness due to an increase in dislocation density. A study by Leiro et al. [209] found that there is a significant increase in microhardness at the surface and sub-surface regions on carbide-free bainitic steel after rolling and sliding wear testing due to work hardening, Figure 4.28. This is also in agreement with the work done by Seo et al. [114] who found that wear on two different rail steels under rolling and sliding contact conditions increased surface microhardness.



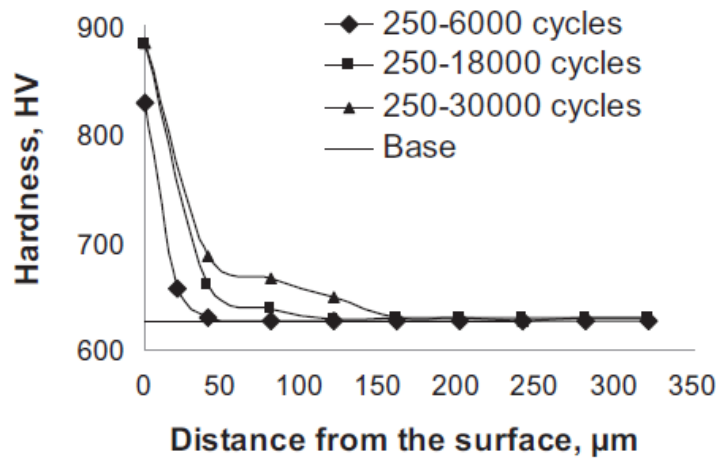


Figure 4.28: Micro hardness profiles for carbide-free bainitic steel after rolling and sliding wear testing at different rolling cycles [209].

A study by Zhong et al. [16] found that when the axle load was increased from 16 to 25 tonnes, the plastic deformation layer,  $h$ , increased and was more on rail specimen, Figure 4.29. The plastic layer thickness is an indication of how much wear has taken place, the thicker the layer the higher the wear rate. The depth of plastic flow depends on the initial hardness of the wheel and rail materials as well as the contact conditions. Rodríguez-Arana et al. [22] also found that the depth of plastic deformation increased with slip ratio, Figure 4.30.

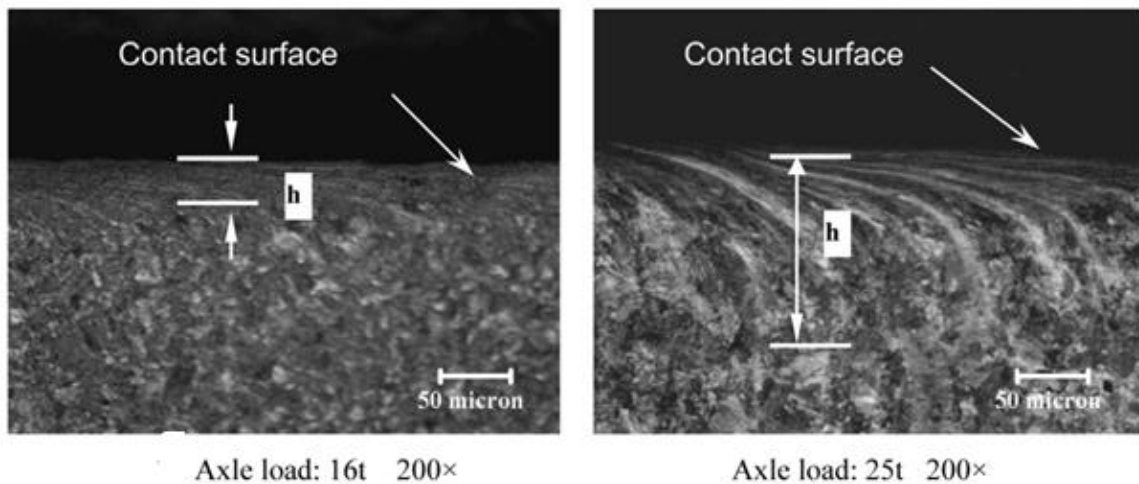


Figure 4.29: Deformation depth of rail specimens under different contact loads [16].

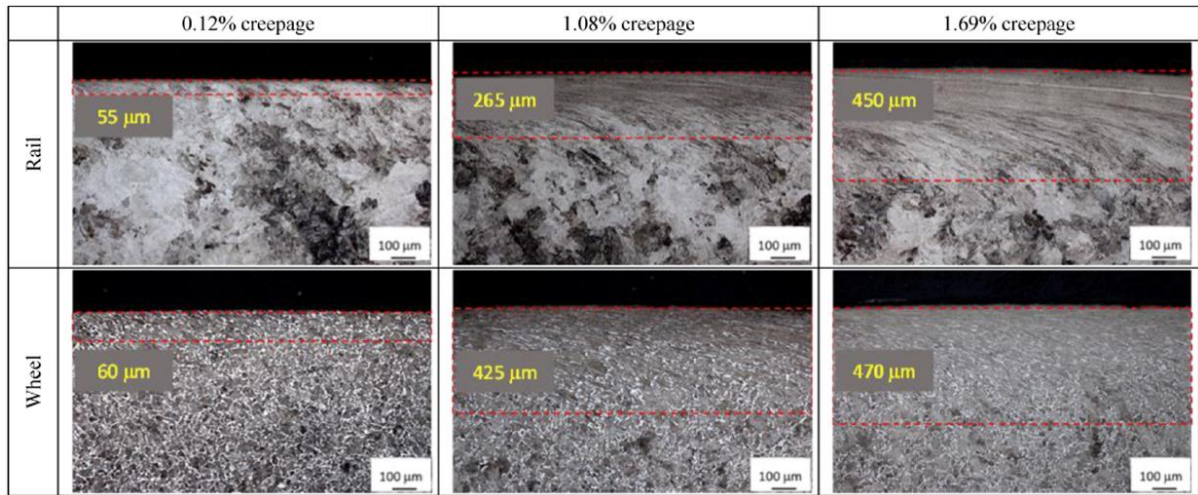


Figure 4.30: Plastic deformation of rail and wheel specimens under different creepages (slip ratio) [22].

#### 4.9 Effect of slip ratio on wear and RCF

The train experiences different slip ratios at the wheel/rail interface as it moves along the rail tracks which influences the RCF and wear properties of wheel and rail materials. This variation in slip ratios maybe caused by a change in contact area between the wheel and rail head at curves as the slip ratio increases compared to when a train is moving on a straight track [23]. When the train is moving on a straight track, the wheel is found to be in contact with the rail head but that changes when moving in curves as the wheel flange will now be in contact with the gauge corner of the rail [23]. For a twin disc simulator setup, slip ratio is given by equation 4.3:

$$Slip\ ratio\ (\%) = \left( \frac{V_w \cdot R_w - V_r \cdot R_r}{V_w \cdot R_w + V_r \cdot R_r} \right) \times 200 \quad 4.3$$

Where  $V_w$  and  $V_r$  are the rotational velocities of the wheel and rail discs in revolutions per minute (rpm), and  $R_w$  and  $R_r$  are the rolling radii of the wheel and rail discs respectively [210]. For this study, the radii of the wheel and rail discs were equal ( $R_w=R_r$ ), so equation 4.3 becomes:

$$Slip\ ratio\ (\%) = \left( \frac{V_w - V_r}{V_w + V_r} \right) \times 200\% \quad 4.4$$

For the actual wheel-rail contact, the rail is not moving so the creepage/slip ratio is the percentage difference based on the angular speed of the wheel and rolling radius and the actual



speed of the train defined by 4.6, where  $V_w$  is the angular velocity of the wheel,  $R_w$  is the nominal rolling radius of the wheel  $V$  is the forward train velocity [211] whereas the slip velocity ( $V_s$ ) is defined by equation 4.5. Slip is normally required for a train to function safely because it allows the wheels to grip the rails more effectively. However, excessive slip can cause the wheels to lose traction, resulting in derailments.

$$\text{Slip velocity } (V_s) = V_w R_w - V \quad 4.5$$

$$\text{Slip ratio } (\%) = \left( \frac{V_w R_w - V}{V} \right) \times 100\% = \frac{V_s}{V} \times 100\% \quad 4.6$$

Studies have been conducted to find out the effects slip ratio has on wear properties of wheel and rail materials. Makino et al. [143] have found that increasing the slip ratio increased the friction coefficient at the wheel/rail interface in AAR class C wheel steels under twin disc setup, which reduced the fatigue strength of the materials. This is a problem as reduction in fatigue strength causes rapid increase in crack initiation which may result in RCF [156, 143]. This is in agreement with a study conducted by Ma et al. [212] who showed that increasing the slip ratio at the wheel/rail contact in a twin disc setup increased the coefficient of friction and surface hardness of the contacting discs, Figure 4.31 [212]. The surface hardness increased until steady state where the number of dislocations generated equalled the rate of dynamic recovery. On the same study by Ma et al., it was observed that increasing the slip ratio also changed the wear mechanism from mild oxidation wear to severe fatigue and spalling and may result in fatigue failure [212].

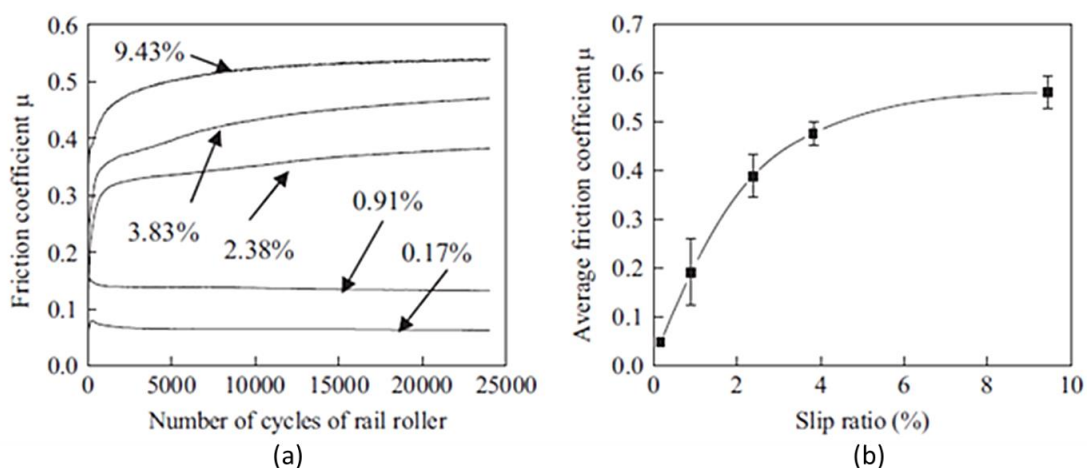


Figure 4.31: (a) Coefficient of friction against number of rolling cycles at different slip ratios, (b) average coefficient of frictions versus slip ratio for wheel and rail discs on twin disc setup [212].

Wang et al. have also discovered that increasing slip ratio reduced the fatigue life of rail disc materials significantly, Figure 4.32. This was tested using the Sheffield University Rolling Sliding (SUROS) twin-disc wear test rig [23]. The reduced fatigue life was due to an increase in the growth angle of cracks as well as the transformation of damage mechanism from mild surface crack to severe fatigue [23]. Keeping the slip ratio at zero resulted in a very small coefficient of friction making it difficult for cracks to grow as there was no driving force for crack growth and therefore, increasing the RCF life [23]. Wang et al. [23] found that the depth of deformation and the size of branching cracks increased with slip ratio. This was found to be harmful to RCF since it decreased the fatigue life [23]. On the same study by Wang at al. [23], it was found that an increase in slip ratio also increased the wear rate on both wheel and rail materials. Similar trend was also found by Seo et al. [213] whereby low slip ratios of 0.1 to 0.3% caused surface cracks which led to spalling, but when the slip ratio was increased to 1.5%, plastic flow and fine surface cracks developed, Figure 4.33 [213]. From the same study by Seo et al. pitting is also observed (Figure 4.33) at high slip ratio of 1.5% which is an indication of fatigue [213].

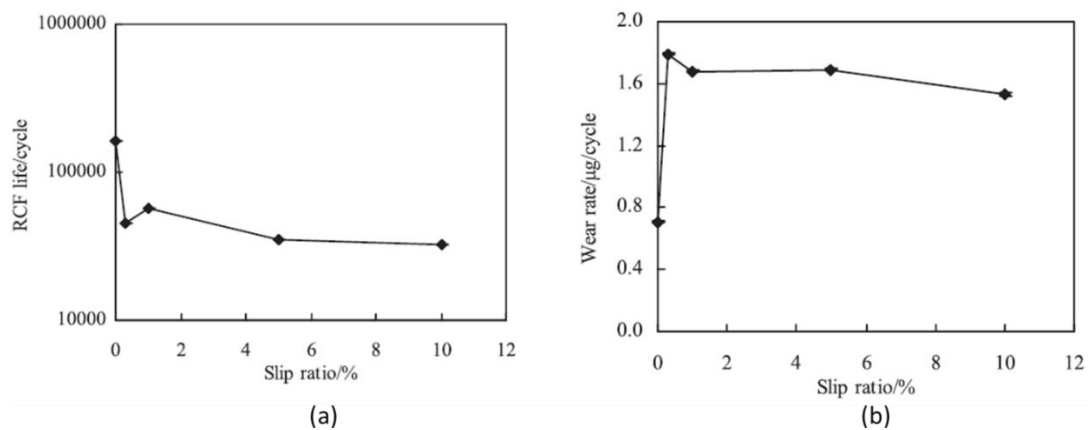


Figure 4.32: (a) RCF life of rail discs vs. slip ratio and (b) Wear rate of rail discs vs. slip ratio [23].

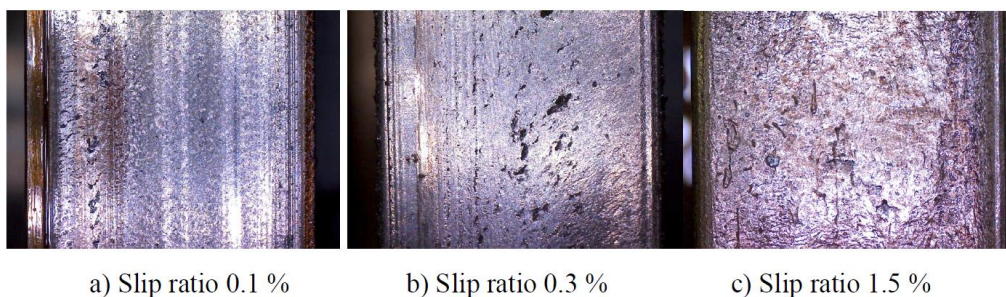


Figure 4.33: Wheel specimen surfaces after wear testing at different slip ratios on a twin disc testing machine [213].

#### 4.10 Effect of third body materials on wear and RCF

The rail-wheel interface is a very complex system, and it is made worse by the presence of third body materials as they affect the performance at the contact. Third body materials include naturally occurring humidity, precipitation, solids such as sand and leaves from nearby trees and vegetation as classified in Figure 4.34 [28]. Some are applied on purpose such as friction modifiers, greases, traction gels etc to help with adhesion and friction, Figure 4.34 [28]. Third body materials affect the adhesion of the wheel onto the rail, influencing the performance of the braking system. Some tends to reduce friction resulting in an increase in braking distance by trains while others such as sand do the opposite. Solid third body materials such as oxides and wear debris are very detrimental to wear resistance of wheel-rail materials as they tend to increase wear and RCF in the wheel-rail contact area [28]. Lubrication is applied on the wheel-rail contact to try to reduce wear, but this tend to affect adhesion and fatigue whereas sand is applied to try to help with adhesion and fatigue, which end up having a negative impact on wear resistance of the materials [27, 28]. Therefore, it is important to strike a balance between the two by having proper scheduled maintenance procedures to improve performance and safety of railway systems. The effect of different third body materials on the performance of rail and wheel steels at different slip ratios is shown in Figure 4.35.

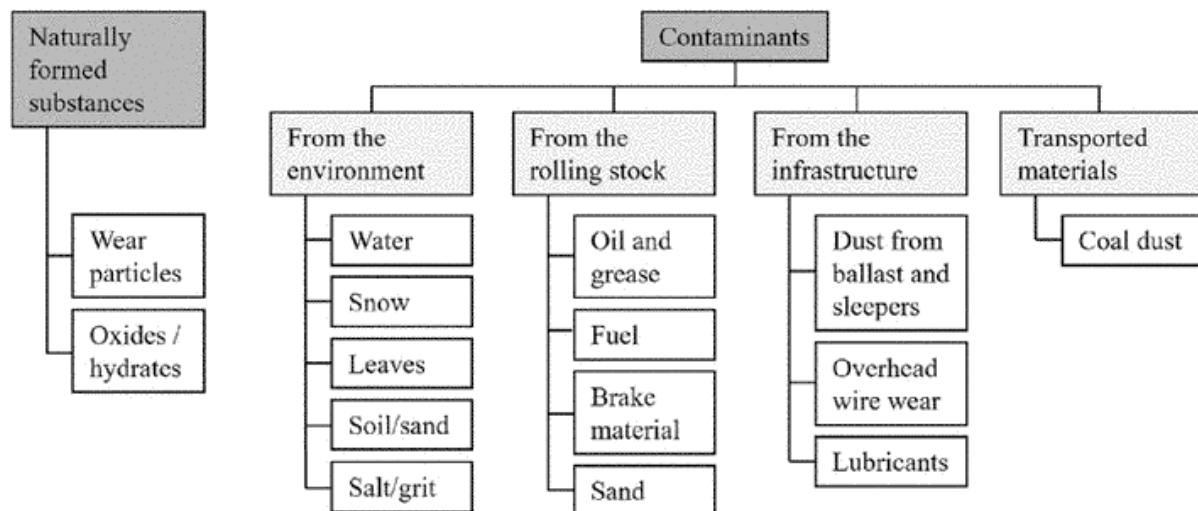


Figure 4.34: Classification of various wheel/rail contact contaminants [31].

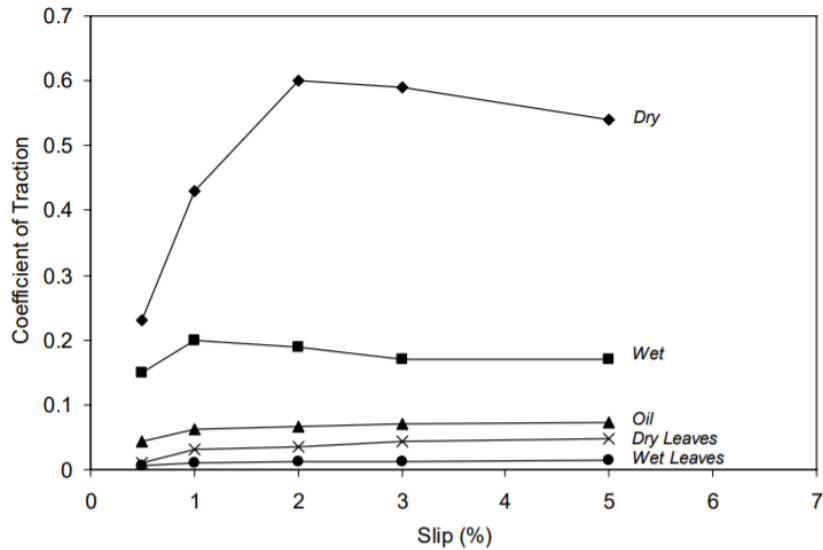


Figure 4.35: Coefficient of traction (friction) against slip ratio at different contact conditions (third body materials) when R8T wheel was run against 900A rail under 1500 MPa contact pressure [214].

#### 4.10.1 Liquid lubricants

Liquid lubricants such as water, oil and grease have been found to reduce wear rates by lowering the coefficient of friction. Water enters the railway system at the wheel-rail contact from different forms such as morning dew, fog, and light or heavy rain [215]. All these different forms of water can result in different adhesion levels [215]. Although water can reduce wear, it has been found to have detrimental effect in RCF as it widens the crack by different mechanisms which include: (a) shear mode crack growth, accelerated by fluid reduction of friction between the crack faces, (b) hydraulic transmission of contact pressure, (c) entrapment and pressurisation of fluid inside the crack (fluid crack pressurisation) and (d) squeeze film pressure generation as seen in Figure 4.36 [216, 217]. Fluid crack pressurisation is whereby water enters a crack at the wheel rail-contact, as the force is applied, the water inside the crack is forced towards the crack tip causing tearing and widening of the crack, Figure 4.36 [28, 195]. Water has also been found to increase corrosion and uptake of hydrogen at the contact which may cause RCF [75]. A study by Wang et al. [23] found that water accelerates crack growth during wear testing on wheel and rail materials using the twin-disc setup by hydraulic crack growth mechanism, which is a similar mechanism studied by Lewis et al. [28]. The concept of ‘fluid crack pressurisation’ was also confirmed using 2D finite element model of an edge crack by Dallago et al. [218] who found that as a fluid entered the crack there was a pressure build up, which could result in crack initiation and propagation.

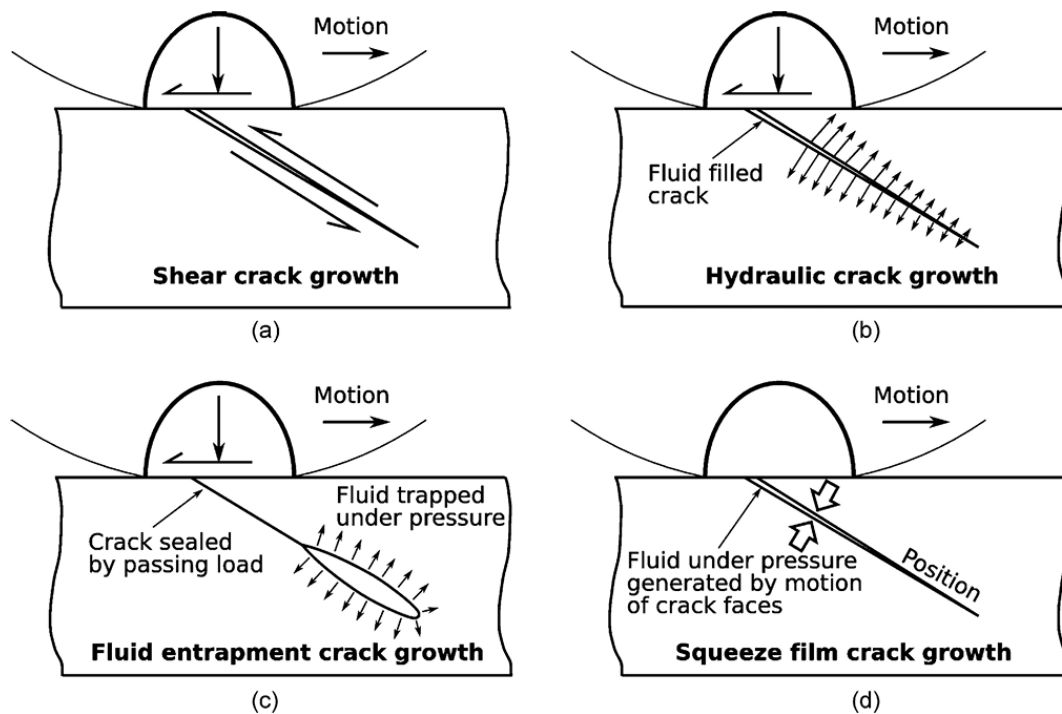


Figure 4.36: Fluid assisted mechanisms of crack growth: (a) shear mode crack growth, (b) hydraulic transmission of contact pressure, (c) entrapment and pressurisation of fluid inside the crack and (d) squeeze film pressure generation [216, 217].

When Wang et al. observed a sudden drop in adhesion coefficient after introducing water to the contact surface in a dry contact condition, Figure 4.37 [76]. This sudden loss in adhesion is bad for the safety of the train as it may lead to longer braking distance which may result in an overrunning.

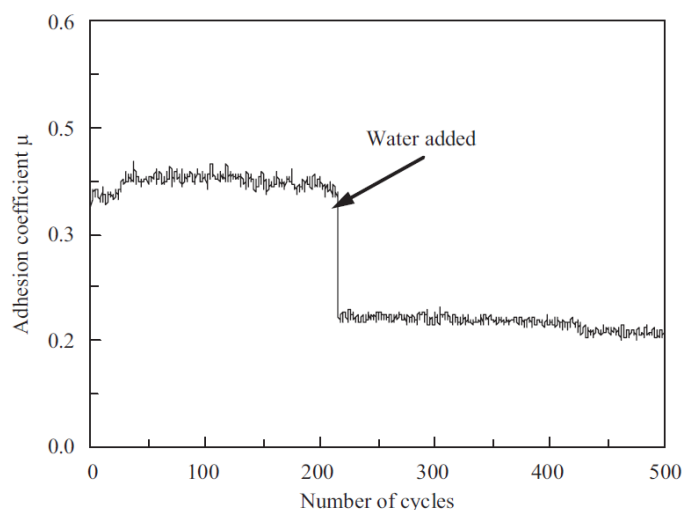


Figure 4.37: Coefficient of friction versus number of rolling cycles at the wheel/rail under dry and after water was added [76].

#### 4.10.2 Solid lubricants

Solid lubricants include soil dust, concrete, sand and others. The use of sand in railway systems have been used when there is loss of traction to help with adhesion at the wheel/rail contact [219]. Sand is also added to the wheel-rail contact to help with adhesion in case of emergency braking [28]. Sand improves adhesion by reducing the braking distance [220]. Poor adhesion can also lead to delays in movement of trains due to reduced acceleration. The most constituent of sand is quartz which is very hard and abrasive and even harder than steel. This is a problem because when hard particles become in contact with steel at the wheel-rail contact they cause some abrasion, severe plastic deformation and damage [219].

#### 4.10.3 Leaves

Leaves have also been found to affect adhesion between the wheel and rail [221]. They are crushed onto the rail surface forming a slippery layer lowering the adhesion between the wheel and rail, Figure 4.38 [221, 222]. Just like water and oil, wet leaves have more effect on the reduction of adhesion between the rail and wheel than dry leaves [222]. The costs associated with leaf problems are estimated to be over 50 million British Pounds in the UK and 100 million Swedish krona in Sweden because of maintenance procedures done to improve traction at the wheel/rail contact [210, 222]. To solve the problem, friction modifiers such as sand are often used to improve adhesion which comes at cost as studies have shown that sand increases wear on wheel and rail materials. To overcome this, sand is usually mixed with some water gel and delivered through a pumping system connected either to the train or rail track [223].

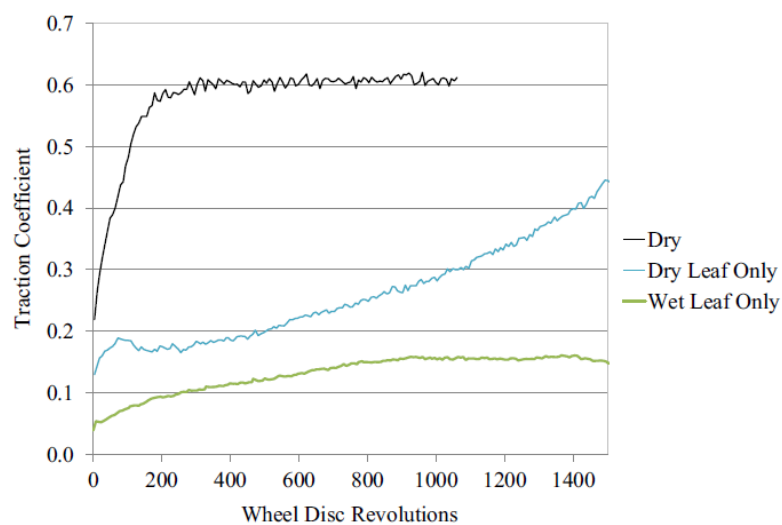


Figure 4.38: A plot showing the relationship between the rotational number and the traction coefficient of wheel materials at different conditions of leaves on a twin disc setup [223].



## 4.11 Measures to mitigate wear and RCF

Many techniques can be used to reduce wear and RCF, which include the application of surface coatings or treatments, lubrication, altering the composition of the material or developing new materials, and modifying the component's or system's design. Some of the methods also involve the application of friction modifiers, which reduce wear, particularly where there are severe contact conditions, such as the contact between the rail gauge face and the wheel flange.

### 4.11.1 Development of new materials

To improve the wear performance of bainitic steels for wheel and rail application, carbide free bainitic steels have been developed and studied as replacement to conventional material. Recent studies have shown that carbide free bainitic steels are emerging as good materials to be used to make rail due to their remarkable strength and hardness, good ductility, high toughness, high resistance to wear as well as low production costs [224, 225, 226]. The remarkable mechanical properties are due to their microstructure which have thin plates of bainite in a matrix of retained austenite better than those of quenched and tempered alloys of the same hardness [224]. Carbides have been found to be responsible for many engineering failures in early bainitic steels as compared to quenched and tempered martensitic steels with finer dispersions of carbide particles [105]. The development of carbide free bainitic steels is made possible by non-carbide forming alloying elements such as silicon and aluminium, which prevents cementite from precipitating from the carbon-enriched austenite during bainitic transformation [108, 227, 228]. Silicon has long been found to inhibit precipitation of cementite with concentrations of ~2 wt% silicon [229, 230, 231]. Carbide-free bainitic steels are made up of films of retained austenite surrounding carbide-free bainitic ferrite plates with no evidence of inter-lath carbide precipitation, Figure 4.39 [105, 108].

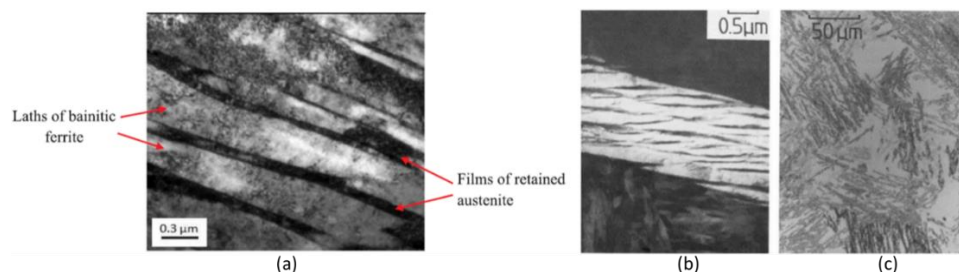


Figure 4.39: (a) TEM micrograph of a carbide free bainitic steel with evidence of no inter-lath carbide precipitation [108], (b) TEM micrograph showing bainitic ferrite plates separated by films of stable austenite and (c) OM micrograph showing the large blocks of austenite left untransformed [105].

In a recent study by Hasan et al. [108], carbide-free bainitic steels have been found to improve wear resistance due to presence of retained austenite. In the same study, carbide-free bainitic steels have been found to have superior rolling and sliding wear resistance compared to conventional pearlitic rail steel due to their higher initial hardness [108]. Carbide-free bainitic wheel steels have better impact toughness, yield strength and fracture strength than most conventional wheel steels, Figure 4.40 [228, 232]. Even though most studies have shown that carbide free bainitic steels can improve the wear resistance of rail materials, research is still lacking on the influence of bainitic ferrite lath thickness has on wear performance of rail steel, which limits the understating of such materials.

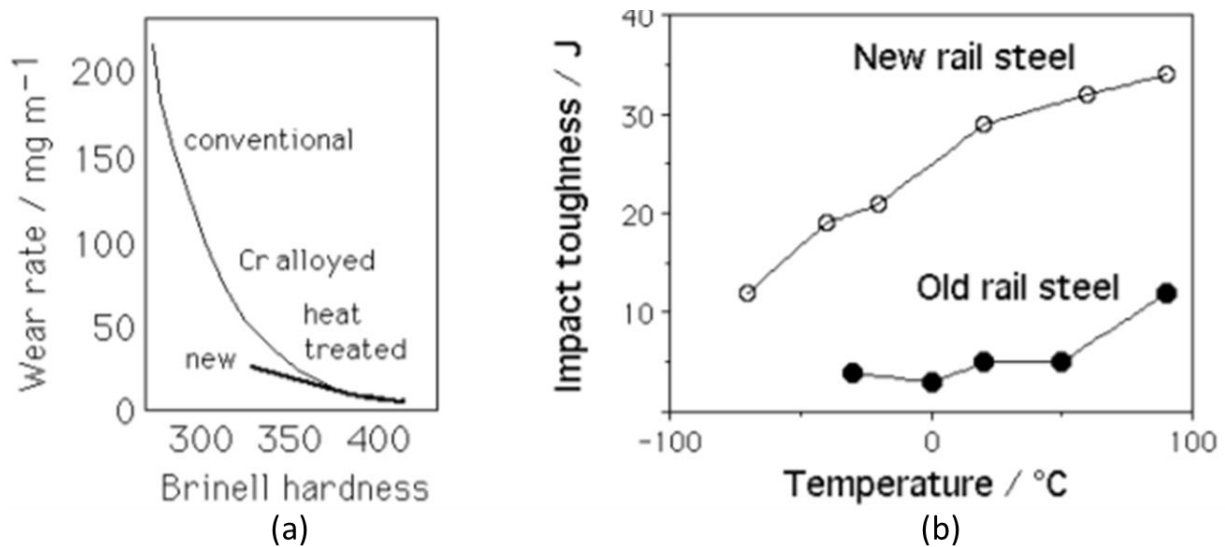


Figure 4.40: (a) Wear rates of new carbide free bainitic steels compared to conventional rail steels, (b) charpy impact toughness of new carbide free bainitic steels compared to old conventional rail steels [232].

#### 4.11.2 Friction modifiers

The use of friction modifiers (FMs) has resulted in a significant decrease in wheel and rail wear especially in areas where extreme contact conditions are experienced such as between rail gauge face and wheel flange contact. There are different categories of friction modifiers depending on how they influence the coefficient of friction, Figure 4.41. One of the common FM materials is grease. Grease is added at the wheel and rail contact especially at the rail gauge face and wheel flange contact where severe contact conditions are experienced in order to reduce wear and noise [42, 233]. Several studies [21, 156, 234], have found that when grease was applied to the wheel-rail interface, lower wear rates were observed even at high wear index ( $T\gamma/A$ )



values, whereas when using dry test high wear rates were observed even at low  $T\gamma/A$  values, Figure 4.41b [21].

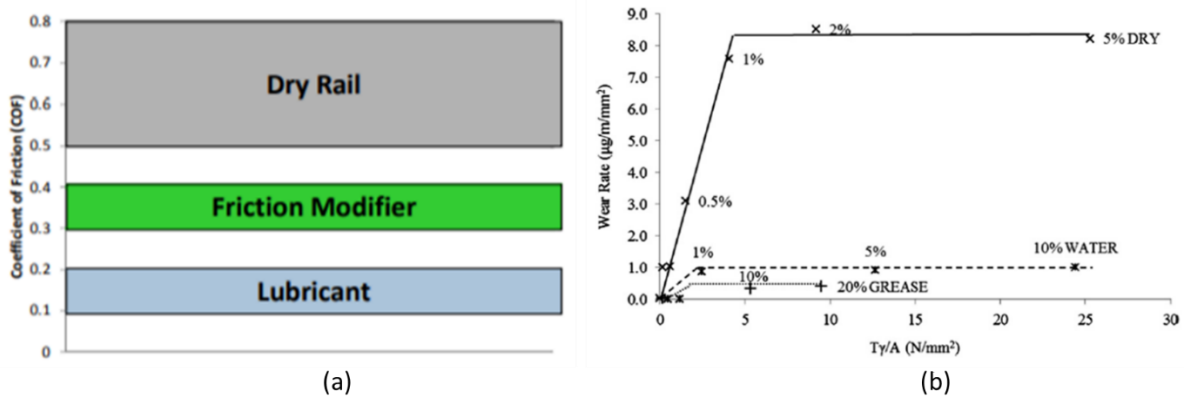


Figure 4.41: (a) Typical coefficient of friction ranges for dry rail, friction modifiers, and lubricants [235]; (b) wear rates vs  $T\gamma/A$  for R8T wheel against R260 rail for run dry, water and grease (1500MPa, varying slip, 400rpm) [21].

#### 4.12 Wear prediction models

There are several wear prediction models used to study wear behaviour of wheel and rail materials and to predict their life. Some wear prediction models use the work done in the wheel-rail contact to predict wear whereas some use sliding distance, normal force and hardness of the material. The two main wear models are the Archard wear model and the energy dissipation model. Wear models are used to predict when wheel reprofiling can be done whereby the worn surface of the wheel flange and tread are machined to geometric size of the standard contour. Wheel reprofiling cycles depends on the rail operating companies for example in China the wheels are reprofiled after 250 000 km [236]. In Great Britain, passenger train wheels have a diameter of 840 mm and are reprofiled periodically until they reach a diameter of 790 mm after which they will be scrapped [237]. In Brazil, the wheels of diameter 38 inches (965 mm) are also reprofiled until 2 inches (50.8 mm) of wheel rim is removed [238], which is similar to the UK case. The wheel wear prediction procedure was first developed by Jendel [239] at the Royal Institute of Technology (KTH) in Stockholm, Sweden using the Archard wear model, Figure 4.42. It is used to determine the wear volume of the material removed and has been used in different studies [240].

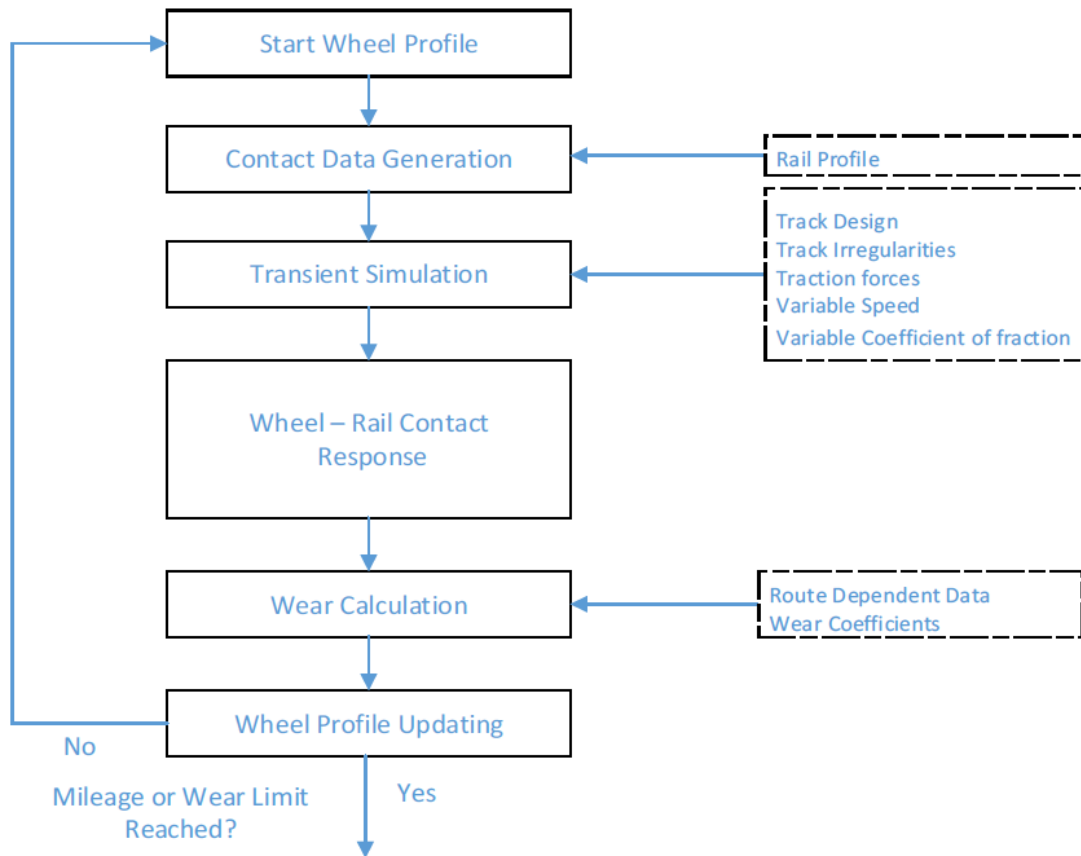


Figure 4.42: Methodology of wheel wear prediction [240].

#### 4.12.1 Archard wear model

In 1953 Archard formulated the wear equation relating the volume of material removed to material hardness, load applied and sliding distance is given by equation 4.7 [241]:

$$V = k \frac{WL}{H} \quad 4.7$$

Where  $V$  is the volume of worn material ( $m^3$ ),  $k$  is a dimensionless wear coefficient,  $W$  is the normal load (N),  $L$  sliding distance (m),  $H$  is the hardness of the softer contacting surface ( $N/m^2$ ). The wear coefficient,  $k$  can be obtained experimentally from the plot of wear volume versus sliding distance.

#### 4.12.2 The energy dissipation model

The energy dissipation model relates the wear rate to work done at the wheel–rail contact developed by Pearce and Sherratt and is given by equation 4.8 [242]:

$$\text{wear rate} = \frac{KT\gamma}{A} \quad 4.8$$

Where  $T$  is tractive force and  $\gamma$  is the slip,  $K$  is the wear coefficient and  $A$  is the contact area [124]. The wear rate ( $\mu\text{g}/\text{m}/\text{mm}^2$ ) is the weight of lost material ( $\mu\text{g}$ ), per distance travelled (m), per contact area ( $\text{mm}^2$ ) [112]. From the model three wear regimes are identified as mild, severe and catastrophic as may be seen in Figure 4.43, Figure 4.44, and Figure 4.45 from different studies [114, 243, 244]. Each wear regime and corresponding  $K$  values are shown in Table 4.1. At low values of  $T\gamma/A$  (wear index), wear is mainly due to oxidation. As  $T\gamma/A$  increases, the wear regime transforms from mild to severe and to catastrophic under regions  $K_1$ ,  $K_2$  and  $K_3$  respectively. The catastrophic region is associated with severe delamination due to an increase in the severity of the contact conditions.

Table 4.1: Wear regimes and their corresponding  $T\gamma/A$  and wear rate coefficients for R8T wheel and UIC60 900A rail steels [243].

Regime	$T\gamma/A$	Wear rate ( $\mu\text{g}/\text{m}/\text{mm}^2$ )
$K_1$	$T\gamma/A < 10.4$	$5.3T\gamma/A$
$K_2$	$10.4 < T\gamma/A < 77.2$	55.0
$K_3$	$77.2 < T\gamma/A$	$61.9T\gamma/A$

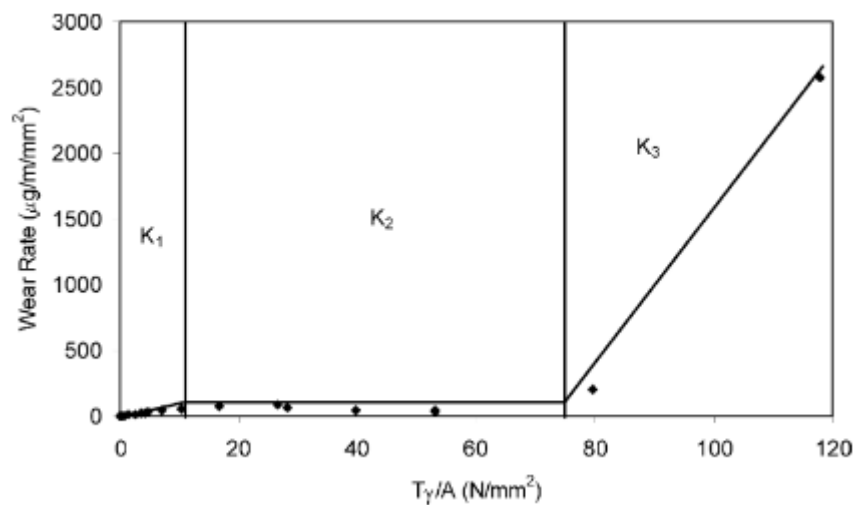


Figure 4.43: Wear rate as a function of wear index,  $T\gamma/A$  showing different regimes [243].

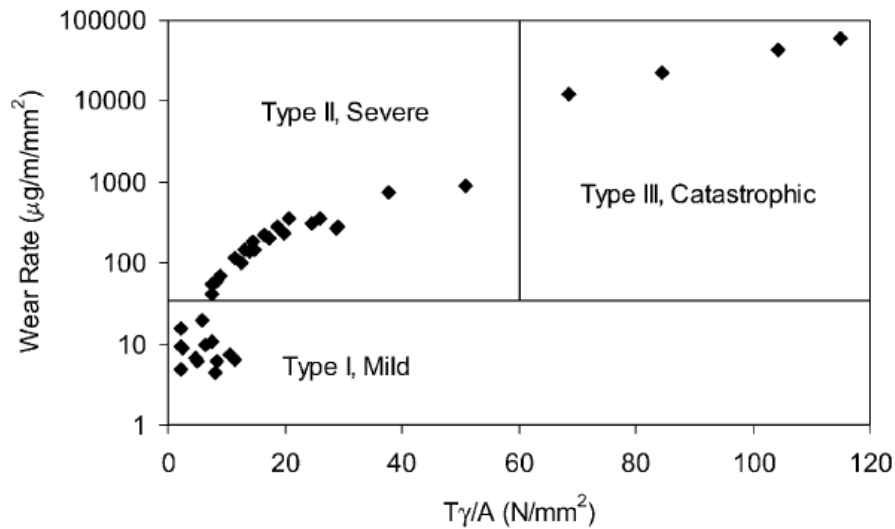


Figure 4.44: Wear regimes identified during twin disc testing of BS11 rail material vs. Class D wheels, adapted by Lewis and Olofsson [37] from Bolton and Clayton [244].

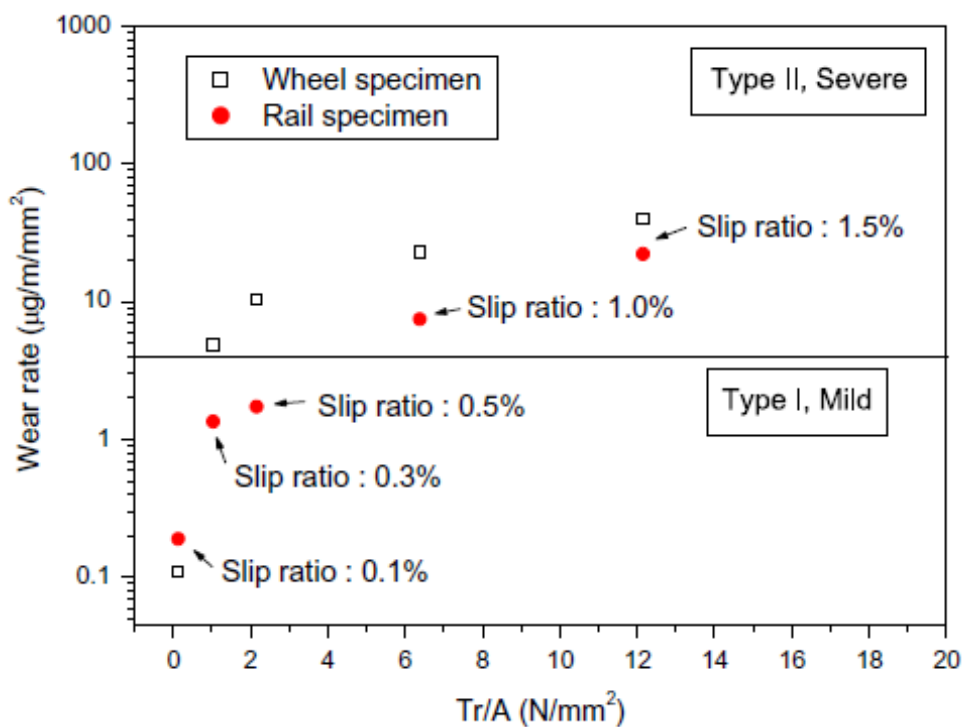


Figure 4.45: Wear rate as a function of  $T\gamma/A$  [114].

#### 4.12.3 Sliding distance consideration in the wear model

Some of the wear prediction models consider the sliding distance or distance travelled in the contact patch. For example, the Archard wear model defined by equation 4.7 takes into consideration the sliding distance ( $L$ ) to calculate the wear volume. The energy dissipation model by Pearce and Sherratt [242] estimates the material loss at the area of the cross-section

removed by distance covered ( $\text{mm}^2/\text{km}$ ) [245, 246], taking into consideration the accumulated traffic distance by the wheel. Another energy model by Zobory [247] assumes that there are two zones in the contact patch being the adhesion and sliding zones with a major part of the wear being located at the sliding zone and greatly dependent on the sliding speed [245, 246]. With the known sliding speed, the sliding distance can be obtained then related to wear.

A wheel profile wear prediction tool developed by Jendel [248] based on the real track data on rail network in Stockholm, Sweden, was used to study the wheel-rail contact mechanics. The wheel-rail contact was modelled using the Hertz theory and Kalker's simplified theory (FASTSIM) with the wheel wear being measure after a particular interval up until a running distance of 200,000 km. Using Kalker's simplified contact theory, Jendel was able to estimate wear in the sliding zone [249]. The model applied Archard's wear model by splitting the contact patch into cell elements with each element's wear depth ( $\Delta\delta$ ) given by equation 4.9, where  $s$  is the magnitude of the sliding distance,  $H$  is the material hardness,  $k$  is the wear coefficient and  $P$  is the contact pressure. Equation 4.9 was obtained from dividing the wear volume (in equation 4.7) by the area of the element,  $dx dy$  ( $\text{m}^2$ ) [250]. The sliding distance ( $s$ ) is given by equation 4.10, where  $\Delta x$  is the longitudinal element length (m),  $v_{slip}$  is the relative velocity (slip velocity) and  $V_{vehicle}$  is the vehicle speed ( $\text{m/s}$ ). Finally, by adding the wear depths for each element in the slip zone for all longitudinal strips of the contact surface, the overall wear distribution from the wheel-rail contact is obtained [248]. This model was able to take into consideration the sliding distance (accumulated traffic distance) into account for prediction of wheel wear.

$$\Delta\delta = k \frac{|s|P}{H} \quad 4.9$$

$$S = |v_{slip}| \frac{\Delta x}{V_{vehicle}} \quad 4.10$$

Another wear model by Braghin et al. [124] considered the circumference of the rolling wheel ( $2\pi R$ ) as well as the contact area ( $A$ ) of the contact patch for calculating the wear depth ( $\delta$ ). The wear depth ( $\delta$ ) at the contact patch is given by equation 4.11. Where  $T\gamma/A$  is the wear index ( $T$  is tractive force,  $\gamma$  is the slip, and  $A$  is the contact area),  $K$  is the wear coefficient obtained experimentally,  $v\Delta t$  is the actual travelled distance ( $\Delta t$  is the time interval between subsequent integration steps and  $v$  is the speed of the train),  $2\pi R$  is the length of the circumference over the rolling radius  $R$  of the wheel corresponding to the considered contact patch, and  $\rho$  being the

density of the wheel material [124]. The model was validated by experimental results from a full-scale wear test rig and was found to be in agreement with the latter.

$$\delta(x, y) = k \frac{T\gamma}{A} \frac{v\Delta t}{\rho} \frac{v\Delta t}{2\pi R} \quad 4.11$$

### 4.13 Wear test rigs for railway applications

In the railway industry, test rigs are used as a less expensive alternative to field testing to gather data on the dynamics and mechanics of railway systems under controlled conditions [251]. Data collected from test rigs is utilized to better understand the behaviour of the interaction between the rail and wheel to create quicker and safer trains by being able to foresee failure and plan for preventative maintenance. Different experimental techniques are utilized to investigate the processes of wear by replicating the operating conditions of wheel and rail materials in full-scale or small-scale setups, Figure 4.46. These experimental techniques provide useful information on wear rates, friction coefficients, damage mechanisms of contacting materials etc [252]. It is vital to select the appropriate testing approach for a given application to ensure that the test method represents as close as possible the real-life system. Several factors need to be considered when deciding the test method:

- Materials of the two contacting bodies;
- Test geometry including both the shape and dimensions of the samples;
- Applied load and contact pressure;
- Sliding speed; and
- Test environment [252].

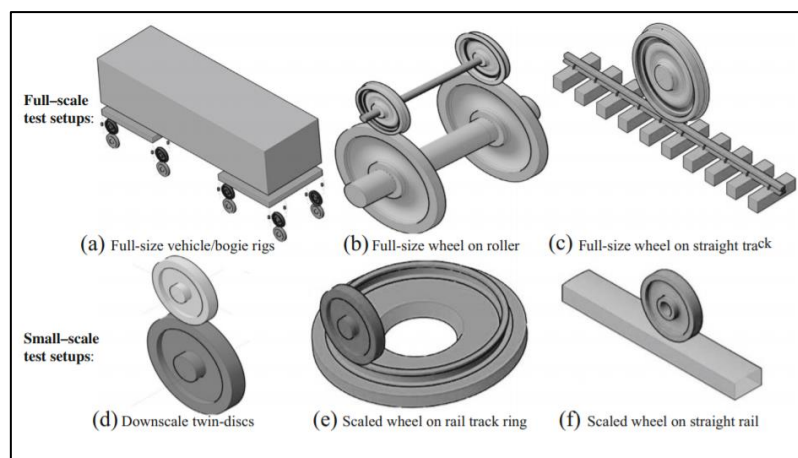


Figure 4.46: Schematic illustration of the different possible wear test rig configurations for studying the wheel-rail interface [253].

#### 4.13.1 Pin-on-disc

Figure 4.47 shows the Pin-on-disc wear test rig design consisting of two materials being the pin with a ball rigidly held perpendicular rotating disc [254]. The sliding wear track on the disk surface is circular. The orientation of the plane of the disk may be horizontal or vertical depending on the machine setup [254]. The disc is connected to a rotating motor and its speed can be set to a specific value. A specified amount of load is applied by either a lever or arm attached to weights pressing the pin against the disc. Other loading techniques such as hydraulics or pneumatics can also be used for this setup [254]. This setup is very useful as it gives researchers information on wear performance of the two materials (disc and pin) during sliding under a specified velocity, temperature, lubrication, load and time [255]. This setup has some limitation as it only provides information on sliding wear and, therefore cannot simulate the real systems. In other words, it cannot simulate a combination of RCF, rolling and sliding wear of a train wheel on a rail. Although the pin-on-disc rig has limitations, the information obtained is still crucial for the prediction of wear.

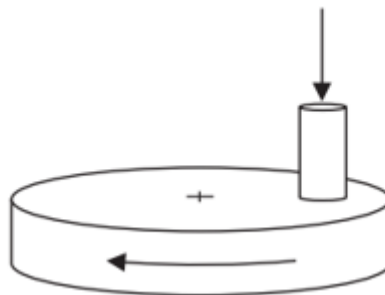


Figure 4.47: A schematic diagram showing pin-on-disc wear test rig design [252].

#### 4.13.2 Block-on-ring

According to the ASTM International (ASTM G77) [256], a block-on-ring wear test setup consists of a test block loaded against a test ring rotating at a specified rotational speed resulting in a wear scar being made on a block, Figure 4.48 and Figure 4.49 [256]. From that scar (wear track), the block wear volume can be calculated from the block scar width while the ring wear volume is calculated from its weight loss [256]. Using a load cell, the frictional force keeping the block in place can be measured during the test: data obtained can be combined with the normal force data to calculate the coefficient of friction values [256]. This type of test has limitations when used to simulate a combination of rolling and sliding wear as experienced by



the rail and wheel, as only one side of the block is in contact with the hence not suitable for this study.

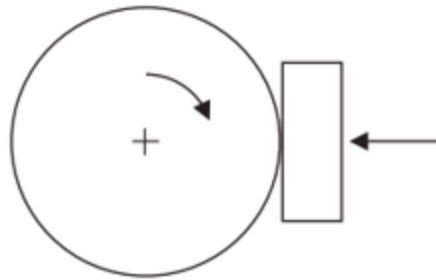


Figure 4.48: A schematic diagram showing block-on-ring wear test rig design [252].

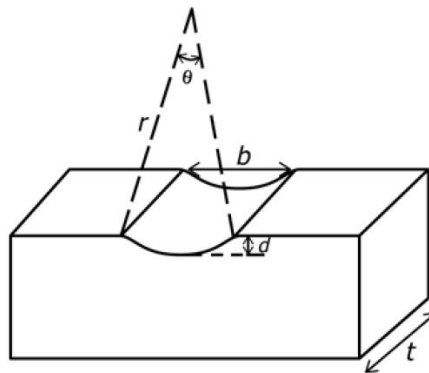


Figure 4.49: Block scar volume based on the width of the scar [256].

#### 4.13.3 Pin-on-reciprocating plate

This design consists of pin (sometimes with a spherical end ball) under vertical loading in contact with a reciprocating horizontally mounted flat plate, Figure 4.50 [257]. The two materials move relative to one another in linear motion with a back and forth sliding motion. The velocity, normal loading, time, stroke length and environment conditions can be controlled in this setup. The changes in dimensions and weight for both the pin and flat plate are used to calculate the wear volumes and wear rates [257]. Load cells are used to measure frictional forces, which are then used with the normal forces to obtain the coefficients of friction. There are limitations to this approach as there is no rolling wear as the two materials in contact are only experiencing sliding wear. Secondly, this design produces low sliding speeds since the pin (ball) cannot continuously run over the reciprocating plate as it moves back and forth in a cyclic manner to simulate the repeated contact and constant velocity conditions are not maintained [253]. Therefore, this is not an ideal design to develop a wear test rig that can

simulate combined rolling and sliding wear experienced during the rolling of a train wheel on a rail as required by this study.

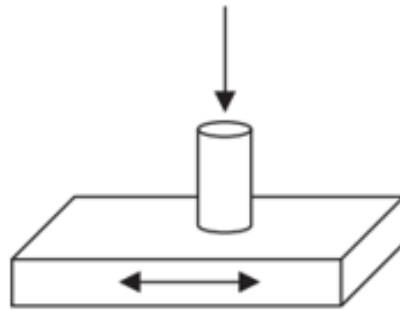


Figure 4.50: A schematic diagram showing pin-on-reciprocating plate wear test rig design [252].

#### 4.13.4 *Twin-disc*

The use of twin-disc setup goes back to 1935 when an apparatus to test worm gears by Merritt [258] was developed to predict their load-carrying capacity and efficiency. As shown in Figure 4.51, the twin-disc wear test rig operates on the basis of two rotating cylinders (discs) contacting each other under load while rotating in opposite directions [259]. To produce a rolling and sliding contact, both discs are attached to some pivoting shafts powered by separate motors [259]. The motors produce enough torque that will overcome the frictional force between the two rotating discs being tested. The two discs rotate at different velocities to simulate rolling and sliding at the same time. In the railway industry, the two discs are used to simulate both the wheel and rail. The twin disc setup is one of the best methods to simulate both rolling and sliding wear by rotating the two discs at different velocities. Both discs are weighed before and after testing to calculate the wear rate. Using Hertz theory, equation 2.6, the maximum contact pressure can be calculated using the disc dimensions as well as the applied load. The main limitation of the twin-disc test rig design is the inability to take the rail profile into consideration as it is neglected and assumed to have the same geometry as the wheel. The other limitation of the twin-disc design is inability to directly compare experimental results with those from moving trains as conditions such as contact pressure and geometry are different. Therefore, an alternative to this design would be the use of a full-scale or scaled roller-rigs which comes at a cost.

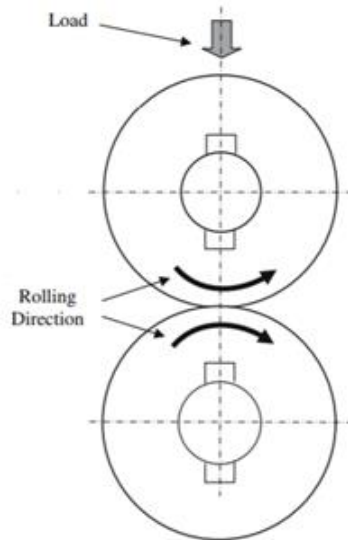


Figure 4.51: Schematic diagram showing a twin-disc test rig design [260].

#### 4.13.5 Requirements for downscaling twin-disc testing

As stated from literature [261, 262], the results obtained from twin-disc simulators are not fully identical to those in the field. This is so because the rail is simulated by a disc with a finite radius of curvature in the tangential direction [263], but the rail has actually an infinite curvature [264]. Furthermore, it is difficult to simulate the movement of a wheel in curves on a twin-disc simulator due of centrifugal forces, and most roller rigs ignore the different distance to be traversed on inner and outer track [261]. Different roller rigs have been developed around the world with scaling factors ranging from large scale 1:1 to small scale 1:20 [253, 265, 266], some are shown in Table 4.2, to try to simulate the actual wheel-rail contact conditions. The scaling strategy selection is based on the type of work to be carried out on the rig [267]. The geometrical scaling factor ( $\varphi_l$ ) is defined by equation 4.12, where  $l_1$  is a characteristic length of the full scale and  $l_0$  characteristic length of the scale model [262]. For example, a scale factor of 1:7 means the disc is 7 times smaller than the actual train wheel [268].

$$\varphi_l = \frac{l_1}{l_0} \quad 4.12$$

To be as close as possible to field conditions the following Hertzian downscaling requirements must be met in twin-disc laboratory testing:

- Choice of material; the contacting materials should be a true representation of the actual wheel and rail steels used in the field and should remain the same throughout testing.
- The maximum contact stress in the laboratory must equal to that in the field i.e.

$$(P_{max})_{lab} = (P_{max})_{field} \quad 4.13$$

Where  $(P_{max})_{field}$  and  $(P_{max})_{lab}$  are the maximum contact stresses in the field and in the laboratory respectively.

- The ratio of the semi-major axis to the semi-minor axis of the contact ellipse between the wheel and rail in the laboratory must equal to that in the field i.e.

$$\left(\frac{a}{b}\right)_{lab} = \left(\frac{a}{b}\right)_{field} \quad 4.14$$

Where  $(a/b)_{lab}$  and  $(a/b)_{field}$  are the ratios of the semi-major axis, a to the semi-minor axis, b of the contact ellipses between the wheel and rail in the laboratory and in the field, respectively [16, 103, 269].

- Lastly, downscaling of ‘wheel diameter to disc diameter’ must roughly equal to downscaling of major axis of the contact ellipse between actual wheel-rail and laboratory twin disc i.e.

$$\left(\frac{D_w}{D_d}\right) = \left(\frac{a_{field}}{a_{lab}}\right) \quad 4.15$$

Where  $D_w$  and  $D_d$  are the diameter of the wheel and disc, respectively.

Table 4.2: Available test rig to study the wheel-rail contact, adapted from [253].

No.	Name of the testing setup	Scale	Location
1	Full-scale Roller Rig	1:1	Southwest Jiaotong University, Chengdu, China
2	Reduced-scale Rolling Rig	1:3	TNO-TPD, Delft, Netherlands
3	Twin-Disc Machine	1:2-1:4	East Japan Railway Company, Saitama, Japan
4	Wheel/Rail Tribological Rolling Rig	1:4	Southwest Jiaotong University, Chengdu, China
5	UNSW Wheel-Rail Rolling Rig	1:5	University of New South Wales, Sydney, Australia
6	Scale Roller Rig	1:5	University of Huddersfield, Huddersfield, UK
7	Oerlikon Test Machine	1:10	Delft University of Technology, Delft, Netherlands
8	SUROS Twin-Disk Test Machine	1:20	University of Sheffield, Sheffield, UK

## Chapter 5: Test rig design and development

### 5.1 Introduction

For this work, it was proposed that a twin-disc approach be adopted to design and develop a wear test rig that would be able to simulate a combined rolling and sliding wear experienced during the rolling of a wheel on a rail. The twin-disc setup has been found to be the best method to simulate RCF, rolling and sliding wear of wheel and rail due to its easy usage and good comparability of test results to the actual components in service [270]. In addition, the ability to control the cylindrical geometries of the discs makes it easier to obtain precise frictional force at the contact. Experimental variables such as rotational speeds, applied force, slip ratios can be easily controlled. The setup also saves costs rather than having to use full-size components, which are expensive not only expensive to manufacture but would require more complicated systems to simulate wear and RCF [271]. The twin-disc setup also allows the study of effects of third body materials such as grease, water, sand etc. to be investigated easily by controlling the amount being introduced at the wheel-rail contact.

In this study, two separate 50 mm diameter and 10 mm wide discs were machined from the actual AAR class B wheel, R350HT and R260 rail steels used by the local rail industry. For the test rig used for this work, the maximum load that can be applied is 1.8 kN, corresponding to maximum contact pressure of 740 MPa. With the current setup and width of the contacting disc of 10 mm the contact pressure cannot exceed 1 GPa. To solve this problem, the disc's width needs to be reduced to 5 mm to reach a maximum contact pressure of 1.03 GPa. Literature [245, 272, 273] has demonstrated that having one of the contacting discs with a contacting length of 5 mm allows high contact pressures with reasonable normal loads. For this current setup, this would cause some misalignment between the contacting discs. Therefore, in this work, the scaling factor was approximately 1:18 as per equation 4.12, using the class B wheel diameter of approximately 915 mm to the disc diameter of 50 mm chosen for this study.

Both the rail and wheel discs were connected to some pivoted shafts run by independent electric motors to create a rolling and sliding contact, Figure 5.1, Figure 5.2 and Figure 5.3. Full drawings of the rig are shown in appendix A (section 9.4.1). A keyed joint was used to secure each disc into the shaft to prevent relative movement between the shaft and the disc. The two discs rotate at different velocities to simulate rolling and sliding at the same time. The load was applied on the upper disc (wheel material) using a scissor jack loading system connected to a

load cell to measure the direct normal load. The discs were connected to two independent tachometers to measure the individual rotational speeds of each disc.

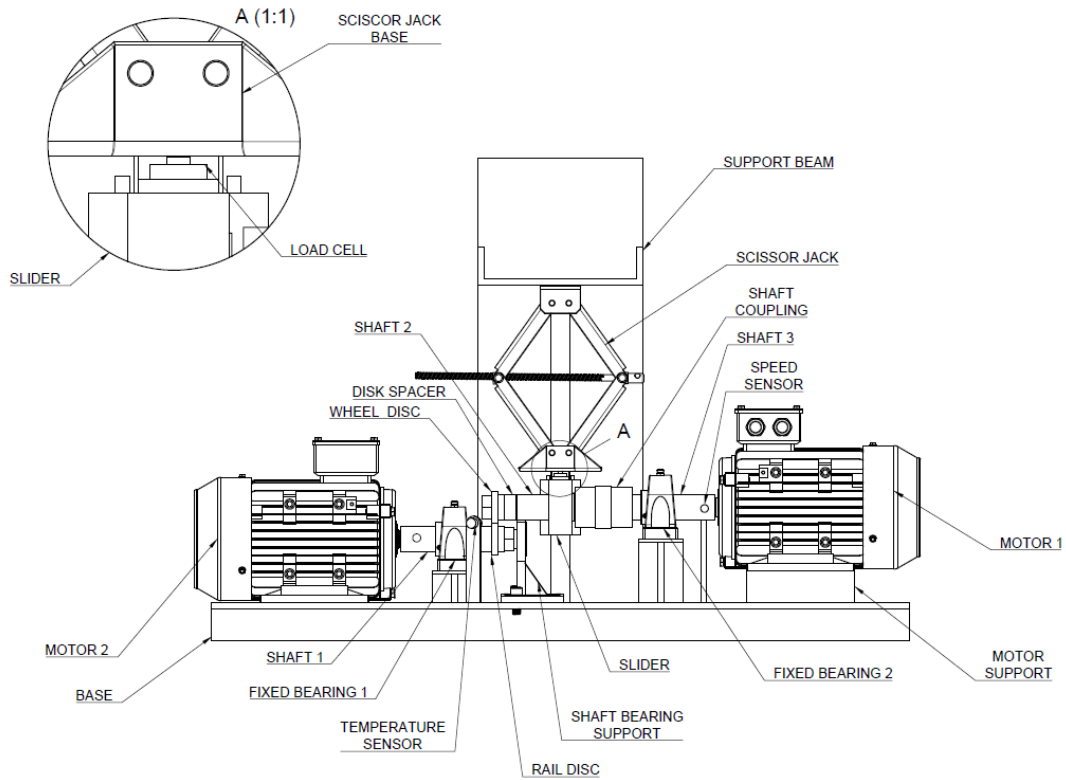


Figure 5.1: A schematic diagram of the twin disc test rig design showing its components.

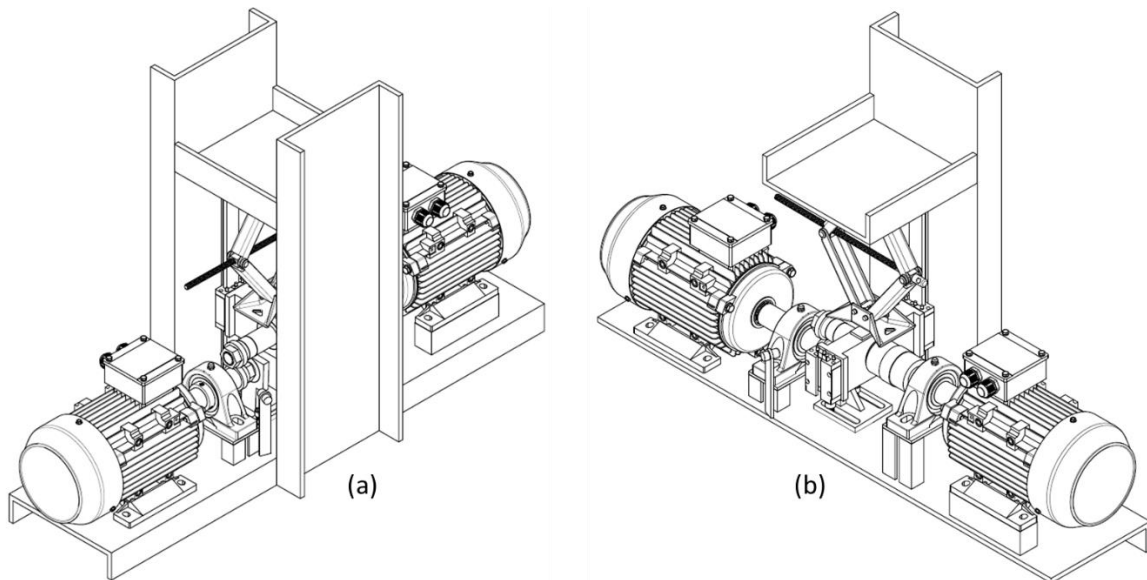


Figure 5.2: A schematic diagram of the twin disc test rig showing; (a) full 3D and (b) isometric drawings.



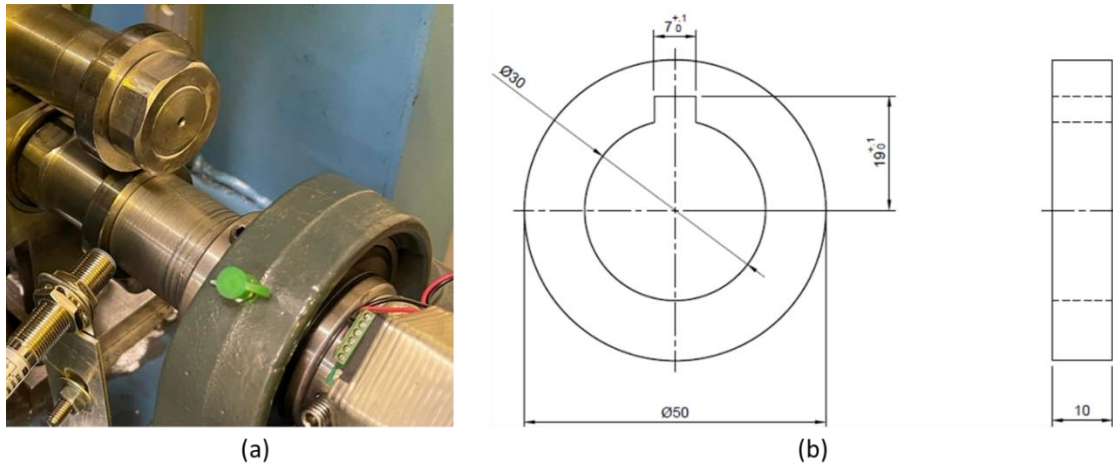


Figure 5.3: (a) Wear test rig configuration, (b) dimensions of the wheel and rail disc specimen.

## 5.2 Motors and variable speed drives

Two identical three phase, four pole, 3 kW motors were used for this work. Each motor was connected to its own 4 kW variable speed drive (VSD) to control speed over a range of 0-1400 rpm shown in Figure 5.4. The variable speed drives had controls where rotational speed and direction of rotation could be changed. To measure the actual rotational speeds of each motor tachometers, with digital display were used, with a magnet mounted on shaft used as a sensor shown in Figure 5.5. The digital tachometers have a measurement range of 10-9999 rpm and an accuracy of 0.1%.

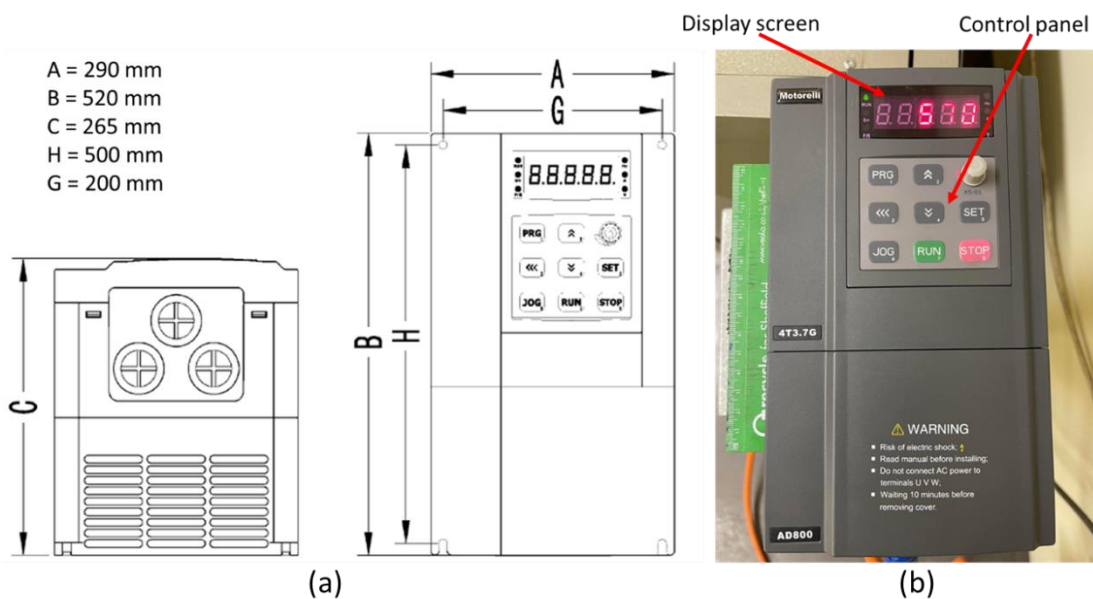


Figure 5.4: (a) A drawing of the variable speed drives (VSD) showing their dimensions and (b) a photograph of one of the variable speed drives used to make the rig.

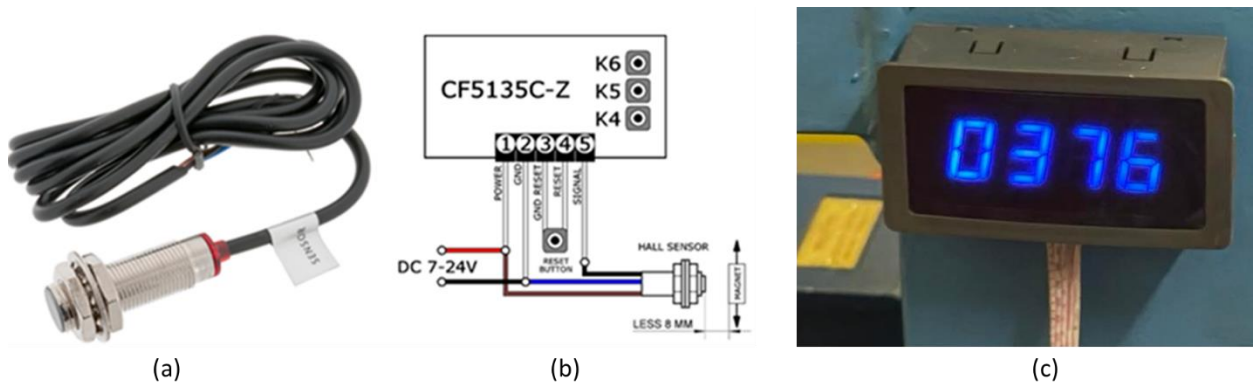


Figure 5.5: (a) Photograph of tachometer and (b) wiring diagram, (c) photograph of the LED speed digital display mounted on the rig.

### 5.3 Load measurement

A 10 kN C9C compressive force transducer (load cell) equipped with a 1.5 m long cable was used to measure the amount of load applied at the wheel-rail discs contact, Figure 5.6. The load cell was connected to a QuantumX (MX440B) data acquisition system (DAQ) which was connected to Catman software installed into a computer.



Figure 5.6: (a) A photograph of the 10 kN C9C Force Transducer, (b) a photograph of the force transducer mounted into a holder.

### 5.4 Torque and friction measurement

The strain gauges were mounted on the lower shaft connected to the TorqueTrak 10K-LP Torque Telemetry system to obtain the torque measurements, Figure 5.7. The TorqueTrak 10K-LP Torque Telemetry system was connected to a QuantumX (MX440B) data acquisition system (DAQ) which was connected to Catman software installed in a computer. The strain gauges were calibrated by applying a known amount of torque using a high torque wrench with the end of the shaft fixed to prevent motion. This was done to determine the telemetry voltage output corresponding to the applied torque with the help of the equipment supplier. The volts/torque relationship was put into the data acquisition software and corrected for any zero

offset. This was done multiple times to get the average results. To obtain frictional force from torque measurements, equation 5.1 was used:

$$T = FR_r \quad 5.1$$

Where T is the Torque (Nm), F is the tractive force (N), and  $R_r$  is the radius of the lower disc (m). The coefficient of friction was obtained using equation 5.2:

$$\mu = \frac{F}{W} \quad 5.2$$

Where  $\mu$  is the coefficient of friction or tractive coefficient at the wheel and rail discs contact, F is the tractive force (N), and W is the applied load (N).

Equation 5.2 can be simplified into equation 5.3:

$$\mu = \frac{T}{WR_r} \quad 5.3$$

Where T is torque (Nm), W is the applied load (N), and  $R_r$  is the radius of the lower disc (m).

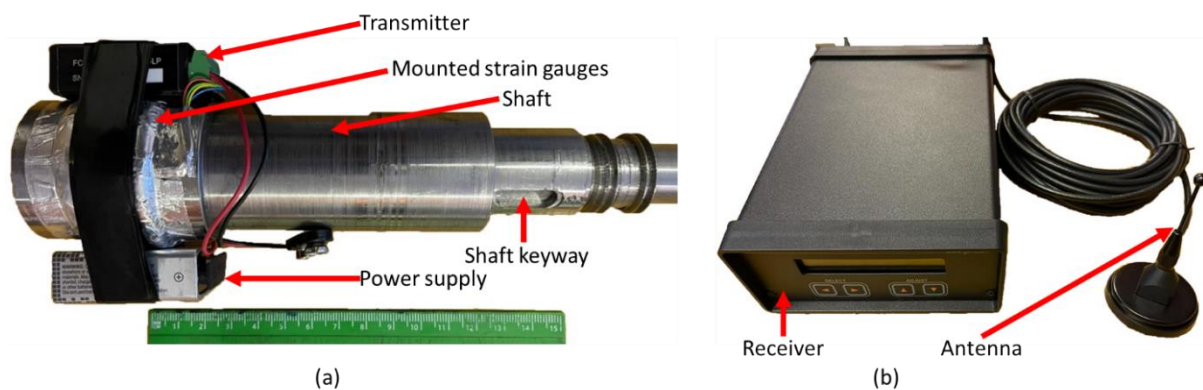


Figure 5.7: (a) Shaft mounted with strain gauges, transmitter, and power supply (battery); (b) receiver and antenna which are part of the TorqueTrak 10K-LP Torque Telemetry system.

## 5.5 Wheel disc temperature measurement

For the current twin-disc setup, it is not easy or not practical to measure the flash temperature at the wheel-rail contact patch, so the wheel disc temperature was measured instead as discussed in section 4.7.1. To measure the wheel disc temperature during testing, a PyroMiniUSB Infrared temperature sensor was used which was connected to CalexConfig software for data logging and acquisition, Figure 5.8. The infrared temperature sensor had an accuracy of  $\pm 1$  °C with a response time of just 125 ms. The sensor had a measuring distance of

up to 200 mm. For this work, the measuring distance was less than 50 mm hence more accuracy. With this high accuracy and a response time of 125 ms, the sensor was able to measure the wheel disc temperature without any significant loss in temperature [112].



Figure 5.8: (a) PyroMiniUSB Infrared temperature sensor and (b) CalexConfig data acquisition software display.

## 5.6 Application of third body materials

The rig was designed to accommodate variable contact conditions by introducing third body materials at the wheel-rail discs contact. It was fitted with RS PRO diaphragm positive displacement pump, Figure 5.9. The pump was capable of pumping both gases and liquids with a maximum flow rate of 150 ml/min, working pressure of 1 bar. For this work, the flow rate was set to 25 mL/min for both water and oil application as it was found to maintain the same film thickness during testing.



Figure 5.9: RS PRO diaphragm electric operated positive displacement pump.



Table 6.1: Chemical composition of the as-received wheel and rail steels.

Material	Wheel	Rail 1	Rail 2
Standard	AAR M-107/M-208 [55]	BS EN 13674- 1:2011 [56]	BS EN 13674- 1:2011 [56]
Grade	AAR Class B	R350HT	R260
Element	Chemical Composition (wt%)		
C	0.670	0.790	0.700
Mn	0.810	1.170	0.910
P	0.020	0.013	0.025
S	0.008	0.016	0.005
Si	0.347	0.388	0.354
Ni	0.065	0.061	0.045
Cr	0.150	0.197	0.036



Table 6.2: Mechanical properties and interlamellar spacing of the as-received wheel and rail steels.

Material	Wheel	Rail 1	Rail 2
Grade	AAR Class B	R350HT	R260
Hardness, HV 10	$348 \pm 3$	$372 \pm 5$	$298 \pm 6$
Tensile Strength (MPa)	1070	1175 [91]	880 [91]
Elongation (%)	14	9 [91]	10 [91]
Interlamellar spacing (nm)	$270 \pm 35$	$112 \pm 12$	$341 \pm 94$

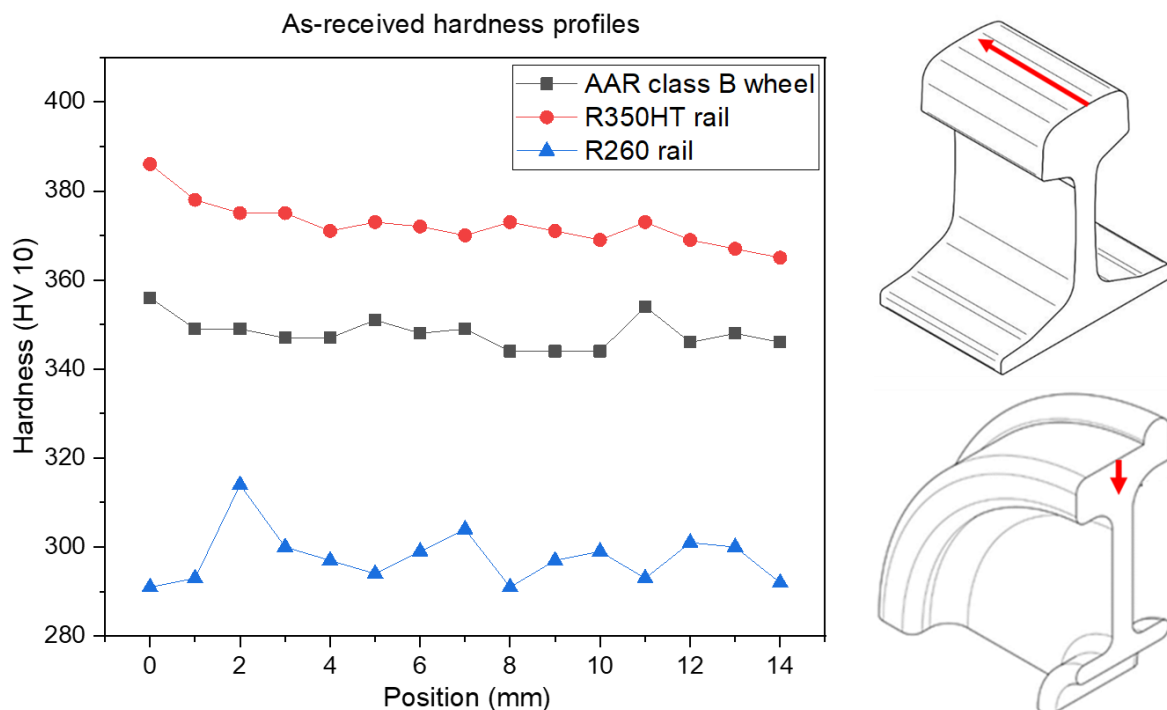


Figure 6.2: As-received hardness profiles of wheel and rail specimen, obtained at the rim and centre line of the rail head respectively.



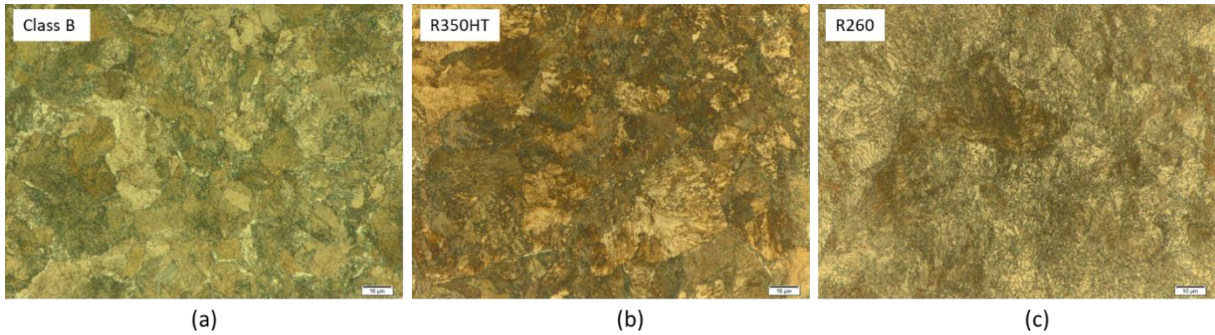


Figure 6.3: OM micrographs of the as-received (a) Class B wheel specimen obtained at the rim, (b) R350HT rail specimen and (c) R260 rail specimen showing pearlitic microstructures obtained at the rail head.

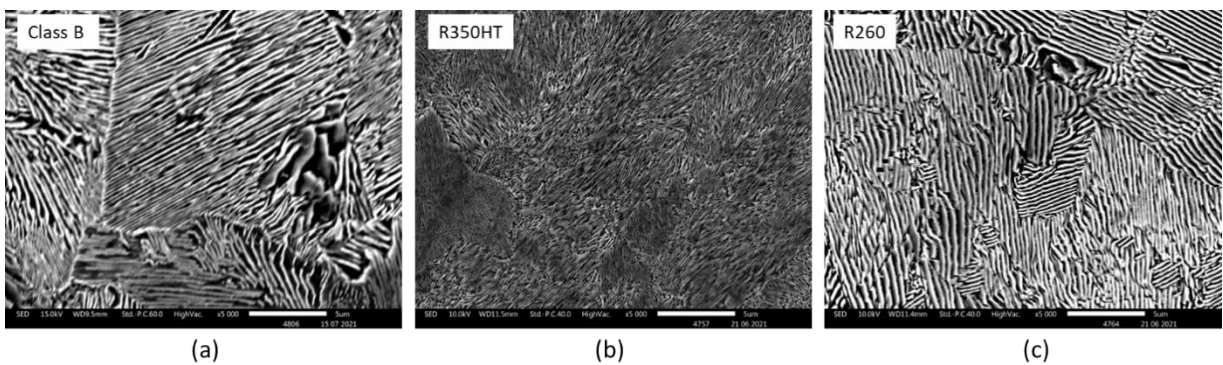


Figure 6.4: SEM micrographs of the as-received (a) Class B wheel specimen obtained at the rim, (b) R350HT rail specimen and (c) R260 rail specimen showing different colonies of pearlite consisting of alternating layers of ferrite and cementite.

### 6.1.1 Wheel steel

Figure 6.5 show OM micrographs of wheel material obtained at the rim, tread and flange. All three regions show pearlitic microstructure which confirms the wheel steel to be a hypoeutectoid steel with a carbon content of 0.67%. The rim had a higher Vickers hardness of 348 HV compared to flange and tread having hardness values of 331 HV and 328 HV respectively.

Table 6.3: Vickers hardness values of the wheel steel at the rim, flange and tread respectively.

Position	Average hardness (HV10)
Wheel rim	$348 \pm 3$
Wheel flange	$331 \pm 13$
Wheel tread	$328 \pm 8$

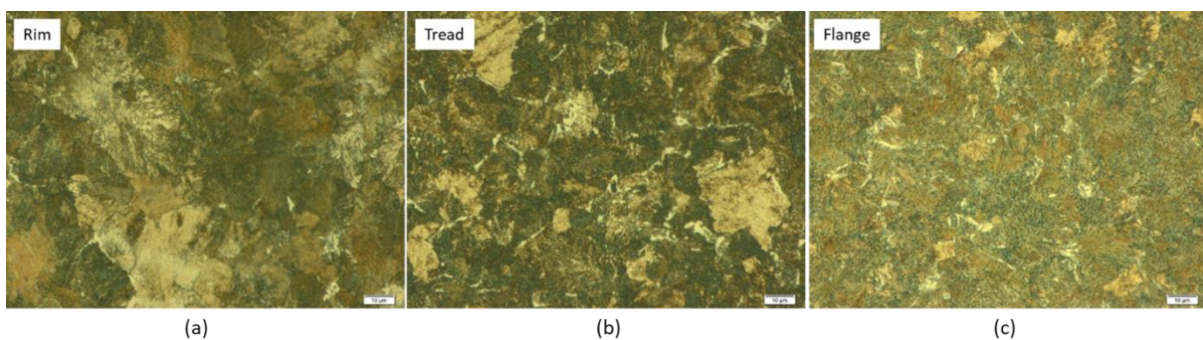


Figure 6.5: OM micrographs of the as-received wheel specimen obtained at the rim, tread and flange showing a pearlitic microstructure.

### 6.1.2 Rail steels

Figure 6.6 shows the SEM micrographs of R350HT and R260 rail steels obtained at depth of 10 mm from the rail head surface. As may be seen, both rail steels were fully pearlitic consisting. The 350HT rail appeared to have finer lamellar spacing compared to R260 rail steel. This was confirmed by the hardness values and interlamellar spacing, Table 6.2.

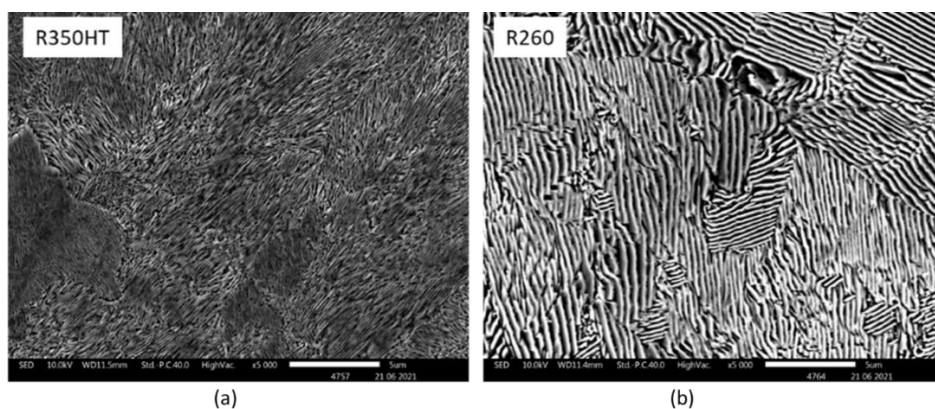


Figure 6.6: SEM micrographs of the as-received (a) R350HT (b) R260 rail steels showing different interlamellar spacing and pearlite colonies.

## 6.2 Sectioning

Wheel and rail discs were sampled as shown in Figure 6.7. As illustrated in Figure 6.8, the sectioned wheel and rail discs had an exterior diameter of 50 mm, an internal diameter of 30 mm, and a thickness of 10 mm. The sizes of the rail discs were restricted to the widths of the rail heads, which are 72 mm and 70 mm for the 60E1 and 54E1 rail profiles respectively. To stop relative movement between the shafts and the discs, the discs were locked into each of their corresponding shafts using a keyed joint. According to some studies [27, 73, 275] sampling of the wheel and rail materials should be done in a way to minimise variation in surface hardness across the discs. As seen from the hardness profile plots of the wheel and rail specimens (Figure 6.2), there was insignificant hardness variation in the direction where sectioning was done.

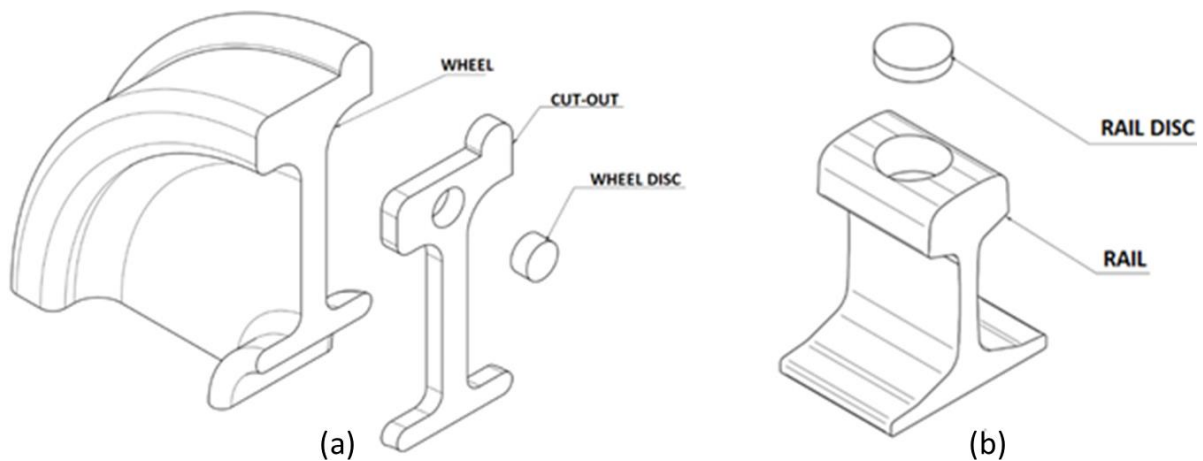


Figure 6.7: A schematic illustration showing specimen sampling from: (a) the wheel and (b) the rail.



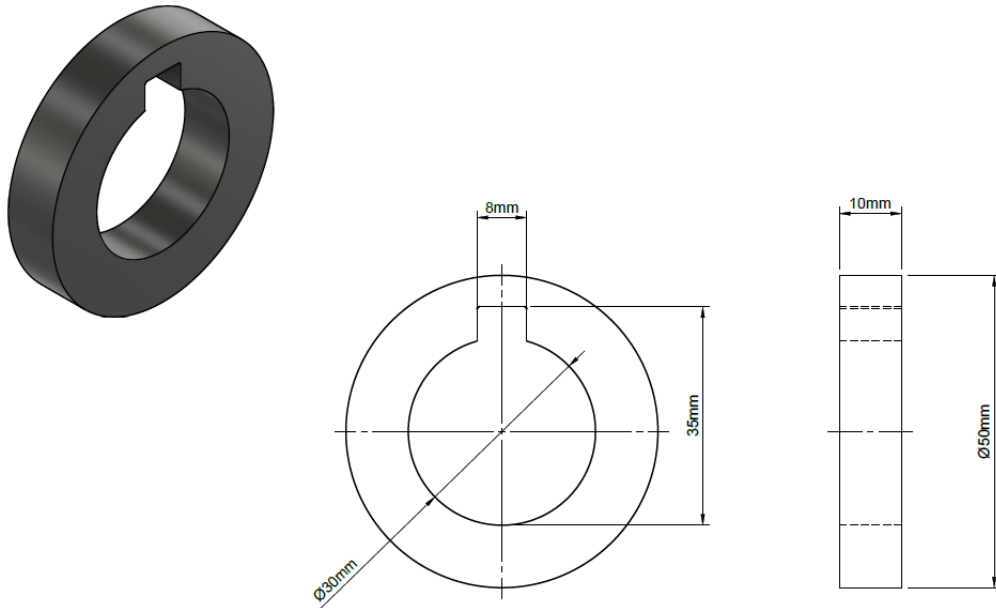


Figure 6.8: A schematic diagram showing dimensions of wheel/rail disc shaped specimens.

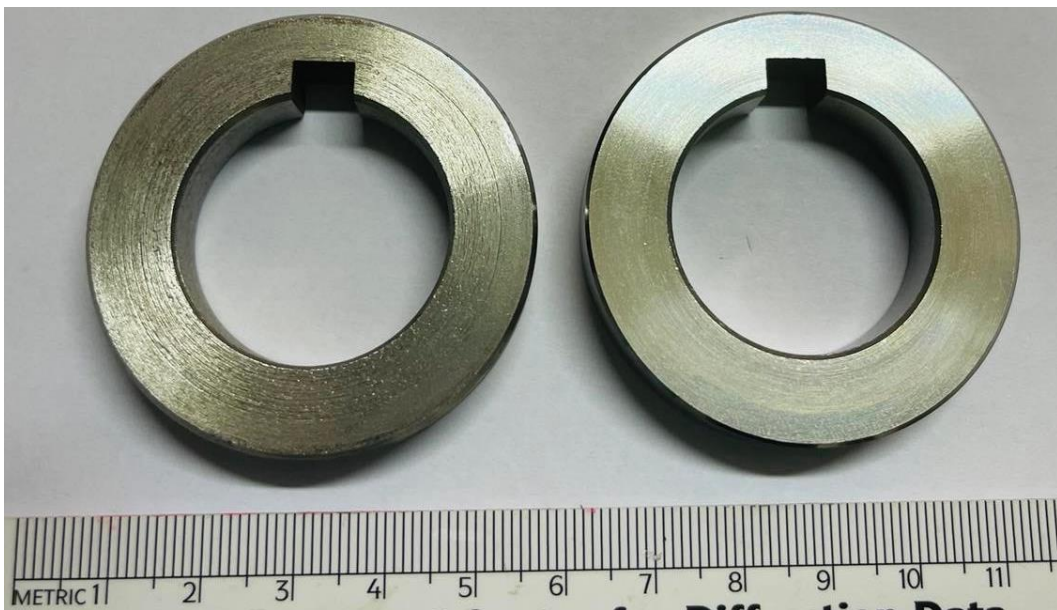


Figure 6.9: Photograph of the wheel and rail discs after machining showing the keyway.

### 6.3 Testing procedure

To ensure consistency of results a standard operating procedure was developed. Before wear testing under the designed wear test rig, both wheel and rail discs were cleaned in an ultrasonic bath of ethanol to remove any contamination that might be present. Using the variable speed drives of each motor, the rotational speed of the rail disc was kept constant at 340 rpm while the wheel disc speed was varied to achieve slip ratios of 2%, 5%, 10%, 20% and 27%. For a twin disc setup, the slip ratio ( $\% \gamma$ ) is defined by equation 4.3. High slip ratios (10%, 20% and

27%) were chosen in order to induce RCF cracks that causes severe and catastrophic wear on contacting materials as previously discussed in literature [23, 143, 212]. Literature [23] has demonstrated that slip ratio varies at the wheel-rail contact as the wheel moves along the track. Also, the high slip ratios were introduced to compensate for low contact pressures used in this study (Max. 740 MPa due to limitation of the rig) in order to induce the RCF cracks. In reality, the wheel-rail contact experiences up to 2% slip ratios under steady speeds whereas under acceleration or braking the slip ratio can become severe reaching up to 9% [276].

Two digital tachometers were used to validate the speeds of each motor, making sure that the slips are maintained throughout the test. The number of rolling cycles was kept constant at 62 000 cycles for all tests. To obtain the coefficient of friction from torque measurements equation 5.3 was used. The average coefficient of friction for each contact condition was obtained as the arithmetic mean value of the dynamic friction coefficient from the beginning to the end of the test after 62 000 rolling cycles. Before applying the load, both motors were allowed to reach the set test speeds, after which the test load was applied using a scissor jack. Three test loads were used namely 1, 1.4 and 1.8 kN, corresponding to maximum contact pressures of 552, 645 and 740 MPa respectively: thus, according to Hertz theory [44, 45]. Literature [37] has demonstrated that the wheel-rail interface experiences pressure from 500 to 1500 MPa especially between the rail head and the wheel tread. A review study by Rocha et al. [277] has shown that twin-disc rigs have an operating contact pressure ranging from 300 to 1500 MPa. A summary of the test parameters used for this study is shown in Table 6.4.

After testing, the discs were also cleaned in an ultrasonic bath of ethanol and the worn contact surfaces of the discs were observed under the stereo microscope. For surface roughness measurements, a Mitutoyo Surftest (SJ-210) surface roughness tester was used. The arithmetic mean of roughness value (Ra) was determined according to the ISO 4287:1997. The surface roughness was measured along the transverse direction of the worn discs. The discs had a roughness of 0.1  $\mu\text{m}$  before tests. The worn wheel and rail discs were sectioned, ground and polished in order to analyse the morphology of the worn surfaces and sub-surface cracks using optical and scanning electron microscopes. Vickers microhardness tests were conducted using a Struers Duramin-40 tester under a load of 200 gf along the cross-sections of both wheel and rail steels to investigate the depth of plastic deformation and work hardening. Different contact conditions were used being dry and wet (oil and water). Oil and water were added to the wheel-rail contact to investigate the effect of lubrication on wear. For each test, new sets of wheel and rail discs were used.

Table 6.4: Test matrix, note that the number of cycles and rail disc speed were kept at 62000 and 340 rpm respectively.

Contact load (kN)	Wheel disc speed (rpm)	Slip Ratio (%)
1	347	2
1	358	5
1	376	10
1	416	20
1	448	27
1.4	347	2
1.4	358	5
1.4	376	10
1.4	416	20
1.4	448	27
1.8	347	2
1.8	358	5
1.8	376	10
1.8	416	20
1.8	448	27

## 6.4 Validation of the test rig and results

### 6.4.1 Repeatability and reproducibility of the results

To check the repeatability of the wear test results, the test was repeated three times under the same conditions i.e., dry contact, 10% slip ratio, 1.8 kN contact load and 62 000 rolling cycles. It was found that the three tests produced similar results. The average coefficient of friction was found to be 0.45 with a standard deviation of 0.02, which is  $\pm 4\%$  error, Figure 6.10. There was a sudden drop in the coefficient of friction in test run 2 after 30 000 rolling cycle which eventually stabilised. This sudden drop could have been due to the removal of wear debris at the contact faster than the other tests as wear debris influence friction properties. The cumulative mass loss (wheel + rail) was found to be an average of 0.59 g and a standard deviation of 0.05 g which is  $\pm 8\%$  error, Figure 6.11. The contact surface morphologies were similar, i.e., consistent for all three tests, Figure 6.12. In brief, the rig's test results were repeatable and comparable to literature.

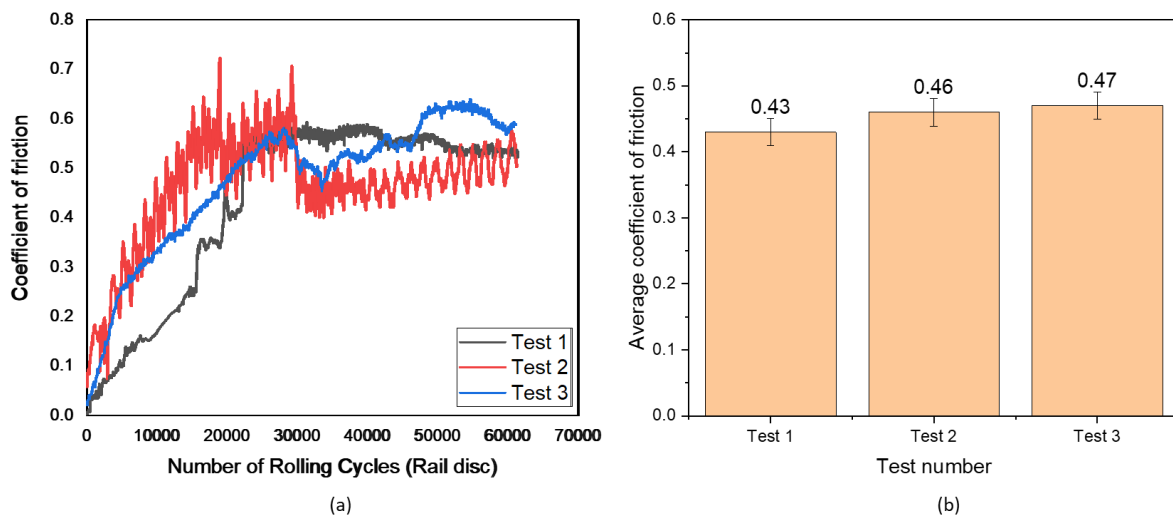


Figure 6.10: (a) Coefficient of friction as a function of the number of rolling cycles, (b) average coefficient of friction for three tests under same test conditions (1.8 kN, dry contact, 62 000 rolling cycles and 10% slip ratio).



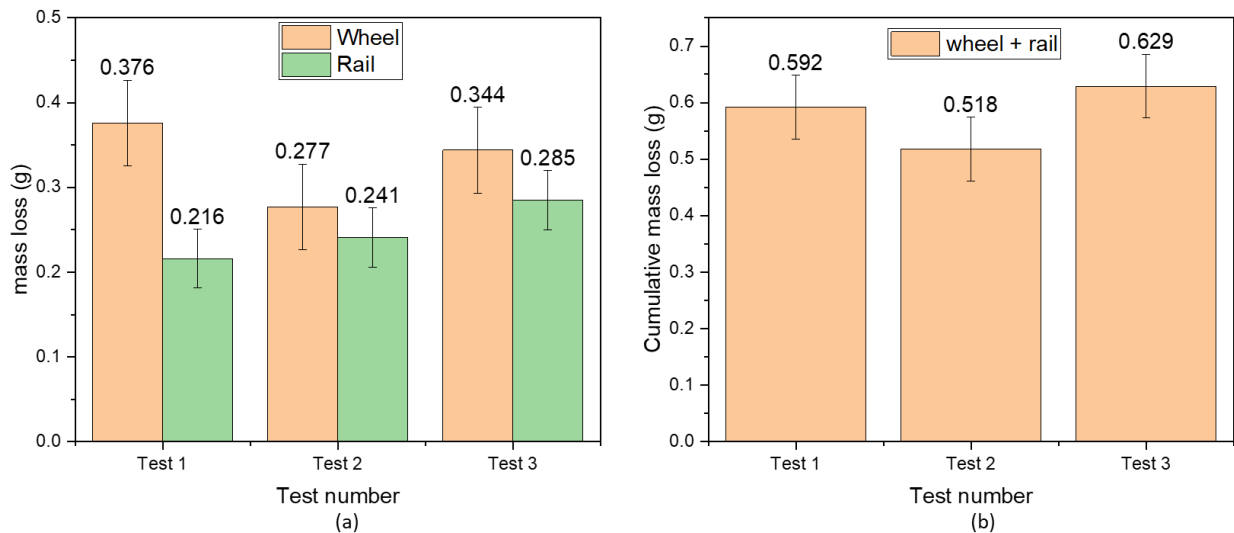


Figure 6.11: (a) Mass loss of the wheel and R350HT rail after three tests under same test conditions as in Figure 6.10 and (b) cumulative mass loss (wheel + rail) after three tests under same test conditions.

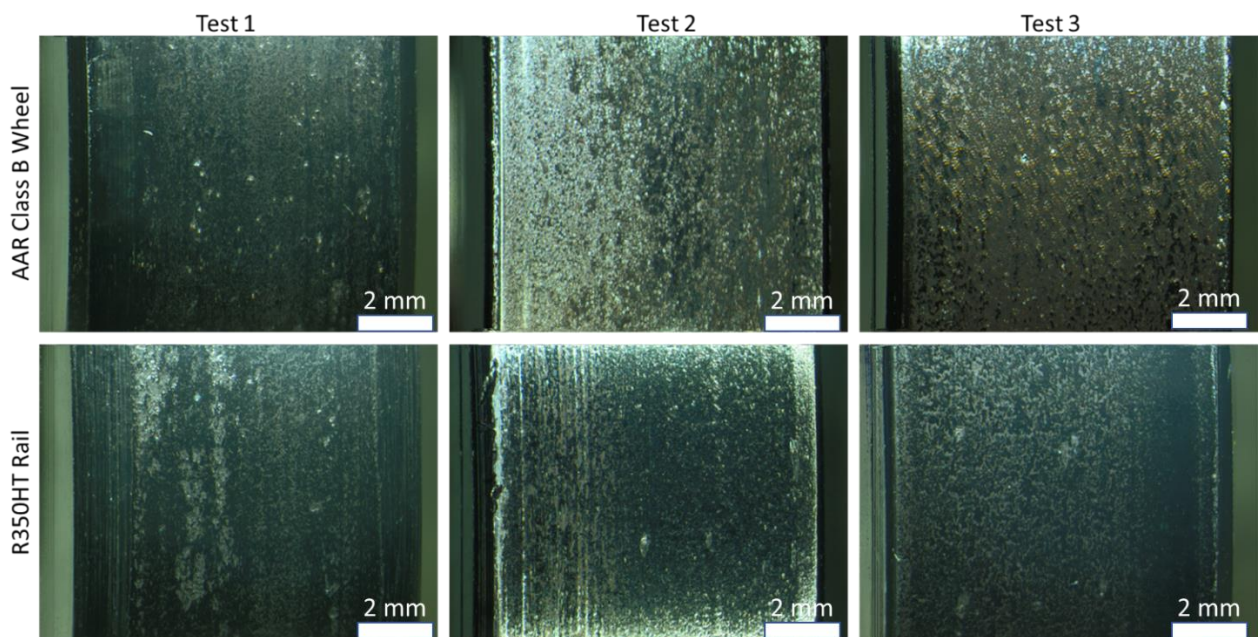


Figure 6.12: The contact surfaces of (a) the R350HT rail and (b) the wheel under the same test conditions as in Figure 6.10.

#### 6.4.2 Load stability during testing

The contact loads were set at 1, 1.4 and 1.8 kN and were stable throughout the tests, with average values of  $1.02 \pm 0.02$  kN,  $1.41 \pm 0.02$  kN and  $1.81 \pm 0.03$  kN respectively, at 10% slip ratio and under dry contact, Figure 6.13. The same load stability was observed in all tests under dry contact. However, when water and oil were introduced at the contact; the load was more

stable compared to dry testing, with average values of  $1.81 \pm 0.02$  kN and  $1.81 \pm 0.01$  kN respectively, Figure 6.14. This proved that the test rig was successful in providing a stable load over the set test period of 62 000 rolling cycles for all contact conditions.

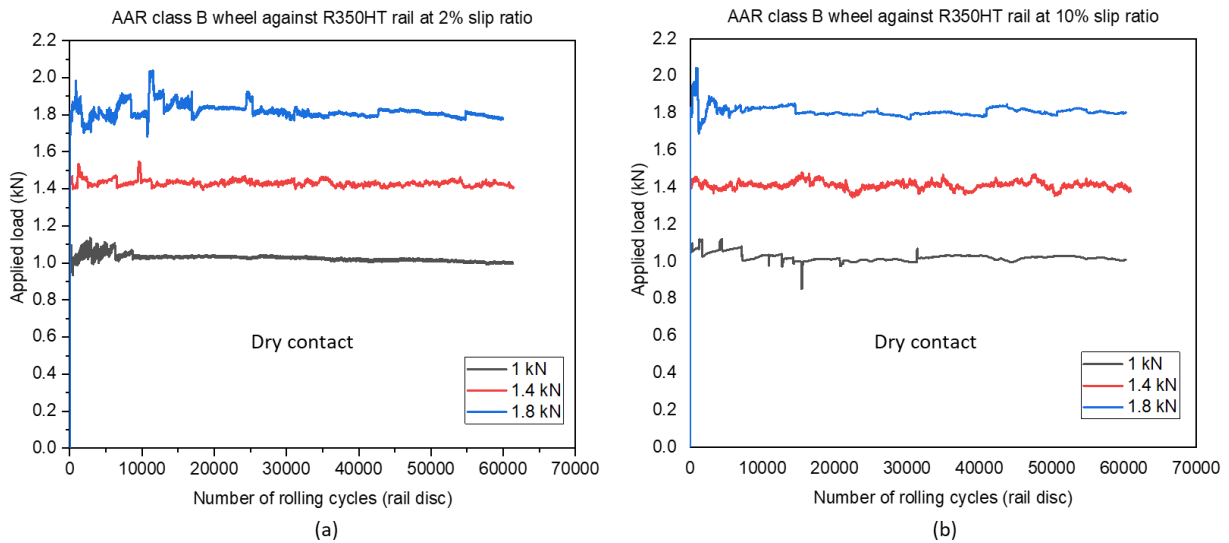


Figure 6.13: Contact load variation about nominal values of 1, 1.4 and 1.8 kN during testing for 62000 rolling cycles under dry contact, at slip ratios of (a) 2% and (b) 10% when the wheel was run against R350HT rail under dry contact conditions.

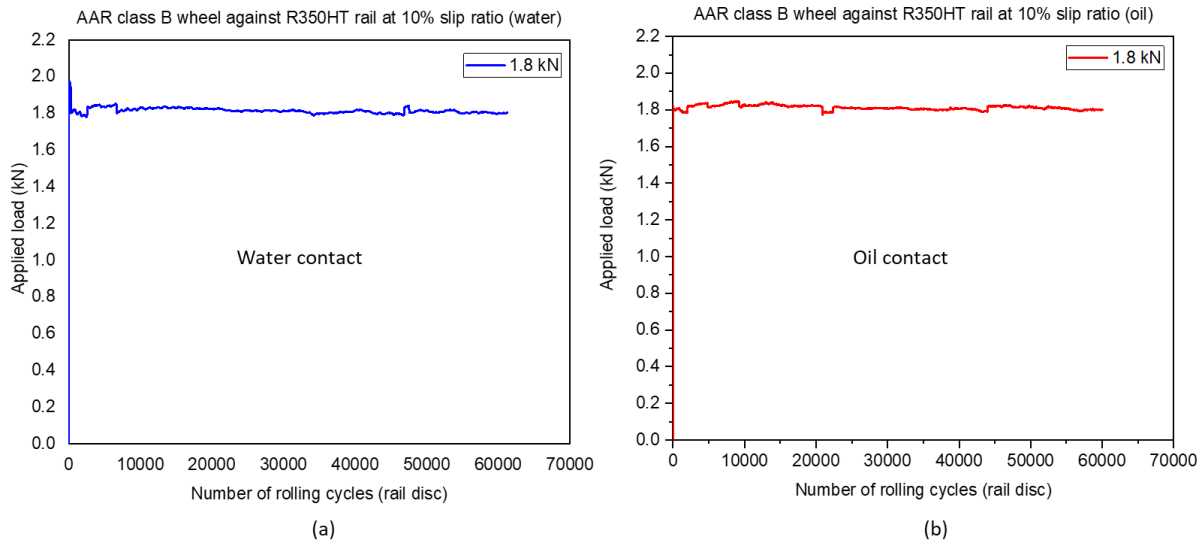


Figure 6.14: Contact load variation about nominal value of 1.8 kN during testing for 62000 rolling cycles at 10% slip ratio under (a) water and (b) oil contacts when the wheel was run against R350HT rail.

## Chapter 7: Results and analysis

### 7.1 Dry contact

The effect of dry contact on wear performance of wheel and rail steels was investigated under different contact conditions. The coefficient of friction and wheel disc temperature were obtained for each test under dry contact to see how both are affected by slip ratio and contact load when AAR class B wheels were run against the softer R260 and harder R350HT rail steels. Thereafter, the surface morphology, roughness and deformation depth of worn specimen were analysed. The three wear regimes being mild, severe and catastrophic wear were identified based on the results.

#### 7.1.1 Coefficient of friction

Figure 7.1 and Figure 7.2 show the coefficient of friction as a function of number of rolling cycles. As may be seen, the coefficient of friction increased sharply at the beginning of the test before reaching steady. Some tests took longer to reach the steady state compared to others due to differences in contact conditions. Several studies [21, 28, 73, 74, 75, 144] have shown that friction plays an important role in wear and RCF at the wheel-rail contact. Low coefficient of friction at the wheel-rail contact may result in low adhesion causing braking problems by increasing the braking distance which may cause the train to overrun whereas high coefficient of friction may cause accelerated wear. Figure 7.3 shows the average coefficient of friction as a function of the slip ratio. It is evident that the coefficient of friction increased with slip ratio for all loads, with more increase being observed at lower loads. The decrease in coefficient of friction with load was also observed in other studies on twin-disc setup [122, 278, 279]. This is attributed to wear debris sticking together easily at lower loads increasing the surface roughness of the wheel and rail steels resulting in an increase in the coefficient of friction, whereas at higher loads, wear debris are easily worn away. It can also be seen in Figure 7.1 and Figure 7.2 that the coefficient of friction reached values close to 1 at 20 and 27% slip ratios, this can be attributed to the change in wear mechanisms from mild to severe and catastrophic as evident in Figure 7.6 and Figure 7.7 where severe surface damage was observed at 20 and 27% slip ratio. Also, coefficient of friction increase could be attributed to an increase in the surface roughness values, Figure 7.8 and Figure 7.9 i.e., the rougher the surface the higher the coefficient of friction, which is discussed further in section 7.1.3.

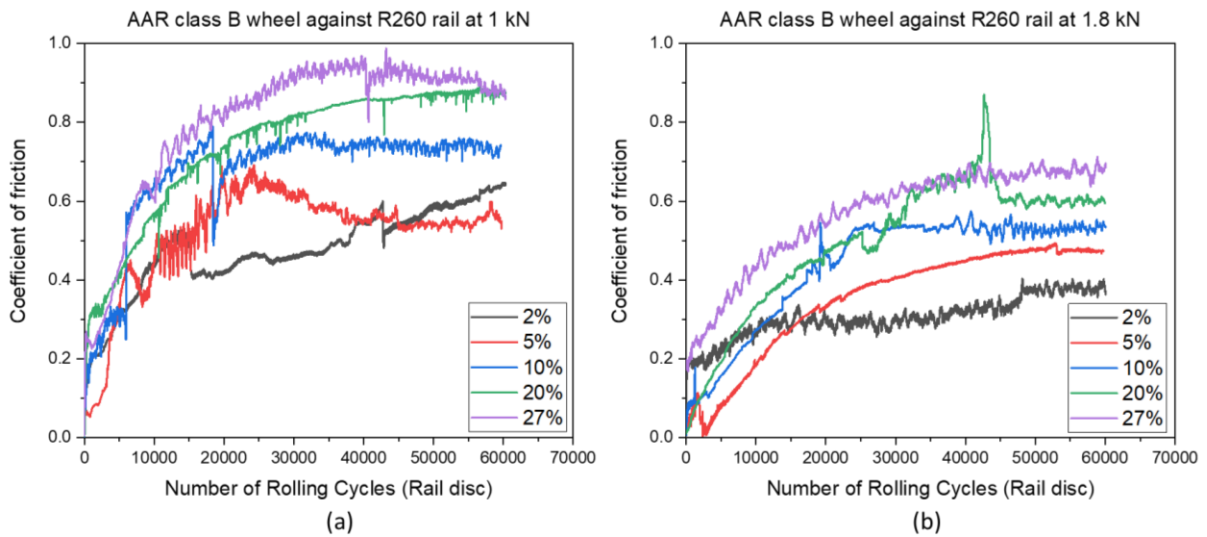


Figure 7.1: Coefficient of friction as a function of the number of rolling cycles at different slip ratios; the wheel rolling and sliding against R260 rail under an applied load of (a) 1 kN and (b) 1.8 kN.

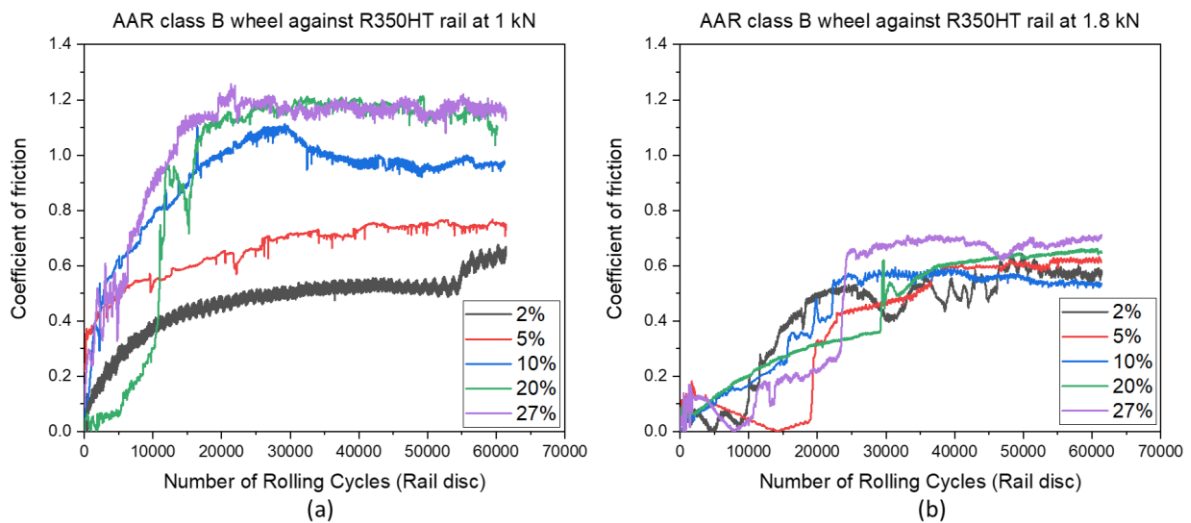


Figure 7.2: Coefficient of friction as a function of the number of rolling cycles at different slip ratios; the wheel rolling and sliding against R350HT rail under an applied load of (a) 1 kN and (b) 1.8 kN.

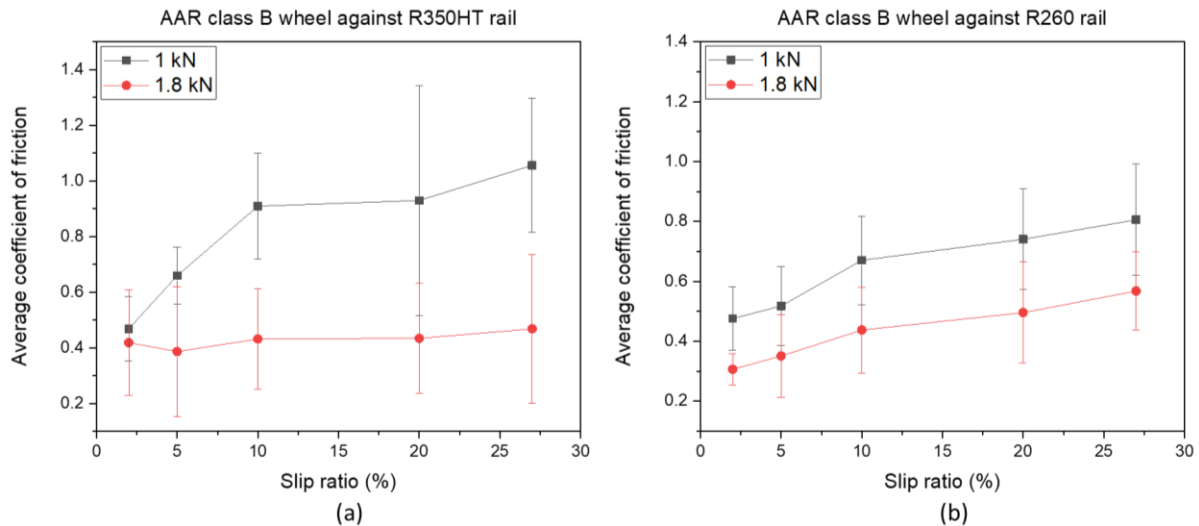


Figure 7.3: Average coefficient of friction as a function of slip ratio of the wheel when run against (a) R350HT and (b) R260 rails under applied loads of 1 kN and 1.8 kN for 62 000 rolling cycles.

### 7.1.2 Mass loss, wear rate and wear index

Figure 7.4 shows the mass loss of AAR Class B wheel, R350HT rail and R260 rail discs as a function of slip ratio under contact loads of 1 and 1.8 kN respectively. The AAR class B wheels were found to perform better against the softer R260 rails with low wear rates at all slip ratios and loads, Figure 7.4b. On the contrary, they performed relatively poorly when run against the harder R350HT rail, Figure 7.4a. In other words, AAR class B wheels were substantially harder than R260 rails and softer than R350HT rails. Literature [86, 102, 204, 241, 280] show that harder steels perform better than softer steels. The hardness of pearlitic steels is inversely related to the pearlite interlamellar spacing and, therefore, it is not a surprise that steels with finer pearlite interlamellar spacing (PIS) exhibited lower wear rates. In other words, the AAR class B wheel, with average PIS equal to 270 nm, performed better against R260 than R350HT rail with average PISs of 341 and 112 nm respectively. The mass loss was also found to increase with slip ratio and applied load for both wheel and rail steels except at 5% slip ratios under an applied load of 1.8 kN when AAR class B wheels were run against R260 rail and at 1 kN where AAR class B wheels were run against R350HT rail respectively. The increase in mass loss with slip ratio was also confirmed by other studies [23, 213, 281, 282].

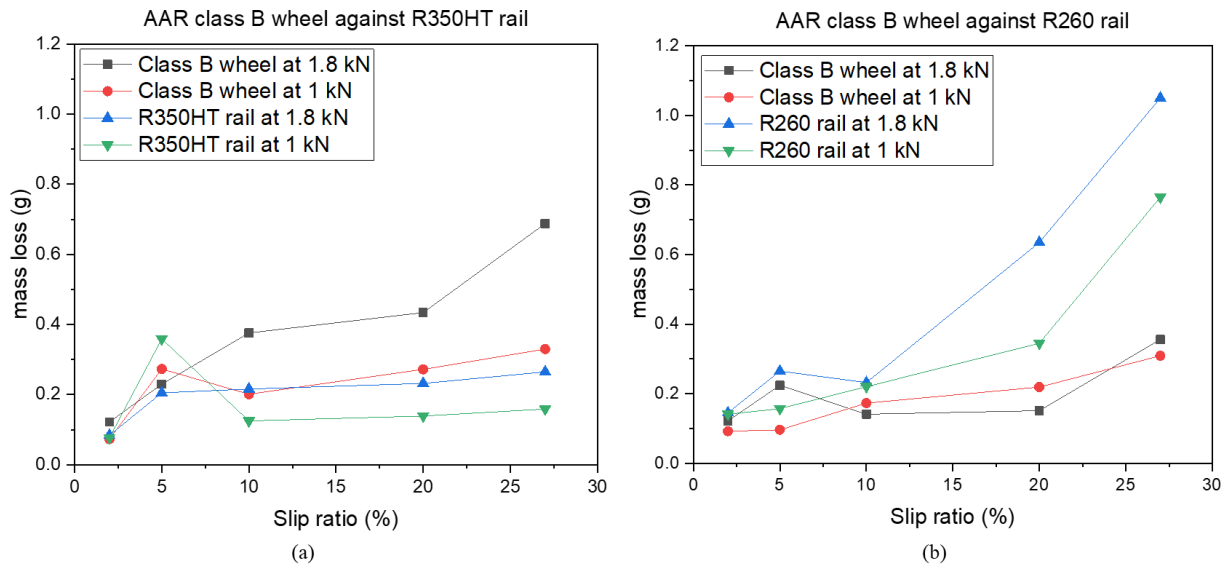


Figure 7.4: Mass loss of the wheel when run against (a) R350HT rail discs and (b) R260 rail as a function of slip ratio under different contact loads of 1 kN and 1.8 kN for 62 000 rolling cycles.

The plotting of wear rate against  $T\gamma/A$  approach was used to define wear regimes first by Bolton and Clayton [244] in 1984. Several studies [122, 212, 283] have used the same model to identify the three wear regimes being mild, severe and catastrophic. A similar trend was observed with the highest values of  $T\gamma/A$  seen at 27% slip ratio under an applied load of 1.8 kN when AAR class B wheel were run against R260 and R350HT rail, Figure 7.5b. However, when AAR class B wheels were run against the harder R350HT rail, only mild wear was seen, Figure 7.5a. The wear regimes were identified using plot of wear rates as a function of wear indexes being grouped according to the wear coefficient values ( $K$ ) which correspond to the gradient defined using equation 4.1. The AAR class B wheels showed lower wear rates across all slip ratios at both applied loads of 1 and 1.8 kN when run against R260 rail compared to when run against R350HT. At 1.8 kN and 27% slip ratio, AAR class B wheels had a wear rate of  $14 \mu\text{g}/\text{m}/\text{mm}^2$  when run against R260 rail compared to  $27 \mu\text{g}/\text{m}/\text{mm}^2$  when run against R350HT rail. As found using SEM fractography, increasing the slip ratio transformed the wear mechanisms from mild oxidation wear to severe fatigue and spalling which causes RCF, which was also observed in a study by Ma et al. [212]. Figure 7.6 and Figure 7.7 show pitting, delamination and breakouts formations at the higher slip ratios.



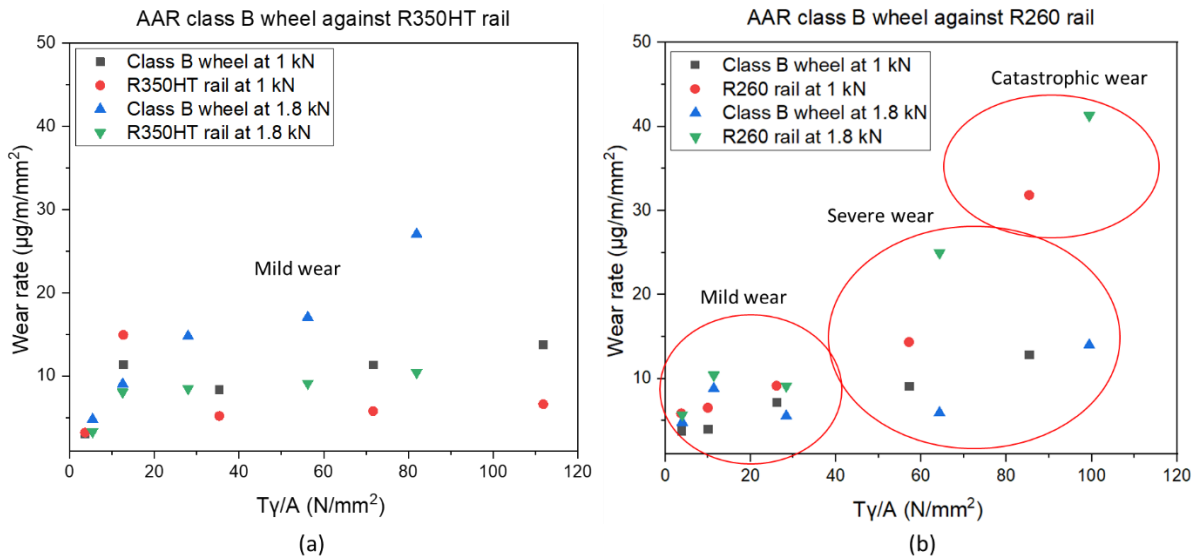


Figure 7.5: Plots of wear rates (for wheel and rail discs) as a function of wear indexes ( $T\gamma/A$ ); AAR Class B wheel versus (a) R350HT rail and (b) R260 rail at applied loads of 1 kN and 1.8 kN and 62 000 rolling cycles.

### 7.1.3 Surface morphology, roughness and topography

The SEM was used to observe the worn surface morphology and topography to study the damages. It was observed that the severity of wear increases with both slip ratio and load. At lower slip ratios (2% and 5%), wear was mainly due to abrasive wear and oxidative wear. At higher slip ratios (10%, 20% and 27%) there was evidence of severe and catastrophic wear due to delamination, pitting and formation of breakouts (craters), Figure 7.6 and Figure 7.7. This was also confirmed by the presence of crack branching in AAR Class B wheel at 27% slip ratio, in Figure 7.19 and Figure 7.20. Previous studies [23, 212, 213] have also confirmed that the presence of delamination, pitting and breakouts indicate severe and catastrophic wear. At 1.8 kN, more delamination and fatigue (pitting and breakouts) were observed indicating that the severity of wear also increases with applied load, Figure 7.6.



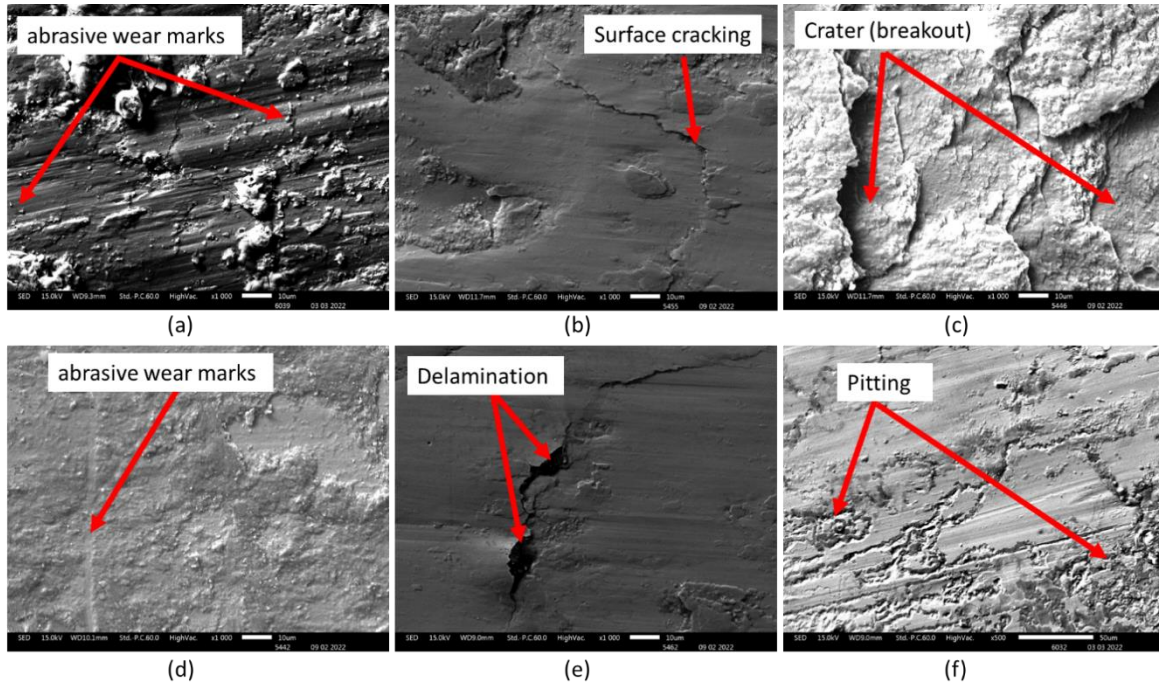


Figure 7.6: SEM micrographs of AAR class B wheel surfaces (a) 2%, (b) 10% and (c) 27% slip ratios; R350HT rail surfaces (d) at 2%, (e) 10% and (f) 27% slip ratios under an applied load of **1.8 kN** and 62 000 rolling cycles.

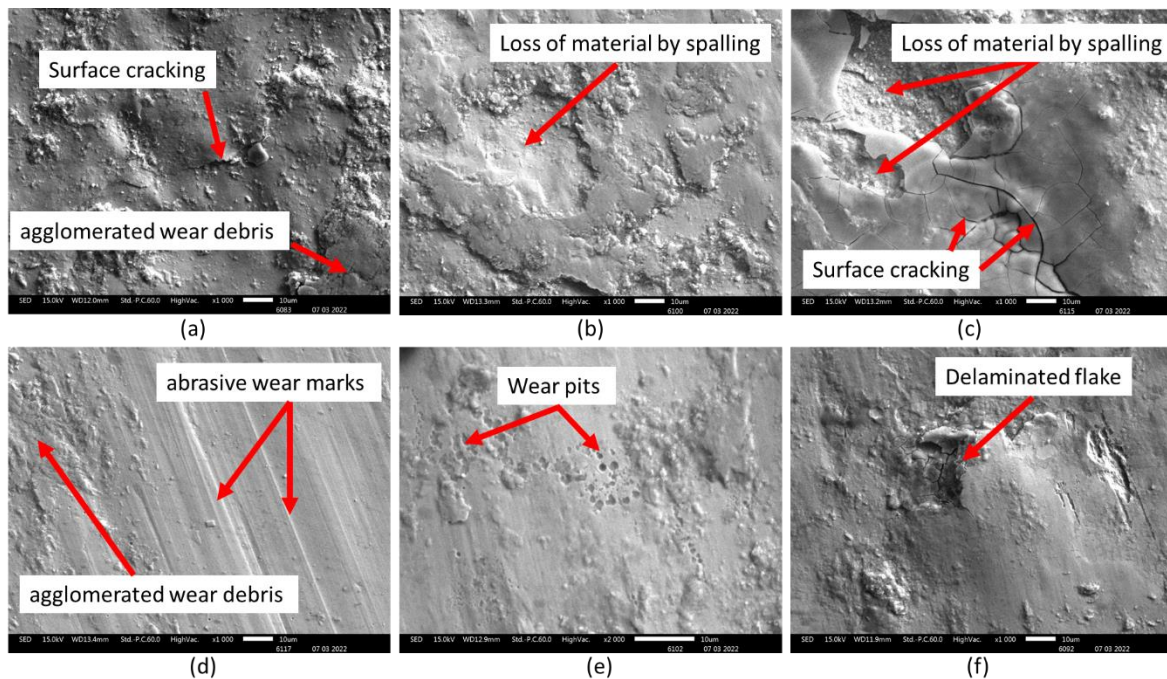


Figure 7.7: SEM micrographs of AAR class B wheel surfaces (a) 2%, (b) 10% and (c) 27% slip ratios; R350HT rail surfaces (d) at 2%, (e) 10% and (f) 27% slip ratios under an applied load of **1 kN** and 62 000 rolling cycles.

As expected, the surface roughness, Ra value ( $\mu\text{m}$ ) increased with slip ratio across all applied loads when the AAR class B wheel was run against both R350HT and R260 rails, Figure 7.8 and Figure 7.9. The coefficient of friction also increased with the Ra value i.e., the rougher the surface the higher the coefficient of friction. The increase in coefficient of friction with surface roughness is because of an increase in fraction of solid-to-solid micro-contacts within the nominal contact area, producing larger variations in the contact area. Both surface roughness and coefficient of friction increased with slip ratio. The same observation was also found in a study by Chen et al. [284]. The only exceptions were at 5% and 10% slip ratios under applied loads of 1 kN and 1.8 kN respectively, where there was a sudden drop in roughness values for both R260 rail and AAR class B wheel. Both R260 rail and AAR class B wheel had lower Ra values than AAR class B wheel across all slip ratios and loads after wear test. This could be attributed to the wheel being the driving disc and moving faster whereas the rails were the braking ones affecting the formation of the wear debris and damage mechanisms hence roughness. Literature [19] has shown that driving mode of the disc influence the wear and damage mechanisms of wheel and rail. The Ra value also decreased with increase in load across all slip ratios, Figure 7.8 and Figure 7.9. The decrease in Ra value with increase in load might explain why the average coefficient of friction also decreased with an increase in applied load, Figure 7.3.

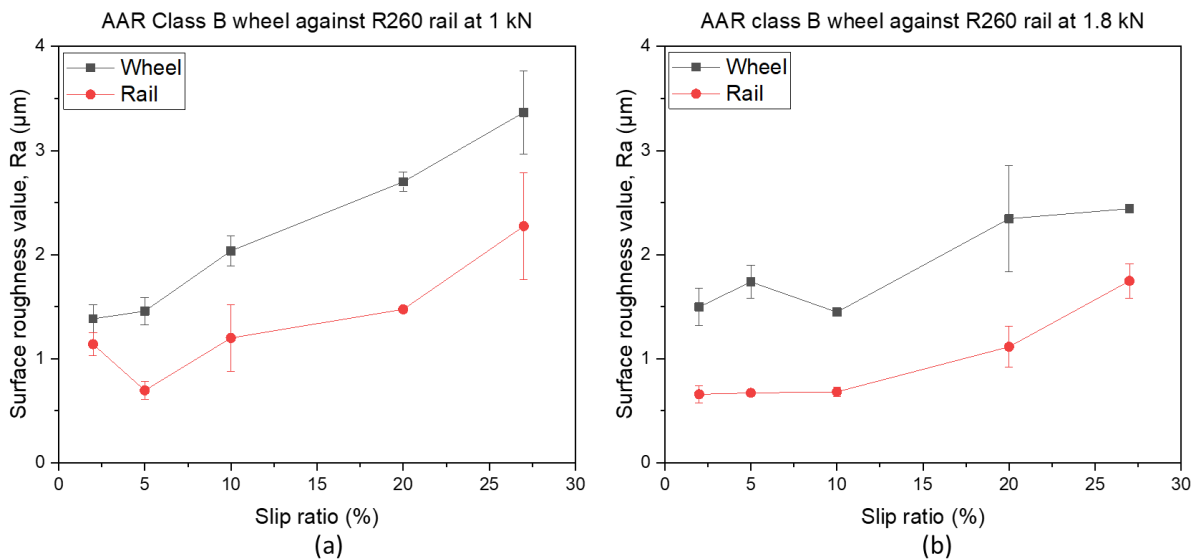


Figure 7.8: The arithmetic mean of roughness value (Ra) of wheel and R260 rail at applied loads of (a) 1 kN and (b) 1.8 kN and 62 000 rolling cycles.

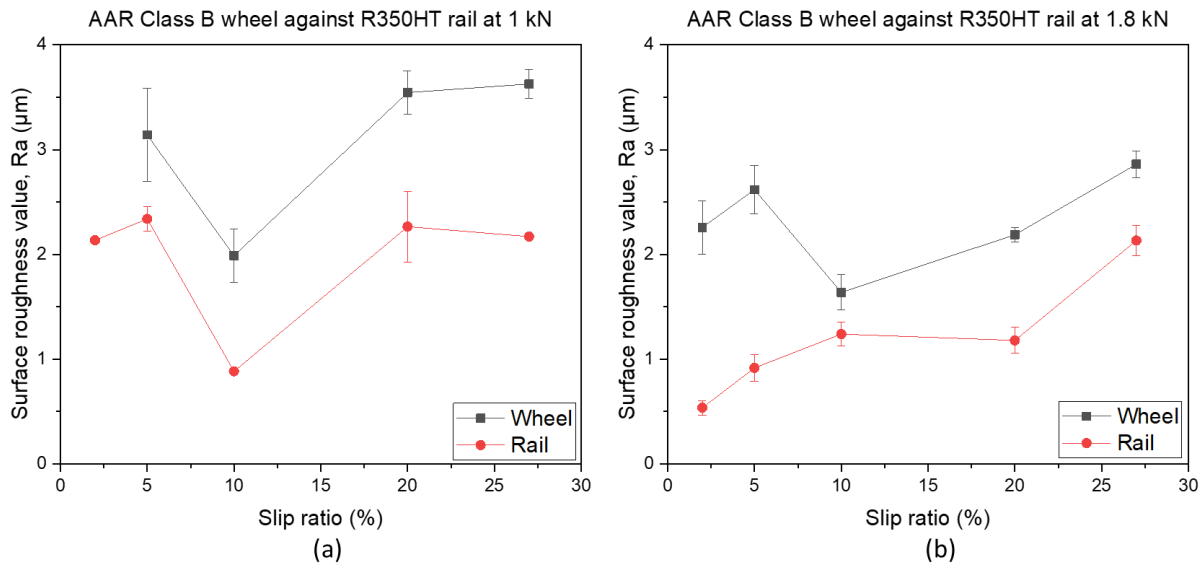


Figure 7.9: The arithmetic mean of roughness value (Ra) of wheel and R350HT rail at applied loads of (a) 1 kN and (b) 1.8 kN and 62 000 rolling cycles.

#### 7.1.4 Plastic deformation and sub-surface damage

Figure 7.11, Figure 7.12, Figure 7.13 and Figure 7.14 are optical micrographs showing sub-surface work hardening due to plastic deformation in both wheel and rail steels. The plots of sub-surface hardness as a function of depth are shown in Figure 7.15, Figure 7.16, Figure 7.17 and Figure 7.18. Higher hardness values were observed in wheel compared to R350HT rail specimens as the as-received wheel was softer than the R350HT i.e., 348 versus 372 HV10 respectively. On the other hand, the AAR Class B wheel specimens were found to perform better against R260 rail specimens as the depth of plastic deformation was less compared to the R260 rails as seen in Figure 7.14. This is so because the AAR class B wheel specimens had a higher as-received hardness of 348 HV10 compared to R260 rails of 298 HV10. The same can be said with interlamellar spacing as AAR class B wheel specimens had larger interlamellar spacing compared to R350HT rail steels and finer interlamellar spacing compared to R260 rails hence having the effect on plastic deformation depth as observed on Figure 7.12 and Figure 7.14. From both wheel and rail, plastic deformation depth was found to be dependent on slip ratio and load, i.e., the depth of plastic deformation increased with both slip ratio and load, Figure 7.10, as expected, this was due to the increased stresses on the wheel-rail contact. The sub-surface hardness also increased, Figure 7.16. This agrees with [275] who found that increasing the slip ratio increases the coefficient of friction as well as the surface hardness of wheel and rail after wear testing using the twin disc setup. This increase in surface hardness would be caused by an increase in dislocation density resulting in high rate of work hardening.



Another study by Seo et al. [275] confirmed that surface hardness of wheel/rail increases with slip ratio after testing on twin-disc setup.

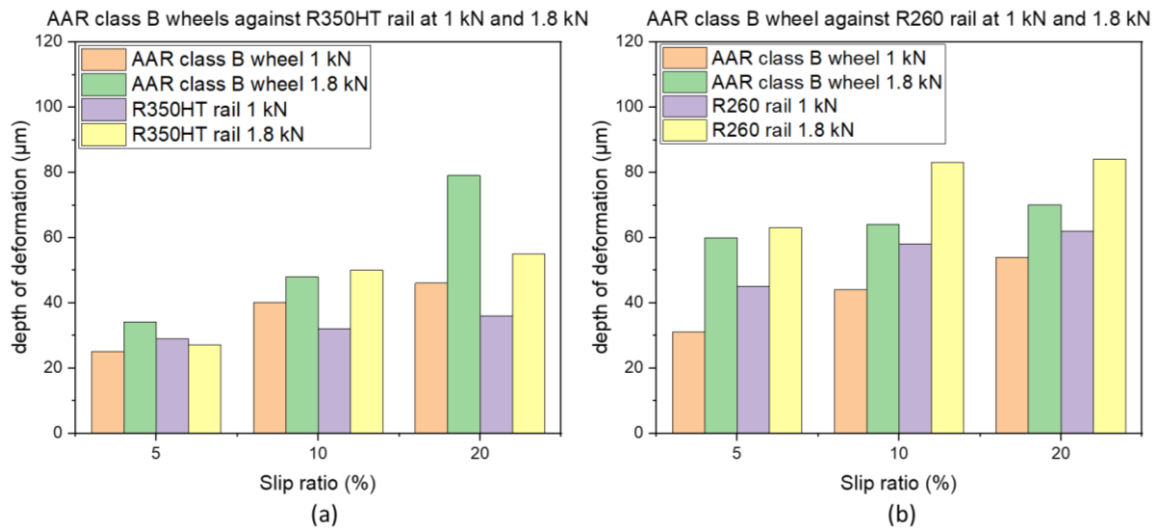


Figure 7.10: Depth of deformation as a function of slip ratio at applied loads of 1 kN and 1.8 kN when the wheel was run against (a) R350HT rail and (b) R260 rail under dry conditions for 62 000 rolling cycles.

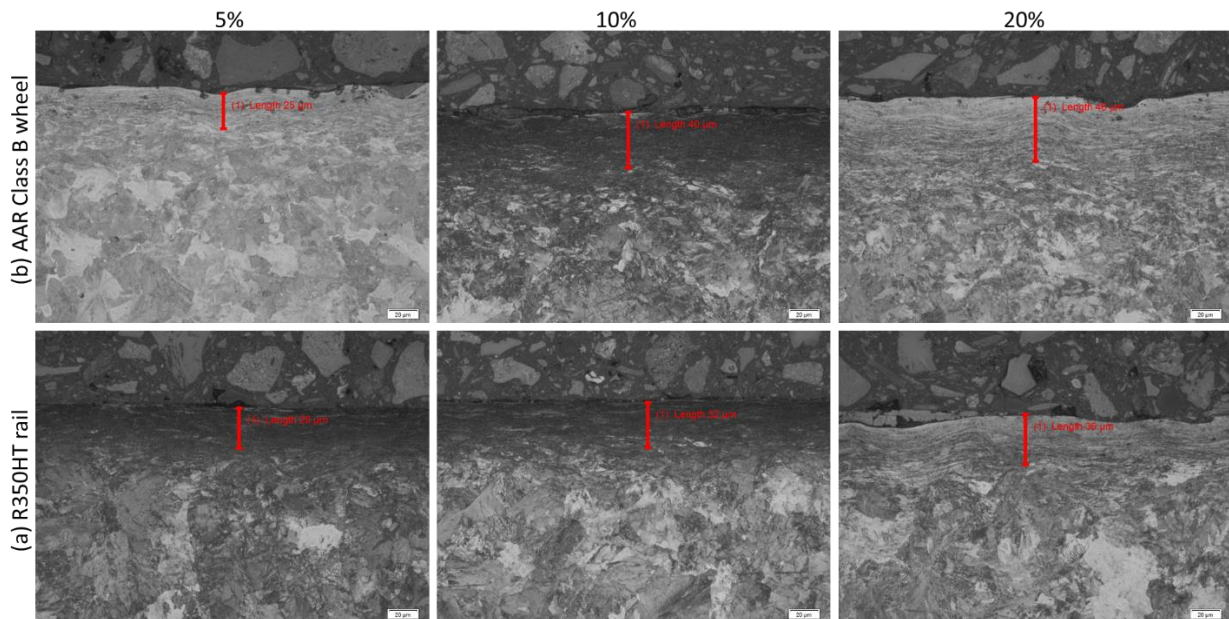


Figure 7.11: OM micrographs of sub-surface layer (a) R350HT rail and (b) wheel showing the plastically deformed region at 5, 10 and 20% slip ratios, 1 kN load and 62 000 rolling cycles.

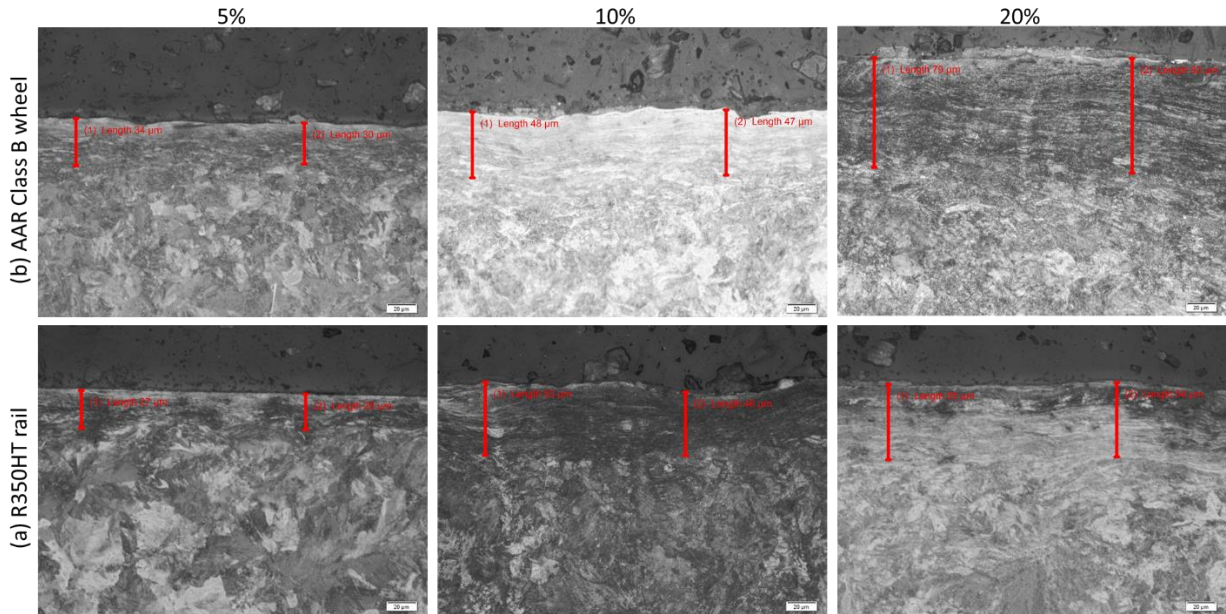


Figure 7.12: OM micrographs of sub-surface layer (a) R350HT rail and (b) wheel showing the plastically deformed region at 5, 10 and 20% slip ratios, 1.8 kN load and 62 000 rolling cycles.

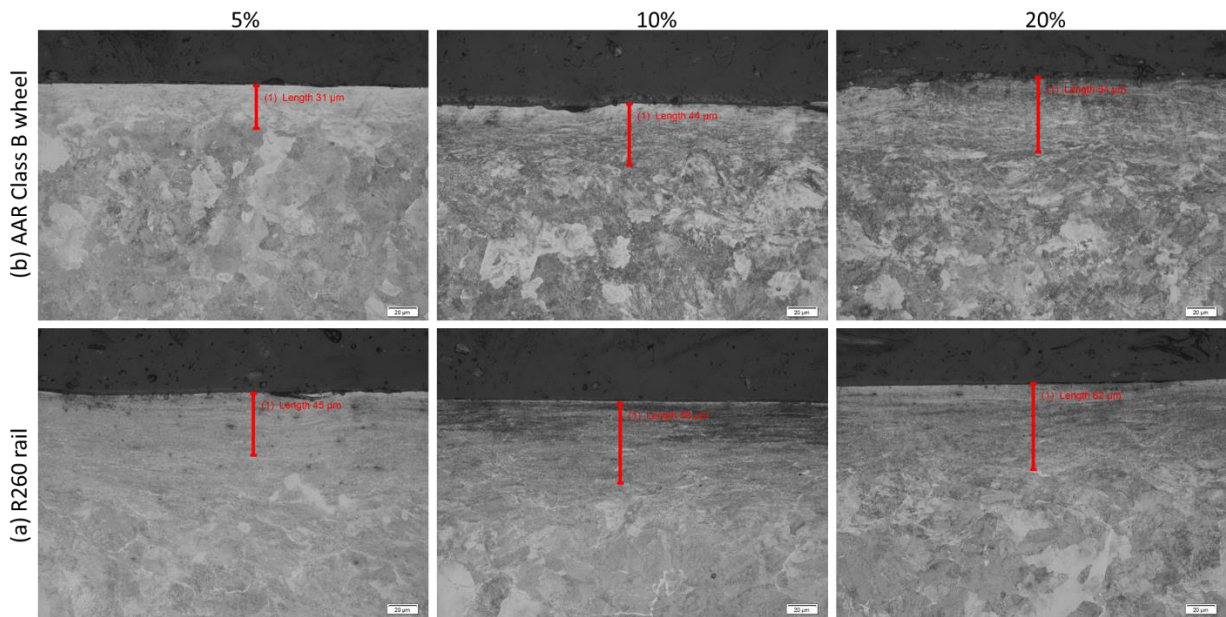


Figure 7.13: OM micrographs of sub-surface layer (a) R260 rail and (b) wheel showing the plastically deformed region at 5, 10 and 20% slip ratios, 1 kN load and 62 000 rolling cycles.

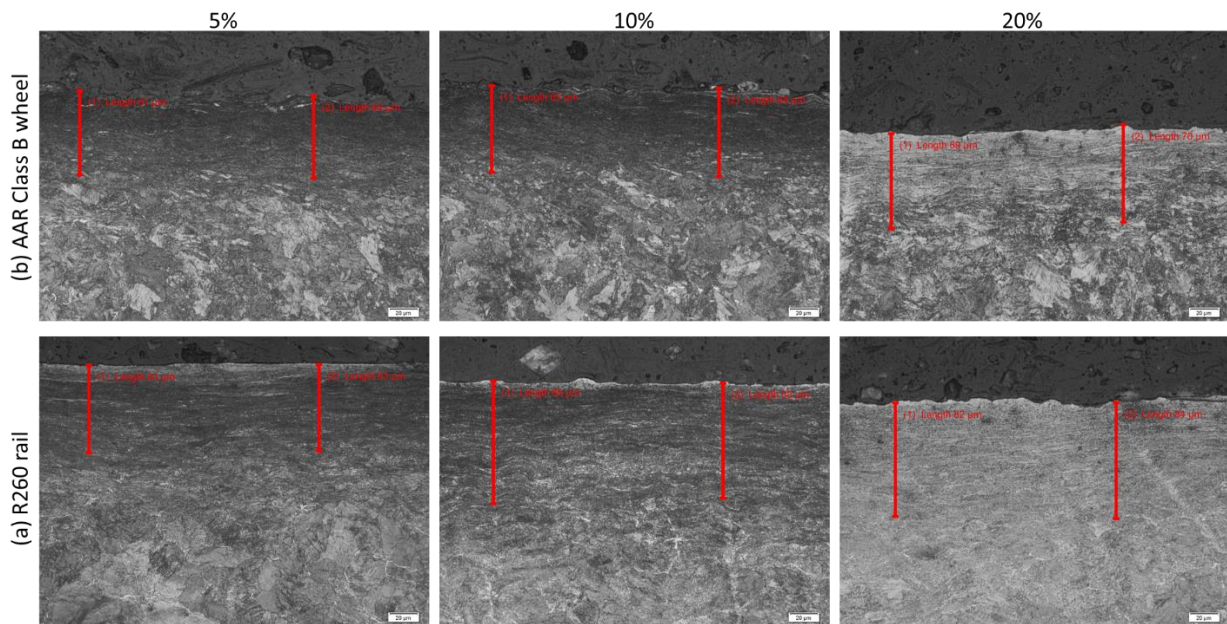


Figure 7.14: OM micrographs of sub-surface layer (a) R260 rail and (b) wheel showing the plastically deformed region at 5, 10 and 20% slip ratios, 1.8 kN load and 62 000 rolling cycles.

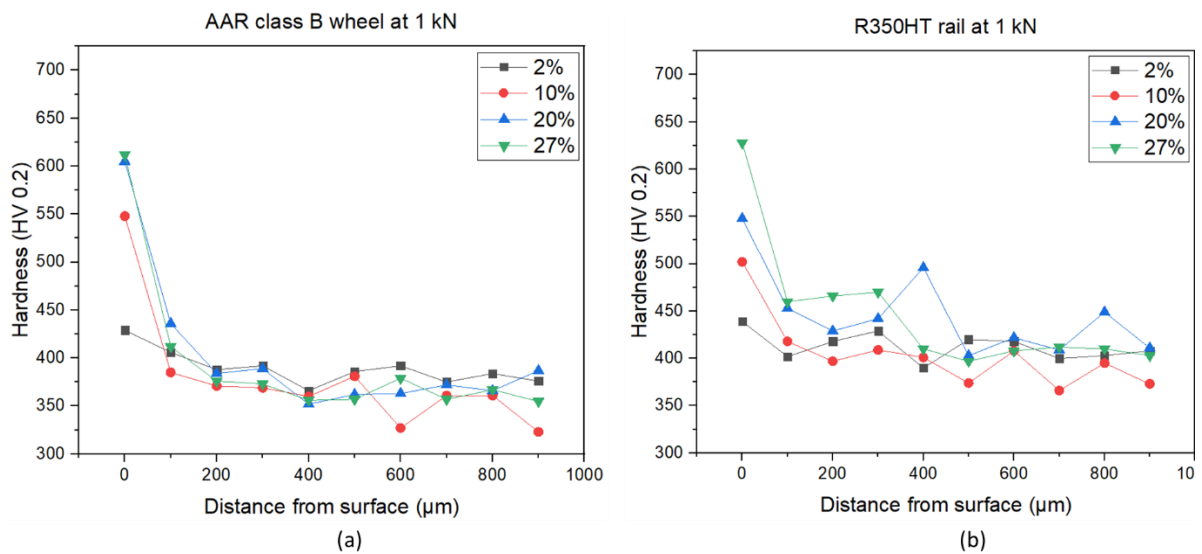


Figure 7.15: Micro hardness (HV0.2) variation with depth at different slip ratios; (a) wheel and (b) R350HT at 1 kN and 62 000 rolling cycles confirming that work hardening occurred at the contact surface and sub-surface.



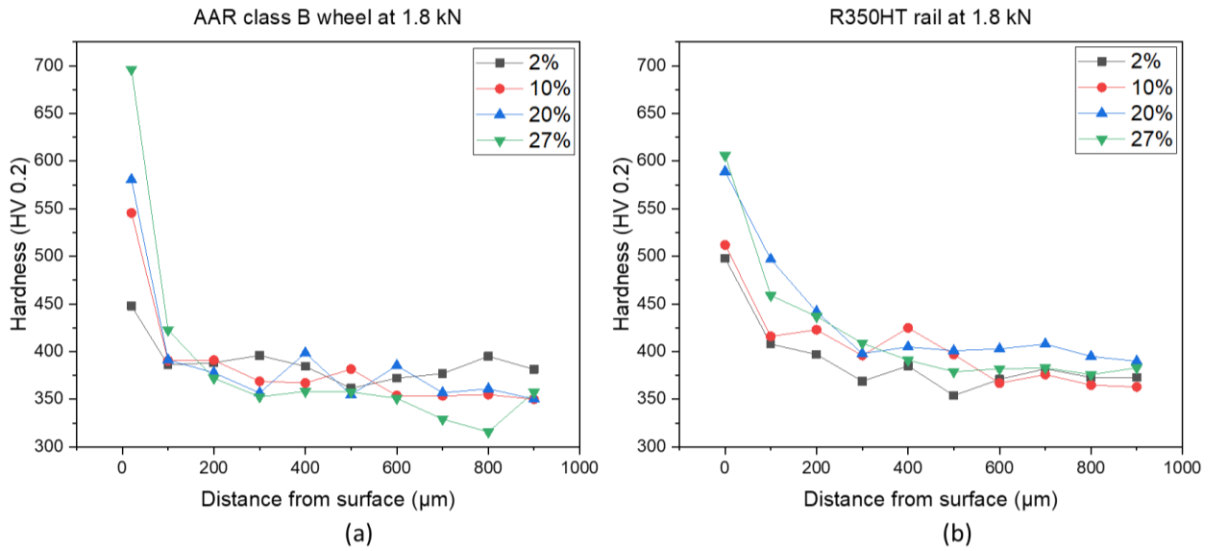


Figure 7.16: Micro hardness (HV0.2) variation with depth at different slip ratios; (a) wheel and (b) R350HT at 1.8 kN and 62 000 rolling cycles confirming that work hardening occurred at the contact surface and sub-surface.

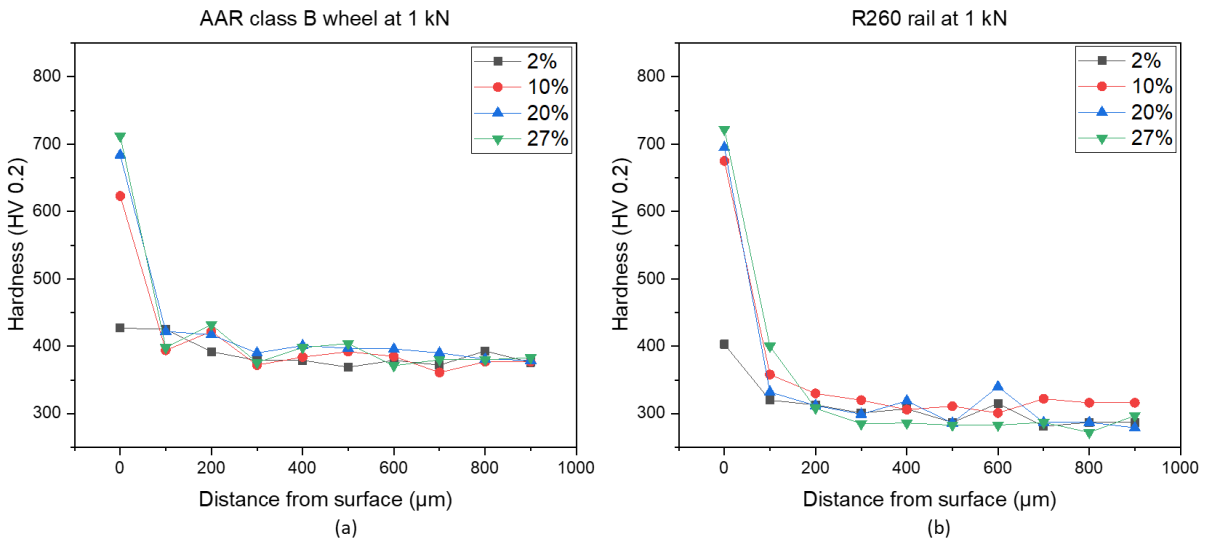


Figure 7.17: Micro hardness (HV0.2) variation with depth at different slip ratios; (a) wheel and (b) R260 at 1 kN and 62 000 rolling cycles confirming that work hardening occurred at the contact surface and sub-surface.



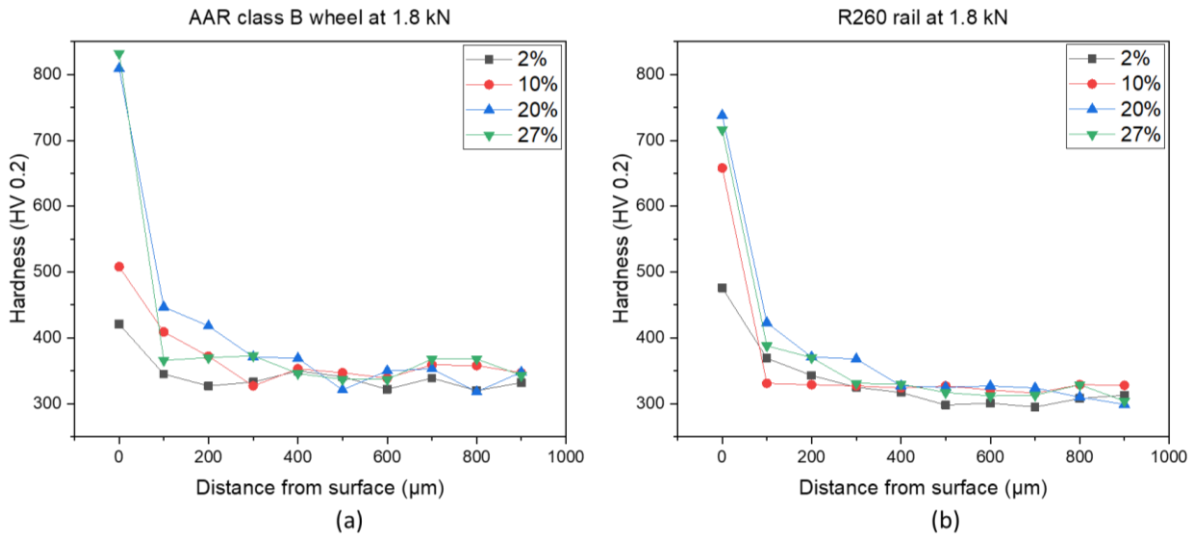


Figure 7.18: Micro hardness (HV0.2) variation with depth at different slip ratios; (a) wheel and (b) R260 at 1.8 kN and 62 000 rolling cycles confirming that work hardening occurred at the contact surface and sub-surface.

The RCF was observed only at higher slip ratios with evidence of sub-surface cracks and crack branching on both wheel and rail, Figure 7.19, Figure 7.20, Figure 7.21 and Figure 7.22. Crack branching is evidence of crack growth and propagation, which decreases the RCF life, which lead to catastrophic failure. The RCF was found to be a function of slip ratio as it increased with slip ratio in agreement with literature [23, 285]. Seo et al. [213] also found that increasing the slip ratio resulted in plastic flow and appearance of fine sub-surface cracks. The wheel performed better against the R260 rail in terms of RCF as less sub-surface cracks were observed compared to R350HT. Literature has demonstrated that [157, 286, 287] RCF cracks are mainly initiated at the mostly strained ferrite phase and tends to propagate along the grain boundaries by cavitation. This may lead to severe and/or catastrophic wear and growth of RCF cracks which may cause failure to occur at the wheel/rail contact.

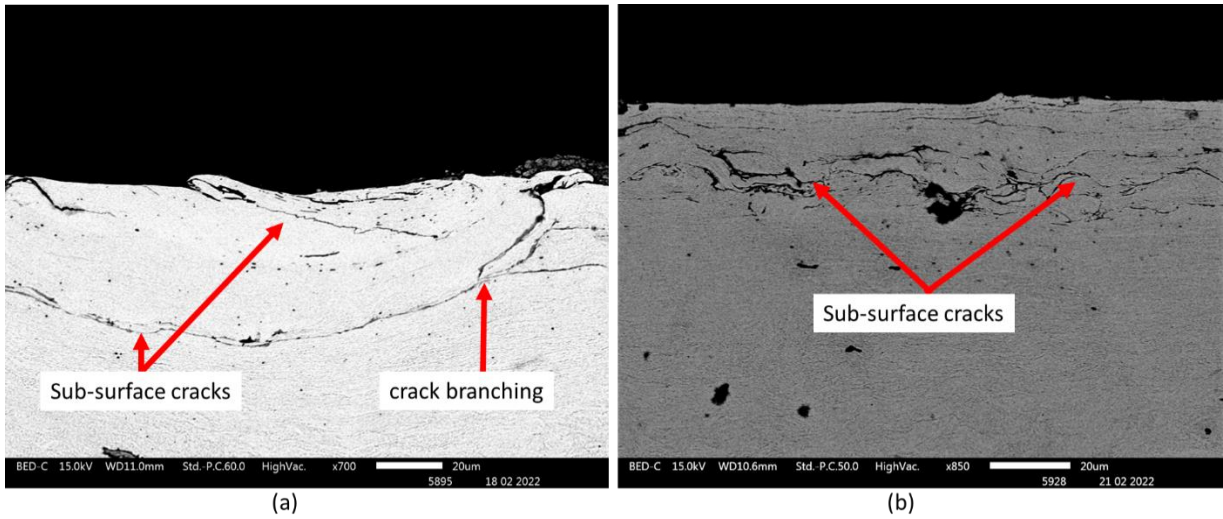


Figure 7.19: SEM micrographs of (a) the wheel specimen and (b) R350HT rail showing sub-surface crack and crack branching at 27% slip ratio, 1.8 kN and 62 000 rolling cycles.

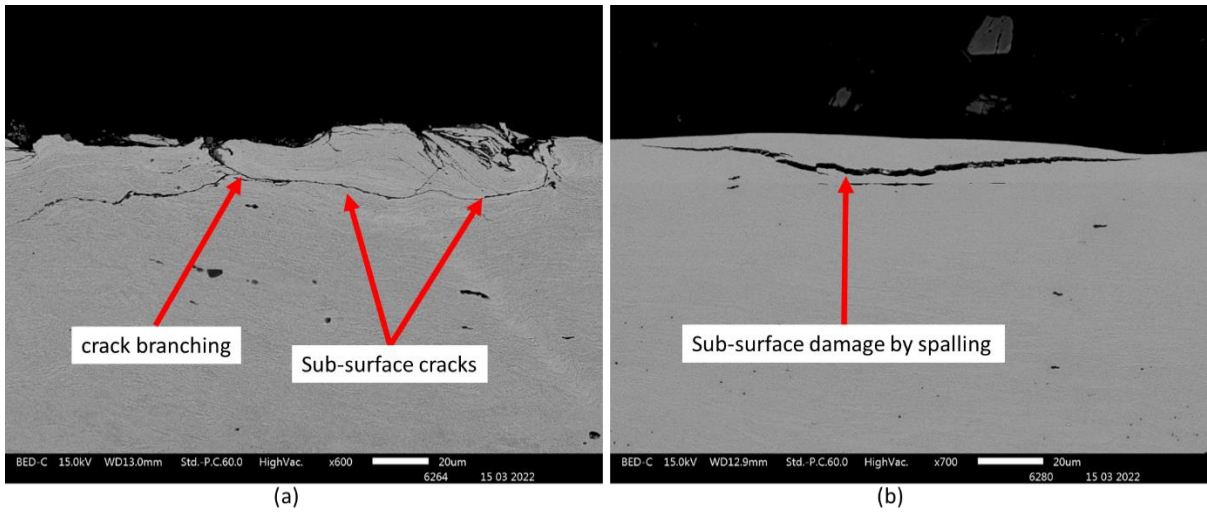


Figure 7.20: SEM micrographs of (a) the wheel and (b) R260 rail showing sub-surface cracks and crack branching at 27% slip ratio, 1.8 kN and 62 000 rolling cycles.

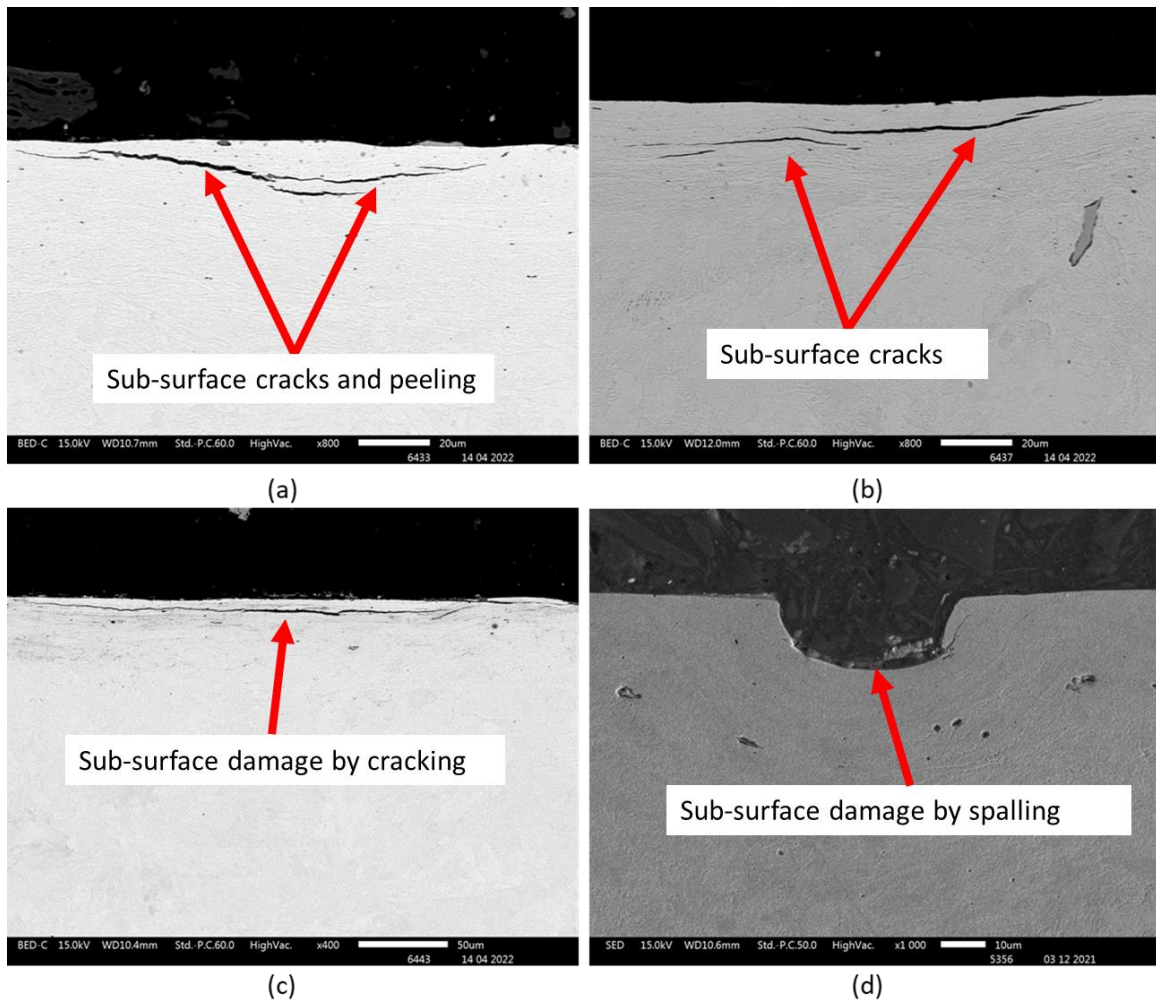


Figure 7.21: R350HT rail after testing at 1 kN (a) 2%, (b) 5% (c) 10% and (d) 20% slip ratios showing sub-surface damage and cracking.

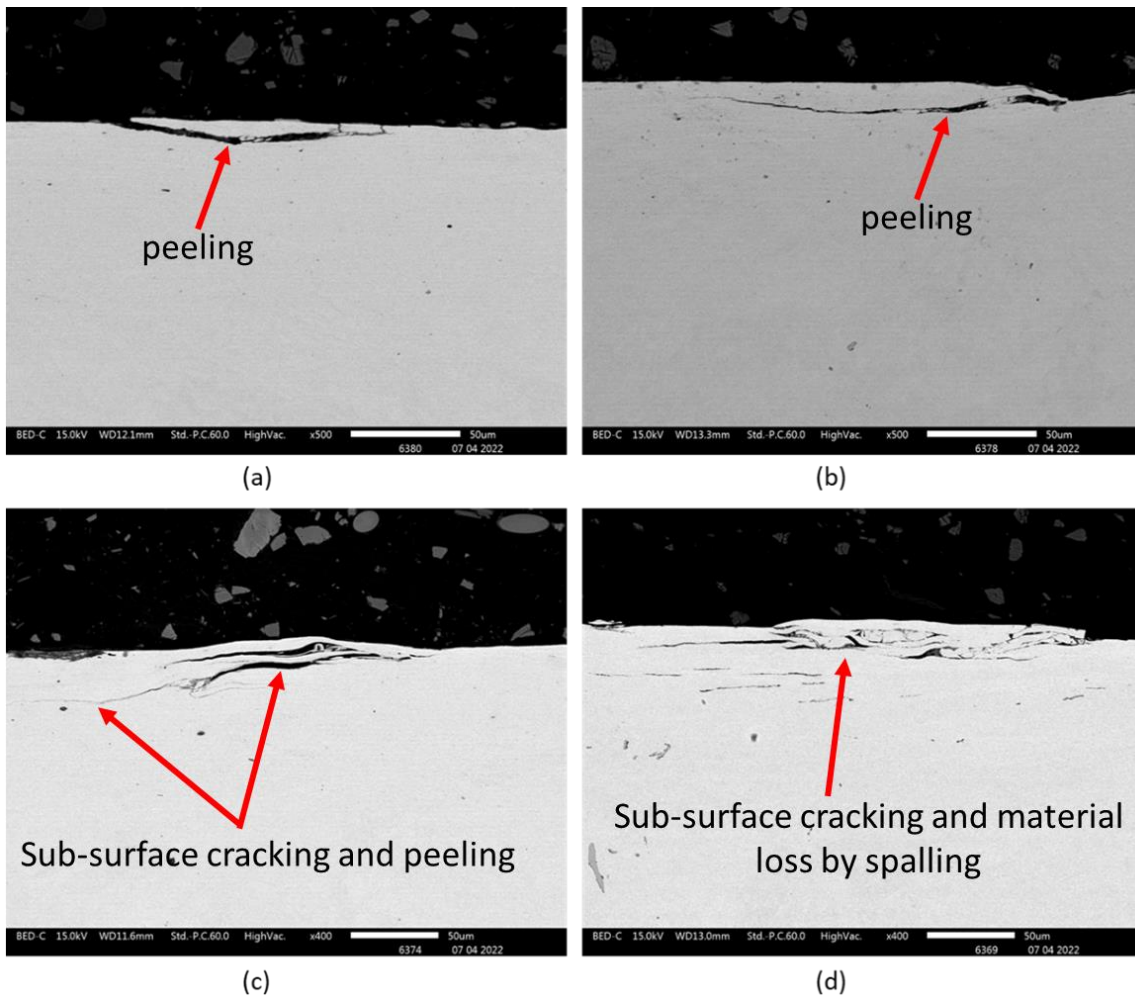


Figure 7.22: The wheel after testing at 1 kN against R260 rail (a) 5%, (b) 10%, (c) 20% and (d) 27% slip ratio showing sub-surface damage and cracking.

### 7.1.5 Wheel disc temperature

Figure 7.23 shows the maximum wheel disc temperature as a function of slip ratio. As expected, the temperature increased with both slip ratio and applied load due to increase frictional heat. The highest maximum wheel disc temperature of 117 °C was observed when the wheel was run against R350HT rail at 27% slip ratio under the load of 1.8 kN. Some workers [184, 185] observed some phase transformation such as transformation of austenite to martensite because of the increase in in temperature which can indirectly adversely affect the wheel and rail performance since both wear and RCF are affected by both hardness and yield strength, [84, 102, 204]. However, in this work, the temperature was too low for phase transformations to take place.

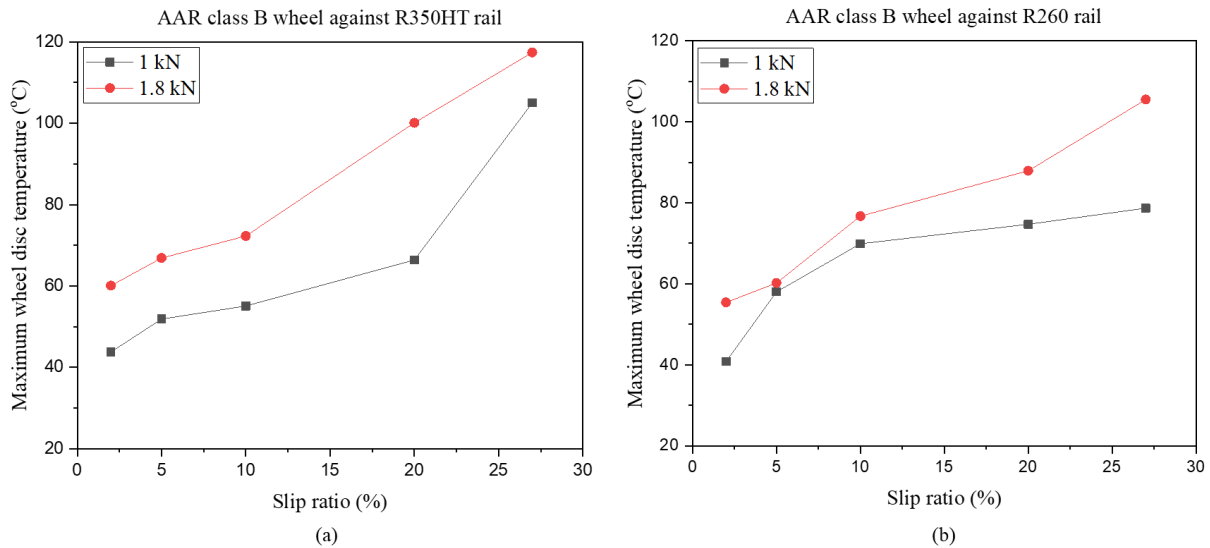


Figure 7.23: Maximum wheel disc temperature as a function of slip ratio at 1 and 1.8 kN for 62000 rolling cycles under dry conditions for the wheel versus (a) R350HT and (b) R260 rail.

## 7.2 Lubricated contact (oil and water)

The effect lubrication has on the wear performance of wheel and rail steels was investigated by introducing oil and water at the wheel/rail contact at different slip ratios. The results were obtained and compared to dry contact using coefficient of friction, mass loss (wear rates), depth of deformation, sub-surface damage, wheel disc temperature, surface damage and roughness. Results show that lubricating the wheel/rail contact reduces wear significant with oil showing the least wear. Under water contact there more RCF crack with some evidence of fluid crack pressurisation.

### 7.2.1 Effects of lubrication on coefficient of friction and wear rate

Water and oil reduced the coefficient of friction significantly compared to dry contact, Figure 7.24a and Figure 7.24b at 10 and 20% slip ratios respectively. This effect is as a result of the low traction due to the presence of water and oil molecules which provided some form of lubrication. Oil caused more reduction in coefficient of friction than water as it is more viscous than water. The results agree with literature [76, 118, 210, 214, 288] as dry contact leads to high coefficient of friction, which is bad for wear but good for adhesion at the wheel-rail interface. At lower slip ratios of 2, 5 and 10% oil did not reach the steady state at the end of the test (62 000 cycles) while at 20% slip ratio, the steady state was reached. This could be attributed to the wear debris being embedded into the contacting surface, affecting the coefficient of friction at lower slip ratio whereas at 20% slip ratio, the higher slip was able to prevent that embedment. However, both dry and water contacts reached the steady state across



all slip ratios. Oil and water had lower coefficient of friction values, which resulted in lower wear rates (cumulative mass loss) compared to dry contact, Figure 7.25b. However, low coefficient of friction leads to poor adhesion at the contact. Poor adhesion is a cause for concern as it may affect performance and safety of the train causing longer braking distance which can result in platform overruns and collisions between trains. For all the three contact conditions (dry, water and oil) cumulative mass loss was found to increase with slip ratio with the highest increase being under dry contact. Therefore, lubrication either due to water or oil significantly reduced wear and the trend is in agreement with previous studies [76, 214].

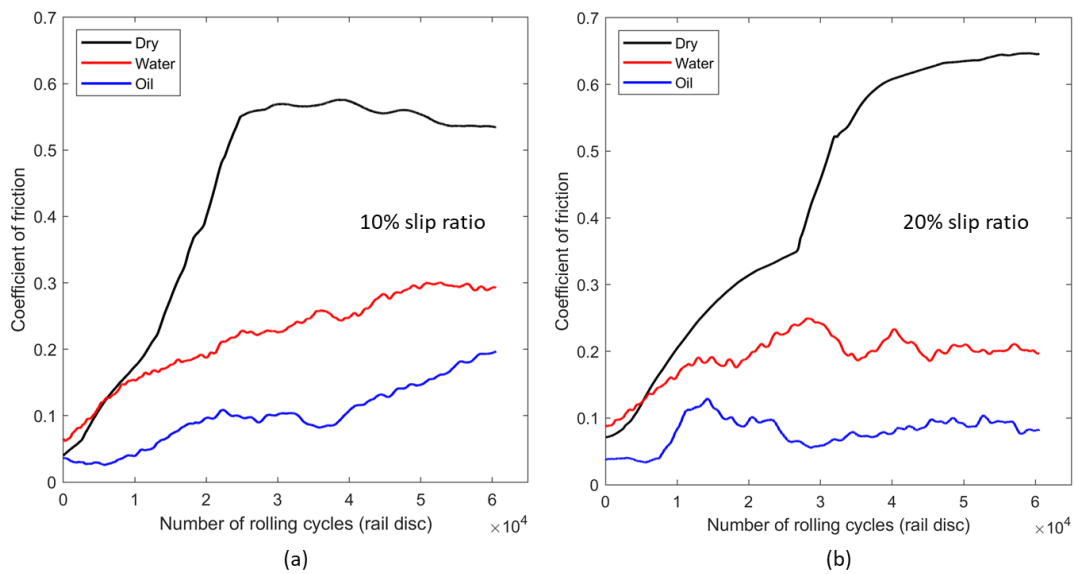


Figure 7.24: (a) Coefficient of friction versus number of rolling cycles at (a) 10% and (b) 20% slip ratios under dry, water and oil contact conditions.

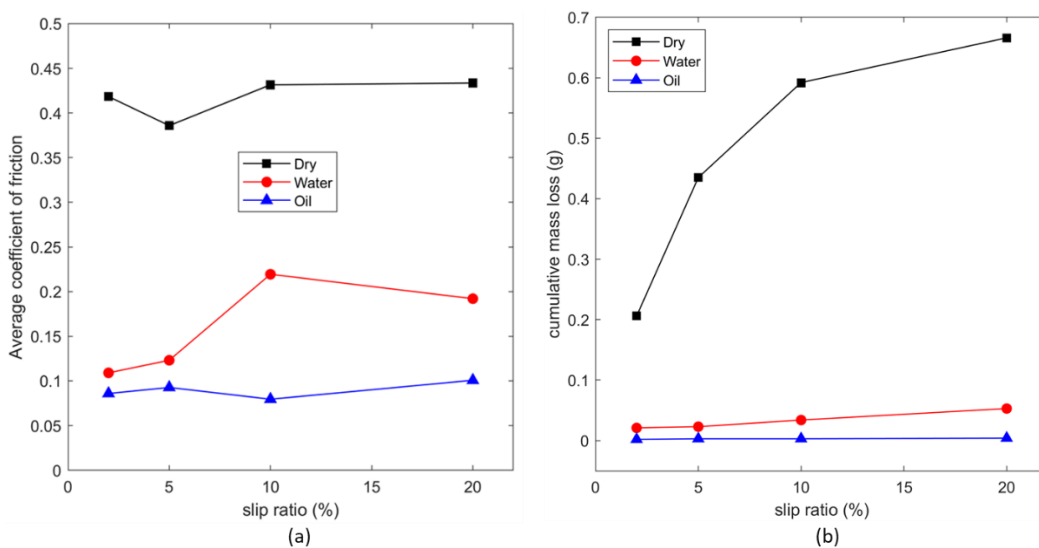


Figure 7.25: (a) Average coefficient of friction versus slip ratio; (b) Cumulative mass loss (wheel + rail) versus slip ratio under dry, water and oil contact conditions



### ***7.2.2 Effects of lubrication on surface morphologies and roughness***

There was no evidence of surface damage by fatigue, delamination, or material loss by spalling when testing under both water and oil compared to dry testing where surface fatigue and cracking, delamination and material loss by spalling were observed on wheel and rail, Figure 7.26 and Figure 7.27. When lubrication was used, wear was mainly by abrasion as evident from abrasive wear marks and smoother surface which are an indication of mild wear whereas under dry contact material loss by spalling and delamination is an indication of severe and catastrophic wear. Previous works [20, 122, 283] indicated that the presence of abrasive wear marks is an indication of mild wear. Figure 7.27a and Figure 7.27b provides evidence of RCF due to the presence of parallel surface cracks which is an indication of fatigue under dry contact. Pitting was observed on the wheel when water was used at 2% slip ratio and on the rail at 20% slip ratio. Pitting is an indication of surface corrosion due to the presence of water molecules. Water increases the likelihood of corrosion and uptake of hydrogen, which may cause more cracking and in the process reducing the fatigue life of wheel and rail steels as previously observed by Wang et al. [23] and Cookson et al. [75]. These negative consequences of water were also observed in the current study, as will be discussed later.

Lubrication by water and oil reduced surface roughness on both wheel and rail steels. Surface roughness was measured using the surface roughness value ( $R_a$ ), Figure 7.28. Oil showed lower  $R_a$  values across all slip ratios compared to both dry and water contacts with dry having the highest values. Oil had high viscosity making it easier for oil particles to accumulate and induce the elastohydrodynamic lubrication (EHL) at the wheel/rail contact. This causes oil to form a thicker film increasing its load carrying capacity by making it more viscous. Therefore, causing less surface damage or roughness compared to water. The wheel exhibited higher roughness values compared to the rail specimen under the same contact conditions especially under dry and water contact. Surface roughness has been found to have an effect in wheel polygonal wear, which is a periodic wear type of the wheel tread along its circumference causing the wheel to be out-of-round resulting in different surface profiles on the wheel [119, 166]. Wheel polygonal wear causes vibrations between the wheel and rail resulting in damage to train components such as such as wheels, axles, rails, rail joints, bearings and concrete sleepers [119, 167]. These vibrations also cause some form of discomfort and high levels of noise to passengers in trains [119]. A study by Zhang et al. [168] on the influence of wheel polygonal wear on interior noise of high-speed trains has found that there is a link between wheel roughness and interior noise. They found that higher wheel roughness causes high levels of interior noise [168]. Figure

7.28a demonstrates that water contact at high slip ratios produces bad wheel roughness, similar to that of dry contact. This causes high levels of noise due to severe contact conditions at high slip ratio while this is not the case with oil contact.

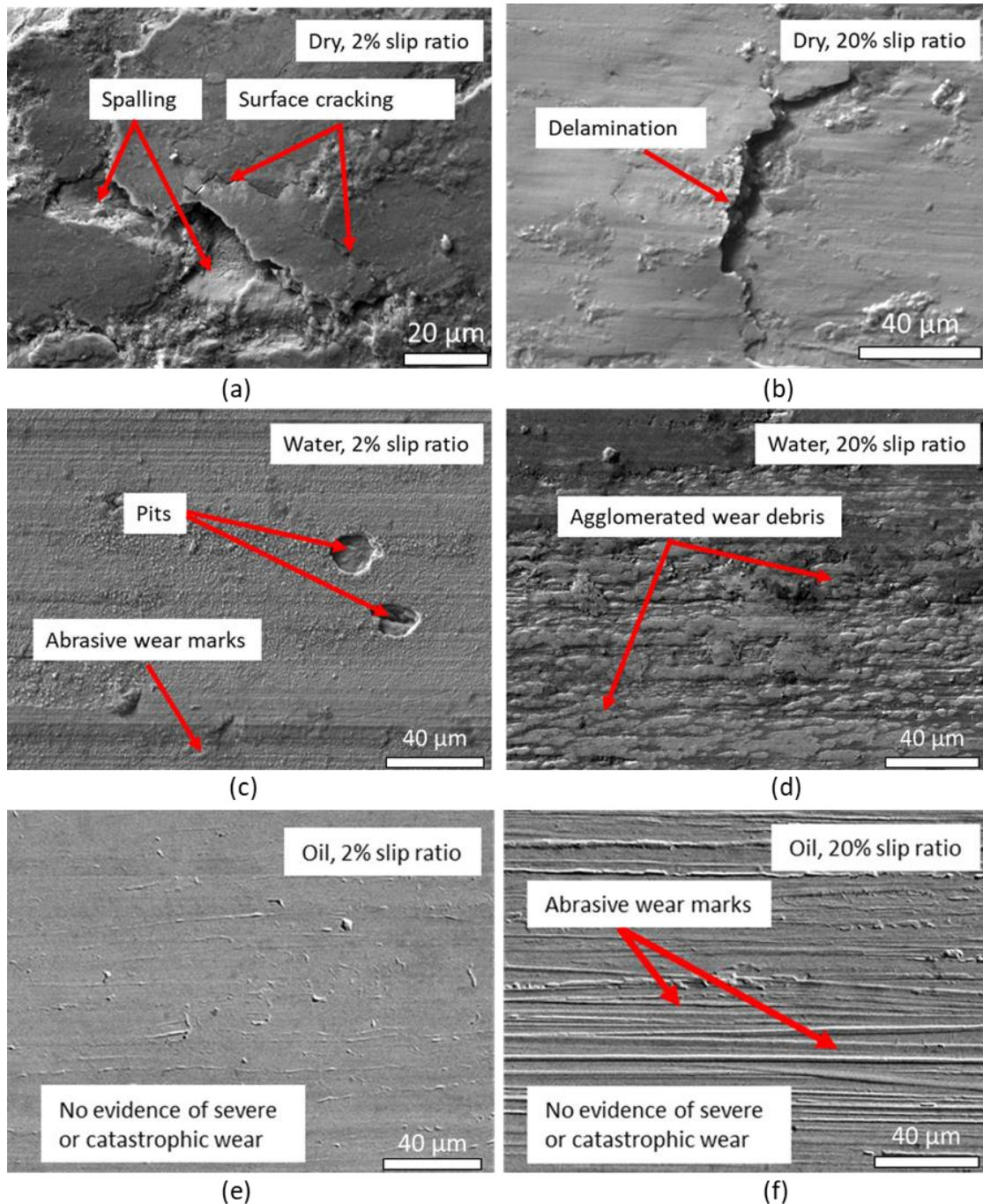


Figure 7.26: SEM micrographs of the wheel showing worn surface morphologies; (a) dry contact at 2% and (b) dry at 20% slip ratios; (c) water at 2% and (d) water at 20% slip ratios; (e) oil at 2% and (f) oil at 20% slip ratios.



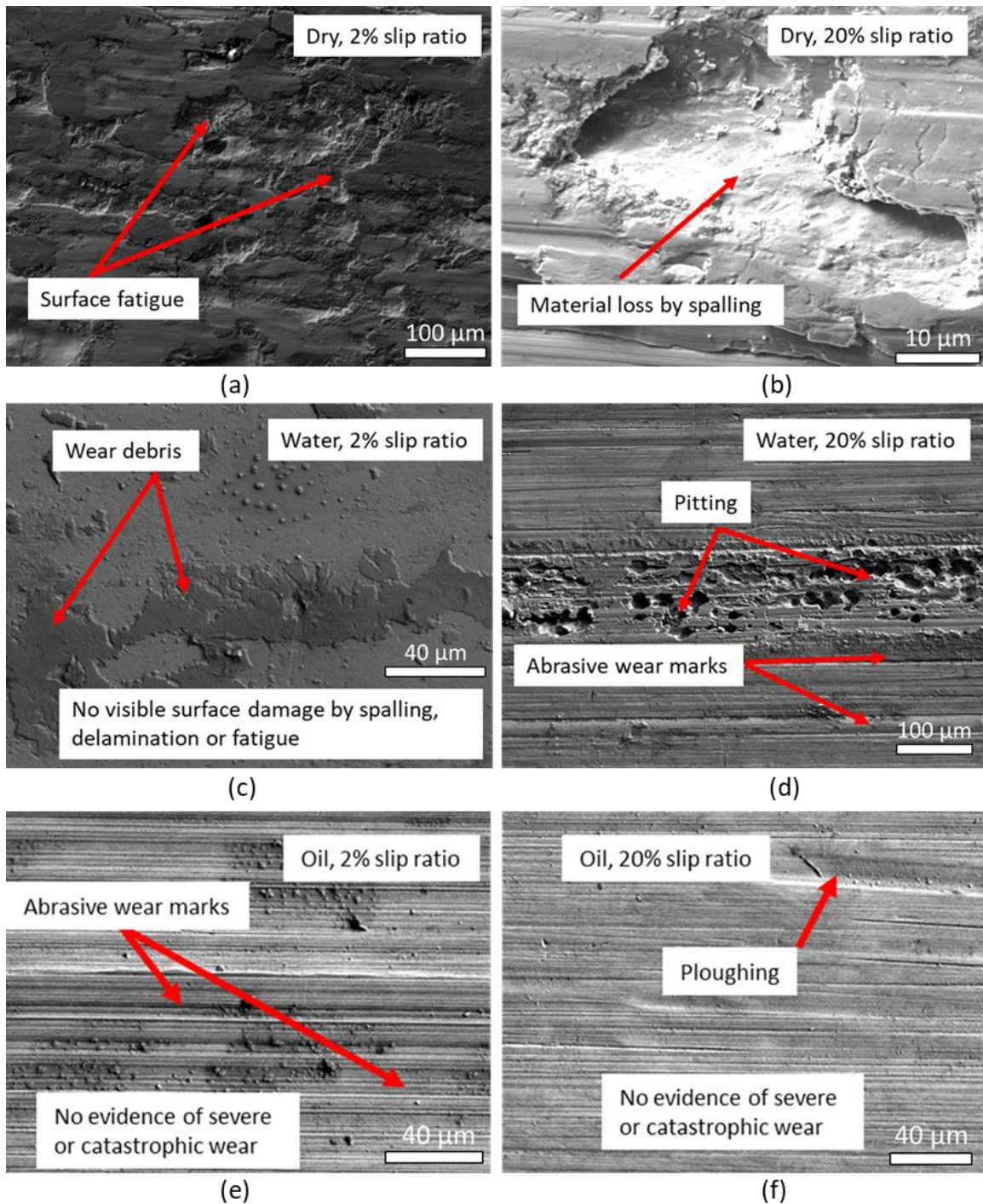


Figure 7.27: SEM micrographs of the R350HT rail showing worn surface morphologies; (a) dry contact at 2% and (b) dry at 20% slip ratios; (c) water at 2% and (d) water at 20% slip ratios; (e) oil at 2% and (f) oil at 20% slip ratios.

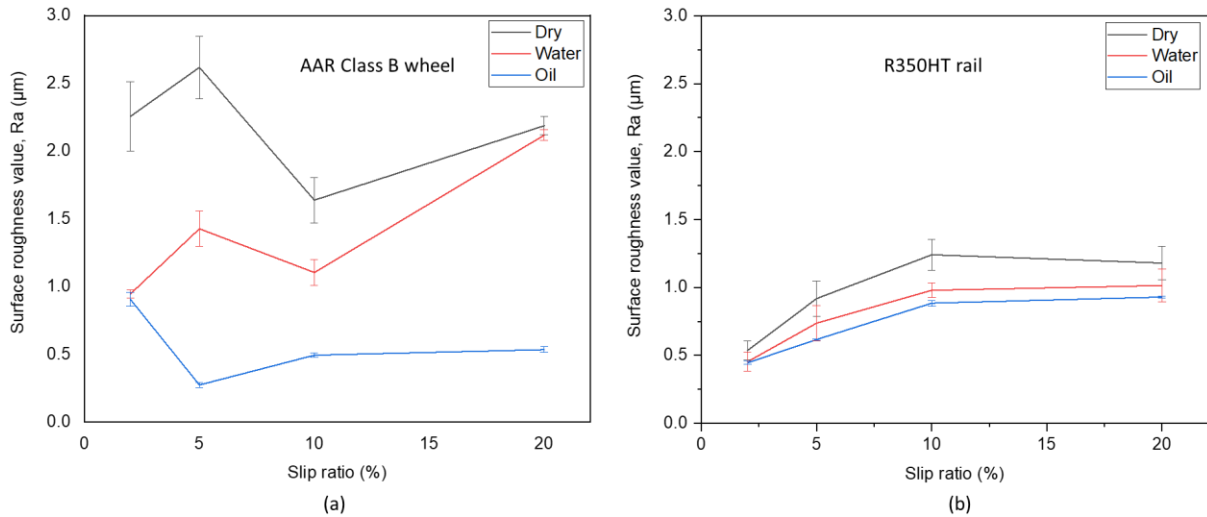


Figure 7.28: Surface roughness value as a function of slip ratio of (a) wheel and (b) rail under dry, water and oil conditions.

### 7.2.3 Effects of lubrication on plastic deformation

The depth of deformation was found to be more sensitive to slip ratio under dry contact conditions than under water and oil contacts, with dry contact specimens showing more plastic deformation and being highest at 20%, Figure 7.29, Figure 7.30. The same trend was observed at 2, 5 and 10% slip ratios but with a slight increase with slip ratio. For the wheel under dry contact conditions, the depth of plastic deformation increased from 7 to 50  $\mu\text{m}$  when slip ratio was increased from 2 to 20%, an increase of 614% compared to 80% increase under water contact, where the depth of plastic deformation increased only from 5 to 9  $\mu\text{m}$  for the same slip ratios. Further to confirm that plastic deformation had occurred, a Vickers' micro hardness test was performed to quantify the increase in sub-surface hardness. As may be seen from Figure 7.31 and Figure 7.32, there was a significant increase in sub-surface hardness for all slip ratios and conditions and the hardness was highest under dry contact.

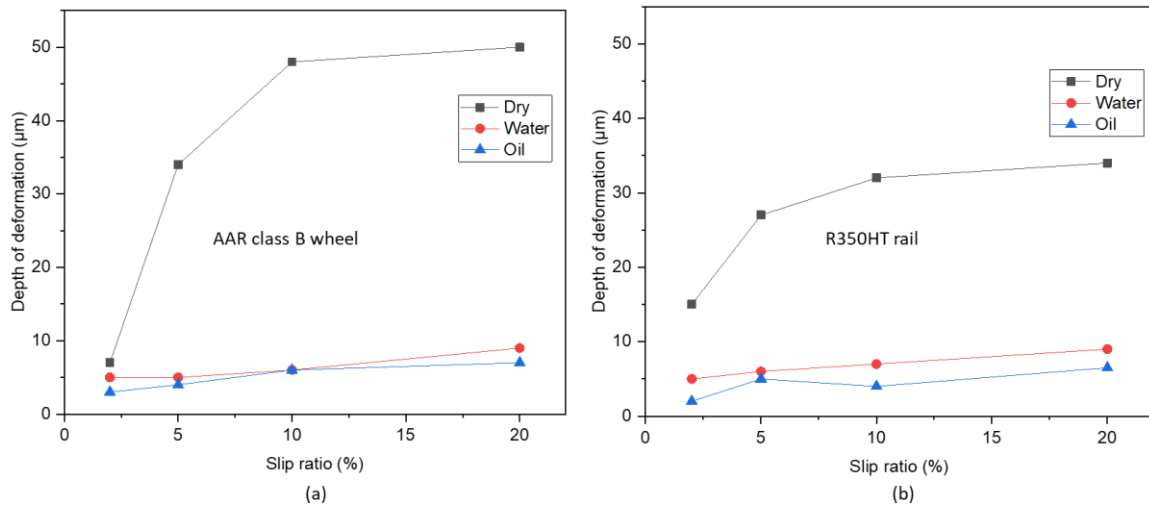


Figure 7.29: Depth of deformation versus slip ratio of (a) the wheel and (b) R350HT rail under dry, water and oil conditions.

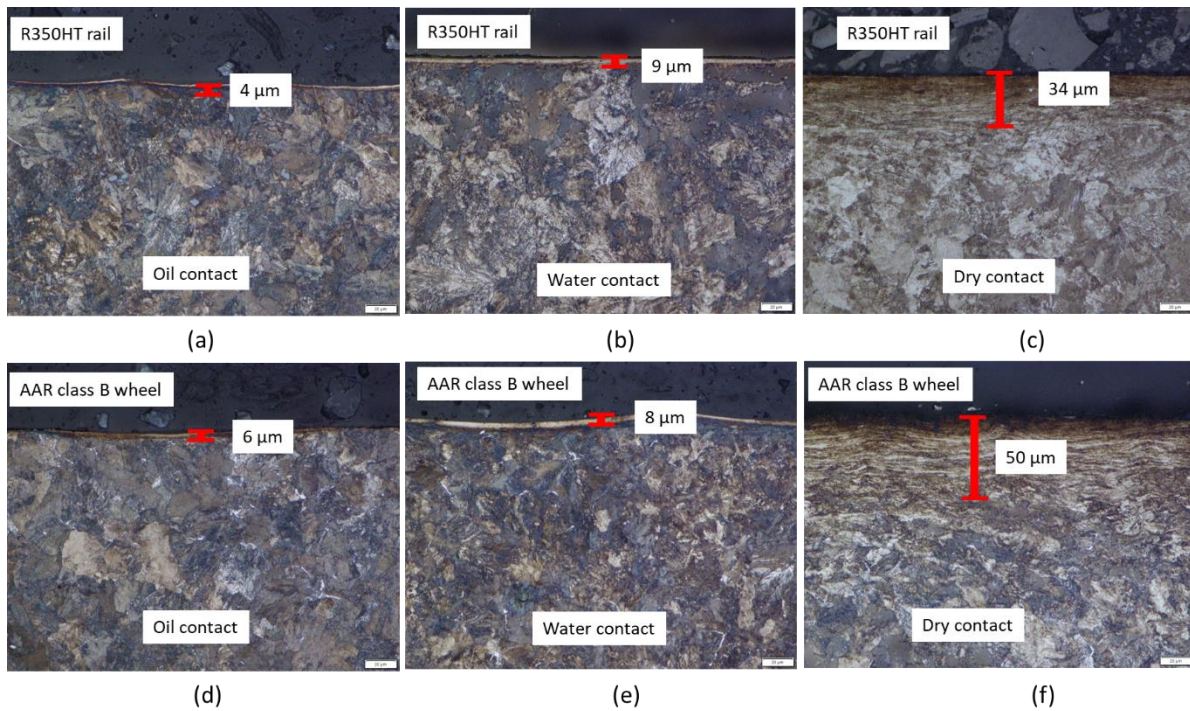


Figure 7.30: OM micrographs of R350HT rail (a,b and c) and wheel (d, e and f) showing the depth of plastic deformation after testing at 20% slip ratio under different contact conditions (dry, water and oil).

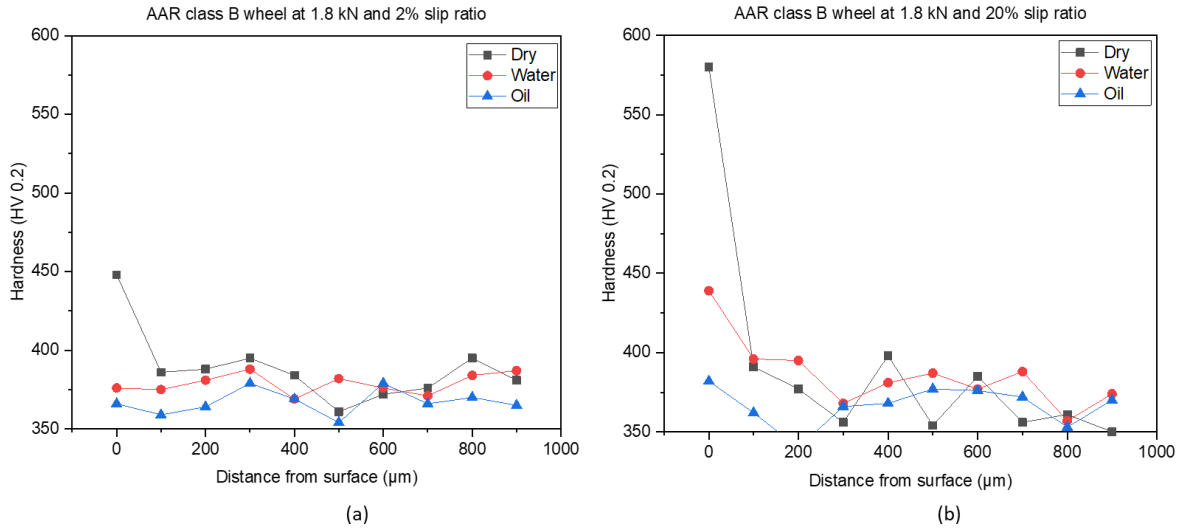


Figure 7.31: Micro hardness (HV0.2) variation with depth under dry, water and oil conditions for the wheel at (a) 2% and (b) 20% slip ratios.

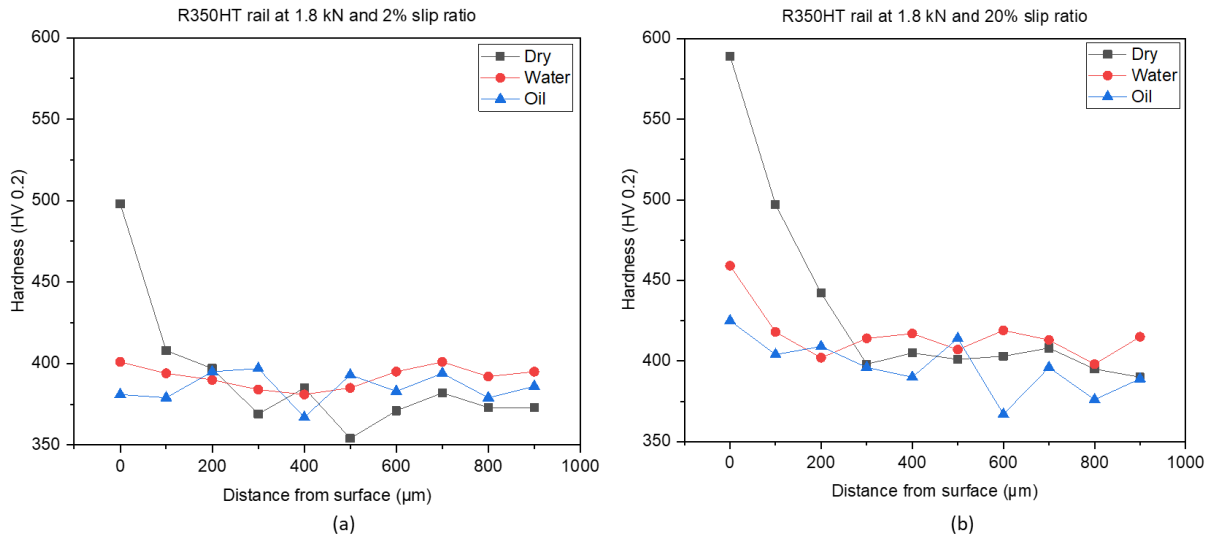


Figure 7.32: Micro hardness (HV0.2) variation with depth under dry, water and oil conditions for R350HT rail steel at (a) 2% and (b) 20% slip ratios.

#### 7.2.4 Effects of lubrication on rolling contact fatigue and sub-surface damage

Even though oil and water reduced wear on both wheel and rail, it has earlier been found that it accelerates the RCF by fluid crack pressurisation. Wear and RCF have been found to have a competitive relationship with RCF being dominant when wear rate is lower than crack growth resulting in crack growth until failure occurs [275]. In this study, water was found to accelerate propagation of RCF cracks on both wheel and rail where sub-surface RCF cracks with branching were observed, Figure 7.33c and Figure 7.33d. This acceleration may be due to fluid crack pressurisation and was also observed by Wang et al. [23] when water was introduced at



the wheel/rail contact. Fluid crack pressurisation occurs due to a liquid being entrapped into a crack due to both rolling and sliding of the wheel on rail surface under load resulting in tearing and widening of the crack due to shear stresses. From this study, there was some form of evidence of fluid crack pressurisation having occurred, Figure 7.33c, Figure 7.33d and Figure 7.34a.

More RCF cracks and crack branching were observed under dry and water contact with no observation of any formation of RCF cracks when oil. The reason for no RCF damage (no spalling, shelling or cracking) under oil was due to the lubricant's high viscosity. High viscosity makes the oil particles to easily accumulate elastohydrodynamic lubrication (EHL) at the wheel-rail contact [289, 290]. Elastohydrodynamic lubrication (EHL) is a type of lubrication that occurs when two solid surfaces come into contact under high pressure and are separated by a thin layer of lubricant that is thick enough to provide a fluid film but not thick enough to prevent contact between the surfaces. In EHL, the pressure between the two surfaces causes the lubricant to deform and flow, creating a highly viscous fluid film that supports the load and reduces friction and wear between the contacting surfaces. The same was observed in a study by Wang et al. [156] in which the rate of crack growth was significantly reduced under oil conditions compared to water. Only the deformed layer was visible when oil was introduced at the contact in agreement with observation made by Hardwick et al. [291], Figure 7.33e and Figure 7.33f.

Sub-surface spalling and peeling were observed in the wheel under dry contact, Figure 7.33a and Figure 7.33b; an indication of severe and catastrophic wear. More sub-surface damage and cracking were observed at high slip ratio with crack length and crack branching increasing with slip ratio. As may be seen from Figure 7.33c, Figure 7.33d and Figure 7.34b, the RCF cracks originated from the surface and propagated tangentially in the depth direction, eventually splitting into branches, extending towards the surface and the other towards the interior. Larger multi layered RCF cracks formed under dry contact at 20% slip ratio, which propagated by branching, other branches propagated towards the surface causing shelling, Figure 7.34b. The same phenomenon was also observed in a study by Makino et al. [143]. Shelling is an indication of fatigue and has been found to reduce the fatigue life of wheel and rail steels.

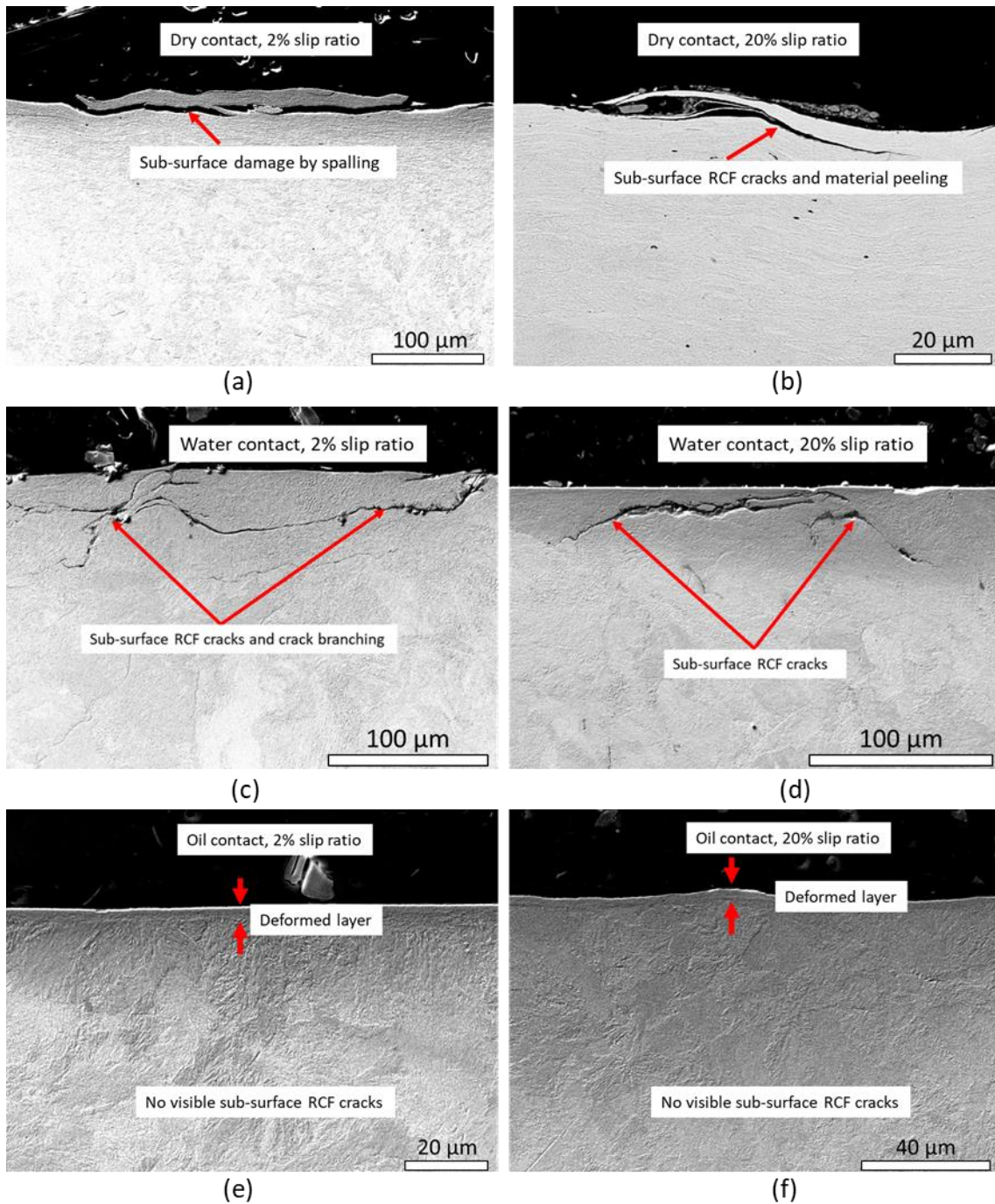


Figure 7.33: SEM micrographs of the wheel showing sub-surface damage and RCF cracks, (a) dry at 2% and (b) dry at 20% slip ratios; (c) water at 2% and (d) water at 20% slip ratios; (e) oil at 2% and (f) oil at 20% slip ratios.

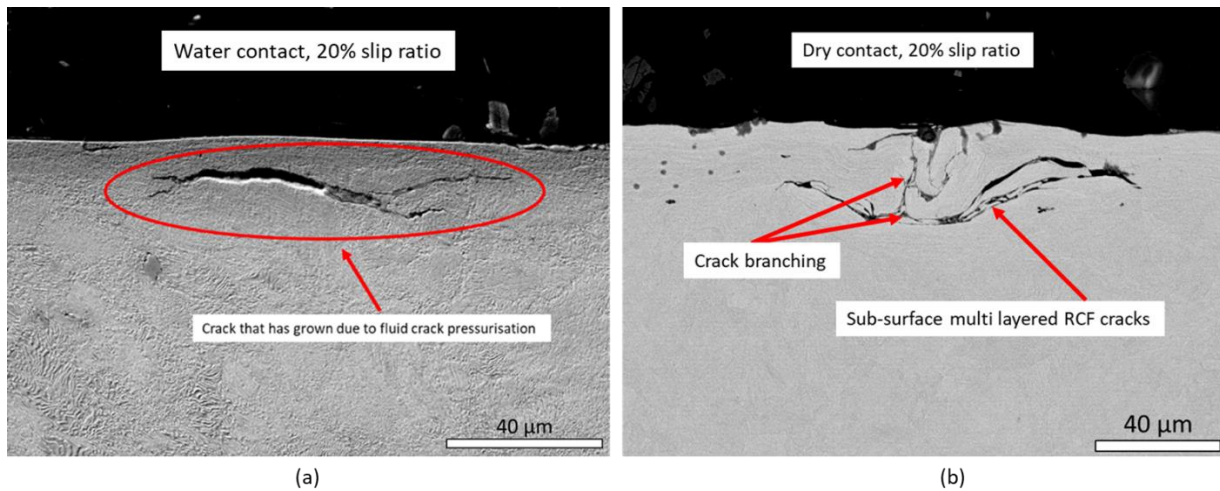


Figure 7.34: R350HT rail (a) RCF cracks that might have propagated by fluid crack pressurisation at 20% slip ratio under water, and (b) sub-surface multi layered RCF cracks with branching under dry contact.

### 7.2.5 Effects of lubrication on wheel disc temperature

Oil and water reduced the wheel disc temperature significantly compared to dry contact, Figure 7.35 and Figure 7.36. Both oil and water acted as coolants with water having more impact in lowering wheel disc temperature than oil due to its high specific heat capacity and high thermal conductivity compared to oil, hence faster cooling rate. At 20% slip ratio, the dry contact showed a maximum wheel disc temperature of 100 °C compared to 49 °C and 32.4 °C for oil and water respectively, Figure 7.36. The maximum wheel disc temperature increased with slip ratio for all the three contact conditions. The wheel disc temperature was found to increase with increasing number of rolling cycles until steady state, Figure 7.35. Change in temperature of the wheel disc has been found to affect wear performance of wheel and rail steels due to microstructural changes which may result in formation of hard and brittle martensite layer [115, 185]. For this study, the change in wheel disc temperature was not high enough to cause any microstructural change.

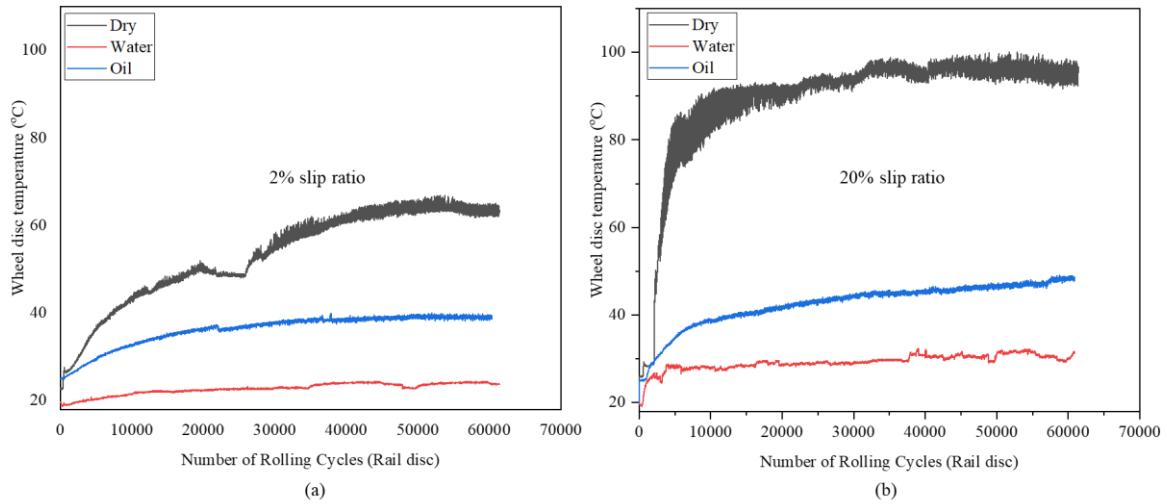


Figure 7.35: Wheel disc temperature as a function of the number of rolling cycles under different contact conditions (dry, water and oil) at (a) 2% and (b) 20% slip ratios.

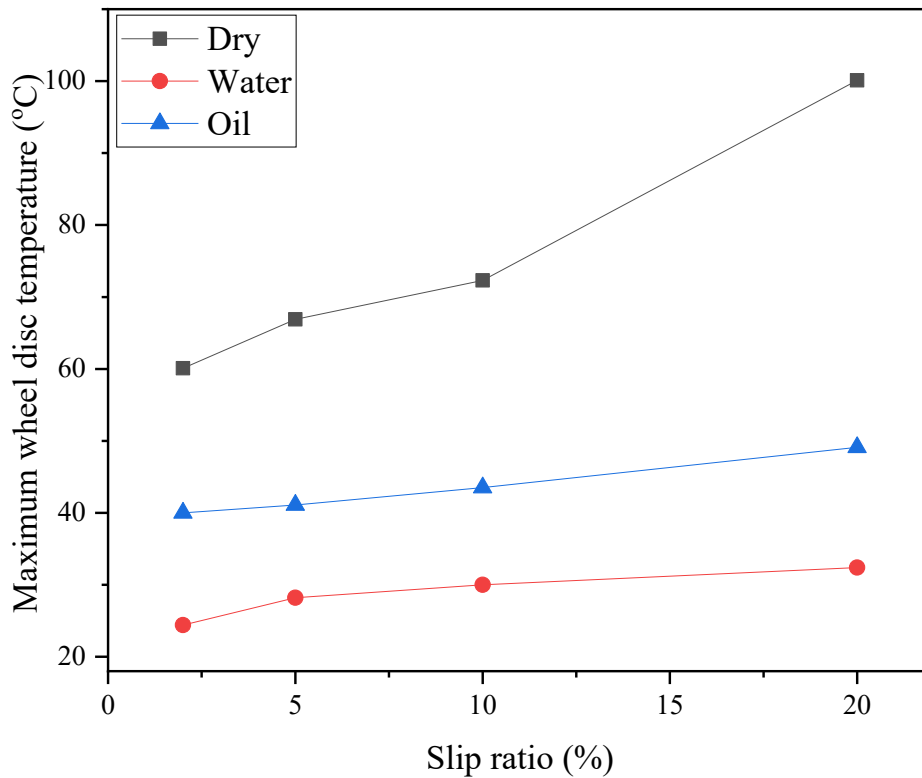


Figure 7.36: Maximum wheel disc temperature as a function of slip ratio at different contact conditions (dry, water and oil).

## Chapter 8: Discussion

### 8.1 Wear regimes and mechanisms

Previous studies [20, 122, 212, 283] have led to the identification of the three wear regimes being mild, severe, and catastrophic with the first two regimes previously identified by Bolton and Clayton [244] in 1984. These wear regimes are identified in terms of wear rates and wear debris [20]. They occur by one or a combinations of different wear mechanisms being abrasion, corrosion, delamination, fatigue, peeling, spalling, pitting just to mention a few. From this study, it was found that wear mechanisms were heavily dependent on slip ratio and contact load with severity of wear increasing with both. At mild wear, wear was mostly due to abrasion due to the presence of abrasive wear marks, with no material loss of delamination being observed, Figure 7.6 and Figure 7.7. There was also some appearances of brown rusty material of oxidative wear, an indication of mild wear. An increase in the slip ratio resulted in the change of the wear type from mild to severe or catastrophic by ratchetting process (process that causes material deformation, which leads to the emergence of cracks and the subsequent removal of material) [123]. For severe wear, it was mostly by loss of material through spalling. Peeling was also observed at high slip ratio on both wheel and rail materials. Crack branching was mostly visible under dry contact, which is an indication of catastrophic wear. Introducing water and oil at the wheel/rail contact resulted in reduction in wear, with only mild wear being visible due to the presence of abrasive wear marks with no indication of fatigue or loss of material by delamination or spalling. In other words, no new mechanisms were observed in this specific combination of wheel and rail materials, i.e. besides what is already reported in literature [23, 212, 213].

### 8.2 Wear prediction model for the wheel

In this work, wear maps were used to predict the wear after a particular distance travelled by the wheel against R350HT rail using the lab data taking into account the contact patch area. The information obtained from the models is intended for predict preventive maintenance such as reprofiling of wheels, which is done to prevent further damage on wheels by RCF and wheel polygonal wear. During wheel reprofiling, the worn surface of the wheel flange and tread are machined to geometric size of the standard contour by restoring wheel's roundness, tread taper and flange thickness. For this study, wear models were used to estimate the mass loss of the wheel after travelling a particular distance using the wear rates plots. The chosen distances of 100 000 and 200 000 km were to be used as the reprofiling cycle, which can be used to estimate



the number of reprofiling times to determine the wheel life under different contact conditions. The local rail industry in South Africa use 36 inch (approx. 915 mm) diameter wheels for general freight as per the AAR standard [90]. Therefore, using the density of 7850 kg/m<sup>3</sup> [292] and Fusion 360 computer-aided design software, the actual mass of a wheel was found to be 387 kg, Figure 8.1. A data correlation coefficient was thereafter determined to relate the twin disc wear rates to field wear rates from literature [293].

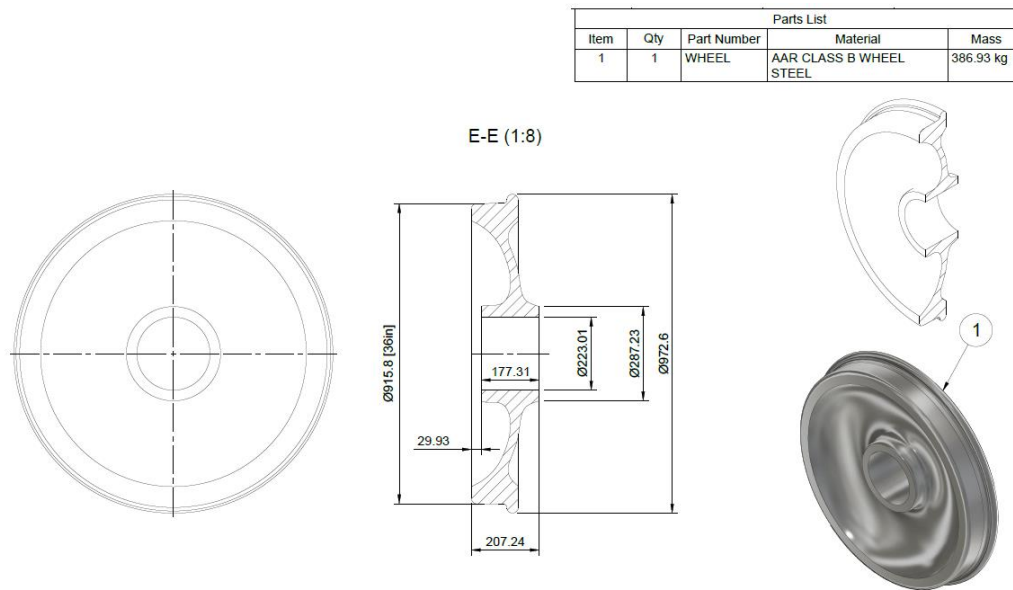


Figure 8.1: Detailed drawing of the AAR class B wheel obtained using Fusion 360 computer-aided design software.

### 8.2.1 Wheel wear rate and reduction in diameter

To calculate the actual linear distance travelled by the wheel (D) during wear simulation using the twin disc rig equation 8.1 was used:

$$D = 2\pi RN \quad 8.1$$

Where N is the number of rolling cycles by the wheel (62 000 cycles) and R is the radius of the disc (25 mm). The equivalent distance travelled was calculated as 9.74 km. The tests were conducted at 1, 1.4 and 1.8 kN which corresponds to maximum contact pressures of 552, 645 and 740 MPa respectively according to Hertz theory [44, 45]. This is within the range of real-life contact pressure on the wheel-rail interface, which is from 500 MPa upwards, especially between the rail head and the wheel tread [37]. The twin-disc contact areas were found to be 2.33, 2.78 and 3.15 mm<sup>2</sup> corresponding to Hertzian contact pressures of 552, 645 and 740 MPa respectively. The areas are relatively similar to the ones in literature obtained by twin disc tests,



for example work by Rodríguez-Arana et al. [22] the contact area of the contacting disc was found to be  $3.743 \text{ mm}^2$  at a maximum contact pressure of 1240 MPa under a twin disc setup. The contact areas, mass loss of the wheels and rails as well as the equivalent linear travelled distance (9.74 km) were used to calculate the wear rates ( $\mu\text{g}/\text{m}/\text{mm}^2$ ) at different slip ratios and contact pressures, Figure 8.2. These wear rates are high compared to the actual field conditions. This is because the twin disc simulation ignores the curvature of the rail and assumes the wheel-rail contact to be flat and, therefore does not follow the Hertzian downscaling rules for the contact patch. This is discussed further in sections 8.2.3 and 8.3.1.

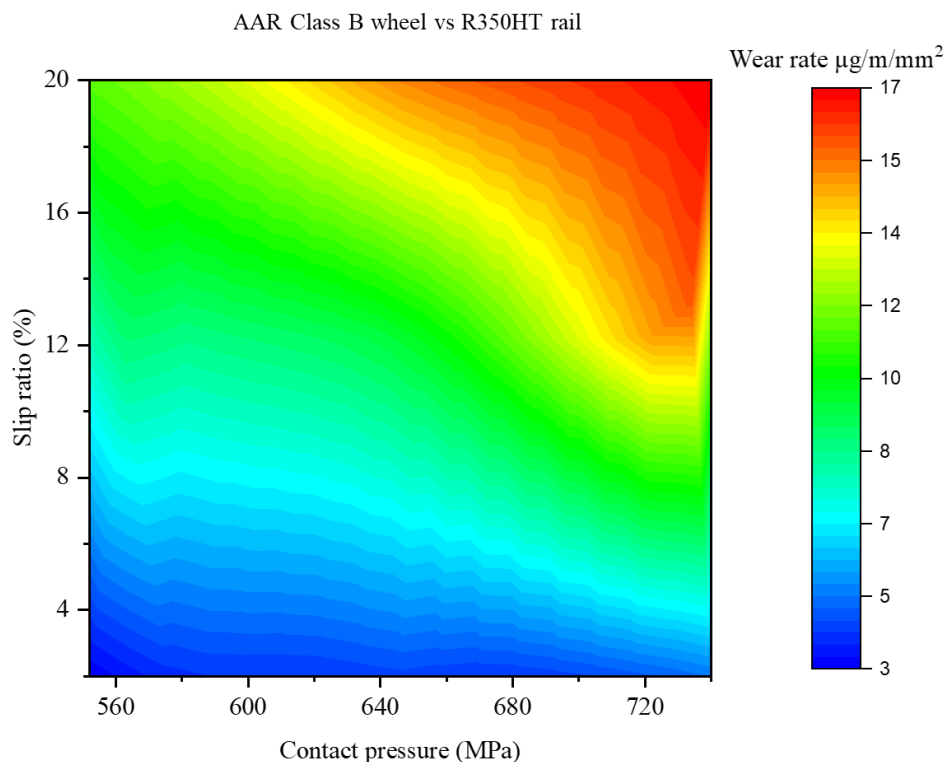


Figure 8.2: Contour plot of twin discs wear rates of AAR class B wheel against R350HT rail at different slip ratios and contact pressures under dry contact and after 62 000 rolling cycles or 9.74 km of linear distance.

Using field measured wear rates from a study by Muhamedsalih et al. [293], a data correlation coefficient between the field wear rates and twin disc wear rates was determined. From literature [293], the measured field tread wear rate for P6 wheel design profile was 0.04 mm/1000 miles, Table 8.1, which translates to 2.49 mm per 100 000 km. This wear rates agree with a study by Shi et al. [169] where the tread wear was found to increase approximately linearly with the operating distance. The correlation data coefficient is only valid assuming that the wear is uniform across the actual wheel diameter and the wheel tread is cylindrically shaped

similar to twin disc, ignoring the flange wear, assuming that the contact is flat ignoring the curvature of the rail. Therefore, the wheel is only experiencing wear at the tread. This prediction can only be true assuming that the train is moving in a straight line whereby the rail head is in contact with the wheel tread. However, when moving in curves it is not the case as the contact changes to wheel flange-rail gauge face contact, increasing the severity of wear from mild to severe or catastrophic.

Twin disc wear rates corresponding to a maximum contact pressure of 740 MPa and 2% slip ratio were used to determine the correlation coefficient. The 740 MPa was used as it falls within the lower range of the load experienced by the tread in the field from the study by Muhamedsalih et al. [293]. The reason for using a 2% slip ratio was due to the wheel tread contact experiencing field slip velocity of 0.5 m/s [293], which corresponds to the twin disc slip ratio of 2.25 % as per equations 4.5 and 4.6. This assumes that the train speed is 80 km/h, which is the maximum speed for local freight trains in South Africa [14, 15]. Therefore, twin disc wear rate of 4.8  $\mu\text{g}/\text{m}/\text{mm}^2$  corresponding to slip ratio of 2% at a maximum contact pressure of 740MPa, was used to determine the correlation coefficient.

Table 8.1: Tread and flange wear rates for different wheel profiles from a study by Muhamedsalih et al. [293].

Wheel profile	Tread wear rate, $\varnothing$ mm/1000 miles	Flange wear rate, $\varnothing$ mm/1000 miles	Average turning interval
Design P6 – measured Data	0.04	0.13	25,000
Design P6 – simulated Data	0.03	0.12	30,000
27 mm – P6	0.03	0.12	16,000
26 mm – P6	0.03	0.11	9300
25 mm – P6	0.03	0.1	4200

From the tread measured field wear rate of 2.49 mm per 100 000 km [293], the mass after wear ( $m_{\text{after}}$ ) and the wheel diameter after wear ( $D_{\text{after}}$ ) were determined as 383.07 kg and 913.31 mm using Fusion 360 computer-aided design software, Figure 8.3. To find the reduction in diameter after wear ( $D_{\text{reduction}}$ ) with an actual wheel diameter of 915.8 mm before wear ( $d_{\text{before}}$ ), equation 8.2 was used;

$$\begin{aligned}
 D_{\text{reduction}} &= D_{\text{before}} - D_{\text{after}} && 8.2 \\
 &= 915.8 \text{ mm} - 913.31 \text{ mm} \\
 &= 2.49 \text{ mm}
 \end{aligned}$$

To calculate the mass loss ( $m_{loss}$ ) after 100 000 km of travel equation 8.3 was used with an actual wheel mass of 386.93 kg before wear ( $m_{before}$ );

$$m_{loss} = m_{before} - m_{after} \quad 8.3$$

Therefore.

$$\begin{aligned} m_{loss} &= 386.93 \text{ kg} - 383.07 \text{ kg} \\ &= 3.86 \text{ kg} \end{aligned}$$

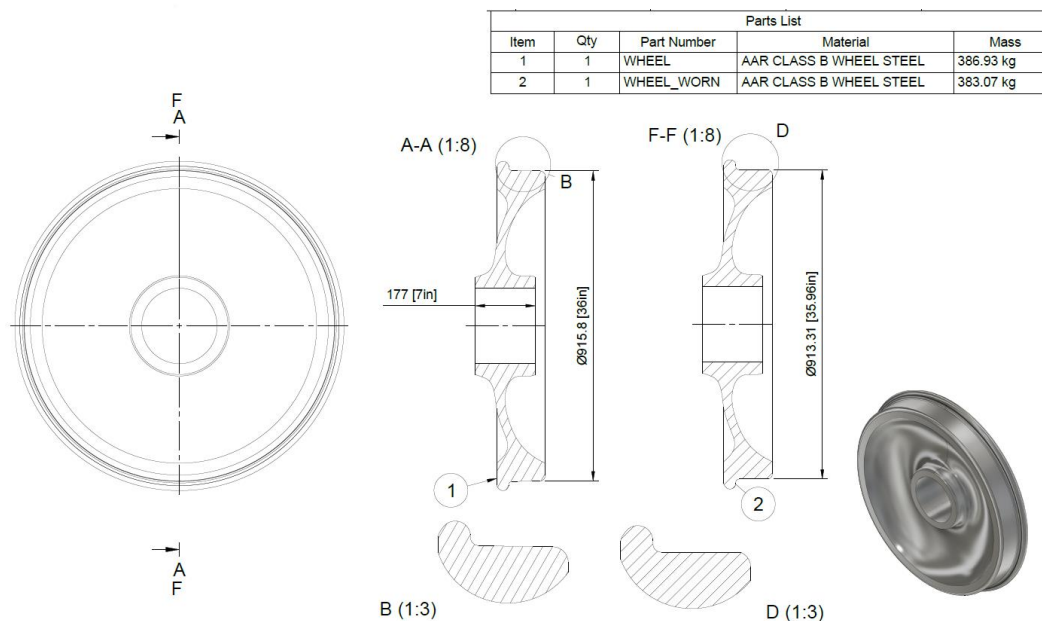


Figure 8.3: A schematic diagram showing the wheel before (1) and after wear (2) with their respective masses and diameters obtained using Fusion 360 computer-aided design software.

To calculate the actual field wear rates, equation 8.4 was used. From literature [22, 60, 295], the actual wheel-rail contact area has been found to be between 1 to 2 cm<sup>2</sup> (100 to 200 mm<sup>2</sup>) depending on the contact conditions. To calculate the wear rates of the actual wheel an average contact area of 150 mm<sup>2</sup> was used for simplicity. This prediction can only be true assuming that the train is travelling under dry conditions and there is no contamination at the wheel-rail contact similar to lab testing conditions on twin disc simulator. Therefore, with an actual contact patch area of 150 mm<sup>2</sup>, travel distance of 100 000 km or 100 000 000 m and mass loss of 3.86 kg or 3.86 x 10<sup>9</sup> µg the field wear rate (µg/m/mm<sup>2</sup>) was calculated as follows:

$$\begin{aligned}
 \text{wear rate} &= \frac{\text{mass loss } (\mu\text{g})}{\text{distance } (m) \times \text{Actual contact patch area } (mm^2)} & 8.4 \\
 &= \frac{3.86 \times 10^9 \mu\text{g}}{100\,000\,000\,m \times 150\,mm^2} \\
 &= 0.257 \mu\text{g}/m/mm^2
 \end{aligned}$$

To find data correlation coefficient between the field and lab wear rates (from twin disc simulations at 750 MPa and 2% slip ratio) equation 8.5 was used:

$$\begin{aligned}
 \text{data correlation coefficient} &= \frac{\text{field wear rates } (\mu\text{g}/m/mm^2)}{\text{lab wear rates } (\mu\text{g}/m/mm^2)} & 8.5 \\
 &= \frac{0.257 \mu\text{g}/m/mm^2}{4.8 \mu\text{g}/m/mm^2} \\
 &= 0.0535
 \end{aligned}$$

This correlation coefficient was used to determine the field wear rates corresponding to other twin discs wear rates, contact loads and slip ratios, Table 8.2 and the reduction in diameter at different travel distances, Figure 8.4. At 5% slip ratio and 552 MPa, apparently, a slightly higher wear rate was observed to some extent when the wheel was run against both R350HT and R260 rails, Figure 7.4. The mechanism responsible for this behaviour was not obvious.

It is worth mentioning that these predictions assume that the wear rate is greater than the rate of RCF crack formation, as wear has competitive relationship with RCF [145, 146]. In real life, the wheel is not always experiencing high slip ratios as it does only when moving in curves where the wheel-rail contact changes from rail head-wheel tread to wheel flange-rail gauge face contact. In other words, the wheel does not experience high slip ratios at all times as it does only when moving in curves. Also in real life, the wheel contact geometry is not cylindrical as it is changes due to varying contact conditions. Therefore, data correlation coefficient can only be used as a guide for wheel reprofiling back to standard conditions as per the AAR standard [90]. There is no direct correlation between twin disc wear rates and the field wear rates of wheels.

Table 8.2: Wear rates of ARR class B wheel at different slip ratios and maximum contact pressures from twin disc simulation with their estimated field wear rates obtained using a correlation coefficient of 0.0535.

Max Pressure (MPa)	Slip ratio (%)	Twin disc wear rate ( $\mu\text{g}/\text{m}/\text{mm}^2$ )	Estimated field wear rates ( $\mu\text{g}/\text{m}/\text{mm}^2$ )	Estimated field mass loss after 100 000 km (kg)	Reduction in diameter (mm)
552	2	3.04	0.162	2.44	1.98
552	5	11.36	0.608	9.11	3.83
552	10	8.36	0.447	6.71	3.28
552	20	11.32	0.605	9.08	3.82
645	2	4.12	0.221	3.31	2.31
645	5	4.87	0.261	3.91	2.51
645	10	7.91	0.423	6.35	3.19
645	20	15.03	0.804	12.06	4.40
740	2	4.80	0.257	3.85	2.49
740	5	9.04	0.484	7.26	3.41
740	10	14.79	0.791	11.87	4.37
740	20	17.07	0.910	13.65	4.68

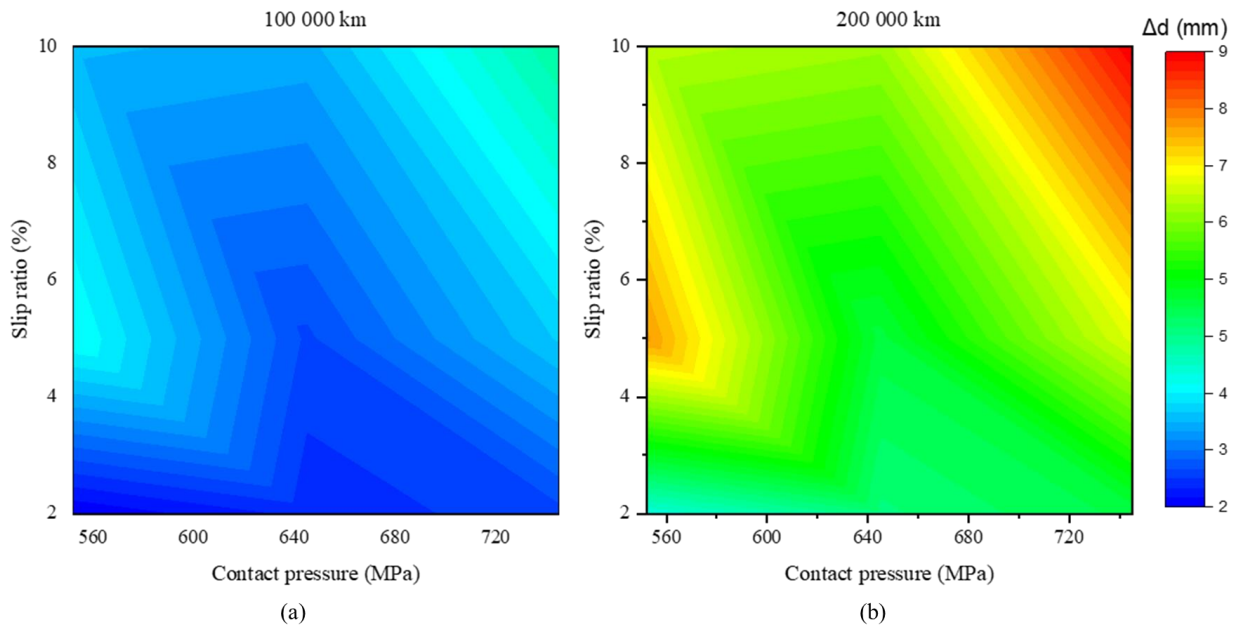


Figure 8.4: Contour plots of the predicted reduction in wheel diameter ( $\Delta d$ ) as a function of the slip ratio and pressure after (a) 100 000 and (b) 200 000 km of travel distances under dry contact conditions.

### 8.2.2 The wheel reprofiling model

The data from Table 8.2 can be used to determine the number of reprofiling times before the wheel can be replaced. In addition to the material lost due to wear, reprofiling also removes material from the wheel's diameter as indicated in Figure 8.5. The wheel reprofiling can be done after every 250 000 km until the wheel reaches a total reduction in diameter of 50 mm or has travelled 1 100 00 km (approximately 700 000 miles), whichever come first, before it is scrapped by the UK standard [236]. The same conditions were adopted for this study. Depending on the desired final profile and the degree of the existing wear on the wheel, the amount of material removed can be anywhere between a few millimetres and several millimetres [293]. For example, to reprofile the worn wheel with 915 mm diameter, 4 mm of material is removed from the wheel diameter to achieve a thinner flange of 26 mm or 14 mm is removed to achieve a thicker flange of 28.7 mm similar to the original profile [293]. For this study, a thinner flange of 26 mm was chosen as per the AAR standard, therefore 4 mm of wheel diameter will be removed by each reprofiling cycle of the wheels in order to achieve a standard contour on the wheel flange by machining away some material from the wheel tread.



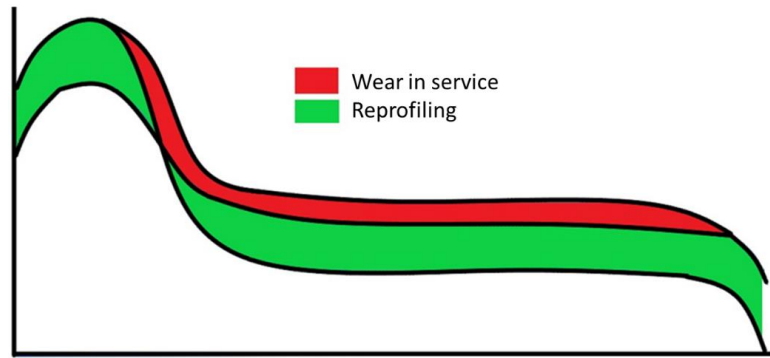


Figure 8.5: A schematic diagram showing the removal of material by wear (red) and reprofiling (green) to restore the new profile.

During wheel reprofiling, the flange thickness increases to a standard contour whereas the wheel diameter decreases further as the diameter of the wheel is reduced by reducing the thickness of the wheel rim [294, 295]. This can only be done only if wear is greater than the RCF crack formation as Railway Group Standard GM/RT2466 [296] states that if multiple cracks appear on the wheel tread and one of them is longer than 40 mm, the wheelset must be removed from service within 24 hours. From Figure 8.6, wheel reprofiling times was found to be 7 and 5 for reprofiling every 100 000 and 200 000 km respectively, which is similar to the ones found in literature [236, 293, 297] where it was found to be between 3 and 7 times depending on the operating conditions. As seen from Figure 8.6, reprofiling every 200 000 km resulted in a longer wheel life of 1 100 000 km with a smaller reprofiling times compared to reprofiling every 100 000 km which had a shorter wheel life of 800 000 km with larger profiling times of 7.

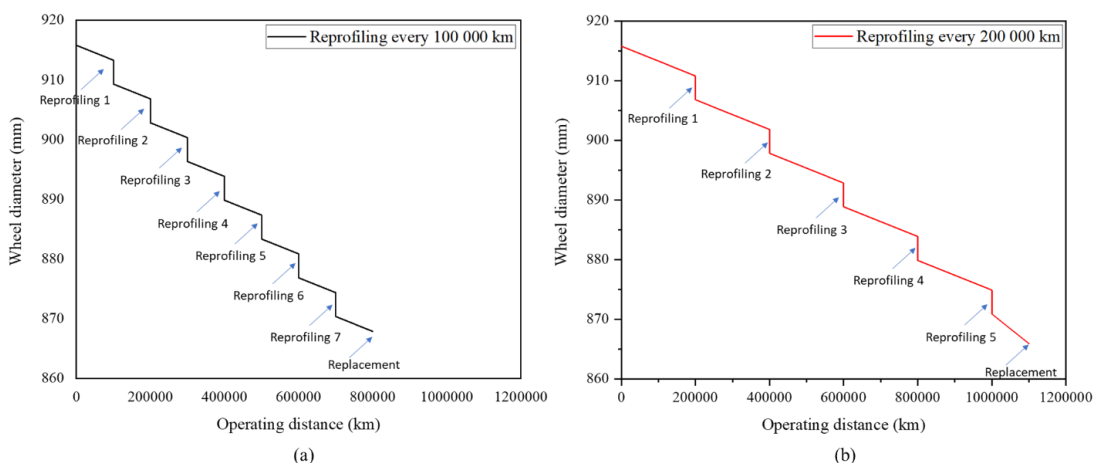


Figure 8.6: Predicted reduction in diameter of the 915 mm wheel after reprofiling every (a) 100 000 km and (b) 200 000 km estimated from the twin disc wear rates at 740 MPa and 2% slip ratio.

For any set of rail and wheel materials, there is always a need to optimise the maintenance strategy to lower the maintenance costs and extend the life of the wheels. In other words, increasing the frequency of reprofiling decreases the availability of the wheels and increases the machining costs and, therefore, increases the total costs of maintenance. Whereas decreasing the frequency of reprofiling increases the availability of the wheels and decreases the machining costs but risks failure by RCF. This reprofiling model does not take into consideration RCF cracks. It assumes that wear is dominant, but in reality, this is not the case especially in heavy haul freight railway where high contact stresses are experienced [298]. Also, reprofiling after a longer cycle risks the development and growth of RCF cracks deeper into the wheel tread, by crack branching. Therefore, removing 4 mm of wheel tread every reprofiling cycle might not be enough to remove RCF cracks, especially at a longer reprofiling cycle of 200 000 km, even though it was found to increase the life of the wheels by this study. Hence the need for an optimal strategy for removing the right amount of material in order to control surface and sub-surface crack initiation as well as to remove grown cracks while the rate of propagation is still slow by having shorter reprofiling cycles on wheel and shorter grinding cycles on rails [121]. As seen in Figure 8.7, as the running distance increase so does the crack length on wheel hence a need to optimise the reprofiling process by not having longer reprofiling cycles that might allow crack growth and propagation.

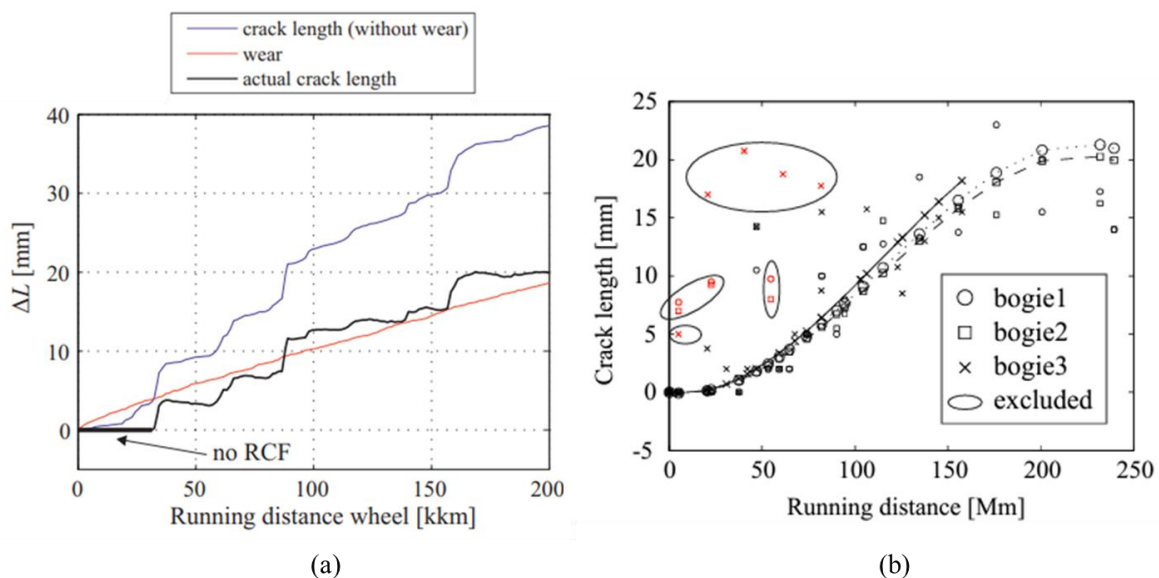


Figure 8.7: (a) The predicted development of the surface crack length ( $\Delta L$ ) on a wheel of the Stockholm commuter train [164] (b) Measured length of the surface crack versus running distance for wheels [299].

### ***8.2.3 Problems with the proposed wheel wear prediction model***

As already mentioned, there is no direct correlation of the twin disc performance to the field performance of wheels as the former does not follow the downscaling rules of the contact patch. Also, the conditions at the wheel-rail contact patch during lab testing are controlled and considered steady state whereas in field they can vary as the wheel-rail contact in field is an open system and can be influenced by the ever-changing environment [300]. For example, the loads during lab testing are consistent and controlled whereas in the field, they vary due to the weight of the train, speed and the curvature of the track. In lab testing, the contact between the discs is flat and ignore the convex shape of the actual wheel-rail contact which is a feature of the rail gauge corner. Furthermore, in twin disc testing, the wheel contact is assumed to be a parallel cylindrical contact with rectangular shaped contact patch, whereas in reality it can be simplified as a cross cylindrical arrangement with an elliptical contact patch.

The wheel reprofiling model ignores RCF and assumes that wear is dominant and removes RCF cracks. It is also assumed that by removing 4 mm of wheel diameter during reprofiling, developed RCF cracks are removed by machining which might not be the case in reality. RCF cracks can grow as deep as 8 mm in heavy haul environment where high contact stresses are experienced [121] and have been found to develop deeper into the wheel tread perpendicular to the direction of traction [121]. In future work, a digital twinning model would be the appropriate approach replicating real life conditions in a virtual environment taking into account both wear and RCF to optimise the predictive maintenance. Despite its limitation of simulating the field conditions, the twin disc testing is an important test rig for determining the wear mechanisms of wheel-rail interactions [253]. Researchers can acquire insights into how different factors affect wear rate by conducting twin disc testing under a variety of controlled inputs such as loads, speeds and lubrication. Also, different combinations of wheel and rails can be studied. The data obtained can then be used to understand better the wheel-rail contact mechanics to create strategies for reducing wear and extending the life of wheel and rail systems.

## 8.3 Limitations of the test rig

### 8.3.1 *The Hertzian downscaling rule*

As stated in section 4.13.5, in order to link the twin disc results to the actual field results, the Hertzian downscaling rules must be complied with. For the current rig design, one of the Hertzian downscaling rules for the contact patch was not followed, which is the case for most twin-disc rigs. The downscaling of actual wheel diameter to disc diameter is not equal to the downscaling of major axis of the contact ellipse between actual wheel-rail and twin disc. The actual wheel diameter for AAR class B wheel was assumed to be the typical 915 mm, whereas the disc diameter was 50 mm. Applying the downscaling rule (915 mm divided by 50 mm) the diameter downscale becomes approximately 18 times. For the three contact stresses (552, 645 and 740 MPa) used for this work, the twin disc contact width was found to be 0.233, 0.278, 0.315 mm respectively according to Hertz theory. For the actual ellipse contact along the major axis, literature [301, 302, 303, 304, 305] has demonstrated that would be between 14 and 20 mm obtained using FE modelling, Hertz theory and other numerical analysis methods, Table 8.3. The size of the major and minor semi-axes of the contact ellipse depends on the radii and the radii of curvature of the contacting bodies as well as the normal load [202]. The contact downscale for the major axis of the actual ellipse contact and twin disc contact width i.e., 20 mm divided by 0.315 mm is approximately 63 times and not close to the diameter downscale of 18 times.

Even though the rig did not follow one of the Hertzian downscaling rule, it was able to produce results that are comparable to literature and was efficient in investigating the different wear and RCF mechanisms. Similar rigs used in literature [21, 73, 74, 144, 272] also did not follow this rule, as they also ignored the convex shape of the actual wheel-rail contact patch as they assume it to be a flat surface for simplicity, which was also the case by in this study.

Table 8.3: Actual wheel-rail contact patch sizes by different approaches at different maximum pressures.

Approach	Maximum pressure (MPa)	Major semi axis, a (mm)	Minor semi axis, a (mm)	Contact area (mm <sup>2</sup> )	Authors
Finite element method	1344	8	6.03	151.55	Zhao et al. [60]
CONTACT	1347	7.8	5.69	139.68	Zhao et al. [60]
Hertz	1340	7.73	5.86	142.31	Zhao et al. [60]
Hertz	637	4	4	47.4	Vollebregt et al. [306]
Hertz	1091	6.8	6	139	Vollebregt et al. [306]
Hertz	1240	6.574	5.267	108.77	Rodríguez-Arana et al. [22]

### 8.3.2 Maximum contact load

The developed rig could only reach a maximum contact load of 1.8 kN which corresponds to the Hertzian contact pressure of 740 MPa due to the limitation on the scissor jack and motors. Nevertheless, the three wear regimes mild, severe and catastrophic were observed similar to the ones achieved at higher contact stresses reported in literature [23, 307]. This was made possible by being able to test at higher number of rolling cycles (62 000) and slip ratios (up to 27%). Beyond 27% slip ratio, the motors started to slip resulting in fluctuating and unstable speeds. In literature, higher contact pressures were used, which produced similar results but at lower rolling cycles and slip ratios. For example, in a study by Wang et al. [23] where

maximum contact pressure of 1500 MPa, slip ratio ranging from 0 to 10% and 30 000 rolling cycles were used on a SUROS rig and similar wear regimes and mechanism were observed such as RCF multi layered cracks and crack branching. Another study by Zhao et al. [308] used maximum contact pressures of 300, 500 and 700 MPa and slip ratios ranging from 0.91 to 4.55% which are similar to the ones used in this study producing similar results. This was an indication that the test rig used in this study produced comparable results despite its load limitation. The same can be said about adding oil and water at the wheel-rail contact where the drop in coefficient of friction and low wear rates were observed, compared to dry contact.

An easier way of increasing the maximum contact pressure is to reduce the twin disc contact width e.g. from 10 to 5 mm width, which would give a contact length of 5 mm instead of 10 mm. This would increase the maximum contact pressure from about 750 and 1000 MPa at a load of 1.8 kN. Literature [245, 272, 273] has demonstrated that reducing the contact length of the discs to 5 mm increases the maximum contact pressures with reasonable normal loads.

### ***8.3.3 The negative slope effect***

In a twin disc setup, the coefficient of friction generally increases with the slip ratio until a saturation point is reached and thereafter it starts to drop, a phenomenon where known as the negative slope effect, Figure 8.8. This is due to the fact that at high slip ratio, the contacting materials starts to slip more resulting in a decrease in the coefficient of friction. However, for this study this was not the case, Figure 7.3 and Figure 7.25a. This could have been due to wear debris being agglomerated onto the surfaces; affecting the surface roughness and indirectly the friction coefficient. Also, the test rig used for this work had a vertical configuration between the contacting discs which could have made easier for wear debris to agglomerate affecting the wear and RCF mechanisms hence friction coefficient. Work by Ma et al. [212] used a similar test rig configuration had similar results and did not observe any negative slope with increase in slip ratio.



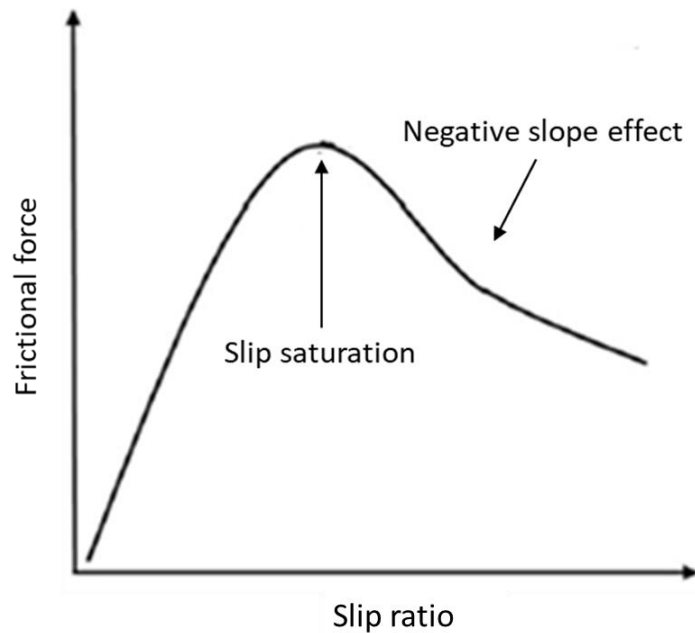


Figure 8.8: Slip as a function of friction showing the negative slope effect, adapted from [28].

The negative slope is also dependent on the properties of the contacting bodies as well as the roughness, environmental conditions (such as temperature and humidity). Previous works [62, 309, 310] have stated that the decrease in coefficient of friction with increasing slip ratio at the saturation point might be due to an increase in the contact temperature at the wheel interface. From this study, the wheel disc temperature was found to increase with slip ratio across all loads, with maximum wheel disc temperature of 117 °C observed when the wheel was run against R350HT rail at 27% slip ratio under the load of 1.8 kN, Figure 7.23. However, the temperature was too probably low for phase transformations such as the formation of white-etching layers (WEL) to take place. This could have been the reason why the negative slope was not observed. WELs are usually formed at temperatures exceeding 700 °C [311, 312]. They get their name from the white appearance they have after being etched with Nital [313]. A study by Al-Juboori et al. [314] has discovered that there are two types of WELs; one consists of fine nanocrystalline martensite and the other a mixture of retained austenite and martensite. The nanocrystalline martensite was found to have been induced by severe plastic deformation whereas the one consisting of a mixture of retained austenite and martensite was probably thermomechanically induced [314]. WELs have been found to influence frictional properties at the wheel-rail interface as they provide some form of lubrication which might increase or reduce the coefficient of friction [315]. From this study there was no evidence of the formation of any of the WELs due to low wheel disc temperature, which might be the reason for no negative slope observed with an increase in slip ratio, in the friction vs slip ratio plot.

## Chapter 9:

### 9.1 Conclusions

A twin-disc instrumented wear rig was designed and constructed which was able to simulate the three wear mechanisms of RCF, sliding and rolling wear as experienced by the wheel and rail during movement of train wheels on rail tracks. This rig was able to produce repeatable and comparable results which agree with other works. The contact conditions such as load and slip ratio were easily varied to determine their effects on wear and RCF using coefficient of friction and temperature data. The coefficient of friction and severity of wear were found to be dependent on the slip ratio and applied load. The severity of wear increased with an increase in the applied load and slip ratio, and it was evident from the worn surfaces of the contacting discs. The wear and RCF performance of the AAR class B wheel steel against the harder R350HT rail and softer R260 rail steels was investigated under dry, water and oil contact conditions and the following conclusions were made under dry conditions:

- Despite the rig's limitation of load, it was able to simulate RCF and wear with three wear regimes identified as mild, severe and catastrophic.
- AAR class B wheel performed better against the softer R260 rail compared to the harder R350HT rail with low wear rates for all slip ratios and loads. There was evidence of RCF due to plastic deformation, formation of multi-initiated crack networks and severe delamination due to formation of pits and breakouts when the wheel was run against R260 and R350HT rails. Less surface damage and plastic deformation was observed on wheels when run against R260 compared to R350HT rails.
- The negative slope effect was not observed in this study, which may have been caused by the wheel-rail contact temperature not being high enough to cause any phase transformation (for example formation of white-etching layers) which has been found to affect frictional force with an increase in slip ratio beyond the saturation point. In thus regard, the test rig's vertical configuration could have played a role by making the wear debris to be easily embedded at the surfaces.

When water and oil were introduced at the wheel-rail interface, wear significantly reduced compared to dry test but more RCF cracks were observed under water contact when the wheel was run against the harder R350HT rail. Water was found to promote RCF crack propagation by fluid crack pressurisation which has a negative impact on RCF resistance. A significant drop

in coefficient of friction was also observed under both water and oil, which was also confirmed by lower roughness values.

A data correlation coefficient to link twin disc and field wear rates was determined and was used to predict the field wear rates, which were used to determine the reprofiling times for different reprofiling cycles i.e., for 100 000 and 200 000 km. This twin disc based model did not consider the curvature of the rail and also assumed the wheel-rail contact to be flat. In actual wheel-rail contact, the rail curvature has a convex shape especially in curves where the wheel flange and rail gauge face are in contact. This study was intended to help local rail industries using AAR class B wheels against R350HT or R260 rail combinations to understand the wear and RCF performance under different contact conditions for the predictive maintenance. Last but not least, the designed and developed test rig could be modified to test wear behaviour of ball mill grinding media alloys for the mining industry, rolls for the hot strip and plate mills among other applications.

## **9.2 Recommendations for future work**

The following suggestions can be considered for future work:

- The developed rig's load limit is 1.8 kN. To investigate the effect of higher contact loads, the rig could be redesigned to accommodate bigger motors for higher torques.
- The noise and vibrations generated at the wheel/rail contact can be measured and related to the roughness of the contacting discs to determine the polygonal wear behaviour of these combinations of rail and wheel steels.
- Lastly, to use FEM and numerical analysis to determine the wheel-rail contact patch flash temperature.

### 9.3 References

- [1] J. Pombo, J. Ambrósio, M. Pereira, R. Lewis, R. Dwyer-Joyce, C. Ariaudo and N. Kuka, “Development of a wear prediction tool for steel railway wheels using three alternative wear functions,” *Wear*, vol. 271, pp. 238-245, 2011.
- [2] Transnet, “Transnet Freight Rail,” Transnet, [Online]. Available: <https://www.transnet.net/Divisions/Pages/FreightRail.aspx>. [Accessed 17 August 2023].
- [3] Department of Transport, “Welcome to Rail Branch,” Department of Transport, Republic of South Africa, 2023. [Online]. Available: <https://www.transport.gov.za/rail>. [Accessed 17 August 2023].
- [4] Transnet, “Chapter 3: Rail development plan,” [Online]. Available: <https://www.transnet.net/BusinessWithUs/LTPF%202017/LTPF%20Chapter%203%20Rail%20Development%20Plan.pdf>. [Accessed 17 August 2023].
- [5] C. Pyrgidis and E. Christogiannis, “The Problems of the Presence of Passenger and Freight Trains on the Same Track,” *Procedia - Social and Behavioral Sciences*, vol. 48, pp. 1143-1154, 2012.
- [6] S. Zakharov, I. Goryacheva, V. Bogdanov, D. Pogorelov, I. Zharov, V. Yazykov, E. Torskaya and S. Soshenkov , “Problems with wheel and rail profiles selection and optimization,” *Wear*, vol. 265, no. 9-10, pp. 1266-1272, 2008.
- [7] SA-Venues, “Gautrain,” [Online]. Available: <https://www.sa-venues.com/attractionsga/gautrain.php>. [Accessed 17 August 2023].
- [8] D. P. Thomas , “The Gautrain project in South Africa: a cautionary tale,” *Journal of Contemporary African Studies*, vol. 31, no. 1, pp. 77-94, 2011.
- [9] Transnet, “Annual results announcement,” Transnet, 31 March 2021. [Online]. Available:

- <https://www.transnet.net/InvestorRelations/AR2021/2021%20ANNUAL%20RESULTS%20PRESENTATION.pdf>. [Accessed 15 November 2022].
- [10] Transnet, “Annual results announcement,” 31 March 2022. [Online]. Available: <https://www.transnet.net/InvestorRelations/AR2022/TRANSNET%202022%20YEAR%20END%20RESULTS%20PRESENTATION.pdf>. [Accessed 15 November 2022].
- [11] Transnet, “Transnet Freight Rail,” 2021. [Online]. Available: <https://www.transnet.net/InvestorRelations/AR2021/Transnet%20Freight%20Rail.pdf>. [Accessed 22 March 2022].
- [12] International Trade Administration, “International Trade Administration,” International Trade Administration, 11 September 2021. [Online]. Available: <https://www.trade.gov/country-commercial-guides/south-africa-rail-infrastructure>. [Accessed 19 February 2023].
- [13] K. Magubane, “news24,” 12 May 2022. [Online]. Available: <https://www.news24.com/fin24/economy/back-on-track-government-releases-sas-draft-plan-to-revive-rail-20220512>. [Accessed 19 February 2023].
- [14] C. P. D. de Charmoy and P. J. Gräbe, “Quantifying the economic benefits of gauge changes on the South African core railway network,” *Journal of the South African Institution of Civil Engineering*, vol. 62, no. 3, pp. 23-35, 2020.
- [15] C. KGOSANA, “Transport department has lofty plans for rail expansion,” *businesslive*, MAY 12 2022. [Online]. Available: <https://www.businesslive.co.za/bd/national/2022-05-12-transport-department-has-lofty-plans-for-rail-expansion/>. [Accessed 16 August 2023].
- [16] W. Zhong, J. J. Hu, P. Shen, C. Y. Wang and Q. Y. Lius, “Experimental investigation between rolling contact fatigue and wear of high-speed and heavy-haul railway and selection of rail material,” *Wear*, vol. 271, p. 2485– 2493, 2011.

- [17] D. Fletcher and J. Beynon, “Development of a Machine for Closely Controlled Rolling Contact Fatigue and Wear Testing,” *Journal of Testing and Evaluation*, vol. 28, no. 4, pp. 267-275, 2000.
- [18] J. E. Garnham, “The Wear of Bainitic and Pearlitic Steels, PhD thesis,” The University of Leicester, Leicester, 1995.
- [19] Y. Hu, W. J. Wang, M. Watson, K. Six, H. Al-Maliki, A. Meierhofer and R. Lewis, “Wear of driving versus driven discs in a twin disc rolling-sliding test,” *Wear*, Vols. 512-513, 2023.
- [20] R. Lewis and R. S. Dwyer-Joyce, “Wear mechanisms and transitions in railway wheel steels,” *Proceedings of the Institution of Mechanical Engineers, Part J: Journal of Engineering Tribology*, vol. 218, no. 6, p. 467–478, 2004.
- [21] C. Hardwick, R. Lewis and D. T. Eadie, “Wheel and rail wear—Understanding the effects of water and grease,” *Wear*, vol. 314, no. 1-2, pp. 198-204, 2014.
- [22] B. Rodríguez-Arana, A. Emeterio, M. Panera, A. Montes and D. Álvarez, “Investigation of a relationship between twin-disc wear rates and the slipping contact area on R260 grade rail,” *Tribology International*, vol. 168, pp. 1-15, 2022.
- [23] W. J. Wang, S. R. Lewis, R. Lweis, A. Beagles, C. G. He and Q. Y. Liu, “The role of slip ratio in rolling contact fatigue of rail materials under wet conditions,” *Wear*, Vols. 376-377, Part B, p. 1892–1900, 2017.
- [24] M. Takikawa and Y. Iriya, “Laboratory simulations with twin-disc machine on head check,” *Wear*, vol. 265, no. 9-10, p. 1300–1308, 2008.
- [25] R. A. Smith, “The wheel–rail interface—some recent accidents,” *Fatigue & Fracture of Engineering Materials & Structures*, vol. 26, no. 10, pp. 901-907, 2003.
- [26] Y. Zhu, W. Wang, R. Lewis, W. Yan, S. R. Lewis and H. Ding, “A review on wear between railway wheels and rails under environmental conditions,” *Journal of Tribology*, vol. 141, no. 12, pp. 1-13, 2019.



- [27] R. Lewis, . E. Magel, W.-J. Wang, U. Olofsson, S. Lewis, T. Slatter and A. Beagles, “Towards a standard approach for the wear testing of wheel and rail materials,” *Proceedings of the Institution of Mechanical Engineers, Part F: Journal of Rail and Rapid Transit*, vol. 231, no. 7, p. 760–774, 2017.
- [28] R. Lewis, R. S. Dwyer-Joyce, S. R. Lewis, C. Hardwick and E. A. Gallardo-Hernandez, “Tribology of the Wheel-Rail Contact: The Effect of Third Body Materials,” *International Journal of Railway Technology*, vol. 1, no. 1, pp. 167-194, 2012.
- [29] E. Sheinman, “Wear of rails. A review of the American press,” *Journal of Friction and Wear*, vol. 33, no. 4, p. 308–314, 2012.
- [30] K. J. Sawley, “Materials in railway engineering,” *Metals and materials*, vol. 5, no. 4, pp. 210-214, 1989.
- [31] M. Omasta and H. Chen, “Wheel-rail interface under extreme conditions,” in *Rail Infrastructure Resilience*, Cambridge, Woodhead Publishing, 2022, pp. 137-160.
- [32] O. I. Ahmed, “Wear Analysis on Wheel-Rail contact in Rolling-Sliding contact using FEM: MSc Thesis,” Addis Ababa Institute of Technology, Addis Ababa, 2017.
- [33] R. Lewis and U. Olofsson, “Basic tribology of the wheel-rail contact,” in *Wheel-Rail Interface Handbook*, Cambridge, Woodhead, 2009, pp. 34-57.
- [34] H. Tournay, “Supporting Technologies Vehicle Track Interaction”, in Guidelines to Best Practice for Heavy Haul Railway Operations: Wheel and Rail Interface Issues,” International Heavy Haul Association, Virginia Beach, USA., 2001.
- [35] U. Olofsson and Y. Lyu, “Open System Tribology in the Wheel–Rail Contact—A Literature Review,” *Applied Mechanics Reviews*, vol. 69, no. 6, pp. 1-10, 2017.
- [36] U. Olofsson and T. Telliskivi, “Wear, plastic deformation and friction of two railsteels—a full-scale test and a laboratory study,” *Wear*, vol. 254, no. 1-2, p. 80–93, 2003.

- [37] R. Lewis and U. Olofsson, “Mapping rail wear regimes and transitions,” *Wear*, vol. 257, no. 7-8, pp. 721-729, 2004.
- [38] Y. Zhu, “Adhesion in the wheel–rail contact, PhD Thesis,” Royal Institute of Technology, Stockholm, 2013.
- [39] J. J. Kalker, *Three-Dimensional Elastic Bodies in Rolling Contact*, Berlin: Springer Science & Business Media, 1990.
- [40] R. D. Fröhling, “Wheel/rail interface management in heavy haul railway operations—applying science and technology,” *Vehicle System Dynamics*, vol. 45, no. 7-8, p. 649–677, 2007.
- [41] J.-B. Ayasse and H. Chollet, “Wheel - Rail Contact,” in *Handbook of Railway Vehicle Dynamics*, Boca Raton, Taylor & Francis Group, 2006, pp. 85-120.
- [42] L. E. Buckley-Johnstone, “Wheel/Rail Contact Tribology: Characterising Low Adhesion Mechanisms and Friction Management Products, PhD Thesis,” The university of Sheffield, Sheffield, 2017.
- [43] Q. J. Wang and D. Zhu, “Hertz Theory: Contact of Cylindrical Surfaces,” in *Encyclopedia of Tribology*, Boston, MA, Springer, 2013.
- [44] R. G. Budynas and J. K. Nisbett, *Shigley's Mechanical Engineering Design*, 9th Edition, New York: McGraw-Hill, 2011.
- [45] S. Timoshenko and J. N. Goodier, *Theory of elasticity (second edition)*, New York: McGraw-Hill, 1951.
- [46] W. Yan and F. D. Fischer, “Applicability of the Hertz contact theory to rail-wheel contact problems,” *Archive of Applied Mechanics*, vol. 70, pp. 255-268, 2000.
- [47] M. S. Sichani, “On Efficient Modelling of Wheel-Rail Contact in Vehicle Dynamics Simulation, PhD thesis,” KTH Royal Institute of Technology, Stockholm, 2016.

- [48] S. Damme, “Zur Finite-Element-Modellierung des stationären Rollkontakts von Rad und Schiene, PhD thesis,” Technischen Universität Dresden, Dresden, 2006.
- [49] K. Knothe and H. Le The, “A contribution to the calculation of the contact stress distribution between two elastic bodies of revolution with non-elliptical contact area,” *Computers & Structures*, vol. 18, no. 6, pp. 1025-1033, 1984.
- [50] K. L. Johnson, “Contact Mechanics,” Cambridge University Press, Cambridge, 1985.
- [51] F. W. Carter, “On the action of a locomotive driving wheel,” *Proceedings of the Royal Society of London. Series A, containing papers of a mathematical and physical character*, vol. 112, no. 760, pp. 151-157, 1926.
- [52] J. J. Kalker, “Survey of wheel—rail rolling contact theory,” *Vehicle system dynamics*, vol. 8, no. 4, pp. 317-358, 1979.
- [53] L. Romano, M. Maglio and S. Bruni, “Transient wheel—rail rolling contact theories,” *Tribology International*, vol. 186, p. 108600, 2023.
- [54] K. L. Jonson and P. J. Vermeulen, “Contact of nonspherical bodies transmitting tangential forces,” *Journal of Applied Mechanics*, vol. 31, pp. 338-340, 1964.
- [55] L. K. Johnson, “The Effect of a Tangential Contact Force Upon the Rolling Motion of an Elastic Sphere on a Plane,” *ASME. J. Appl. Mech*, vol. 25, no. 3, p. 339–346, 1958.
- [56] B. Jacobson and J. J. Kalker, *Rolling Contact Phenomena*, Vol. 411, Berlin: Springer Science & Business Media, 2000.
- [57] J. J. Kalker, “Simplified theory of rolling contact,” *Delft Progress Report I.*, pp. 1-10, 1973.
- [58] Z. Y. Shen, J. K. Hedrick and J. A. Elkins, “A Comparison of Alternative Creep Force Models for Rail Vehicle Dynamic Analysis,” *Vehicle System Dynamics*, vol. 12, no. 1-3, pp. 79-83, 1983.

- [59] J. J. Kalker, “Wheel-rail rolling contact theory,” *Wear*, vol. 144, pp. 243-261, 1991.
- [60] X. Zhao and Z. Li, “The solution of frictional wheel–rail rolling contact with a 3D transient finite element model: Validation and error analysis,” *Wear*, vol. 271, no. 1-2, pp. 444-452, 2011.
- [61] O. Polach, “A Fast Wheel-Rail Forces Calculation Computer Code,” *Vehicle System Dynamics Supplement*, vol. 33, pp. 728-739, 1999.
- [62] O. Polach, “Creep forces in simulations of traction vehicles running on adhesion limit,” *Wear*, vol. 258, no. 7-8, pp. 992-1000, 2005.
- [63] T. Telliskivi and U. Olofsson, “Contact mechanics analysis of measured wheel-rail profiles using the finite element method,” *Proceedings of the Institution of Mechanical Engineers, Part F: Journal of Rail and Rapid Transit*, vol. 215, no. 2, pp. 65-72, 2001.
- [64] Z. Li, X. Zhao, C. Esveld, R. Dollevoet and M. Molodova, “An investigation into the causes of squats—Correlation analysis and numerical modeling,” *Wear*, vol. 265, no. 9-10, pp. 1349-1355, 2008.
- [65] Z. Li, X. Zhao, R. Dollevoet and M. Molodova, “Differential wear and plastic deformation as causes of squat at track local stiffness change combined with other track short defects,” *Vehicle System Dynamics*, vol. 46, no. S1, pp. 237-246, 2008.
- [66] J. Williams, *Engineering Tribology*, Cambridge : Cambridge University Press, 2005.
- [67] S. Andersson, “Friction and wear simulation of the wheel–rail interface,” in *Wheel–Rail Interface Handbook*, Cambridge, Woodhead Publishing Limited, 2009, pp. 93-124.
- [68] I. Hutchings and P. Shipway, “3 - Friction,” in *Tribology (Second Edition)*, Oxford, Butterworth-Heinemann, 2017, pp. 37-77.
- [69] B. Bhushan, *Principles and Applications of Tribology*, Second Edition, New York: John Wiley & Sons, Ltd, 2013.

- [70] U. Olofsson and L. Roger, “Tribology of the Wheel-Rail Contact,” in *Handbook of Railway Vehicle Dynamics*, Boca Raton, Florida, Tylor and Francis Group, 2006, pp. 121-141.
- [71] U. Olofsson and L. Hagman, “A model for micro-slip between flat surfaces based on deformation of ellipsoidal elastic bodies,” *Tribology International*, vol. 30, no. 8, pp. 599-603, 1997.
- [72] Y. Berthier, “Background on Friction and Wear,” in *Handbook of Materials Behavior Models*, Cambridge, Massachusetts, Academic Press, 2001, pp. 676-699.
- [73] L. Deters and M. Proksch, “Friction and wear testing of rail and wheel material,” *Wear*, vol. 258, no. 7-8, p. 981–991, 2005.
- [74] L. Deters, S. Engel and M. Proksch, “Friction and Wear at Tractive Rolling of Cylinders,” *Journal of Applied Mathematics and Mechanics*, vol. 80, pp. 37-40, 2000.
- [75] J. M. Cookson and P. J. Mutton, “The role of the environment in the rolling contact fatigue cracking of rails,” *Wear*, vol. 271, no. 1-2, p. 113–119, 2011.
- [76] W. J. Wang, H. Wang, H. Y. Wang, J. Guo, Q. Y. Liu, M. H. Zhu and X. S. Jin, “Sub-scale simulation and measurement of railroad wheel/rail adhesion under dry and wet conditions,” *Wear*, vol. 302, no. 1-2, p. 1461–1467, 2013.
- [77] K. Ishizaka, S. R. Lewis and R. Lewis, “The low adhesion problem due to leaf contamination in the wheel/rail contact: Bonding and low adhesion mechanisms,” *Wear*, Vols. 378-379, p. 183–197, 2017.
- [78] E. E. Magel, “A Survey of Wheel/Rail Friction,” U.S. Department of Transportation, Federal Railroad Administration, Washington, DC, 2017.
- [79] X. C. Li, H. H. Ding, W. J. Wang, J. Guo, Q. Y. Liu and Z. R. Zhou, “Investigation on the relationship between microstructure and wear characteristic of rail materials,” *Tribology International*, vol. 163, p. 107152, 2021.

- [80] H. Yahyaoui, H. Sidhom, C. Braham and A. Baczmanski, “Effect of interlamellar spacing on the elastoplastic behavior of C70 pearlitic steel: Experimental results and self-consistent modeling,” *Materials & Design*, vol. 55, p. 2014, 888-897.
- [81] K. M. Lee and A. A. Polycarpou, “Wear of conventional pearlitic and improved bainitic rail steels,” *Wear*, vol. 259, no. 1-6, pp. 391-399, 2005.
- [82] X. J. Zhao, J. Guo, H. Y. Wang, Z. F. Wen, Q. Y. Liu, G. T. Zhao and W. J. Wang, “Effects of decarburization on the wear resistance and damage mechanisms of rail steels subject to contact fatigue,” *Wear*, Vols. 364-365, pp. 130-143, 2016.
- [83] R. S. Miranda, A. B. Rezende, S. T. Fonseca, F. M. Fernandes, A. Sinatora and P. R. Mei, “Fatigue and wear behavior of pearlitic and bainitic microstructures with the same chemical composition and hardness using twin-disc tests,” *Wear*, Vols. 494-495, 2022.
- [84] D. Markov , “Laboratory tests for wear of rail and wheel steels,” *Wear*, vol. 181, pp. 678-686, 1995.
- [85] R. Ordóñez Olivares, C. I. Garcia and F. C. Robles Henrández, “Metallurgy of high-carbon steels for railroad applications,” *Journal of the Southern African Institute of Mining and Metallurgy*, vol. 113, no. 2, pp. 155-162, 2013.
- [86] R. Stock and R. Pippan, “RCF and wear in theory and practice—The influence of rail grade on wear and RCF,” *Wear*, vol. 271, no. 1-2, pp. 125-133, 2011.
- [87] H. A. Aglan and M. Fateh, “Fracture and Fatigue Crack Growth Analysis of Rail Steels,” *Journal of Mechanics of Materials and Structures*, vol. 2, no. 2, pp. 335-346, 2007.
- [88] J. Tunna, J. Sinclair and J. Perez, “A review of wheel wear and rolling contact fatigue,” *Proceedings of the Institution of Mechanical Engineers, Part F: Journal of Rail and Rapid Transit*, vol. 221, no. 2, p. 271–289, 2007.
- [89] A. J. Perez-Unzueta and J. H. Beynon, “Microstructure and wear resistance of pearlitic rail steels,” *Wear*, vol. 162–164, no. Part A, pp. 173-182, 1993.



- [90] Association of American Railroads (AAR) , “AAR M-107/M-208 Standard: AAR Manual of Standards and Recommended Practices: Wheels and Axles Wheels,” Association of American Railroads , Washington, D.C, 2016.
- [91] British Standards Institution, “Standard for Railway applications. Track. Rail. Vignole railway rails 46 kg/m and above, BS EN 13674-1:2011,” British Standards Institution, London, 2011.
- [92] G. Krauss, *Steels: Processing, Structure, and Performance (Second Edition)*, Materials Park, Ohio: ASM International, 2015, p. 315–333.
- [93] W. D. Callister and D. G. Rethwisch, *Materials Science and Engineering an Intoduction*, seventh Edition, New York: John Wiley & Sons, Inc, 2007.
- [94] M. Militzer, “Austenite Decomposition: Overall Kinetics during Isothermal, and Continuous Cooling Transformation,” in *Encyclopedia of Materials: Science and Technology*, Amsterdam, Elsevier B.V, 2001, pp. 1-5.
- [95] S. Sahay, G. Mohapatra and G. Totten, “Overview of pearlitic rail steel:accelerated cooling, quenching, microstructure, and mechanical properties,” *Journal of ASTM International*, vol. 6, no. 7, pp. 1-26, 2009.
- [96] American Society for Metals, *Atlas of Isothermal Transformation and Cooling Transformation Diagrams*, Detroit: American Society for Metals, 1977.
- [97] M. Masoumi, E. . A. Echeverri, A. P. Tschiptschin and H. Goldenstein, “Improvement of wear resistance in a pearlitic rail steel via quenching and partitioning processing,” *Scientific Reports*, vol. 9, no. 7454, pp. 1-12, 2019.
- [98] K. Ralls, T. H. Courtney and J. Wulff, *Introduction to materials science and engineering*, New York: John Wiley & Sons, Inc, 1976.
- [99] J. M. Hyzak and I. M. Bernstein , “The role of microstructure on the strength and toughness of fully pearlitic steels,” *Metallurgical Transactions A*, vol. 7, p. 1217–1224, 1976.

- [100] N. Ridley, “A Review of the Data on the Interlamellar Spacing of Pearlite,” *Metallurgical and Materials Transactions A*, vol. 15, p. 1019–1036, 1984.
- [101] M. Wang, C. Zhang, D. Sun, Z. Yang and F. Zhang, “Wear behaviour and microstructure evolution of pearlitic steels under block-on-ring wear process,” *Materials Science and Technology*, vol. 35, no. 10, pp. 1149-1160, 2019.
- [102] P. Clayton and D. Danks, “Effect of interlamellar spacing on the wear resistance of eutectoid steels under rolling-sliding conditions,” *Wear*, vol. 135, no. 2, pp. 369-389, 1990.
- [103] W. Bai, L. Zhou, P. Wang, Y. Hu, W. Wang, H. Ding, Z. Han, X. Xu and M. Zhu, “Damage behavior of heavy-haul rail steels used from the mild conditions to harsh conditions,” *Wear*, vol. 496–497, pp. 1-12, 2022.
- [104] S. Zajac , J. Komenda , P. Morris , P. Dierickx, S. Matera and F. Penalba Diaz , “Quantitative structure-property relationship for complex bainitic microstructures, Technical Steel Research,” European Commission, Luxembourg, 2005.
- [105] H. K. D. H. Bhadeshia, *Bainite in Steels: Transformations, Microstructure and Properties* (Second edition), London: The Institute of Materials, University of Cambridge, 2001.
- [106] H. K. D. H. Bhadeshia, “Martensite and bainite in steels: transformation mechanism and mechanical properties,” *Journal de Physique IV Proceedings*, vol. 7, no. 5, pp. 367-376, 1997.
- [107] A. Gianni, A. Ghidin, T. Karlsson and A. Ekberg, “Bainitic steel grade for solid wheels: metallurgical, mechanical, and in-service testing,” *Proceedings of the Institution of Mechanical Engineers, Part F: Journal of Rail and Rapid Transit*, vol. 223, no. 2, pp. 163-171, 2009.
- [108] S. M. Hasan, D. Chakrabarti and S. B. Singh, “Dry rolling/sliding wear behaviour of pearlitic rail and newly developed carbide-free bainitic rail steels,” *Wear*, Vols. 408-409, pp. 151-159, 2018.

- [109] P. Clayton, K. J. Sawley, P. J. Bolton and G. M. Pell, “Wear behavior of bainitic steels,” *Wear*, vol. 120, no. 2, pp. 199-220, 1987.
- [110] C. C. Viafara, M. I. Castro, J. M. Velez and A. Toro, “Unlubricated sliding wear of pearlitic and bainitic steels,” *Wear*, vol. 259, no. 1-6, pp. 405-411, 2005.
- [111] A. Kapoor, I. Salehi and A. M. S. Asih, “Rolling Contact Fatigue (RCF),” in *Encyclopedia of Tribology*, Boston, Springer, 2013, pp. 2736-2969.
- [112] T. P. Leso, C. W. Siyasiya, R. J. Mostert and J. Moema, “Study of rolling contact fatigue, rolling and sliding wear of class B wheel steels against R350HT and R260 rail steels under dry contact conditions using the twin disc setup,” *Tribology International*, vol. 174, pp. 1-14, 2022.
- [113] V. Manoj, K. M. Shenoy and K. Gopinath, “Developmental studies on rolling contact fatigue test rig,” *Wear*, vol. 264, no. 7-8, p. 708–718, 2008.
- [114] J.-W. Seo, H.-K. Jun, S.-J. Kwon and D.-H. Lee, “Rolling contact fatigue and wear of two different rail steels under rolling–sliding contact,” *International Journal of Fatigue*, vol. 83, no. 2, p. 184–194, 2016.
- [115] M. Diener and A. Ghidini, “Materials for Heavy Haul Solid Wheels: New Experiences,” *Proceedings of the Institution of Mechanical Engineers, Part F: Journal of Rail and Rapid Transit*, vol. 224, no. 5, p. 421–428, 2010.
- [116] S. Cummings and S. Kalay, “Development and Testing of High Performance Wheel Steels,” *9th World Congress on Railway research*, pp. 1-11, 2011.
- [117] F. R. Hernández, N. G. Demas, K. Gonzales and A. A. Polycarpou, “Correlation between laboratory ball-on-disk and full-scale rail performance tests,” *Wear*, vol. 270, no. 7-8, pp. 479-491, 2011.
- [118] H. H. Ding, C. G. He, L. Ma, J. Guo, Q. Y. Liu and W. J. Wang, “Wear mapping and transitions in wheel and rail materials under different contact pressure and sliding velocity conditions,” *Wear*, vol. 352–353, pp. 1-8, 2016.

- [119] X. Jin, L. Wu, J. Fang, S. Zhong and L. Ling, “An investigation into the mechanism of the polygonal wear of metro train wheels and its effect on the dynamic behaviour of a wheel/rail system,” *Vehicle System Dynamics*, vol. 50, no. 12, pp. 1817-1834, 2012.
- [120] W. J. Wang, H. M. Guo, X. Du, J. Guo, Q. Y. Liu and M. H. Zhu, “Investigation on the damage mechanism and prevention of heavy-haul railway rail,” *Engineering Failure Analysis*, vol. 35, p. 206–218, 2013.
- [121] E. . E. Magel, “Rolling Contact Fatigue: A Comprehensive Review,” U.S. Department of Transportation, Federal Railroad Administration, Washington, 2011.
- [122] R. Lewis, R. S. Dwyer-Joyce, U. Olofsson, J. Pombo, J. Ambrósio, M. Pereira, C. Ariaudo and N. Kuka, “Mapping railway wheel material wear mechanisms and transitions,” *Proceedings of the Institution of Mechanical Engineers, Part F: Journal of Rail and Rapid Transit*, vol. 224, no. 3, pp. 125-137, 2010.
- [123] R. Lewis, W. J. Wang, M. Burstow and S. R. Lewis, “Investigation of the influence of rail hardness on the wear of rail and wheel materials under dry conditions,” *In Proceedings of the Third International Conference on Railway Technology: Research, Development and Maintenance*, vol. 110, pp. 1-17, 2016.
- [124] F. Braghin, R. Lewis, R. S. Dwyer-Joyce and S. Bruni, “A mathematical model to predict railway wheel,” *Wear*, vol. 261, p. 1253–1264, 2006.
- [125] N. P. Suh, “The delamination theory of wear,” *Wear*, vol. 25, no. 1, pp. 111-124, 1973.
- [126] I. Hutchings and P. Shipway, “Wear by hard particles,” in *Tribology (Second Edition)*, Oxford, Butterworth-Heinemann, 2017, pp. 165-236.
- [127] M. S. Saini, M. Salot, S. Shah and M. Joshi, “Study on Wear Resistance of Al-Si Alloy using a 3-Body Dry Abrasive Wear Testing Machine,” *International Journal of Engineering Research & Technology*, vol. 4, no. 10, pp. 1-6, 2016.

- [128] H. H. Ding, Z. K. Fu, W. J. Wang, J. Gou, Q. Y. Liu and M. H. Zhu, “Investigation on the effect of rotational speed on rolling wear and damage behaviors of wheel/rail materials,” *Wear*, Vols. 330-331, p. 563–570, 2015.
- [129] A. Mahato, Y. Guo, N. K. Sundaram and S. Chandrasekar, “Surface folding in metals: a mechanism for delamination wear in sliding,” *Proceedings of the Royal Society A*, vol. 470, pp. 1-14, 2014.
- [130] D. Y. Li, “Corrosive Wear,” in *Encyclopedia of Tribology*, Boston, MA, Springer, 2013, pp. 590-595.
- [131] G. W. Stachowiak and A. W. Batchelor, “14 Fatigue Wear,” in *Tribology Series*, Amsterdam, Elsevier, 1993, pp. 657-681.
- [132] W. Barrois, “Repeated plastic deformation as a cause of mechanical surface damage in fatigue, wear, fretting-fatigue, and rolling fatigue: A review,” *International Journal of Fatigue*, vol. 1, no. 4, pp. 167-189, 1979.
- [133] G. Stachowiak and A. Batchelor, *Engineering Tribology*, 4th Edition, Oxford: Butterworth-Heinemann, 2014.
- [134] L. Blades, D. Hills, D. Nowell, K. E. Evans and C. Smith, “An exploration of debris types and their influence on wear rates in fretting,” *Wear*, Vols. 450-451, pp. 1-14, 2020.
- [135] V. Done, D. Kesavan, R. Muralikrishna, T. Chaise and D. Nelias, “Semi analytical fretting wear simulation including wear debris,” *Tribology International*, vol. 109, pp. 1-9, 2017.
- [136] Z. Ahmad, “TYPES OF CORROSION: Materials and Environments,” in *Principles of Corrosion Engineering and Corrosion Control*, Oxford, Butterworth-Heinemann, 2006, pp. 120-270.
- [137] S. Kowalski, “Fretting Wear in Selected Elements of Rail Vehicles,” *Tehnicki Vjesnik-technical Gazette*, vol. 25, pp. 481-486, 2018.

- [138] Y. Berthier, L. Vincent and M. Godet, “Fretting fatigue and fretting wear,” *Tribology International*, vol. 22, no. 4, pp. 235-242, 1989.
- [139] A. V. Olver, “The mechanism of rolling contact fatigue: an update,” *Proceedings of the Institution of Mechanical Engineers, Part J: Journal of Engineering Tribology*, vol. 129, no. 5, pp. 313-330, 2005.
- [140] C. Santus, M. Beghini, I. Bartilotta and M. Facchini, “Surface and subsurface rolling contact fatigue characteristic depths and proposal of stress indexes,” *International Journal of Fatigue*, vol. 45, pp. 71-81, 2012.
- [141] D. Nelias, M. L. Dumont, F. Champiot, A. Vincent, D. Girodin, R. Fougères and L. Flamand, “Role of Inclusions, Surface Roughness and Operating Conditions on Rolling Contact Fatigue,” *Journal of Tribology*, vol. 121, no. 2, pp. 240-251, 1999.
- [142] S. Maropoulos and N. Ridley, “Inclusions and fracture characteristics of HSLA steel forgings,” *Materials Science & Engineering A*, vol. 384, pp. 64-69, 2004.
- [143] T. Makino, T. Kato and K. Hirakawa, “The effect of slip ratio on the rolling contact fatigue property of railway wheel steel,” *International Journal of Fatigue*, vol. 36, no. 1, p. 68–79, 2012.
- [144] N. Zani and C. Petrogalli, “Predictive maps for the rolling contact fatigue and wear interaction in railway wheel steels,” *Wear*, vol. 510–511, pp. 1-9, 2022.
- [145] G. Donzella, A. Mazzù and C. Petrogalli, “Competition between wear and rolling contact fatigue at the wheel—rail interface: some experimental evidence on rail steel,” *Proceedings of the Institution of Mechanical Engineers, Part F: Journal of Rail and Rapid Transit*, vol. 223, p. 31–44, 2009.
- [146] G. Donzella, M. Faccoli, A. Mazzù, C. Petrogalli and R. Roberti, “Progressive damage assessment in the near-surface layer of railway wheel–rail couple under cyclic contact,” *Wear*, vol. 271, no. 1-2, pp. 408-416, 2011.



- [147] Y. Muhamedsalih, S. Hawksbee, G. Tucker, J. Stow and M. Burstow, “Squats on the Great Britain rail network: Possible root causes and research recommendations,” *International Journal of Fatigue*, vol. 149, p. 106267, 2021.
- [148] H. Zhu, H. Li, A. Al-Juboori, D. Wexler, C. Lu, A. McCusker, J. McLeod, S. Pannila and J. Barnes, “Understanding and treatment of squat defects in a railway network,” *Wear*, Vols. 442-443, p. 203139, 2020.
- [149] J. W. Ringsberg, M. Loo-Morrey, B. L. Josefson, A. Kapoor and J. H. Beynon, “Prediction of fatigue crack initiation for rolling contact fatigue,” *International Journal of Fatigue* 22, vol. 22, p. 205–215, 2000.
- [150] Y. B. Huang, L. B. Shi, X. J. Zhao, Z. B. Cai, Q. Y. Liu and W. J. Wang, “On the formation and damage mechanism of rolling contact fatigue surface cracks of wheel/rail under the dry condition,” *Wear*, vol. 400–401, pp. 62-73, 2018.
- [151] M. Pletz, W. Daves, W. Yao, W. Kubin and S. Scheriau, “Multi-scale finite element modeling to describe rolling contact fatigue in a wheel–rail test rig,” *Tribology International*, vol. 80, p. 147–155, 2014.
- [152] S. L. Grassie, “Studs and squats: The evolving story,” *Wear*, Vols. 366-377, pp. 194-199, 2016.
- [153] Office of Rail and Road, “Train Derailment at Hatfield: A Final Report by the Independent Investigation Board,” Office of Rail and Road, London, 2006.
- [154] S. L. Grassie, “Rolling contact fatigue on the British railway system: treatment,” *Wear*, vol. 258, no. 7-8, pp. 1310-1318, 2005.
- [155] S. Cantini and S. Cervello, “The competitive role of wear and RCF: Full scale experimental,” *Wear*, Vols. 366-367, pp. 325-337, 2016.
- [156] W. J. Wang, R. Lewis, M. D. Evans and Q. Y. Liu, “Influence of Different Application of Lubricants on Wear and Pre-existing Rolling Contact Fatigue Cracks of Rail Materials,” *Tribology Letter*, vol. 65, no. 2, pp. 1-15, 2017.

- [157] W. J. Wang, W. Zhong, J. Guo, Q. Y. Liu, M. H. Zhu and Z. R. Zhou, “Investigation on rolling contact fatigue and wear properties of railway rails,” *Proceedings of the Institution of Mechanical Engineers, Part J: Journal of Engineering Tribology*, vol. 223, no. 7, p. 1033–1039, 2009.
- [158] W. R. Tyfour, J. H. Beynon and A. Kapoor, “Deterioration of rolling contact fatigue life of pearlitic rail steel due to dry-wet rolling-sliding line contact,” *Wear*, vol. 197, no. 1-2, pp. 255-265, 1996.
- [159] G. Donzella, M. Faccoli, A. Ghidini, A. Mazzu and Roberti, “The competitive role of wear and RCF in a rail steel,” *Engineering Fracture Mechanics*, vol. 72, no. 2, p. 287–308, 2005.
- [160] K. L. Johnson, “The Strength of Surfaces in Rolling Contact,” *Proceedings of the Institution of Mechanical Engineers, Part C: Mechanical Engineering Science*, vol. 203, no. 3, pp. 151-163, 1989.
- [161] A. Ekberg, “Rolling Contact Fatigue of Railway Wheels Towards Tread Life Prediction through Numerical Modelling Considering Material Imperfections, Probabilistic Loading and Operational Data, PhD thesis,” Chalmers University of Technology, Gothenburg, 2000.
- [162] U. Spangenberg, “Reduction of rolling contact fatigue through the control of the wheel wear shape, PhD thesis,” University of Pretoria, Pretoria, 2017.
- [163] C. L. Pun, Q. Kan, P. J. Mutton, G. Kang and W. Yan, “Ratcheting behaviour of high strength rail steels under bi-axial compression–torsion loadings: Experiment and simulation,” *International Journal of Fatigue*, vol. 66, pp. 138-154, 2014.
- [164] B. Dirks, “Simulation and measurement of wheel on rail fatigue and wear, PhD thesis,” KTH Royal Institute of Technology, Stockholm, 2015.
- [165] Y. Xie, W. Wang, J. Guo, B. An, R. Chen, Q. Wu, E. Bernal, H. Ding and M. Spiriyagin, “Rail rolling contact fatigue response diagram construction and shakedown map optimization,” *Wear*, Vols. 528-529, p. 204964, 2023.

- [166] C. Ma, L. Gao, R. Cui and T. Xin, “The initiation mechanism and distribution rule of wheel high-order polygonal wear on high-speed railway,” *Engineering Failure Analysis*, vol. 119, pp. 1-14, 2021.
- [167] D. W. Barke and W. K. Chiu , “A review of the effects of out-of-round wheels on track and vehicle components,” *Proceedings of the Institution of Mechanical Engineers, Part F: Journal of Rail and Rapid Transit*, vol. 219, no. 3, pp. 151-175, 2005.
- [168] J. Zhang, G.-x. Han, X.-b. Xiao, R.-q. Wang, Y. Zhao and . X.-s. Jin, “Influence of wheel polygonal wear on interior noise of high-speed trains,” *Journal of Zhejiang University SCIENCE A*, vol. 15, p. 1002–1018, 2014.
- [169] H. Shi, J. Wang, P. Wu, C. Song and W. Teng, “Field measurements of the evolution of wheel wear and vehicle dynamics for high-speed trains,” *Vehicle System Dynamics*, vol. 56, no. 8, pp. 1187-1206, 2018.
- [170] W. Shan and Y. Song, “Investigations on formation mechanisms of out-of-round wheel and its influences on the vehicle system,” *IOP Conference Series: Materials Science and Engineering*, vol. 397, pp. 1-10, 2018.
- [171] V. Esslinger, R. Kieselbach, R. Koller and B. Weisse, “The railway accident of Eschede – technical background,” *Engineering Failure Analysis*, vol. 11, no. 4, p. 515–535, 2004.
- [172] D. Thompson, *Railway Noise and Vibration - Mechanisms, Modelling and Means of Control*, Amsterdam: Elsevier, 2009, p. 2009.
- [173] C. D. Liu, M. N. Bassim and S. s. Lawrence, “Evaluation of fatigue-crack initiation at inclusions in fully pearlitic steels,” *Materials Science and Engineering: A*, vol. 167, no. 1-2, pp. 107-113, 1993.
- [174] J. E. Garnham, R. G. Ding and C. L. Davis, “Ductile inclusions in rail, subject to compressive rolling–sliding contact,” *Wear*, vol. 269 , p. 733–746, 2010.

- [175] J. Guo, W. Yang, X. Shi, Z. Zheng, S. Liu, S. Duan, J. Wu and H. Guo, “Effect of Sulfur Content on the Properties and MnS Morphologies of DH36 Structural Steel,” *Metals*, vol. 8, no. 11, pp. 1-17, 2018.
- [176] J. Maciejewski, “The Effects of Sulfide Inclusions on Mechanical Properties and Failures of Steel Components,” *Journal of Failure Analysis and Prevention*, vol. 15, p. 169–178, 2015.
- [177] S. K. Dhua, A. Ray, S. K. Sen, M. S. Prasad, K. B. Mishra and S. Jha, “Influence of nonmetallic inclusion characteristics on the mechanical properties of rail steel,” *Journal of Materials Engineering and Performance*, vol. 9, p. 700–709, 2000.
- [178] J. S. Moema, S. M. Semanya and C. Jones, “Qualitative and quantitative determination of inclusions in high-carbon steel alloy (Class B) for rail wheel application by SEM/EDS analysis,” *Journal of the Southern African Institute of Mining and Metallurgy*, vol. 113, no. 2, pp. 73-79, 2013.
- [179] W. E. Duckworth and E. Ineson, “The effects of externally introduced alumina particles on the fatigue life of En24 steel,” *Clean Steels, Iron Steel Institute*, vol. 77, pp. 87-103, 1963.
- [180] D. M. Fegredo, M. T. Shehata, A. Palmer and J. Kalousek, “The effect of sulphide and oxide inclusions on the wear rates of a standard C-Mn and a Cr-Mo alloy rail steel,” *Wear*, vol. 126, no. 3, pp. 285-306, 1988.
- [181] L. O. Uhrus, “Through-Hardening Steels for Ball Bearings – Effect of Inclusions on Endurance,” *Clean Steels, Iron Steel Institute*, vol. 77, pp. 104-109, 1963.
- [182] K. Cvetkovski and J. Ahlström, “Characterisation of plastic deformation and thermal softening of the surface layer of railway passenger wheel treads,” *Wear*, vol. 300, no. 1-2, pp. 200-204, 2013.
- [183] J. P. Srivastava, P. . K. Sarkar and V. Ranjan, “Effects of thermal load on wheel–rail contacts: A review,” *Journal of Thermal Stresses*, vol. 39, no. 11, pp. 1389-1418, 2016.

- [184] K. J. Sawley, “Calculation of temperatures in a sliding wheel/rail system and implications for wheel steel development,” *Proceedings of the Institution of Mechanical Engineers, Part F: Journal of Rail and Rapid Transit*, vol. 221, no. 4, p. 455–464, 2007.
- [185] J. Ahlström and B. Karlsson, “Microstructural evaluation and interpretation of the mechanically and thermally affected zone under railway wheel flats,” *Wear*, vol. 232, no. 1, pp. 1-14, 1999.
- [186] U. Zerbst, K. Madler and H. Hintze, “Fracture mechanics in railway applications—an overview,” *Engineering Fracture Mechanics*, vol. 72, p. 163–194, 2005.
- [187] J. Ahlström and B. Karlsson, “Modelling of heat conduction and phase transformations during sliding of railway wheels,” *Wear*, vol. 253, pp. 291-300, 2002.
- [188] A. Ekberg, B. Åkesson and E. Kabo, “Wheel/rail rolling contact fatigue – Probe, predict, prevent,” *Wear*, vol. 312, no. 1-2, p. 2–12, 2014.
- [189] Y. Wei, Y. Wu and Z. Duan, “Thermal and dynamic behaviors of wheel/rail contact system considering thermal-mechanical coupling effects,” *Journal of Vibroengineering*, vol. 20, no. 6, pp. 2414-2423, 2018.
- [190] E. A. Gallardo-Hernandez, R. Lewis and R. S. Dwyer-Joyce, “Temperature in a twin-disc wheel/rail contact simulation,” *Tribology International*, vol. 39, no. 12, p. 1653–1663, 2006.
- [191] British Steelmakers Creep Committee, BSCC High Temperature Data: British Long Term Creep Rupture and Elevated Temperature Tensile Data on Steels for High Temperature Service, London: Iron and Steel Institute for the British Steelmakers Creep Committee, 1974.
- [192] H. A. Otorabad, D. Younesian, H. P. Tehrani, J. Sietsma and R. Petrov, “Modeling temperature evolution of wheel flat during formation,” *International Journal of Thermal Sciences*, vol. 140, pp. 114-126, 2019.

- [193] M. Ertz and K. Knothe, “A comparison of analytical and numerical methods for the calculation of temperatures in wheel/rail contact,” *Wear*, vol. 253, p. 498–508, 2002.
- [194] F. D. Fischer, W. Daves and E. A. Werner., “On the temperature in the wheel–rail rolling contact,” *Fatigue & Fracture of Engineering Materials & Structures*, vol. 26, no. 10, pp. 999-1006, 2003.
- [195] A. Ekberg and E. Kabo, “Fatigue of railway wheels and rails under rolling contact and thermal loading—an overview,” *Wear*, vol. 258, no. 7-8, p. 1288–1300, 2005.
- [196] H. Azade and P. Hosseini-Tehrani, “Fatigue Analysis of Railway Wheels Under Combined Thermal and Mechanical Loads,” *Journal of Thermal Stresses*, vol. 37, no. 1, pp. 34-50, 2014.
- [197] K. J. Sawley, “Calculation of temperatures in a sliding wheel/rail system and implications for wheel steel development,” *Proceedings of the Institution of Mechanical Engineers, Part F: Journal of Rail and Rapid Transit*, vol. 221, no. 4, pp. 455-464, 2007.
- [198] M. Ertz and K. Knothe , “Thermal stresses and shakedown in wheel/rail contact,” *Archive of Applied Mechanics*, vol. 72, p. 715–729, 2003.
- [199] A. Böhmer, M. Ertz and K. Knothe, “Shakedown limit of rail surfaces including material hardening and thermal stresses,” *Fatigue & Fracture of Engineering Materials & Structures*, vol. 26, no. 10, pp. 985-998., 2003.
- [200] M. Naeimi, S. Li, Z. Li, J. Wu, R. H. Petrov, J. Sietsma and R. Dollevoet, “Thermomechanical analysis of the wheel-rail contact using a coupled modelling procedure,” *Tribology International*, vol. 117, pp. 250-260, 2018.
- [201] L. Wu, Z. Wen, W. Li and Z. Jin, “Thermo-elastic–plastic finite element analysis of wheel/rail sliding contact,” *Wear*, vol. 271, pp. 437-443, 211.
- [202] K. Knothe and S. Liebelt , “Determination of temperatures for sliding contact with applications for wheel-rail systems,” *Wear*, vol. 189, pp. 91-99, 1995.



- [203] E. Magel, P. Sroba, K. Sawley and J. Kalousek, “Control of Rolling Contact Fatigue of Rails,” Centre for Surface Transportation Technology, National Research Council Canada, Calgary, Canada, 2002.
- [204] M. Sato, P. M. Anderson and D. A. Rigney, “Rolling-sliding behavior of rail steels,” *Wear*, Vols. 162-164, pp. 159-172, 1993.
- [205] J. F. Santa, P. Cuervo, P. Christoforou, M. Harmon, A. Beagles, A. Toro and R. Lewis, “Twin disc assessment of wear regime transitions and rolling contact fatigue in R400HT – E8 pairs,” *Wear*, Vols. 432-433, pp. 1-8, 2019.
- [206] R. Lewis, P. Christoforou, W. J. Wang, A. Beagles, M. Burstow and S. R. Lewis, “Investigation of the influence of rail hardness on the wear of rail and wheel materials under dry conditions (ICRI wear mapping project),” *Wear*, Vols. 430-431, pp. 383-392, 2019.
- [207] W. Zhong, L. Dong and X. Y. Liu, “Study on Wear of Wheel Steel under High Speed Working Condition,” *Advanced Materials Research*, vol. 739, pp. 462-465, 2013.
- [208] A. F. Bower and K. L. Johnson, “Plastic flow and shakedown of the rail surface in repeated wheel-rail contact,” *Wear*, vol. 144, no. 1-2, pp. 1-18, 1991.
- [209] A. Leiro, A. Kankanala, E. Vuorinen and v. Prakash, “Tribological behaviour of carbide-free bainitic steel under dry rolling/sliding conditions,” *Wear*, vol. 273, p. 2–8, 2011.
- [210] Z. Li, O. Arias-Cuevas, R. Lewis and E. A. Gallardo-Herna´ndez, “Rolling–Sliding Laboratory Tests of Friction Modifiers in Leaf Contaminated Wheel–Rail Contacts,” *Tribology Letters*, vol. 33, no. 97, p. 97–109, 2009.
- [211] C. Uyulan, M. Gokasan and S. Bogosyan, “Modeling, simulation and slip control of a railway vehicle integrated with traction power supply,” *Cogent Engineering*, vol. 4, no. 1, p. 1312680, 2017.

- [212] L. Ma, C. G. He, X. J. Zhao, J. Guo, Y. Zhu, W. J. Wang, Q. Y. Liu and X. S. Jin, “Study on wear and rolling contact fatigue behaviors of wheel/rail materials under different slip ratio conditions,” *Wear*, Vols. 366-367, pp. 13-26, 2016.
- [213] J. Seo, S. Kwon, D. Lee and H. Choi, “Evaluation of Wear Behavior of Wheel Steel Using Twin-Disc Test,” *Advanced Materials Research*, vol. 716, pp. 434-437, 2013.
- [214] E. A. Gallardo-Hernandez and R. Lewis, “Twin disc assessment of wheel/rail adhesion,” *Wear*, vol. 265, no. 9-10, pp. 1309-1316, 2008.
- [215] R. Galas, M. Omasta, L.-b. Shi, H. Ding, W.-j. Wang, I. Krupka and M. Hartl, “The low adhesion problem: The effect of environmental conditions on adhesion in rolling-sliding contact,” *Tribology International*, vol. 151, pp. 1-11, 2020.
- [216] D. I. Fletcher, P. Hyde and A. Kapoor, “Modelling and full-scale trials to investigate fluid pressurisation of rolling contact fatigue cracks,” *Wear*, vol. 265, no. 9-10, pp. 1317-1324, 2008.
- [217] D. I. Fletcher and A. Kapoor, “Rapid method of stress intensity factor calculation for semi-elliptical surface breaking cracks under three-dimensional contact loading,” *Proceedings of the Institution of Mechanical Engineers, Part F: Journal of Rail and Rapid Transit*, vol. 220, no. 3, pp. 219-234, 2006.
- [218] M. Dallago, M. Benedetti, S. Ancellotti and V. Fontanari, “The role of lubricating fluid pressurization and entrapment on the path of inclined edge cracks originated under rolling-sliding contact fatigue: Numerical analyses vs. experimental evidences,” *International Journal of Fatigue*, Vols. Volume 92, Part 2, pp. 517-530, 2016.
- [219] W. A. Skipper, A. Chalisey and R. Lewis, “A review of railway sanding system research: Wheel/rail isolation, damage, and particle application,” *Proceedings of the Institution of Mechanical Engineers, Part F: Journal of Rail and Rapid Transit*, pp. 1-17, 2019.

- [220] R. Lewis and R. S. Dwyer-Joyce, “Wear at the wheel/rail interface when sanding is used to increase adhesion,” *Proceedings of the Institution of Mechanical Engineers, Part F: Journal of Rail and Rapid Transit*, vol. 220, no. 1, p. 29–41, 2006.
- [221] U. Olofsson, “A multi-layer model of low adhesion between railway wheel and rail,” *Proceedings of the Institution of Mechanical Engineers, Part F: Journal of Rail and Rapid Transit*, vol. 221, no. 3, p. 385–389, 2007.
- [222] U. Olofsson and K. Sundvall, “Influence of leaf, humidity and applied lubrication on friction in the wheel-rail contact: Pin-on-disc experiments,” *Proceedings of the Institution of Mechanical Engineers, Part F: Journal of Rail and Rapid Transit*, vol. 218, no. 3, p. 235–242, 2004.
- [223] S. R. Lewis, R. Lewis, J. Cotter, X. Lu and D. T. Eadie, “A new method for the assessment of traction enhancers and the generation of organic layers in a twin-disc machine,” *Wear*, Vols. 366-367, p. 258–267, 2016.
- [224] S. Sharma, S. Sangal and K. Mondal, “Development of New High-Strength Carbide-Free Bainitic Steels,” *Metallurgical and Materials Transactions A*, vol. 42A, pp. 3921-3933, 2011.
- [225] P. H. Shipway, S. J. Wood and A. H. Dent, “The hardness and sliding wear behaviour of a bainitic steel,” *Wear*, vol. 203–204, pp. 196-205, 1997.
- [226] S. Sharma, S. Sangal and K. Mondal, “Reciprocating Sliding Wear Behavior of Newly Developed Bainitic Steels,” *Metallurgical and Materials Transactions A*, vol. 45A, p. 5451–5468, 2014.
- [227] X. Y. Long, J. Kang, B. Lv and F. C. Zhang, “Carbide-free bainite in medium carbon steel,” *Materials and Design*, vol. 64, pp. 237-245, 2014.
- [228] M. R. Zhang and H. C. Gu, “Microstructure and properties of carbide free bainite railway wheels produced by programmed quenching,” *Materials Science and Technology*, vol. 23, no. 8, pp. 970-974, 2007.

- [229] E. R. Petty, *Physical metallurgy of engineering materials*, London: Allen and Unwin, 1970.
- [230] F. G. Caballero, “12-Carbide-free bainite in steels,” in *Phase Transformations in Steels: Fundamentals and Diffusion-Controlled Transformations Volume 1*, Cambridge, Woodhead Publishing, 2012, pp. 436-467.
- [231] E. Kozeschnik and H. K. D. H. Bhadeshia, “Influence of silicon on cementite precipitation in steels,” *Materials Science and Technology*, vol. 24, no. 3, pp. 343-347, 2008.
- [232] V. Jerath, K. Mistry, P. Bird and R. R. Preston, “British Steel Report Collaborative Research (Report SL/RS/R/S/1975/1/91A), 1–43,” University of Cambridge (H. K. D. H Bhadeshia) and British Steel Corporation, 1991.
- [233] P. D. Temple, M. Harmon, R. Lewis, M. C. Burstow, B. Temple and D. Jones, “Optimisation of grease application to railway tracks,” *Proceedings of the Institution of Mechanical Engineers, Part F: Journal of Rail and Rapid Transit*, vol. 232, no. 5, pp. 1514-1527, 2018.
- [234] S. R. Lewis, R. Lewis, G. Evans and L. E. Buckley-Johnstone, “Assessment of railway curve lubricant performance using a twin-disc tester,” *Wear*, vol. 314, no. 1-2, pp. 205-212, 2014.
- [235] R. Stock, L. Stanlake, C. Hardwick, M. Yu, D. Eadie and R. Lewis, “Material concepts for top of rail friction management – Classification, characterisation and application,” *Wear*, vol. 366–367, pp. 225-232, 2016.
- [236] J. Wang, C. Song, P. Wu and H. Dai, “Wheel reprofiling interval optimization based on dynamic behavior evolution for high speed trains,” *Wear*, Vols. 366-367, pp. 316-324, 2016.
- [237] Y. Muhamedsalih, G. Tucker and J. Stow, “Optimisation of wheelset maintenance by using a reduced flange wear wheel profile,” *Proceedings of the Institution of*

*Mechanical Engineers, Part F: Journal of Rail and Rapid Transit*, vol. 0, pp. 1-13, 2022.

- [238] A. C. Pires, L. A. Pacheco, I. L. Dalvi, C. S. Endlich, J. C. Queiroz, F. A. Antonioli and G. F. Santos, “The effect of railway wheel wear on reprofiling and service life,” *Wear*, vol. 477, pp. 1-12, 2021.
- [239] T. Jendel, “Prediction of wheel profile wear—comparisons with field measurements,” *Wear*, vol. 253, no. 1-2, pp. 89-99, 2002.
- [240] A. Bevan, P. Molyneux-Berry, B. Eickhoff and M. Burstow, “Development and validation of a wheel wear and rolling contact fatigue damage model,” *Wear*, vol. 307, no. 1-2, pp. 100-111, 2013.
- [241] T. P. Leso, C. W. Siyasiya, R. Mostert and J. Moema, “Study of wear performance of wheel and rail steels under dry sliding conditions,” *Suid-Afrikaanse Tydskrif vir Natuurwetenskap en Tegnologie*, vol. 40, no. 1, pp. 44-50, 2021.
- [242] T. G. Pearce and N. D. Sherratt, “Prediction of wheel profile wear,” *Wear*, vol. 144, no. 1-2, pp. 343-351, 1991.
- [243] A. Ward, R. Lewis and R. S. Dwyer-Joyce, “Incorporating a railway wheel wear model into multi-body simulations of wheelset dynamics,” *Tribology Series*, vol. 41, pp. 367-376, 2003.
- [244] P. J. Bolton and P. Clayton, “Rolling—sliding wear damage in rail and tyre steels,” *Wear*, vol. 93, no. 2, pp. 145-165, 1984.
- [245] A. Ramalho, M. Esteves and P. Marta, “Friction and wear behaviour of rolling—sliding steel contacts,” *Wear*, vol. 302, no. 1-2, pp. 1468-1480, 2013.
- [246] A. Ramalho, “Wear modelling in rail—wheel contact,” *Wear*, Vols. 230-231, p. 524–532, 2015.

- [247] I. Zobory, “Prediction of Wheel/Rail Profile Wear,” *Vehicle System Dynamics*, vol. 28, no. 2-3, pp. 221-259, 1997.
- [248] T. Jendel, “Prediction of wheel profile wear—comparisons with field measurements,” *Wear*, vol. 253, no. 1-2, pp. 89-99, 2002.
- [249] J. De Arizon, O. Verlinden and P. Dehombreux, “Prediction of wheel wear in urban railway transport: comparison of existing models,” *Vehicle System Dynamics*, vol. 45, no. 9, pp. 849-866, 2007.
- [250] B. Dirks and R. Enblom, “Prediction model for wheel profile wear and rolling contact fatigue,” *Wear*, vol. 271, no. 1-2, pp. 210-217, 2011.
- [251] S. . Z. Meymand, J. M. Craft and M. Ahmadian, “On the Application of Roller Rigs for Studying Rail Vehicle Systems,” in *Proceedings of the ASME 2013 Rail Transportation Division Fall Technical Conference. ASME 2013 Rail Transportation Division Fall Technical Conference*, Altoona, 2013.
- [252] I. Hutchings and P. Shipway, “5 - Sliding wear,” in *Tribology (Second edition)*, Oxford, Butterworth-Heinemann, 2017, pp. 107-164.
- [253] M. Naeimi, Z. Li, R. H. Petrov, J. Sietsma and R. Dollevoet, “Development of a New Downscale Setup for Wheel-Rail Contact Experiments under Impact Loading Conditions,” *Experimental Techniques volume*, vol. 42, p. 1–17, 2018.
- [254] ASTM International, “Standard Test Method for Wear Testing with a Pin-on-Disk Apparatus: ASTM G99 - 95a,” ASTM International, West Conshohocken, PA, 2000.
- [255] T. M. Albawab, U. Nirmal, I. Halim, M. A. Salem, M. Elsayed and J. Singh, “A Review on Tribological Wear Test Rigs for Various Applications,” *International Journal of Integrated Engineering*, vol. 10, no. 8, pp. 202-217, 2018.
- [256] ASTM International, “Standard Test Method for Ranking Resistance of Materials to Sliding Wear Using Block-on-Ring Wear Test: ASTM G77,” ASTM International, West Conshohocken, PA, 2017.



- [257] ASTM International, “Standard Test Method for Linearly Reciprocating Ball-on-Flat Sliding Wear. ASTM G133 - 05(2016),” ASTM International, West Conshohocken, PA, 2016.
- [258] H. E. Merritt, “Worm Gear Performance,” *Proceedings of the Institution of Mechanical Engineers*, vol. 129, no. 1, p. 127–194, 1935.
- [259] R. Galas, D. Smejkal, M. Omasta and M. Hartl, “Twin-Disc Experimental Device for Study of Adhesion in Wheel-Rail Contact,” *Engineering Mechanics*, vol. 21, no. 5, p. 329–334, 2014.
- [260] W. R. Tyfour, “Predicting the Effect of Grinding Corrugated Rail Surface on the Wear Behavior of Pearlitic Rail Steel,” *Tribology Letters*, vol. 29, no. 3, p. 229–234, 2008.
- [261] M. GRETZSCHEL and L. JASCHINSKI, “Design of an Active Wheelset on a Scaled Roller Rig,” *Vehicle System Dynamics*, vol. 41, no. 5, p. 365–381, 2004.
- [262] A. Jaschinski, H. Chollet, S. Iwnicki, A. Wickens and J. Würzen, “The application of roller rigs to railway vehicle dynamics,” *Vehicle System Dynamics*, vol. 31, no. 5-6, pp. 345-392, 1999.
- [263] F. G. de Beer, M. A. Janssens and P. P. Kooijman, “Squeal noise of rail-bound vehicles influenced by lateral contact position,” *Journal of Sound and Vibration*, vol. 267, no. 3, pp. 497-507, 2003.
- [264] P. P. Kooijman, W. J. Van Vliet, M. H. Janssens and F. G. De Beer, “Curve squeal of railbound vehicles (part 2): set-up for measurement of creepage dependent friction coefficient,” in *Proceedings of Internoise*, Nice, France, 2000.
- [265] P. Sharan, S. Mishra and A. M. Upadhyaya, “The development of laboratory downscale rail-wheel test rig model with optical sensors,” *Optical Fiber Technology*, vol. 77, p. 103287, 2023.
- [266] V. N. M. Gilani, M. Habibzadeh, S. M. Hosseinian and R. Salehfard, “A review of railway track laboratory tests with various scales for better decision-making about

- more efficient apparatus using TOPSIS analysis,” *Advances in Civil Engineering*, vol. 2022, 2022.
- [267] N. Bosso, P. D. Allen and N. Zampieri, “Scale Testing Theory and Approches,” in *Handbook of Railway Vehicle Dynamics, Second Edition*, Boca Raton, CRC Press, 2020, pp. 826-867.
- [268] M. Naeimi, Z. Li and R. Dollevoet, “Scaling Strategy of a New Experimental Rig for Wheel-Rail Contact,” *International Journal of Civil and Environmental Engineering*, vol. 8, no. 12, 2014.
- [269] G. Zhou, C. He, G. Wen and Q. Liu, “Fatigue damage mechanism of railway wheels under lateral forces,” *Tribology International*, vol. 91, pp. 160-169, 2015.
- [270] M. Jakob , F. Grün, M. Stoschka and I. Gódor, “A Novel Two-Disc Machine for High Precision Friction Assessment,” *Advances in Tribology*, pp. 1-16, 2017.
- [271] N. Bosso, A. Gugliotta and N. Zampieri, “Strategies to simulate wheel–rail adhesion in degraded conditions using a roller-rig,” *Vehicle System Dynamics*, vol. 53, no. 5, pp. 619-634, 2015.
- [272] S.-y. Zhang, . M. Spiriyagin, Q. Lin, H.-h. Ding, Q. Wu and J. Guo, “Study on wear and rolling contact fatigue behaviours of defective rail under different slip ratio and contact stress conditions,” *Tribology International*, vol. 169, p. 107491, 2022.
- [273] A. C. de Carvalho, A. B. Rezende, F. d. M. Fernandes, R. d. S. Miranda, E. J. Kina, T. Cousseau and P. R. Mei , “Effect of grease viscosity and thickener on the wear resistance of a class D railway wheel,” *Wear*, Vols. 530-531, p. 205071, 2023.
- [274] ASTM International, “Standard Hardness Conversion Tables for Metals Relationship Among Brinell Hardness, Vickers Hardness, Rockwell Hardness, Superficial Hardness, Knoop Hardness, and Scleroscope Hardness,” ASTM International, West Conshohocken, PA, 2007.

- [275] J.-W. Seo, H.-K. Jun, S.-J. Kwon and D.-H. Lee, “Rolling contact fatigue and wear of two different rail steels under rolling–sliding contact,” *International Journal of Fatigue*, vol. 83, no. 2, p. 184–194, 2016.
- [276] Q. Lian, G. Deng, A. K. Tieu, H. Li , Z. Liu , X. Wang and H. Zhu , “Thermo-mechanical coupled finite element analysis of rolling contact fatigue and wear properties of a rail steel under different slip ratios,” *Tribology International*, vol. 141, p. 105943, 2020.
- [277] R. C. Rocha, H. Ewald, A. B. Rezende and S. T. Fonseca, “Using twin disc for applications in the railway: a systematic review,” *Journal of the Brazilian Society of Mechanical Sciences and Engineering*, vol. 45, no. 191, 2023.
- [278] F. S. Vicente and M. P. Guillamón, “Use of the fatigue index to study rolling contact wear,” *Wear*, Vols. 436-437, pp. 1-9, 2019.
- [279] W. Zhang, J. Chen, X. Wu and X. Jin, “Wheel/rail adhesion and analysis by using full scale roller rig,” *Wear*, vol. 253, no. 1-2, pp. 82-88, 2002.
- [280] D. Markov , “Laboratory tests for wear of rail and wheel steels,” *Wear*, 181–183(PART 2), pp. 678-686, 1995.
- [281] Y. Hu, L. C. Guo, M. Maiorino, J. P. Liu, H. H. Ding, R. Lewis, E. Meli, A. Rindi, Q. Y. Liu and W. J. Wang, “Comparison of wear and rolling contact fatigue behaviours of bainitic and pearlitic rails under various rolling-sliding conditions,” *Wear*, Vols. 460-461, pp. 1-17, 2020.
- [282] N. Tosangthum, R. Krataitong, P. Wila, H. Koiprasert, K. Buncham, P. Kansuwan, A. Manonukul and P. Sheppard, “Dry rolling-sliding wear behavior of ER9 wheel and R260 rail couple under different operating conditions,” *Wear*, Vols. 518-519, pp. 1-14, 2023.
- [283] W. J. Wang, R. Lewis, B. Yang, L. C. Guo, Q. Y. Liu and M. H. Zhu, “Wear and damage transitions of wheel and rail materials under various contact conditions,” *Wear*, Vols. 362-363, p. 146–152, 2016.

- [284] H. Chen, A. Namura, M. Ishida and T. Nakahara, “Influence of axle load on wheel/rail adhesion under wet conditions in consideration of running speed and surface roughness,” *Wear*, Vols. 366-367, p. 303–309, 2016.
- [285] P. Clayton and D. N. Hill, “Rolling contact fatigue of a rail steel,” *Wear*, vol. 117, no. 3, pp. 319-334, 1987.
- [286] S. Maya-Johnson, A. J. Ramirez and A. Toro, “Fatigue crack growth rate of two pearlitic rail steels,” *Engineering Fracture Mechanics*, vol. 138, pp. 63-72, 2015.
- [287] J. E. Garnham and C. L. Davis, “The role of deformed rail microstructure on rolling contact fatigue initiation,” *Wear*, vol. 265, no. 9-10, pp. 1363-1372, 2008.
- [288] E. Niccolini and Y. Berthier, “Wheel–rail adhesion: laboratory study of “natural” third body role on locomotives wheels and rails,” *Wear*, vol. 258, no. 7-8, pp. 1172-1178, 2005.
- [289] B. Wu, G. Xiao, B. An, T. Wu and Q. Shen, “Numerical study of wheel/rail dynamic interactions for high-speed rail vehicles under low adhesion conditions during traction,” *Engineering Failure Analysis*, vol. 137, pp. 1-14, 2022.
- [290] B. Wu, T. Wu, Z. Wen and X. Jin, “Numerical analysis of high-speed wheel/rail adhesion under interfacial liquid contamination using an elastic-plastic asperity contact model,” *Proceedings of the Institution of Mechanical Engineers, Part J: Journal of Engineering Tribology*, vol. 231, no. 1, pp. 63-74, 2017.
- [291] C. Hardwick, R. Lewis and R. Stock, “The effects of friction management materials on rail with pre existing rcf surface damage,” *Wear*, vol. 384–385, pp. 50-60, 2017.
- [292] M. A. C. Zulkifli, K. S. Basaruddin, M. Afendi, W. H. Tan and E. M. Cheng , “Finite Element Simulation on Railway Wheels under Various Loading,” *IOP Conference Series: Materials Science and Engineering*, vol. 429, no. 1, p. 012002, 2018.
- [293] Y. Muhamedsalih, J. Stow and A. Bevan, “Use of railway wheel wear and damage prediction tools to improve maintenance efficiency through the use of economic tyre

- turning,” *Proceedings of the Institution of Mechanical Engineers, Part F: Journal of Rail and Rapid Transit*, vol. 233, no. 1, pp. 103-117, 2018.
- [294] L. Wang, H. Xu, H. Yuan, W. Zhao and X. Chen, “Optimizing the re-profiling strategy of metro wheels based on a data-driven wear model,” *European Journal of Operational Research*, vol. 242, no. 3, pp. 975-986, 2015.
- [295] P. A. de Paula Pacheco, C. S. Endlich, K. L. S. Vieira, T. Reis and G. F. M. dos Santos, “Optimization of heavy haul railway wheel profile based on rolling contact,” *Wear*, vol. 522, no. 1, p. 204704, 2023.
- [296] Railway Group Standard, “Railway Wheelsets (GMRT2466 Iss 3),” Rail Safety and Standards Board Limited, London, 2010.
- [297] R. Müller, P. Gratacos, P. Mora, J. Nielsen, J. Feng and S. Cervello, “Definition of wheel maintenance measures for reducing ground vibration,” International Union of Railways, Paris, 2013.
- [298] U. Spangenberg, R. D. Fröhling and P. S. Els, “The effect of rolling contact fatigue mitigation measures on wheel wear and rail fatigue,” *Wear*, Vols. 398-399, pp. 56-68, 2018.
- [299] B. Dirks, R. Enblom and M. Berg, “Prediction of wheel profile wear and crack growth – comparisons with measurements,” *Wear*, Vols. 366-367, pp. 84-94, 2016.
- [300] S. Zakharov, I. Komarovskiy and I. Zharov, “Wheel flange/rail head wear simulation,” *Wear*, vol. 215, no. 1-2, pp. 18-24, 1998.
- [301] R. Zong and M. Dhanasekar, “Analysis of Rail Ends under Wheel Contact Loading,” *International Journal of Mechanical and Aerospace Engineering*, vol. 6, pp. 452-60, 2012.
- [302] J. P. Srivastava, P. K. Sarkar and V. Ranjan, “An Approximate Analysis for Hertzian Elliptical Wheel-Rail Contact Problem,” *In Proceedings of the 1st International and*

*16th National Conference on Machines and Mechanisms (iNaCoMM2013)*, vol. 18, pp. 249-253, 2013.

- [303] J. F. Antoine, C. Visa, C. Sauvey and G. Abba, “Approximate Analytical Model for Hertzian Elliptical Contact Problems,” *Journal of Tribology*, vol. 128, no. 3, 2006.
- [304] S. Soemantri, W. Puja, B. Budiwanto and M. Parwata, “solution to hertzian contact problem between wheel and rail for small radius of curvature,” *Journal of Solid Mechanics and Materials Engineering*, vol. 4, no. 6, pp. 669-677, 2010.
- [305] E. Vollebregt and G. Segal, “Solving conformal wheel–rail rolling contact problems,” *Vehicle System Dynamics*, vol. 52, no. 1, pp. 455-468, 2014.
- [306] E. Vollebregt and G. Segal, “Solving conformal wheel–rail rolling contact problems,” *Vehicle System Dynamics*, vol. 52, p. 455–468, 2014.
- [307] L. C. Guo, W. T. Zhu, L. B. Shi, Q. Y. Liu, Z. B. Cai and W. J. Wang, “Study on wear transition mechanism and wear map of CL60 wheel material under dry and wet conditions,” *Wear*, Vols. 426-427, pp. 1771-1780, 2019.
- [308] X. J. Zhao, Q. Chen, Y. S. Liu, X. Y. Qiu, E. Meli and A. Rindi, “Effects of slip ratio and contact stress on rolling contact fatigue of defected rail materials,” *Engineering Failure Analysis*, vol. 131, p. 105817, 2022.
- [309] M. Ertz and F. Bucher, “Improved Creep Force Model for Wheel/Rail Contact Considering Roughness and Temperature,” *Vehicle System Dynamics*, vol. 37, pp. 314-325, 2002.
- [310] M. Ertz and K. Knothe, “A comparison of analytical and numerical methods for the calculation of temperatures in wheel/rail contact,” *Wear*, vol. 253, no. 3-4, pp. 498-508, 2002.
- [311] K. D. Vo, A. K. Tieu, H. T. Zhu and P. B. Kosasih, “A tool to estimate the wheel/rail contact and temperature rising under dry, wet and oily conditions,” *Computers in Railways XIV: Railway Engineering Design and Optimization*, vol. 135, 2014.



- [312] W. Lojkowski, M. Djahanbakhsh, G. Bürkle, S. Gierlotka and W. Zielinski, “Nanostructure formation on the surface of railway tracks,” *Materials Science and Engineering A*, vol. 303, p. 97–208, 2001.
- [313] C. Bernsteiner, G. Mülle, A. Meierhofer, K. Six, D. Künstner and P. Dietmaier, “Development of white etching layers on rails: simulations and experiments,” *Wear*, Vols. 366-367, pp. 116-122, 2016.
- [314] A. Al-Juboori, D. Wexler, H. Li, H. Zhu, C. Lu, A. McCusker, J. McLeod, S. Pannil and Z. Wang, “Squat formation and the occurrence of two distinct classes of white etching layer on the surface of rail steel,” *International Journal of Fatigue*, vol. 104, pp. 52-60, 2017.
- [315] Q. Lian, G. Deng, H. Zhu, H. Li, X. Wang and Z. Liu, “Influence of white etching layer on rolling contact behavior at wheel-rail interface,” *Friction*, vol. 8, pp. 1178-1196, 2020.

## 9.4 Appendices

### 9.4.1 Appendix B: Test rig drawings

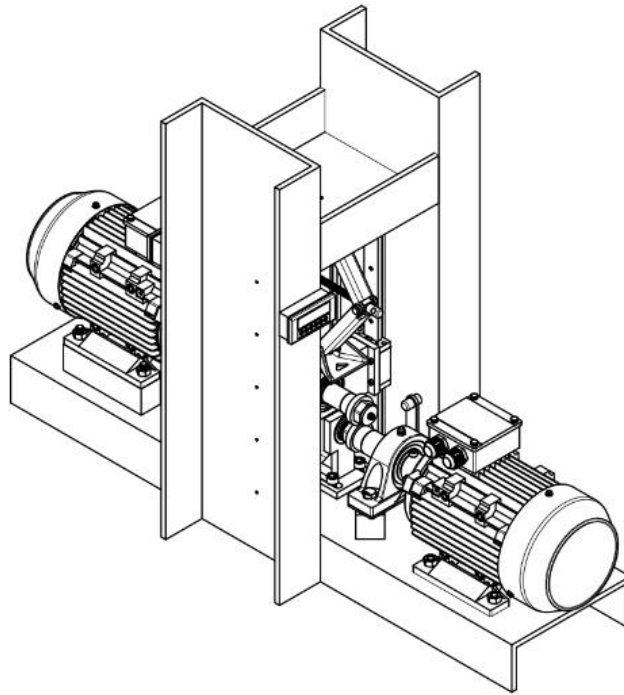


Figure 9.1: A schematic diagram showing the rig in 3D.

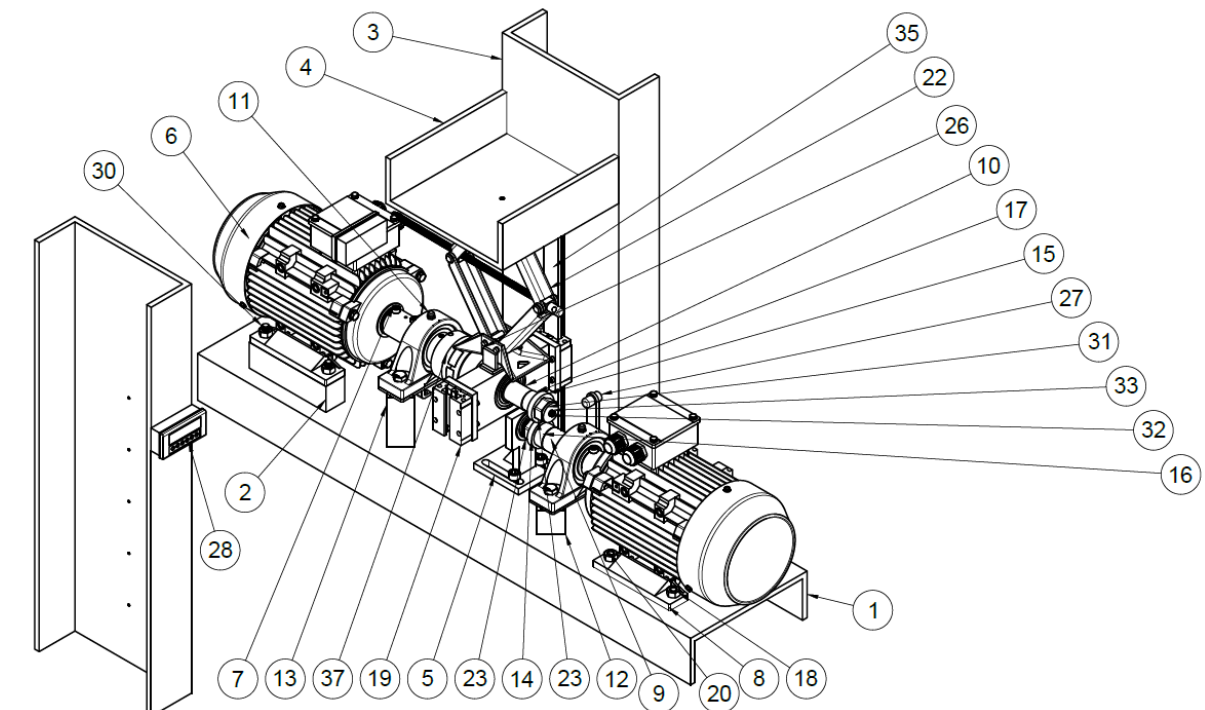


Figure 9.2: Main assembly of the rig showing different components (parts).

Table 9.1: Parts list

Parts List		
Item	Qty	Part Number
1	1	BASE
2	2	MOTOR RAISE
3	2	VERTICAL BEAM
4	1	TOP BEAM v3
5	1	BEARING SUPPORT v16
6	1	3 PHASE MOTOR v2
7	1	SHAFT 3 v15
8	1	3 PHASE MOTOR v2 (1)
9	1	SHAFT 1 v23
10	1	SHAFT 2 v11
11	2	BLOCK BEARING v5
12	1	SHAFT 1 BEARING SUPPORT
13	1	SHAFT 3 BEARING SUPPORT
14	1	RAIL DISC v6
15	1	WHEEL DISC v9
16	1	SPACER 1 v4
17	1	SPACER 2 v3
18	8	Steel Hex Nut
19	1	VERTICAL SLIDER v24

Parts List		
Item	Qty	Part Number
20	4	8.8 Steel Hex Head Screw
21	1	LOAD CELL v2
22	1	SCISSOR JACK v3
23	2	M27 NUT v2
24	1	SPEED SENSOR v2
25	1	SPEED SENSOR v2 (1)
26	2	JACK GUIDE
27	1	TEMP SENSOR v3
28	2	DIGITAL SCREEN
29	2	SHAFT KEY v2
30	4	10.9 Steel Hex Head Screw
31	2	LOCKING DISC
32	2	Steel Socket Head Screw
33	2	Stainless Steel Washer
34	1	LINEAR BEARING BOLT SET v5
35	1	LINEAR BEARING BOLT SET v5 (1)
36	2	SHAFT 3 KEY
37	1	High-Torque Set Screw Flexible Shaft Coupling

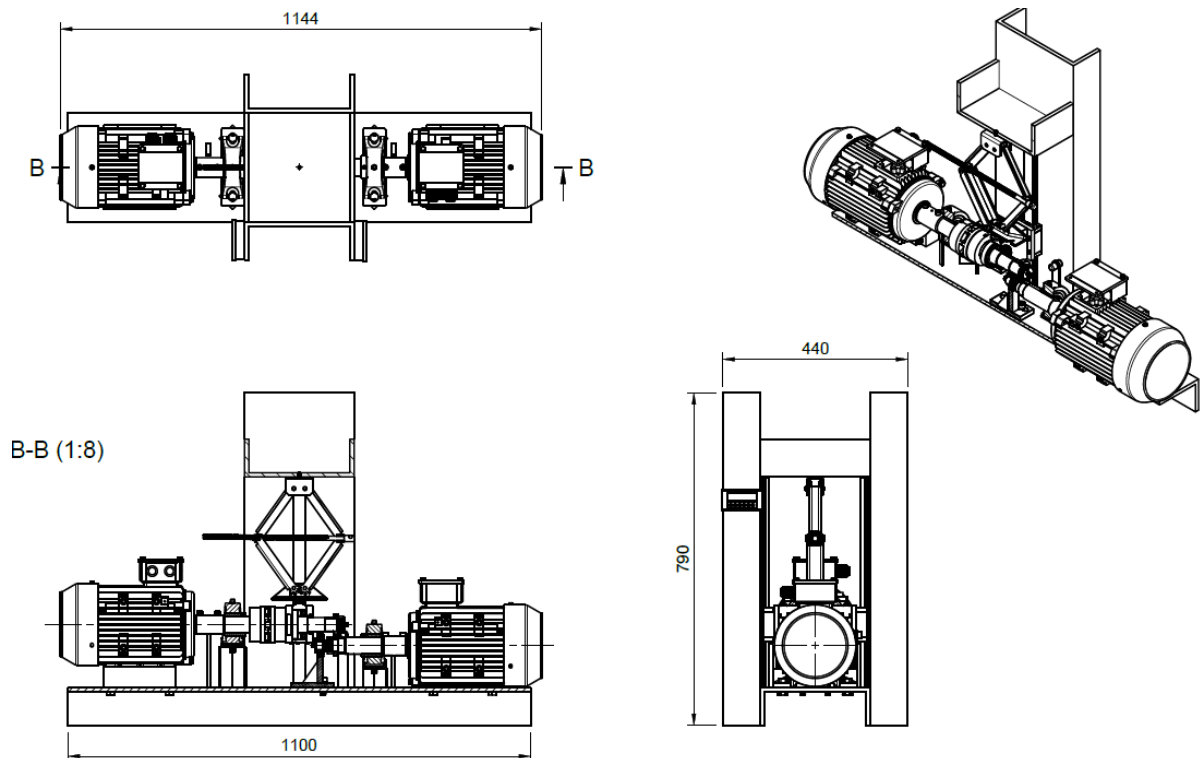
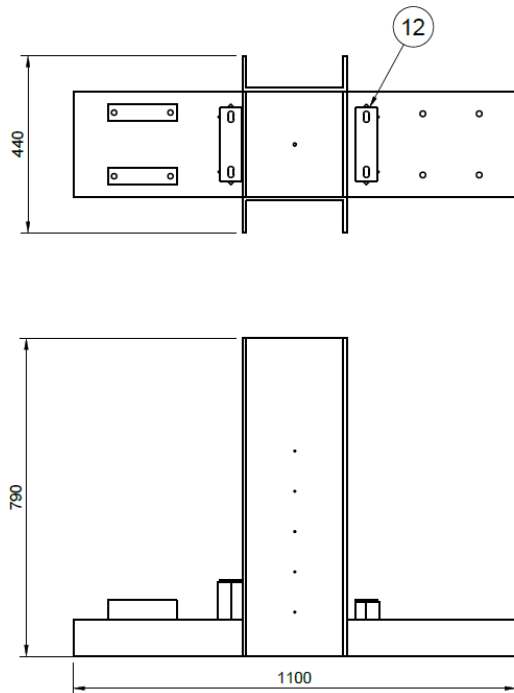


Figure 9.3: An orthographic diagram of the test rig.



Parts List		
Item	Qty	Part Number
1	1	BASE
2	2	MOTOR RAISE
3	2	VERTICAL BEAM
4	1	TOP BEAM v3
12	1	SHAFT 1 BEARING SUPPORT
13	1	SHAFT 3 BEARING SUPPORT

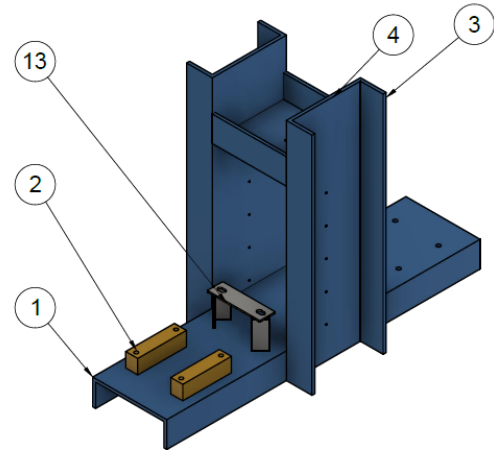


Figure 9.4: A schematic diagram of the main frame of the test rig.

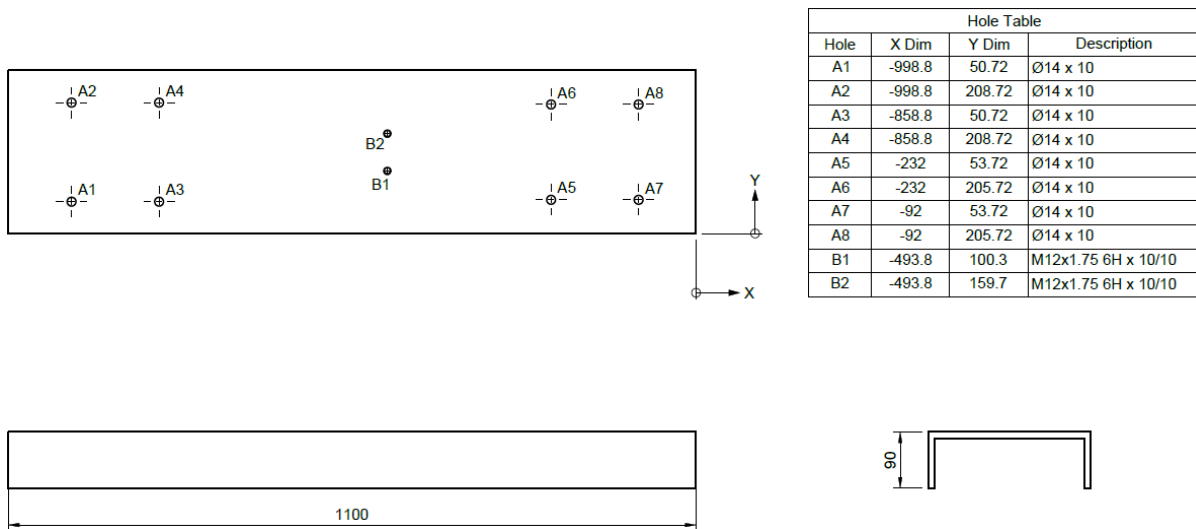


Figure 9.5: A schematic diagram of the base beam.

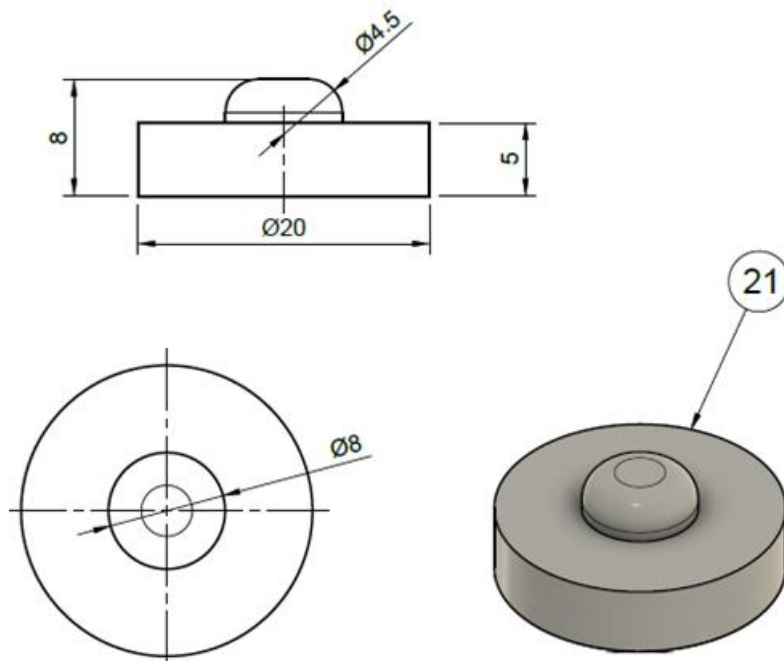


Figure 9.6: A schematic diagram of a 10 kN C9C compressive force transducer (load cell).

#### 9.4.2 Appendix C: Pictures during development of the test rig



Figure 9.7: Pictures showing the test rig during different stages of manufacturing and assembling different components.



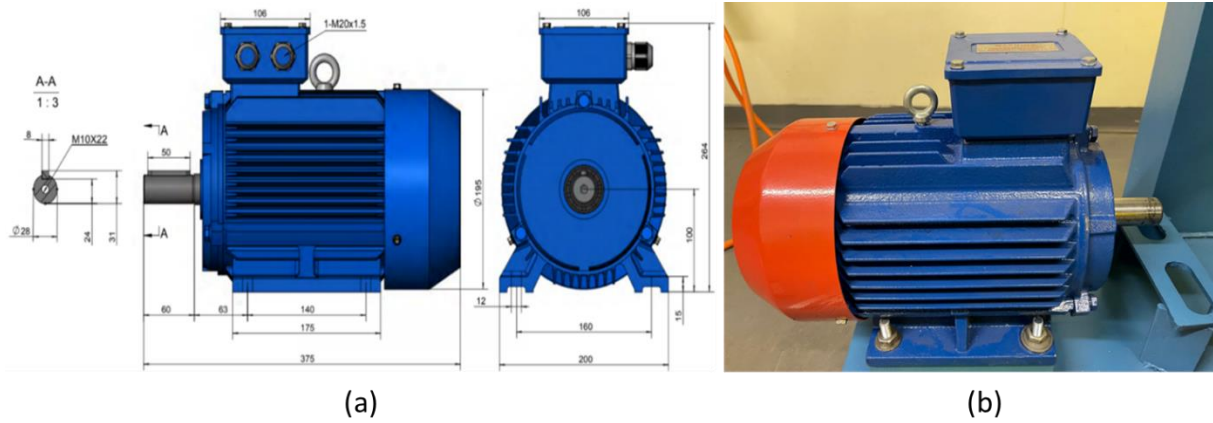


Figure 9.8: (a) A CAD drawing of the motors showing their dimensions (mm) and (b) a photograph of one of the motors used to make the rig.

#### 9.4.3 Appendix A: Wheel model drawings

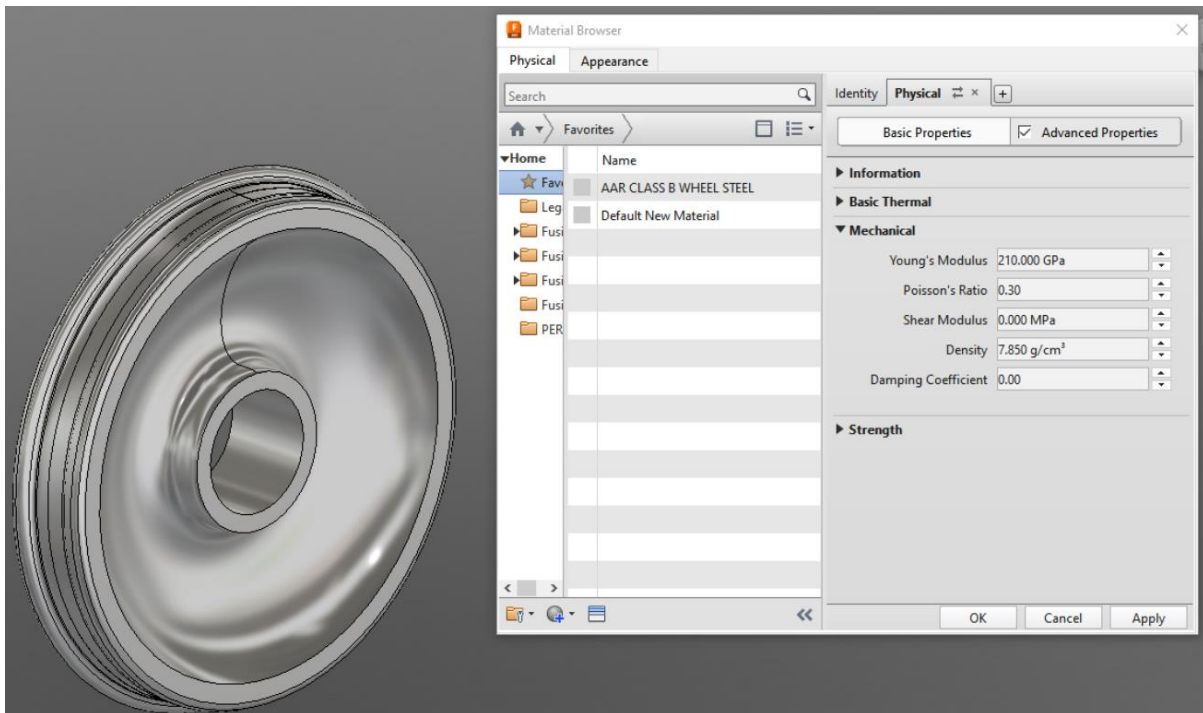


Figure 9.9: Material properties used in Fusion 360 computer-aided design software.



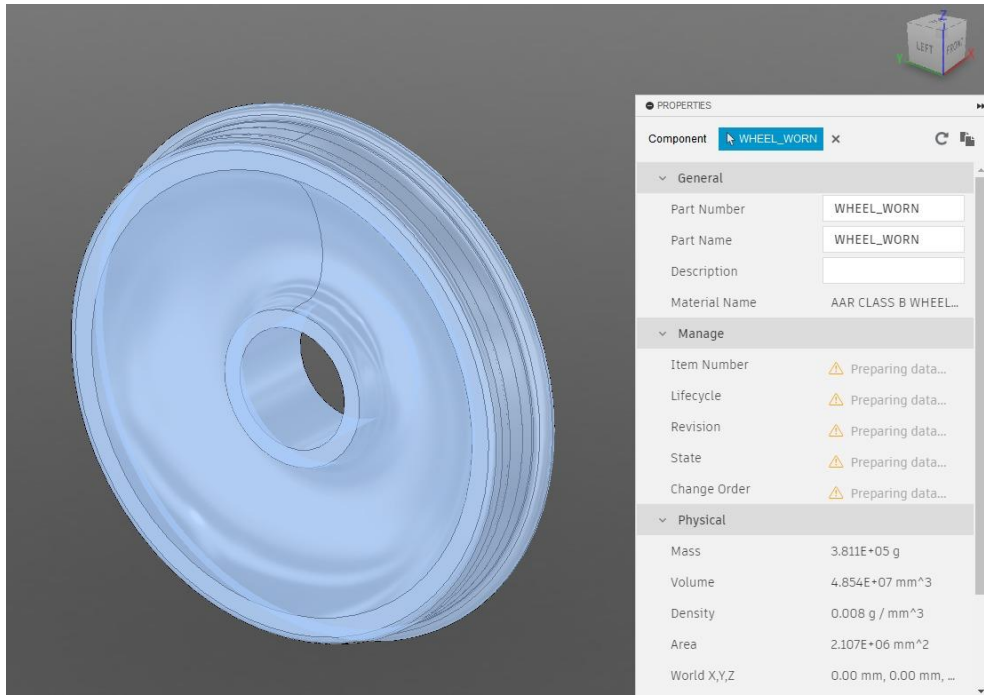


Figure 9.10: Properties of the AAR class B wheel as per the Fusion 360 computer-aided design software.